Analog quantum simulation of spin and charge quasiparticles on a quantum dot ladder

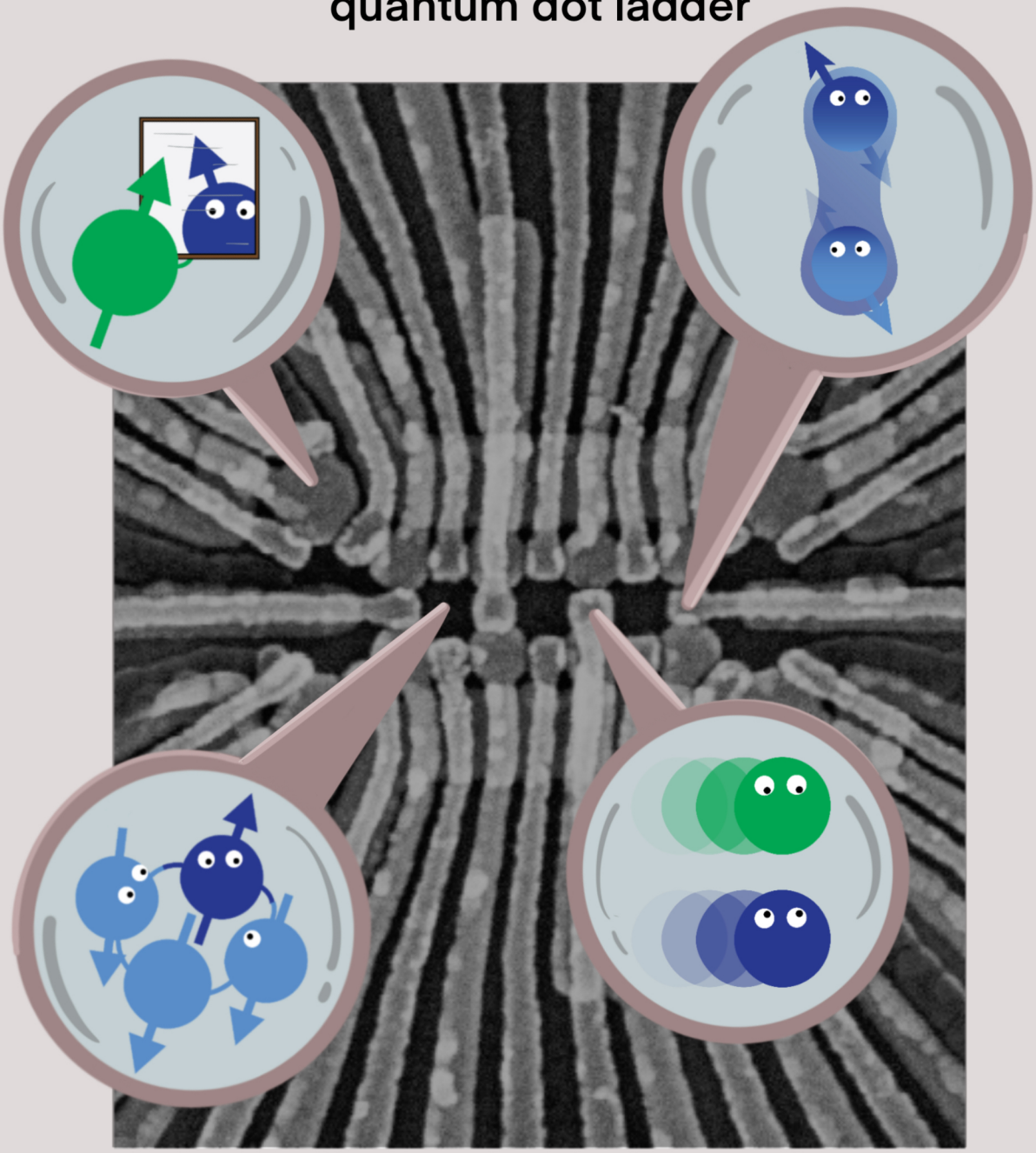

Pablo Cova Fariña

ANALOG QUANTUM SIMULATION OF SPIN AND CHARGE QUASIPARTICLES ON A QUANTUM DOT LADDER

ANALOG QUANTUM SIMULATION OF SPIN AND CHARGE QUASIPARTICLES ON A QUANTUM DOT LADDER

Dissertation

Dissertation for the purpose of obtaining the degree of doctor
at Delft University of Technology
by the authority of the Rector Magnificus, prof. dr. ir. H. Bijl,
chair of the Board for Doctorates
to be defended publicly on
Wednesday 4 March 2026 at 12:30

by

Pablo COVA FARIÑA

This dissertation has been approved by the promotors

Composition of the doctoral committee:

Rector Magnificus,	chairperson
prof. dr. ir. L.M.K. Vandersypen	Delft University of Technology, promotor
dr. G. Scappucci	Delft University of Technology, promotor
Independent members:	
prof. dr. A. F. Otte	Delft University of Technology
dr. A. Chatterjee	Delft University of Technology
prof. dr. I. Bloch	Max Planck Institute of Quantum Optics and Ludwig-Maximilians-Universität München, Germany
prof. dr. G. Platero Coello	Consejo Superior de Investigaciones Científicas, Spain
Reserve member:	
prof. dr. S. D. C. Wehner	Delft University of Technology

Keywords: Ge/SiGe quantum dots, Analog quantum simulations, Spin qubits

Printed by: Gildeprint - www.gildeprint.nl

Cover design: Noa Buijsman & Pablo Cova Fariña

ISBN 978-94-6518-257-5

An electronic version of this dissertation is available at
https://repository.tudelft.nl/.

A mis yeyas
Carmen Rosa y Araceli

CONTENTS

SUMMARY

The field of quantum simulations promises to tackle formidable problems which are inaccessible to classical computers due to their complexity. These questions range from the simulation of many-body effects in materials and fundamental questions of physics, to the exact calculation of chemical and biological processes. A possible way to tackle these problems is through the use of analog quantum simulators, a class of controllable quantum systems in which the underlying Hamiltonian is directly mappable to the problem of interest. Combined with a high degree of control and tunability over individual parameters, analog quantum simulators promise to reach practicality already at intermediate device scales, without the need for scaling up to the hundreds of thousands of sites necessary for their digital counterparts.

In this thesis, we study gate-defined semiconductor quantum dot arrays as a possible candidate for analog quantum simulators. Semiconductor quantum dots have become an attractive system for quantum technologies given their small footprint, fast operation, long coherence times and individual and in-situ tunability of couplings and on-site energies. Additionally, the system is natively described by the Fermi-Hubbard Hamiltonian, a complex many-body Hamiltonian which is predicted to give rise to a variety of interesting phases of matter. This makes quantum dot arrays a promising platform for many-body quantum simulations. However, scaling beyond a few quantum dots while maintaining a high degree of controllability has remained a long-standing challenge for the field.

In this thesis, we study a 2×4 quantum dot array of Ge/SiGe quantum dots as an analog quantum simulator, exploring the emergence of correlated spin and charge phenomena. With the quantum dots arranged in a ladder geometry, this device constitutes one of the first two-dimensional realizations of quantum dot arrays. After introducing the relevant theoretical and experimental concepts, we showcase the experimental simulation of two different types of quasiparticles and their dynamics, each emerging in a different parameter regime of the Fermi-Hubbard model. First, we look at the creation and transport of electron-hole pairs or excitons. Here, we crucially exploit the existence of strong Coulomb repulsion between both legs of the quantum dot ladder. Subsequently, we explore the dynamics of single-spin and two-spin excitations as they evolve through the array. These so-called magnon and triplon excitations propagate thanks to nearest-neighbor exchange interactions which we can locally and independently tune over a large range of parameters. This is achieved thanks to a novel scheme of crosstalk compensation which we develop and showcase in this thesis. In the last chapter, we summarize our findings, discuss challenges going forward and provide a variety of possible experiments which could be attainable with current state-of-the-art quantum dot quantum simulators.

SAMENVATTING

Het vakgebied van kwantumsimulaties belooft formidabele problemen aan te pakken die vanwege hun complexiteit ontoegankelijk zijn voor klassieke computers. Deze vraagstukken variëren van de simulatie van veeldeeltjeseffecten in materialen en fundamentele vragen uit de natuurkunde tot de exacte berekening van chemische en biologische processen. Een mogelijke manier om deze problemen op te lossen is door gebruik te maken van analoge kwantumsimulatoren, een categorie van bestuurbare kwantumsystemen waarvan de onderliggende Hamiltoniaan direct kan worden toegepast op het probleem van interesse. In combinatie met een hoge mate van besturing en instelbaarheid van individuele parameters beloven analoge kwantumsimulatoren reeds nuttig toepasbaar te zijn op gemiddelde systeem grootten, zonder dat opschaling naar de honderdduizenden eenheden nodig is die vereist zijn voor hun digitale tegenhangers.

In dit proefschrift bestuderen we door elektrodes gedefineerde halfgeleider kwantumpunt roosters als een mogelijke kandidaat voor analoge kwantumsimulatoren. Halfgeleider kwantumpunten zijn uitgegroeid tot een aansprekelijk systeem voor kwantumtechnologieën vanwege hun kleine voetafdruk, snelle manipulatie, lange coherentie tijd en de individuele en ter plekke instelbaarheid van koppelingen en lokale energieniveaus. Daarnaast wordt het systeem van nature beschreven door de Fermi-Hubbard Hamiltoniaan, een complexe veeldeeltjes Hamiltoniaan waarvan voorspeld is dat deze leidt tot een verscheidenheid aan interessante fasen van materie. Dit maakt kwantumpunt roosters tot een veelbelovend platform voor veeldeeltjes kwantumsimulaties. Echter is het opschalen voorbij een enkele aantal kwantumpunten met behoud van een hoge mate van bestuurbaarheid een langdurige uitdaging gebleven binnen het vakgebied.

In dit proefschrift bestuderen we een 2×4 kwantumpunt rooster van Ge/SiGe kwantumpunten als analoge kwantumsimulator, een verkenning van het ontstaan van gecorreleerde spin- en ladingsfenomenen. Met de kwantumpunten gerangschikt in een ladder configuratie vormt dit systeem een van de eerste tweedimensionale realisaties van kwantumpunt roosters. Na het introduceren van de relevante theoretische en experimentele concepten demonstreren we de experimentele simulatie van twee verschillende typen quasideeltjes en hun dynamica, die elk ontstaan in een ander parameter bereik van het Fermi-Hubbard model. Eerst onderzoeken we de creatie en het transport van elektron-gat paren, oftewel excitonen. Hierbij is het cruciaal dat we gebruik maken van van het bestaan van sterke Coulomb afstoting tussen beide poten van de ladder. Vervolgens verkennen we de dynamica van enkele spin en twee spin excitaties terwijl deze zich door de array bewegen. Deze zogenoemde magnon en triplon excitaties propageren dankzij verwissel interacties, die we lokaal en onafhankelijk kunnen instellen over een groot bereik van parameters. Dit wordt mogelijk gemaakt door een nieuwe methode voor het compenseren van crosstalk die we in dit proefschrift ontwikkelen en demonstreren. In het laatste hoofdstuk vatten we onze bevindingen samen, bespreken we toekomstige uitdagingen en presenteren we een reeks mogelijke experimenten die haalbaar zouden kun-

nen zijn met de huidige meest geavanceerde kwantumsimulatoren uit kwantumpunt roosters.

1

INTRODUCTION

I understand now that boundaries between noise and sound are conventions. All boundaries are conventions, waiting to be transcended. One may transcend any convention if only one can first conceive of doing so.

David Mitchell, *Cloud Atlas* (2004)

1

1.1. ONE HUNDRED YEARS

It is through the cracks of old theories that scientific revolutions are born. Exactly one hundred years ago, Werner Heisenberg published his seminal work in which he proposed a radically different mathematical structure of physics [1]. His work was followed by Schrödinger's [2], where he wrote down the famous equation that now bears his name. These papers laid the foundation of a ground-breaking theory to describe the behavior of the smallest particles in nature, the constituents of matter: **quantum mechanics**. These one hundred years have not only brought about a paradigm shift in our understanding of the world, but have enabled a technological revolution that has shaped our lives.

Today, as we celebrate the International Year of Quantum Science and Technology [3], and as quantum technologies become more discussed in society than ever before, it is insightful to look at where we have come from, before delving into the actual subject of this thesis.

1.1.1. HOW IT ALL STARTED

Quantum mechanics emerged as a consequence of the failure of classical laws of mechanics, optics and electromagnetism to account for a handful of experimental observations, which puzzled scientists at the end of the 19th and beginning of the 20th century [4]. Concretely, it was Max Planck who laid the foundation of the field in the year 1900, by successfully modeling the sun's black body radiation spectrum [5]. A key for this finding was the **quantization** of light into wave packages of energy $E = h\nu$, with ν the frequency of the light and h the Planck constant. This idea, that light was emitted and absorbed in energy packages, was hard to reconcile with the traditional laws of physics.

Subsequently, Albert Einstein applied this quantization hypothesis to explain two so far unaccounted phenomena: the photoelectric effect [6] and the specific heat of solids at low temperatures [7]. Quantization was also applied later by Bohr in his famous atomic model [8], which successfully predicted the spectral emission of hydrogen by asserting that electrons could only orbit the atomic nucleus at specific, quantized energy orbits. The emerging, unintuitive duality between the wave and the particle descriptions of light became even more explicit with de Broglie's work, where also fundamental particles like electrons are described as matter waves [9]. Following up on these ideas, the Schrödinger equation [2] was proposed: a wave equation which describes the evolution in space and time of an object $\Psi(x,t)$, known as the state vector or the **wavefunction**, as:

$$i\hbar\frac{\partial}{\partial t}\Psi(x,t) = \hat{H}\Psi(x,t), \tag{1.1}$$

with i the imaginary unit and $\hbar = \frac{h}{2\pi}$ the reduced Planck constant. The object $\hat{H}$, known as the **Hamiltonian**, summarizes the system's kinetic and potential terms into a matrix, turning the search for a system's energy and other relevant physical quantities into an eigenvalue problem. The importance of this equation, as one of the most fundamental and useful discoveries of quantum physics, cannot be overstated. In the context of this thesis, it plays a key role in understanding all quantum-mechanical phenomena which will be discussed.

1.1.2. WHAT DOES IT ALL *really* MEAN?

What followed from that first quarter of a century was a bittersweet victory. On the one hand, the new theory was successful in the description of many puzzling, classically forbidden experiments. On the other hand, the prize to pay was large: the introduction of radically new concepts that led to a completely different account of physics, often in full opposition to the classical theories. Indeed, quantum mechanics is strange by all accounts. It describes an unintuitive world in which the state of physical objects has to be described as a **superposition** of different, a priori contrary states. The result of this superposition is classically forbidden and quite challenging to imagine. Furthermore, it states that two or more quantum mechanical particles can be linked into some sort of joint entity, where they are not only individually in a superposition of several states, but where the state of one particle depends on the state of the other. This quantum **entanglement** seems to defy the laws of locality, so cherished by physicists like Einstein [10], or forces a non-realist description of nature [11].

THE SPIN

Take, for instance, the **spin**: a quantum-mechanical, magnetic property which is inherent to elementary particles and which results in a quantized, tiny magnetic moment. Electrons or protons, among other so-called spin-$\frac{1}{2}$ particles, carry a spin that can only take two values with respect to an external magnetic field $\vec{B}$: aligned with $\vec{B}$ or spin-up ($|\uparrow\rangle$), and anti-aligned with $\vec{B}$ or spin-down ($|\downarrow\rangle$). Although only these two states are allowed, the laws of quantum mechanics allow for the particle's wavefunction to be in a superposition of both spin-up and spin-down. States like $\frac{1}{\sqrt{2}}(|\uparrow\rangle + |\downarrow\rangle)$, as depicted in Fig. 1.1a, are not only allowed but fundamental in describing the behavior of electrons in real solids, and of paramount importance for the subsequent chapters of this thesis. Additionally, two interacting electrons form a so-called **singlet** as the state with the lowest energy, their **ground state**. A singlet is an entangled state of the form:

$$|\psi\rangle = \frac{1}{\sqrt{2}}(|\uparrow\downarrow\rangle - |\downarrow\uparrow\rangle), \tag{1.2}$$

where the state of one particle cannot be described without the other, the total wavefunction forming a joint superposition between the two possible, antiparallel spin states $|\uparrow\downarrow\rangle$ and $|\downarrow\uparrow\rangle$.

PARADOXES AND INTERPRETATIONS OF QUANTUM MECHANICS

Quantum theory brings about a handful of paradoxes. Why don't we observe macroscopic superpositions of classical objects, such as Schrödinger's famous cat [12]? Where is the boundary between the classical and the quantum world? What occurs during a measurement? In an attempt to settle (or quieten) these questions, many scientists like Bohr, Dirac, Heisenberg and Schrödinger brought forward the so-called Copenhagen interpretation of quantum mechanics [13] in 1927. It is, in a way, an agnostic framework: it deems questions about the microscopic reality of things meaningless. At the same time, it does ascribe reality to measured values, leading to the widespread notion of wavefunction **collapse**, where the state of a quantum mechanical system gets instantaneously reduced to one of the possible outcomes upon a measurement (Fig. 1.1c).

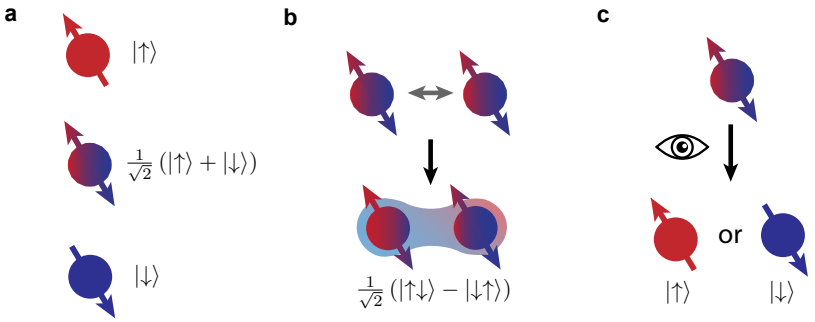

Figure 1.1: Spins and quantum mechanics. (a) The spin of an electron can be pointing in two directions: up ($|\uparrow\rangle$) or down ($|\downarrow\rangle$). Quantum mechanics additionally allows any superposition of both up and down, for example the state $\frac{1}{\sqrt{2}}(|\uparrow\rangle + |\downarrow\rangle)$. (b) Two spins can form an entangled state when they interact, for example the singlet state $\frac{1}{\sqrt{2}}(|\uparrow\downarrow\rangle - |\downarrow\uparrow\rangle)$. (c) An experimentalist who intends to observe a spin in superposition will only retrieve one of its individual states, with a probability given by square of the absolute value of the pre-factor in the superposition (in this case 50 % for both $|\uparrow\rangle$ and $|\downarrow\rangle$.)

Unsatisfied with the answers that the Copenhagen interpretation brought forward, a plethora of other interpretations have emerged over the years, all with their strengths and weaknesses. From the existence of many worlds [14], particles following well-defined, but non-local trajectories [15], and waves traveling back in time [16] to corrections to the Schrödinger equation [17] or relational accounts of physical reality [18]: All these interpretations emerge to solve the questions and paradoxes left unanswered by the standard interpretation of quantum mechanics, but themselves pose other conceptual, philosophical and practical difficulties.

What definitely emerged after one hundred years of physical and philosophical debates is perhaps one of the most perplexing paradoxes of quantum mechanics. Namely, that it is on the one hand one of the most successful theories ever posited in science, while on the other hand it leaves us quite in the dark about physical reality. That, while being a theory that has greatly advanced our scientific understanding, it also seems to be declaring a hard and perhaps unavoidable limit to science itself: That it might just never be possible to discern what is really going on in the microscopic world; and that an experimental observer, by the very process of observation, becomes inextricably linked to the system it is trying to account for. Suddenly, questions about the state of reality, rooted in the understanding of scientific realism, might be something completely outside of the scope of experimental science.

1.1.3. QUANTUM PRACTICALITY

But fear not! All of this does not matter, at least for all practical purposes. Perhaps the most widespread approach to quantum mechanics is the so-called "Shut up and calculate!" [19] method: To follow quantum physics as a recipe to predict the outcome of experiments, without caring too much about the actual philosophical and physical in-

consistencies that the theory bears. This approach has worked remarkably well[1], in that it has enabled some of the most significant technological developments of the 20th century.

As an example, the invention of the now ubiquitous laser [20] would not be conceivable without Einstein's equations for stimulated emissions [21]. The development of band theory [22, 23] allowed for the discovery of semiconductors [24]. Semiconductors themselves have led to the discovery of solar cells, light-emitting diodes and notably **transistors** [25], which themselves are the key enablers of classical processors and computers. Our understanding of atomic physics and light-matter interaction has also enabled significant advances in medicine, such as magnetic resonance imaging [26].

The era of technological development that followed the discovery of quantum physics is currently known as the **first quantum revolution** [27]. All these technological advances, such as the ones outlined above, stem from the understanding of the collective behavior of quantum mechanical particles, such as electrons in solids or photons in a laser cavity. In contrast, the manipulation of single quantum mechanical objects, as well as the explicit use of quantum entanglement as a resource, were long standing technological challenges – until the **second quantum revolution** was kick-started.

1.1.4. QUANTUM TECHNOLOGIES IN THE CONTEMPORARY ERA

Today, when we speak of **quantum technologies**, we refer to technology which is based on the control of individual quantum mechanical objects to achieve an advantage over their classical counterparts. In this context, we distinguish three key technologies: quantum sensing, quantum communication and quantum computing.

In quantum sensing [28], the sensitivity of quantum mechanical objects to perturbations of their environment is harnessed to measure small external quantities like electric or magnetic fields. Quantum communications [29] attempts to use entanglement as a resource to achieve secure communication between distant nodes and distribute quantum information, for instance aiming to enable a so-called quantum internet. In **quantum computing** [30], a system of controllable quantum objects is used to compute problems which are intractable for regular, classical computers. One important sub-field of quantum computing are **quantum simulations** [31, 32], for which we utilize a controllable quantum system to simulate the behavior of real physical systems. It is the latter that the work carried out in this thesis focuses on, and which will be the focus of the following section.

1.2. QUANTUM COMPUTING AND SIMULATIONS WITH QUANTUM DOTS

1.2.1. THE SEARCH FOR A QUANTUM COMPUTER

A quantum computer [30] is a machine which exploits the quantum-mechanical properties of superposition and entanglement to run **quantum algorithms**. These quantum

[1] It is important to remark that this approach fails greatly in the process of science communication. The temptation to avoid the open questions of quantum foundations very often leads to talks with poor, incomplete or plain wrong statements about the quantum world. The general public should be let in into not only the successes, but also the challenges that this remarkable theory entails!

algorithms offer efficient ways of solving certain problems for which no good, classical algorithm has been found. The computation of such problems could enable a number of exciting advances in the fields of materials sciences, quantum chemistry, optimization or cryptography, to name a few [33]. While many small quantum computing units or **quantum processors** exist to date, and while some instances of quantum speedup or **quantum advantage** have been shown in several experiments [34, 35], to date no quantum computer has achieved to run any useful task. This goal, coined **quantum practicality**, is the holy grail of quantum computing research. Current state-of-the-art quantum processors, being limited by their size and noise levels, are often named "noisy, intermediate-scale quantum" or **NISQ** [36] devices. The opposite case, where a quantum machine is able to run all sorts of quantum algorithms and where computational errors can be efficiently corrected, would be considered a **universal, fault tolerant** quantum computer.

THE QUBIT

The main ingredient to develop a quantum computer is a **qubit**: a quantum mechanical two-level system which can encode two logical states, $|0\rangle$ and $|1\rangle$, analogous to the classical "bit" states 0 and 1. Many candidates have been proposed and measured over the last two decades, including superconducting qubits [37], trapped ions [38], neutral atoms [39], photons [40], topological qubits [41], color centers [42], or semiconductor quantum dots [43], to name a few. The spin of an electron is an intuitive example of qubit encoding: The spin states $|\uparrow\rangle$ and $|\downarrow\rangle$ as depicted above and in Fig. 1.1 are a well-defined two-level system which could serve as a natural realization of the qubit states $|0\rangle$ and $|1\rangle$.

THE DIVINCENZO CRITERIA

Additionally, a good candidate for a quantum computer should fulfill a series of requirements known as the DiVincenzo criteria [44]. Apart from the existence of well-defined qubits, a quantum computer should allow for the following operations:

- The **initialization** of a well-defined initial state prior to the computation. An example would the the state where all spins are down: $|\downarrow\downarrow ... \downarrow\rangle = |00...0\rangle$,
- The manipulation of the state of qubits using a universal set of **quantum gates**. Often, we can limit ourselves to single- and two-qubit gates, where the former modifies the state of individual qubits (e.g. bring $|\downarrow\rangle$ to $\frac{1}{\sqrt{2}}(|\uparrow\rangle + |\downarrow\rangle)$), and the latter modifies the entanglement between two qubits (e.g. bringing $|\downarrow\uparrow\rangle$ to $\frac{1}{\sqrt{2}}(|\uparrow\downarrow\rangle - |\downarrow\uparrow\rangle)$),
- The ability to measure or **read out** the state of the qubits,
- The ability to retain the quantum state of the qubits for times much longer than the computation time (i.e. long **coherence** times), and
- The ability to **scale up** to a number of qubits large enough to perform useful quantum computation.

In this thesis, we focus on one type of quantum-mechanical system: spins in semiconductor quantum dots.

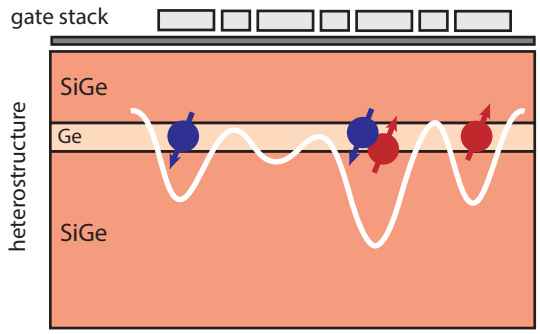

Figure 1.2: Schematics of the Ge/SiGe heterostructure used to define quantum dots for this work. Charges are first confined to a two-dimensional plane near the top interface of a Ge quantum well. A stack of metallic gates is used to further modulate the electrostatic potential by applying voltages. Under the negatively changed gates, positively charged hole can accumulate, forming quantum dots with tunable amount of charges and interactions.

1.2.2. SEMICONDUCTOR QUANTUM DOTS

A quantum dot is a structure which confines particles in all three spatial directions, in order to exploit their optical, electrical or magnetic properties. These zero-dimensional structures can be achieved in multiple ways: from colloidal and self-assembled nanoparticles, to electrostatically defined dots using metallic electrodes (or **gates**) in combination with nanowires or planar structures [45].

In this work, we make use of a planar **heterostructure** made of the semiconductors silicon (Si) and germanium (Ge) (see Fig. 1.2). By varying the material composition as a function of height, charges are confined to a two-dimensional plane in a so-called **quantum well**. Furthermore, the electrostatic potential is modulated using voltages on small gate electrodes patterned on top of the heterostructure, allowing to define the regions where the charges accumulate. For this reason, we refer to these quantum dots as **gate-defined**. The number of charges within a quantum dot, as well as their interaction strengths, can be precisely controlled using voltages (see more information on sections 3.1 and 3.4).

The idea of using spins in quantum dots as a possible platform for quantum computation was first proposed in the work of Loss and DiVincenzo in the year 1998 [46]. Since then, multiple types of **spin qubits** have been realized, steadily enabling the realization of high-fidelity single- and two-qubit gates, as well as reliable initialization and readout [47–53] over the years. Concretely, the study of **hole** spin qubits in planar, Ge/SiGe heterostructures has attracted considerable attention over the past years due to advantages in fabrication reliability, qubit control and scaling beyond one-dimensional chains of quantum dots [54–57]. The physics of quantum dots in germanium will be explained in detail in section 2.2.

1.2.3. ANALOG AND DIGITAL QUANTUM SIMULATIONS

One of the main applications of quantum technologies is the simulation of the physics of real materials, especially those where the underlying interactions between particles

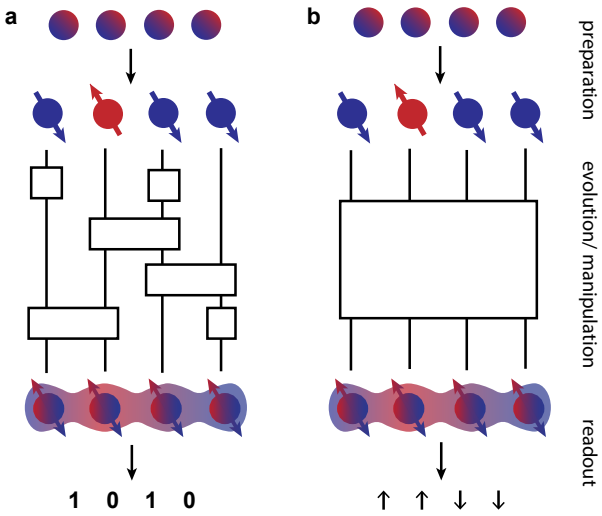

Figure 1.3: Quantum simulations: digital and analog approaches. (a) After the preparation of an initial quantum state, a system of spins is manipulated using single- and two-qubit gates, resulting in a final state which is generally entangled. Readout then retrieves some information about the final state. (b) After the preparation of an initial quantum state, a system of spins is allowed to evolve under the system's native Hamiltonian, resulting in a final state which is generally entangled. Readout then retrieves some information about the final state.

cannot be neglected. These **many-body** phenomena are often hard to calculate or to simulate. One outstanding example in this regard is high-temperature superconductivity, which has eluded a definite explanation even more than 40 years after its first experimental observation [58, 59]. In this context, it was Richard Feynman who famously proposed the idea of using controllable quantum mechanical systems to simulate or emulate the behavior of real quantum mechanical systems [31]: we now refer to this task as quantum simulation.

DIGITAL QUANTUM SIMULATIONS

There are two different ways in which quantum simulations could be performed [32], shown in Fig. 1.3. For this example, and because of its relevance to this thesis, I depict a system consistent of an array of spins. The first approach, called **digital** or gate-based quantum simulation (Fig. 1.3a), makes use of the spins as qubits: With the tools of quantum computation outlined in section 1.2.1 above, the simulation of a particular Hamiltonian of interest can be decomposed into a sequence of single- and two-qubit gates [60, 61], which realize a quantum algorithm. This algorithm can be applied to a system of spins, effectively simulating the evolution of the system under the Hamiltonian of interest, which then can be read out. This approach is, in principle, universal: Many Hamiltonians of interest could be decomposed in such a way that a fault-tolerant quantum computer could efficiently simulate them. However, such a quantum computer does not exist yet, and would often require extremely large qubit counts approaching

the millions [62].

ANALOG QUANTUM SIMULATIONS

An alternative approach is depicted in Fig. 1.3b. An initially prepared system of spins is allowed to evolve under its own interaction Hamiltonian for a certain amount of time. The final state is then read out. This type of simulation is called **analog** [32], in that it does not require any gate decomposition or any qubit-to-spin mapping. The interest lies in observing the behavior of a controllable, quantum-mechanical system (such as an array of spins) under its own, native Hamiltonian. As opposed to directly measuring the properties of real materials, where only global quantities are accessible, analog quantum simulators can offer access to microscopic quantities, as well as the tunability of Hamiltonian parameters over a wide range. This approach is clearly not universal: The system only emulates one class of Hamiltonians, namely the ones that are used to describe the system itself! However, as we will discuss throughout this thesis, analog simulations are worthwhile studying since they require much smaller numbers of quantum particles than their digital counterparts, among other benefits. They are especially appealing for systems where the native Hamiltonian corresponds to an interesting model, and where this model is hard to simulate with classical computers.

A variety of systems have been explored in literature to perform analog quantum simulations. These systems include ultracold atoms [63], trapped ions [64], superconducting qubits [37], neutral atoms in optical tweezers [65], or atoms in surfaces [66]. Recently, as fabrication and control techniques have matured, also semiconductor quantum dot arrays have been used in several quantum simulation experiments [67–70]. Across this thesis, we will often remark key distinctions and similarities between quantum simulation platforms.

Analogous to the aforementioned DiVincenzo criteria, one can define key questions relevant to analog quantum simulators [32, 61, 71, 72]:

- **Mapping**: Which Hamiltonian(s) does the quantum simulator map to? Is the simulation of this Hamiltonian a problem which is both classically intractable and useful to elucidate properties of real (quantum) systems?
- **Initialization and readout**: Which methods can be utilized to prepare any desired initial state? How can observables of interest be retrieved after the system has evolved?
- **Tunability**: How easy is it to modify any Hamiltonian parameter? Can this be done only globally or also locally? How controllable is the speed at which interactions are turned on or off? How much do the target parameters differ from the actual ones?
- **Coherence**: How well-isolated is the quantum simulator from its environment? How long can quantum information be preserved before it is lost to the environment?
- **Scalability**: How easy is it to increase the number of quantum particles, in order to reach large system sizes? How large do these system sizes need to be for a simulation to yield useful answers to a problem of interest?

- **Verifiability**: How can it be verified that the quantum evolution returns the desired state, especially as simulations become classically intractable?

I will get back to and comment on some of these questions throughout the thesis.

1.3. THESIS SCOPE AND OUTLINE

GOALS

In this work, I aim at exploring two different flavors of analog quantum simulation using quantum dot arrays, which emerge from two native Hamiltonians of our system: either the extended Fermi-Hubbard or the Heisenberg model. Despite stemming from the same physical system, the dominant type of interactions are quite distinct between both models: either repulsive, Coulomb interactions in the former, or attractive, magnetic interactions in the latter. In both cases, this thesis explores the creation and propagation of two types of **quasiparticles** emerging from these models: either electron-hole pairs or **excitons**, or spin excitations such as **magnons** and **triplons**. All experiments are performed on arrays of gate defined, Ge/SiGe quantum dots, arranged in a 2×4 fashion. Operating such devices, which can be considered state-of-the-art in terms of quantum dot count and geometry, I explore the challenges that emerge from the attempt to simultaneously initialize, manipulate and readout the state of the full array. Having performed the experiments, I will attempt to assess the potential of quantum dot devices for analog quantum simulations, remarking outstanding challenges and opportunities going forward.

OUTLINE

This thesis is structured as follows. In chapter 2, I will outline the theory of spins in quantum dot arrays, focusing on the mapping of the quantum dot Hamiltonian to the Fermi-Hubbard and the Heisenberg models, as well as the physics of quantum dots in Ge/SiGe. Subsequently, I will give a short overview of the experimental setup and procedure as well as device fabrication and characterization in chapter 3. In chapter 4, I describe the experimental simulation of exciton transport over an array of 2×4 quantum dots, highlighting the role of long-range Coulomb interactions in quantum dot systems. Chapter 5 deals with one of the main issues of scaling up quantum dot arrays for analog simulations, namely the compensation of barrier-barrier crosstalk through a process known as virtualization. The methods developed in chapter 5 are crucial for the experiments carried out in chapter 6, where I showcase the simulation of magnons and triplons as they propagate through the array. Finally, chapter 7 summarizes the findings of this thesis, analyses key advantages and limitations of our system, and proposes a path forward for analog quantum simulations using quantum dot arrays.

BIBLIOGRAPHY

[1] W. Heisenberg. “Über quantentheoretische Umdeutung kinematischer und mechanischer Beziehungen.” *Zeitschrift für Physik* 33.1 (1925), pp. 879–893.

[2] E. Schrödinger. “An Undulatory Theory of the Mechanics of Atoms and Molecules”. *Physical Review* 28.6 (1926), pp. 1049–1070.

[3] *International Year of Quantum Science and Technology | UNESCO*.

[4] W. Heisenberg. *Physics and Philosophy: The Revolution in Modern Science*. Ed. by R. N. Anshen. Amherst, N.Y.: Prometheus Books, 1958.

[5] M. Planck. “Ueber das Gesetz der Energieverteilung im Normalspectrum”. *Annalen der Physik* 309.3 (1901), pp. 553–563.

[6] A. Einstein. “Über einen die Erzeugung und Verwandlung des Lichtes betreffenden heuristischen Gesichtspunkt”. *Annalen der Physik* 322.6 (1905), pp. 132–148.

[7] A. Einstein. “Die Plancksche Theorie der Strahlung und die Theorie der spezifischen Wärme”. *Annalen der Physik* 327.1 (1907), pp. 180–190.

[8] N. Bohr. “I. On the constitution of atoms and molecules”. *The London, Edinburgh, and Dublin Philosophical Magazine and Journal of Science* 26.151 (1913), pp. 1–25.

[9] L. V. P. R. de Broglie. “Ondes et quanta”. *C. R. Acad. Sci. Paris* 177 (1923), p. 507.

[10] A. Einstein, B. Podolsky, and N. Rosen. “Can Quantum-Mechanical Description of Physical Reality Be Considered Complete?” *Physical Review* 47.10 (1935), pp. 777–780.

[11] F. Laloë. “Do we really understand quantum mechanics? Strange correlations, paradoxes, and theorems”. *American Journal of Physics* 69.6 (2001), pp. 655–701.

[12] E. Schrödinger. “Die gegenwärtige Situation in der Quantenmechanik”. *Naturwissenschaften* 23.48 (1935), pp. 807–812.

[13] J. Faye. “Copenhagen Interpretation of Quantum Mechanics”. *The Stanford Encyclopedia of Philosophy*. Ed. by E. N. Zalta and U. Nodelman. Summer 2024. Metaphysics Research Lab, Stanford University, 2024.

[14] H. Everett. “"Relative State" Formulation of Quantum Mechanics”. *Reviews of Modern Physics* 29.3 (1957), pp. 454–462.

[15] D. Bohm. “A Suggested Interpretation of the Quantum Theory in Terms of "Hidden" Variables. I”. *Physical Review* 85.2 (1952), pp. 166–179.

[16] J. G. Cramer. “The transactional interpretation of quantum mechanics”. *Reviews of Modern Physics* 58.3 (1986), pp. 647–687.

[17] G. C. Ghirardi, A. Rimini, and T. Weber. “Unified dynamics for microscopic and macroscopic systems”. *Physical Review D* 34.2 (1986), pp. 470–491.

[18] C. Rovelli. “Relational quantum mechanics”. *International Journal of Theoretical Physics* 35.8 (1996), pp. 1637–1678.

[19] N. D. Mermin. “Could Feynman Have Said This?” *Physics Today* 57.5 (2004), pp. 10–11.

[20] T. H. Maiman. “Stimulated Optical Radiation in Ruby”. *Nature* 187.4736 (1960), pp. 493–494.

[21] A. Einstein. “Zur Quantentheorie der Strahlung”. *Physikalische Zeitschrift* 18 (1917), pp. 121–128.

[22] F. Bloch. “Über die Quantenmechanik der Elektronen in Kristallgittern”. *Zeitschrift für Physik* 52.7 (1929), pp. 555–600.

[23] A. Sommerfeld and H. Bethe. “Elektronentheorie der Metalle”. *Aufbau Der Zusammenhängenden Materie*. Ed. by A. Smekal. Berlin, Heidelberg: Springer, 1933, pp. 333–622. ISBN: 978-3-642-91116-3.

[24] A. H. Wilson and P. A. M. Dirac. “The theory of electronic semi-conductors”. *Proceedings of the Royal Society of London. Series A, Containing Papers of a Mathematical and Physical Character* 133.822 (1931), pp. 458–491.

[25] J. Bardeen and W. H. Brattain. “Physical Principles Involved in Transistor Action”. *Physical Review* 75.8 (1949), pp. 1208–1225.

[26] P. C. Lauterbur. “Image Formation by Induced Local Interactions: Examples Employing Nuclear Magnetic Resonance”. *Nature* 242.5394 (1973), pp. 190–191.

[27] J. P. Dowling and G. J. Milburn. “Quantum technology: the second quantum revolution”. *Philosophical Transactions of the Royal Society of London. Series A: Mathematical, Physical and Engineering Sciences* (2003).

[28] C. L. Degen, F. Reinhard, and P. Cappellaro. “Quantum sensing”. *Reviews of Modern Physics* 89.3 (2017), p. 035002.

[29] N. Gisin and R. Thew. “Quantum communication”. *Nature Photonics* 1.3 (2007), pp. 165–171.

[30] T. D. Ladd et al. “Quantum computers”. *Nature* 464.7285 (2010), pp. 45–53.

[31] R. P. Feynman. “Simulating physics with computers”. *International Journal of Theoretical Physics* 21.6 (1982), pp. 467–488.

[32] I. M. Georgescu, S. Ashhab, and F. Nori. “Quantum simulation”. *Reviews of Modern Physics* 86.1 (2014), pp. 153–185.

[33] A. Montanaro. “Quantum algorithms: an overview”. *npj Quantum Information* 2.1 (2016), p. 15023.

[34] F. Arute et al. “Quantum supremacy using a programmable superconducting processor”. *Nature* 574.7779 (2019), pp. 505–510.

[35] H.-S. Zhong et al. “Quantum computational advantage using photons”. *Science* 370.6523 (2020), pp. 1460–1463.

[36] J. Preskill. “Quantum Computing in the NISQ era and beyond”. *Quantum* 2 (2018), p. 79.

[37] M. Kjaergaard et al. “Superconducting Qubits: Current State of Play”. *Annual Review of Condensed Matter Physics* 11.Volume 11, 2020 (2020), pp. 369–395.

[38] C. D. Bruzewicz et al. “Trapped-ion quantum computing: Progress and challenges”. *Applied Physics Reviews* 6.2 (2019), p. 021314.

[39] L. Henriet et al. “Quantum computing with neutral atoms”. *Quantum* 4 (2020), p. 327.

[40] S. Slussarenko and G. J. Pryde. “Photonic quantum information processing: A concise review”. *Applied Physics Reviews* 6.4 (2019), p. 041303.

[41] V. Lahtinen and J. Pachos. “A Short Introduction to Topological Quantum Computation”. *SciPost Physics* 3.3 (2017), p. 021.

[42] S. Pezzagna and J. Meijer. “Quantum computer based on color centers in diamond”. *Applied Physics Reviews* 8.1 (2021), p. 011308.

[43] G. Burkard et al. “Semiconductor spin qubits”. *Reviews of Modern Physics* 95.2 (2023), p. 025003.

[44] D. P. DiVincenzo. “The Physical Implementation of Quantum Computation”. *Fortschritte der Physik* 48.9-11 (2000), pp. 771–783.

[45] F. P. García de Arquer et al. “Semiconductor quantum dots: Technological progress and future challenges”. *Science* 373.6555 (2021), eaaz8541.

[46] D. Loss and D. P. DiVincenzo. “Quantum computation with quantum dots”. *Physical Review A* 57.1 (1998), pp. 120–126.

[47] M. Veldhorst et al. “An addressable quantum dot qubit with fault-tolerant control-fidelity”. *Nature Nanotechnology* 9.12 (2014), pp. 981–985.

[48] P. Harvey-Collard et al. “High-Fidelity Single-Shot Readout for a Spin Qubit via an Enhanced Latching Mechanism”. *Physical Review X* 8.2 (2018), p. 021046.

[49] J. Yoneda et al. “A quantum-dot spin qubit with coherence limited by charge noise and fidelity higher than 99.9%”. *Nature Nanotechnology* 13.2 (2018), pp. 102–106.

[50] J. Z. Blumoff et al. “Fast and High-Fidelity State Preparation and Measurement in Triple-Quantum-Dot Spin Qubits”. *PRX Quantum* 3.1 (2022), p. 010352.

[51] X. Xue et al. “Quantum logic with spin qubits crossing the surface code threshold”. *Nature* 601.7893 (2022), pp. 343–347.

[52] A. R. Mills et al. “Two-qubit silicon quantum processor with operation fidelity exceeding 99%”. *Science Advances* 8.14 (2022), eabn5130.

[53] W. I. L. Lawrie et al. “Simultaneous single-qubit driving of semiconductor spin qubits at the fault-tolerant threshold”. *Nature Communications* 14.1 (2023), p. 3617.

[54] N. W. Hendrickx et al. “A four-qubit germanium quantum processor”. *Nature* 591.7851 (2021), pp. 580–585.

[55] C.-A. Wang et al. “Operating semiconductor quantum processors with hopping spins”. *Science* 385.6707 (2024), pp. 447–452.

[56] V. John et al. *A two-dimensional 10-qubit array in germanium with robust and localised qubit control*. 2024.

[57] X. Zhang et al. “Universal control of four singlet–triplet qubits”. *Nature Nanotechnology* (2024), pp. 1–7.

[58] K. A. Müller and J. G. Bednorz. “The Discovery of a Class of High-Temperature Superconductors”. *Science* 237.4819 (1987), pp. 1133–1139.

[59] X. Zhou et al. “High-temperature superconductivity”. *Nature Reviews Physics* 3.7 (2021), pp. 462–465.

[60] H. F. Trotter. “On the Product of Semi-Groups of Operators”. *Proceedings of the American Mathematical Society* 10.4 (1959), pp. 545–551.

[61] S. Lloyd. “Universal Quantum Simulators”. *Science* 273.5278 (1996), pp. 1073–1078.

[62] A. M. Dalzell et al. *Quantum Algorithms: A Survey of Applications and End-to-end Complexities*. Cambridge: Cambridge University Press, 2025. ISBN: 978-1-009-63964-4.

[63] I. Bloch, J. Dalibard, and S. Nascimbène. “Quantum simulations with ultracold quantum gases”. *Nature Physics* 8.4 (2012), pp. 267–276.

[64] R. Blatt and C. F. Roos. “Quantum simulations with trapped ions”. *Nature Physics* 8.4 (2012), pp. 277–284.

[65] A. M. Kaufman and K.-K. Ni. “Quantum science with optical tweezer arrays of ultracold atoms and molecules”. *Nature Physics* 17.12 (2021), pp. 1324–1333.

[66] D.-J. Choi et al. “Colloquium: Atomic spin chains on surfaces”. *Reviews of Modern Physics* 91.4 (2019), p. 041001.

[67] T. Hensgens et al. “Quantum simulation of a Fermi–Hubbard model using a semiconductor quantum dot array”. *Nature* 548.7665 (2017), pp. 70–73.

[68] J. P. Dehollain et al. “Nagaoka ferromagnetism observed in a quantum dot plaquette”. *Nature* 579.7800 (2020), pp. 528–533.

[69] C. J. van Diepen et al. “Quantum Simulation of Antiferromagnetic Heisenberg Chain with Gate-Defined Quantum Dots”. *Physical Review X* 11.4 (2021), p. 041025.

[70] C.-A. Wang et al. “Probing resonating valence bonds on a programmable germanium quantum simulator”. *npj Quantum Information* 9.1 (2023), p. 58.

[71] I. Buluta and F. Nori. “Quantum Simulators”. *Science* 326.5949 (2009), pp. 108–111.

[72] J. I. Cirac and P. Zoller. “Goals and opportunities in quantum simulation”. *Nature Physics* 8.4 (2012), pp. 264–266.

2

THEORY

Students' questions were met with such nonsense as 'If you think you've understood quantum mechanics then you don't.' [...] - a hallmark of bad philosophy.

David Deutsch, *The beginning of infinity*, 2011

2.1. THE FERMI-HUBBARD MODEL

One of the most important early achievements of quantum theory is the explanation of a wide range of phenomena observed in solids. Starting from the Schrödinger equation, it was possible to calculate the electronic properties of materials in the form of their **band structure**: the set of energy levels that electrons can or cannot occupy, and which determine electrical, magnetic and optical properties of materials. Two early models could successfully explain the properties of a variety of materials. On the one hand, the nearly free electron model [1], successful at accounting for the properties of metals, assumes electron wavefunctions which are only slightly perturbed by the underlying atomic potentials. On the other hand, the tight-binding model [2] assumes localized electronic orbitals where electrons can hop from site to site with hopping amplitude t, yielding the band structure of many semiconductor materials. Both models crucially neglect the interactions between electrons, an assumption that turns out to work for a wide range of materials and significantly eases calculations.

However, it was soon discovered that band theory fails to describe a variety of materials. For instance, transition metal oxides like NiO were experimentally shown to be insulating [3], while band theory would otherwise predict them to be metallic. To account for these phenomena, and as an extension to the tight binding model, the **Fermi-Hubbard model** [4–6] was developed. Next to the hopping amplitude t, the Fermi-Hubbard model includes electron-electron (Coulomb) interactions in the form of an energy penalty U that electrons have to pay if they occupy the same site. In second quantization, the Fermi-Hubbard model reads:

$$H_{\mathrm{FH}} = -t \sum_{\langle i,j\rangle,\sigma} \left(c^{\dagger}_{i,\sigma} c_{j,\sigma} + c^{\dagger}_{j,\sigma} c_{i,\sigma} \right) + U \sum_{i} n_{i,\uparrow} n_{i,\downarrow}, \tag{2.1}$$

with $c^{\dagger}_{i,\sigma}$, $c_{i,\sigma}$ the creation and annihilation operators, adding or removing a spin $\sigma \in \{\uparrow, \downarrow\}$ to or from site i; the angle brackets denoting nearest neighbours; and $n_{i,\sigma} = c^{\dagger}_{i,\sigma} c_{i,\sigma}$ the number operator on site i with spin σ. At half filling, i.e. one electron per site, this model successfully explained the transition from a metallic state to an insulating state at sufficiently large electron-electron interaction strengths U, a state of matter known as **Mott insulator**.

Since its development, the Fermi-Hubbard model has become a paradigmatic example of strongly correlated electronic systems, being applied to describe a wealth of phases of matter, such as itinerant ferromagnetism, antiferromagnetic ordering, spin liquids and even unconventional superconductivity [7]. One particularly striking feature of this model is its complexity: Despite the Hamiltonian's compactness, exact solutions are only known for one-dimensional systems [8]. However, the physics of many systems of interest, such as high-temperature superconductors, is often determined by electronic correlations within two-dimensional planes [9]. This points to the central motivation behind the study of the Fermi-Hubbard model: Unraveling its mysteries beyond what is classically computable could shed light on the physics of materials with potentially impactful applications. And, as we will discuss below (section 2.1.2), quantum dot arrays are precisely a controllable, fermionic system whose Hamiltonian can be directly mapped to a two-dimensional Fermi-Hubbard model.

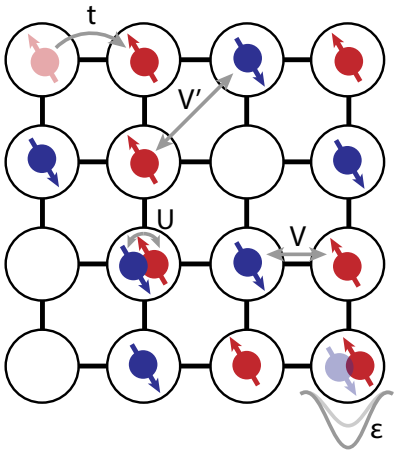

Figure 2.1: A Fermi-Hubbard lattice. In the original Fermi-Hubbard model, hopping charges with hopping amplitude t have to pay an energy penalty U to doubly occupy a lattice site. Quantum dot systems are described by an extended Fermi-Hubbard model which allows for differences in tunnel coupling ($t_i \neq t_j$) and onsite repulsion ($U_i \neq U_j$), as well as additional terms like single-site detunings $\{\varepsilon_i\}$ and long-range Coulomb repulsion terms $\{V_i, V_i'\}$.

2.1.1. THE HEISENBERG MODEL AND THE ZEEMAN HAMILTONIAN

Before describing the connection between quantum dot arrays and the Fermi-Hubbard model, it is important to mention one of the limiting cases of the Fermi-Hubbard Hamiltonian. At half filling and large enough ratios of U/t, tunneling between neighboring sites is suppressed. In this case, an effective spin Hamiltonian can be derived by projecting the Fermi-Hubbard Hamiltonian to its low-energy subspace [10]. This yields the celebrated Heisenberg model [11]:

$$H_J = J \sum_{\langle i,j \rangle} \mathbf{S_i} \cdot \mathbf{S_j}, \tag{2.2}$$

with the vector of spin operators $\mathbf{S_i} = \frac{1}{2}\hbar(\sigma_x, \sigma_y, \sigma_z)$, where the σ operators represent the three Pauli matrices. The spin-spin **exchange coupling** $J = \frac{4t^2}{U}$ emerges as a second-order coupling term between neighboring, occupied sites, representing virtual hopping processes which lower the total (kinetic) energy of the system.

The Heisenberg model was developed early on to account for a variety of magnetic phenomena in solids and remains a subject of active research, given that its implications for certain geometries and system sizes are still unclear [12, 13]. Concretely, in the case of frustrated lattices like the triangular lattice, the Heisenberg model might allow for highly entangled, high entropy ground states coined quantum spin liquids. Again we recognize that the study of this Hamiltonian with controllable quantum systems could be of interest for the solid-state community.

Finally, we introduce an additional term that stems from the application of an external magnetic field B, which causes an energy splitting between the spin states $|\downarrow\rangle$ and

$|\uparrow\rangle$. This so-called Zeeman energy term reads:

$$H_Z = g\mu_B B \sum_i S_z. \tag{2.3}$$

The constant $\mu_B = \frac{e\hbar}{2m_e}$ is the Bohr magneton, representing the magnetic moment of an electron, with e the elementary charge and m_e the bare electron mass. The term g is the so-called g-factor, which characterizes the strength of the coupling of the spin of a particle to an external magnetic field. For free electrons, the g-factor is approximately 2, but it can significantly deviate from this value for charge carriers in solids.

2.1.2. THE FERMI-HUBBARD MODEL AND QUANTUM DOTS

As outlined in section 1.2.2, charges in semiconductor gate-defined quantum dots are confined in three spatial dimensions by the combination of a quantum well and voltages on gate electrodes [14]. The quantum well confinement of charges along the z direction, which leads to the formation of a two-dimensional electron or hole gas (2DEG or 2DHG, respectively), will be more thoroughly discussed in section 2.2.2 for the case of Ge/SiGe quantum dots. Within this two dimensional plane, it is the geometry and size of the gate electrodes, together with the applied voltages, which define the **potential landscape** in which the charges are confined along the x and y directions. In this context, there are two types of gates: the **plunger** gates, which control the individual electrochemical potentials μ_i of each quantum dot; and the **barrier** gates, which control the tunneling amplitudes between neighboring dots t_{ij}. An example of a quantum dot device can be seen in Fig. 3.1, its corresponding gate layout is described in section 3.1.2.

A gate-defined quantum dot array forms precisely a lattice of localized charges, which are allowed to hop between nearest neighbor sites and where electron-electron interactions are typically strong with respect to the hopping amplitude, very much like in the Fermi-Hubbard picture of strongly correlated electrons. In fact, this resemblance is not just conceptual: Quantum dot arrays are actually described by an extended Fermi-Hubbard model which includes a few modifications to Eq. 2.1. First, this model allows for site-dependent $\{U_i\}$ and $\{t_{ij}\}$ terms. Secondly, it introduces individually tunable electrochemical potentials $\{\mu_i\}$ as well as long-range Coulomb repulsion terms between distant sites $\{V_{ij}\}$. The full model then reads [15, 16]:

$$H_{\text{FH, QD}} = \sum_{i,\sigma} \mu_i n_{i,\sigma} - \sum_{\langle i,j\rangle,\sigma} t_{ij} \left(c^\dagger_{i,\sigma} c_{j,\sigma} + c^\dagger_{j,\sigma} c_{i,\sigma} \right) + \sum_i U_i n_{i,\uparrow} n_{i,\downarrow} + \sum_{i,j} V_{ij} n_i n_i \tag{2.4}$$

For quantum dot systems, the Coulomb terms U and V are the dominant energy scales, with typical values of 1-3 meV and 200-300 µeV, respectively [15, 17, 18]. These values are mainly set by the device geometry: The size of the quantum dots allows to estimate the term U, often referred to as the **charging energy**. The distance between neighboring quantum dots mainly sets V. Note that the decay of Coulomb repulsion over distance does not follow a simple $\frac{1}{r}$ decay, as is typical for charges in vacuum, but screening effects by the gate electrodes need to be taken into account, leading to a faster decay [18].

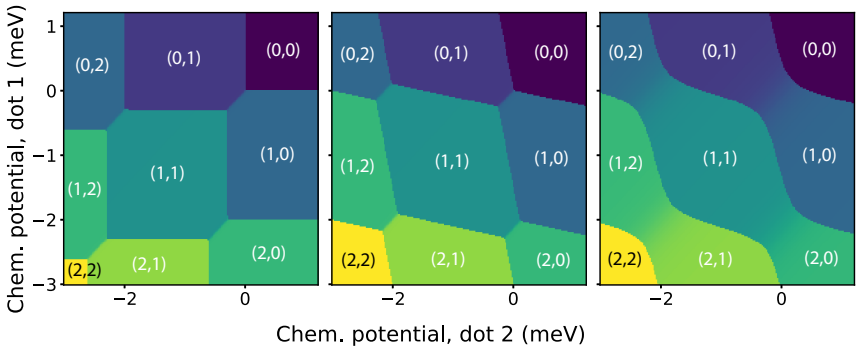

Figure 2.2: Simulated charge stability diagrams for a pair of quantum dots using the extended Fermi-Hubbard model. The input parameters are: $U_1 = U_2 = 2\,\text{meV}$, $V_{12} = 300\,\mu\text{eV}$. (a) Virtualized charge stability diagram at low tunnel coupling ($t_{12} = 10\,\mu\text{eV}$). (b) Unvirtualized charge stability diagram, with a capacitive coupling between quantum dots of 0.1 and $t_{12} = 10\,\mu\text{eV}$. (c) Unvirtualized charge stability diagram, with a capacitive coupling between quantum dots of 0.1 and $t_{12} = 200\,\mu\text{eV}$.

CHARGE STABILITY DIAGRAMS

This Fermi-Hubbard description of quantum dot arrays allows us to compute **charge stability diagrams** (CSD) [16, 19]. These are the voltage maps that are typically used in the early tuning stages of quantum dot arrays and which allow to pinpoint the charge state of the quantum dots as a function of the individual electrochemical potentials, which can be tuned electrically. Experimentally, the charge state can be measured using charge sensors (see sections 3.4.1 and 3.4.2).

Three typical simulated charge stability diagrams for a pair of quantum dots are depicted in Fig. 2.2. These are obtained by calculating the charge ground state of Eq. 2.4 as a function of electrochemical potentials μ_1 and μ_2, and inputting realistic values for U, t and V (see Fig. caption). Regions with different color correspond to different charge states (n_1,n_2), the top right region corresponding to the "empty" charge state (0,0).

Fig. 2.2a corresponds to the ideal case where the electrochemical potentials are tuned up independently of each other. Experimentally, however, the default case is that the voltage used to control the electrochemical potential of a quantum dot affects that of its neighbors due to the presence of crosstalk (see section 3.4.3), leading to charge stability maps such as Fig. 2.2b. These linear shifts can be easily compensated in software with the aid of a rotation matrix, a process known as **virtualization** [20]. Experimentally, we would refer to Figs. 2.2a and b as a virtualized or unvirtualized CSD, respectively. Finally, Fig. 2.2c shows the effect of high interdot tunnel coupling to the charge stability diagram. The waviness of the charge transition lines is a sign of charge hybridization.

Calculating charge stability maps by diagonalizating Eq. 2.4 becomes computationally expensive for a large number of quantum dots and high charge occupations. However, if tunnel coupling terms are ignored, the Hamiltonian of Eq. 2.4 becomes diagonal. The task of finding the ground state of the system can then be classically computed as an energy minimization problem, significantly enhancing computational speed. This is relevant for computing multi-dot charge stability diagrams or for including higher occupations, and has allowed for efficient computation algorithms [21].

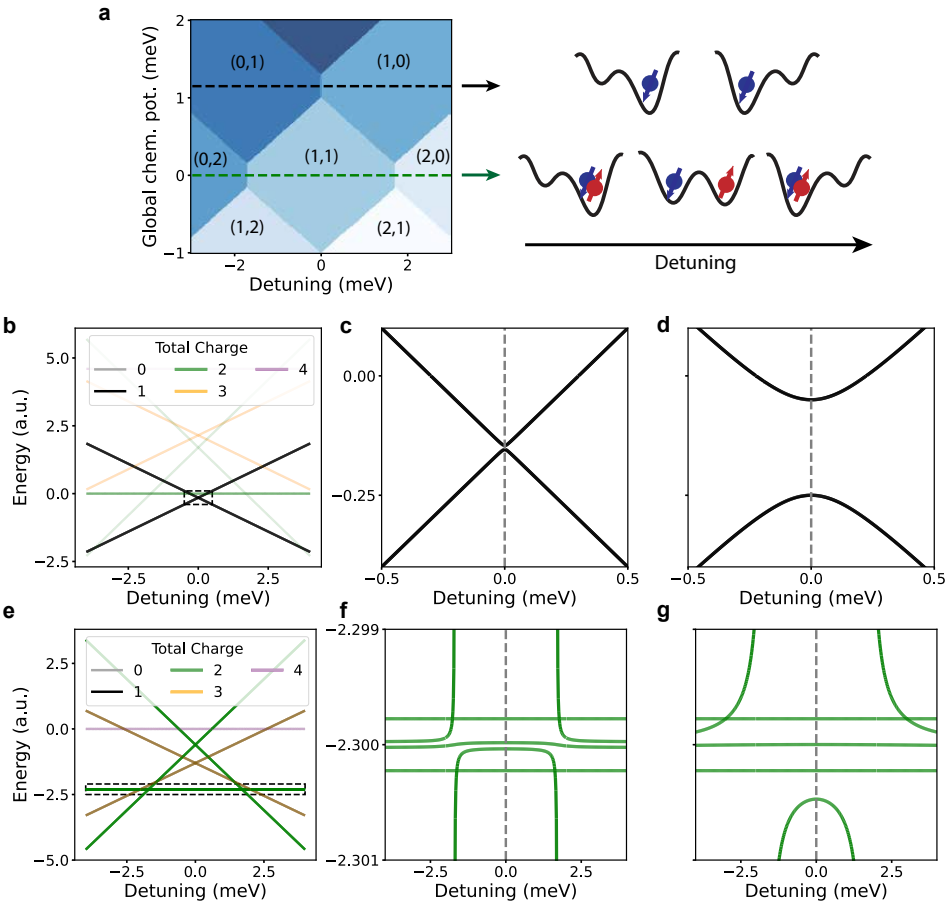

Figure 2.3: Energy level structure of a pair of quantum dots. (a) Charge stability diagram as a function of detuning ε_{12} and global electrochemical potential μ_{12}. The dashed black and green lines represent line cuts crossing the (0,1)-(1,0) and (0,2)-(1,1)-(2,0) transitions, respectively. (b) Full energy spectrum across the black dashed line (see above). The energy levels are color-coded as a function of total charge state N. The dashed box indicates the region plotted in panel (c). (c) Zoom-in on the $N = 1$ charge sector at low tunnel coupling (t_{12} =4 μeV). (d) Zoom-in on the $N = 1$ charge sector at higher tunnel coupling (t_{12} =100 μeV). (e) Full energy spectrum across the green dashed line (see above). The energy levels are color-coded as a function of total charge state N. The dashed box indicates the region plotted in panel (f). (f) Zoom-in on the $N = 2$ charge sector at low tunnel coupling (t_{12} =4 μeV). (g) Zoom-in on the $N = 1$ charge sector at higher tunnel coupling (t_{12} =20 μeV).

ENERGY LEVEL STRUCTURE

Beyond the charge ground state of quantum dot arrays, the Fermi-Hubbard model allows us to compute the system's higher energy levels, which reveal a wealth of interesting charge and spin physics. Fig. 2.3a shows a double dot charge stability diagram as a function of global electrochemical potential $\mu = \mu_1 + \mu_2$ and **detuning**, defined as $\varepsilon_{12} = \mu_1 - \mu_2$. We subsequently plot the full energy level diagrams as a function of detuning, corresponding to the two plotted black and green dashed lines. Along those lines, the total charge state of the system $N = n_1 + n_2$ is conserved ($N = 1$ and $N = 2$, respectively).

Fig. 2.3c shows the full energy spectrum as a function of detuning, corresponding to the black dashed line in Fig. 2.3a. Highlighted in black are the levels with total charge state $N = 1$, which remains the system's ground state occupation through the plotted detuning range. Zooming in on the dashed region reveals two branches corresponding to the charge occupations (0,1) and (1,0), which are the ground state at negative and positive detunings, respectively. At $\varepsilon = 0$, the ground state is a superposition between the left and the right occupation. The splitting between the upper and the lower branch is equal to $2t$. Increasing the tunnel coupling thus leads to a higher splitting, as seen in Fig. 2.3d.

At lower electrochemical potentials (green dashed line in Fig. 2.3a), the charge occupation of the system is $N = 2$, as shown in Fig. 2.3e. Isolating only the $N = 2$ reveals a more complex energy spectrum. This is captured by the effective Hamiltonian [22]:

$$H_{\mathrm{DD}} = \begin{pmatrix} U+\varepsilon & 0 & 0 & t & -t & 0 \\ 0 & U-\varepsilon & 0 & t & -t & 0 \\ 0 & 0 & \tilde{E}_z & 0 & 0 & 0 \\ t & t & 0 & \Delta E_z/2 & 0 & 0 \\ -t & -t & 0 & 0 & -\Delta E_z/2 & 0 \\ 0 & 0 & 0 & 0 & 0 & -\tilde{E}_z \end{pmatrix}, \tag{2.5}$$

written in the basis $\{S(0,2), S(2,0), |\downarrow\downarrow\rangle, |\downarrow\uparrow\rangle, |\uparrow\downarrow\rangle, |\uparrow\uparrow\rangle\}$. Additionally to the Hubbard parameters U and t, we include a splitting of energy levels due to a difference in Zeeman energies (Eq. 2.3).

The structure of this energy diagram captures some essential features of spin initialization and control. At detunings $\varepsilon > U$ or $\varepsilon < U$, and as can be inferred from Fig. 2.3a, both charges sit in the same quantum dot. Due to Pauli exclusion principle, they form a singlet ground state $|S(0,2)\rangle$ or $|S(2,0)\rangle$. The eigenstate structure at zero detuning and finite Zeeman energy difference depends on the tunnel coupling between the quantum dots. In fact, at $\varepsilon = 0$ we can define an effective exchange coupling between quantum dots as $J = 4\frac{t^2}{U}$ as previously discussed in sec. 2.1.1. For $\Delta E_z \gg J$, the eigenstates at zero detuning correspond to the four product states $\{|\downarrow\downarrow\rangle, |\uparrow\downarrow\rangle, |\downarrow\uparrow\rangle, |\uparrow\uparrow\rangle\}$, as depicted in Fig. 2.3f. Out of the two antiparallel states, the one with spin-up for the spin with the lowest g-factor has a lower energy. At high tunnel couplings (Fig. 2.3g), the eigenstates are given by the singlet and three triplet states $\{|S(1,1)\rangle, |\downarrow\downarrow\rangle = |T^-\rangle, |\uparrow\downarrow\rangle + |\downarrow\uparrow\rangle = |T^0\rangle, |\uparrow\uparrow\rangle = |T^+\rangle\}$.

2.2. THE PHYSICS OF HOLES IN GERMANIUM QUANTUM DOTS

In the previous section, we have introduced an abstract notion of quantum dot systems as Fermi-Hubbard lattices with tunable electrochemical potentials and tunnel couplings, as well as the presence of strong intra-site and inter-site Coulomb repulsion. As a following step, we will reconcile this theoretical description with the actual experimental realization using real, physical platforms. Concretely, we will discuss the realization of quantum dot arrays in planar heterostructures, focussing on the specificities of holes in Ge/SiGe heterostructures.

2.2.1. PHYSICAL PLATFORMS FOR QUANTUM DOT EXPERIMENTS

The field of spin qubits with gate-defined quantum dots was kick-started with the use of GaAs/AlGaAs heterostructures. GaAs is a III-V semiconductor with excellent crystal purity, with very high electron mobilities reported early on [23]. This points to a low level of material disorder, a crucial ingredient to be able to electrostatically define quantum dots. Early quantum dot research on GaAs showed basic spin-qubit operations including spin initialization, control and readout [24–27]. However, the achievable fidelities, i.e. a measure of how close a quantum operation is to the ideal, target operation, were limited by the large number of nuclear spins present in the material. As we will discuss in sec. 2.2.5 below, fluctuations of the spin state of nuclear spins can quickly lead to the loss of the encoded quantum information and the reduction of operation fidelities.

In contrast to III-V semiconductors, the use of type-IV semiconductor materials like Si and Ge has the advantage of a low concentration of nuclear spins. As a result, the demonstration of high-fidelity operations in SiMOS, a material platform with high compatibility with CMOS processes for classical electronics, was demonstrated [22, 28]. However, electrons in SiMOS are confined directly at the interface between Si and a silicon-oxide (SiO_2) layer, which constitutes a source of noise and disorder. A compromise in this regard was the use of Si/SiGe, where electrons are accumulated within a Si quantum well, separated from the oxide layer by a SiGe barrier. In Si/SiGe, high-fidelity initialization, readout, single- and two-qubit gates have been demonstrated [29–32], rendering this one of the most promising platforms for the realization of spin-qubit-based quantum processors. However, the need for micromagnets for qubit addressability, as well as the small required footprint of the gate electrodes have mostly allowed for one-dimensional demonstrations of Si/SiGe quantum dot arrays.

In contrast, holes in Ge/SiGe heterostructures have attracted interest in recent years due to the prospects of all-electrical spin control, spin addressability, low nuclear spin noise and relaxed fabrication constraints [33]. All of these properties stem from the physics of holes in Ge/SiGe heterostructures which we will discuss in the following section.

2.2.2. BAND STRUCTURE OF GE/SIGE

Semiconductor materials are characterized by a band structure in which the Fermi energy lies within a **band gap** of unavailable states. In contrast to insulators, the band gap of semiconductors is narrow, such that thermal excitations can promote charges from the highest, occupied band (the **valence band**) to the lowest, unoccupied band (the **conduction band**). Removing a single electron from the valence band leaves behind a **hole**,

a quasiparticle of positive electric charge $+e$ and with similar properties as electrons. The exact properties of holes in a semiconductor material are precisely determined by the nature of the band structure around the valence band. By the same logic, electrons in semiconductors are susceptible to the conduction band structure.

For a bulk germanium crystal, the valence band maximum is found at the Γ point, where the crystal momentum is zero [33, 34]. Here, the orbital is p-type, meaning that the holes carry not only their intrinsic spin of 1/2, but also an angular momentum $l = 1$ (in units of $\hbar$). This results in a complex energy spectrum with six available states, characterized by their total spin quantum number j and spin projection m_j: **heavy holes**, with $j = \frac{3}{2}$ and $m_j = \left|\frac{3}{2}\right|$; **light holes**, with $j = \frac{3}{2}$ and $m_j = \left|\frac{1}{2}\right|$; and the split-off bands with $j = \frac{1}{2}$ and $m_j = \left|\frac{1}{2}\right|$. The latter can be disregarded in the following discussion, since they are split away from the valence band maximum by an intrinsic spin-orbit coupling term [35].

The addition of strain to the system by the quantum well confinement lifts the degeneracy between heavy-hole and light-hole states [35, 36]. The lowest energy levels, whose wavefunction mainly consists of heavy-hole states, form an effective spin-1/2 system, where we define $|\downarrow\rangle$ as the ground state and $|\uparrow\rangle$ as the excited state. Furthermore, the confinement of charges within the quantum well, together with the spatial dependence of the electric fields applied by the gates, break the inversion symmetry present for carriers within the bulk crystal. Together, this results in strong Rashba **spin-orbit** interaction, which heavily impacts the spin physics of holes in germanium, as will be discussed in the sections below.

One further consequence of the electronic band structure is the renormalization of the mass of the charge carriers in semiconductors. This **effective mass** is the inverse of the curvature of the energy band $m^* = \left(\frac{1}{\hbar^2}\frac{\partial^2 E}{\partial k^2}\right)^{-1}$. Interestingly, the effective mass of heavy holes under strain becomes lighter than that of light holes for Ge/SiGe heterostructures. Concretely, $m^*_{\mathrm{HH}} \approx 0.05 m_0$ [36, 37]. When confining single quantum dots, the energy level splitting is proportional to the inverse of the effective mass [33]. Thus, a low effective mass yields high orbital energy splittings even for relatively large quantum dot structures. From an experimental point of view, the combination of a small effective mass and low material disorder allows for the fabrication of large Ge/SiGe quantum dots of diameter $d \sim 100$ nm, easier to fabricate than smaller quantum dot structures. This has led to the fabrication of two-dimensional Ge/SiGe quantum dot devices [38–41] earlier than for their Si counterparts, which typically require gates of half the size to achieve a similar confinement.

2.2.3. ZEEMAN ENERGY AND ELECTRIC DIPOLE SPIN RESONANCE

As a result of spin-orbit interaction and the complex band structure of holes in germanium, the Zeeman formula of Eq. 2.3 needs to be revisited. Concretely, holes in germanium experience a highly anisotropic behavior of the Zeeman energy. Instead of a g-factor, a **g-tensor** is required to account for this anisotropy [42]:

$$H_Z = \mu_B \mathbf{S} \cdot \hat{g} \cdot \mathbf{B}. \tag{2.6}$$

For a fixed magnetic field orientation, one can still define an effective g-factor as $g =$

$\frac{|\hat{g}\cdot\mathbf{B}|}{|\mathbf{B}|}$. For magnetic fields applied in plane, as is the case for the spin experiments carried out in this thesis, typical effective g-factors of $\sim 0.1-0.3$ are theoretically predicted and experimentally measured [43, 44]. In contrast, out-of-plane g-factors > 10 have been measured with out-of-plane magnetic fields [45], highlighting the highly anisotropic character of this quantity.

To extract these values experimentally, one would require the ability to pinpoint each individual spin's resonance frequency using an external, oscillating field. In fact, one of the most important techniques for spin qubit control precisely relies on the ability to drive transitions between the spin-up and spin-down states of each individual spin. Given a Zeeman energy splitting E_z, a straight-forward way of doing this is by applying an oscillating magnetic field with an oscillation frequency which matches the Zeeman splitting (see Sec. 2.3.2). This technique is called electron spin resonance (ESR) [26]. ESR in quantum dot devices requires the close proximity of wire through which an oscillating current is applied, which in turn results in an oscillating magnetic field. This can cause significant heating and pose difficulties for scaling up beyond one-dimensional arrays. An alternative is the use of an oscillating electric field coupled to a Zeeman energy gradient, in a process coined electric-dipole spin resonance (EDSR) [27, 46]. This is often achieved with the use of micromagnets to create a magnetic field gradient (typical for Si devices), or via the intrinsic spin-orbit interaction for GaAs quantum dots, in both cases allowing for the direct coupling of an oscillating electric field to the state of the spin.

For Ge/SiGe quantum dots, additionally to the intrinsic spin-orbit coupling, the demonstrated EDSR drive is mainly caused by g-tensor modulation [47, 48]: by driving a gate in the vicinity of the quantum dot, the periodic deformation and movement of the hole's wavefunction causes oscillations of the effective g-factor, which in turn drives transitions between the $|\uparrow\rangle$ and $|\downarrow\rangle$ states. While this has enabled high-fidelity single-spin qubit control, it can also be used as a spectroscopic tool as utilized in chapter 6.

2.2.4. DOUBLE QUANTUM DOTS IN GE/SIGE

SPIN-ORBIT TUNNELING

An important consequence of the presence of strong spin-orbit coupling is its spin-nonconserving character. Concretely, the Hamiltonian of Eq. 2.5, directly derived from the Fermi-Hubbard model, should be extended to allow for spin-flip tunneling elements of the form [49, 50]

$$H_{\mathrm{SO}} = i\,t_{\mathrm{SO,z}}\,|T_0\rangle\langle S_{20}| - \sum_{\pm}(t_{\mathrm{SO,y}} \pm i\,t_{\mathrm{SO,x}})\,|T_{\pm}\rangle\langle S_{20}| + \mathrm{h.c.}, \tag{2.7}$$

with $\mathbf{t}_{\mathrm{SO}} = (t_{\mathrm{SO,x}}, t_{\mathrm{SO,y}}, t_{\mathrm{SO,z}})$ a vector of spin-orbit tunneling matrix elements coupling the singlet and the triplet states. The full Fermi-Hubbard Hamiltonian including spin-orbit terms then reads:

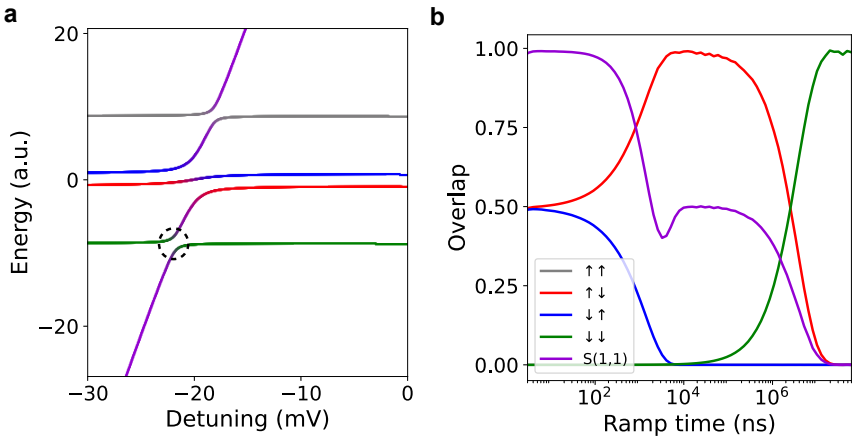

Figure 2.4: (a) Energy level structure of a pair of Ge/SiGe quantum dots in the presence of spin-orbit coupling and at low tunnel coupling. Spin-orbit coupling opens up an anticrossing between the singlet and T_- branches (black dashed circle). At zero detuning, the eigenstates are the four product states. (b) Simulation of state initialization as a function of ramp speed between the (0,2) and (1,1) charge states. As the ramp time is increased, the initialized state changes from $|S\rangle$ to $|\uparrow\downarrow\rangle$ to $|\downarrow\downarrow\rangle$.

$$H = \begin{pmatrix} U+\varepsilon & 0 & -t_{\mathrm{SO,y}}+it_{\mathrm{SO,x}} & t-it_{\mathrm{SO,z}} & -t-it_{\mathrm{SO,z}} & -t_{\mathrm{SO,y}}-it_{\mathrm{SO,x}} \\ 0 & U-\varepsilon & -t_{\mathrm{SO,y}}+it_{\mathrm{SO,x}} & t-it_{\mathrm{SO,z}} & -t-it_{\mathrm{SO,z}} & -t_{\mathrm{SO,y}}-it_{\mathrm{SO,x}} \\ -t_{\mathrm{SO,y}}-it_{\mathrm{SO,x}} & -t_{\mathrm{SO,y}}-it_{\mathrm{SO,x}} & \bar{E}_z & 0 & 0 & 0 \\ t+it_{\mathrm{SO,z}} & t+it_{\mathrm{SO,z}} & 0 & \Delta E_z/2 & & 0 \\ -t+it_{\mathrm{SO,z}} & -t+it_{\mathrm{SO,z}} & 0 & 0 & -\Delta E_z/2 & 0 \\ -t_{\mathrm{SO,y}}+it_{\mathrm{SO,x}} & -t_{\mathrm{SO,y}}+it_{\mathrm{SO,x}} & 0 & 0 & 0 & -\bar{E}_z \end{pmatrix}. \tag{2.8}$$

One of the most important consequences of this additional spin-orbit term is the opening of an anticrossing between the singlet and the triplet branches (see Fig. 2.4a, black dashed circle) with strength Δ_{SO}. As we will see, this S-T^- anticrossing is very relevant for spin initialization and readout in Ge/SiGe quantum dots.

INITIALIZATION AND READOUT

To discuss initialization and readout, it is useful to revisit the energy levels of a double quantum dot but adding spin-orbit coupling and labeling the energy branches, as seen in Fig. 2.4a. Starting from the $|S(2,0)\rangle$ state at very large absolute detuning, a pulse to the $\varepsilon = 0$ point with speed τ separates the charges into two different quantum dots. Which spin state is initialized crucially depends on τ. If the ramp is slow enough, the system is adiabatically initialized into the double-dot ground state $|\downarrow\downarrow\rangle$. If the ramp speed is fast enough compared to the S-T^- anticrossing strength, the state $|\downarrow\uparrow\rangle$ is initialized, with the spin-up corresponding to the site with the lowest effective g-factor. At very fast ramp speeds, the initial spin state is retained, resulting in the state $S(1,1)$. Fig. 2.4b shows a

simulation of this initialization process, using realistic parameters for the Hamiltonian of Eq. 2.8, showcasing the transition from singlet (in purple) to $|\uparrow\downarrow\rangle$ (in red) to $|\downarrow\downarrow\rangle$ (in green) initialization with increasing ramp time. This well-known pairwise initialization method is used and explained in more detail in chapters 5 and 6.

As for spin readout, two methods are typically used in quantum dot experiments: Elzerman-style (or single-spin) readout [24] and **Pauli spin blockade** (PSB) [51]. Elzerman readout relies on the tunneling of one of the two single-spin states into a nearby reservoir, provided that the quantum dot's electrochemical potential is tuned such that the reservoir Fermi energy lies in between both spin states. This method, apart from relying on the presence of such a reservoir, requires Zeeman energy splittings large enough to overcome thermal broadening. In contrast, PSB relies on the projection of the two spin states onto a small region close to the polarization line at the (1,1)-(2,0) transition. From the four possible two-spin states, the Pauli exclusion principle only allows one to be projected onto the $|S(2,0)\rangle$ ground state. As for the initialization case, which state is unblocked depends on the ramp time τ to the PSB region.

SPIN-SPIN INTERACTIONS

Another crucial consequence of spin-orbit coupling in germanium quantum dots is a recently observed quantization axis tilt between neighboring quantum dots, stemming from differences in each quantum dot's wave function [52, 53]. In essence, each individual g-tensor will generally not only exhibit different components, but also differences in their principal axes. When describing spin-spin interactions, it is in general not sufficient to use the Heisenberg model as written in Eq. 2.2, but spin-orbit-related anisotropic terms [42] have to be included. This anisotropy is captured by a more general Hamiltonian:

$$H_{\text{J,anis}} = \frac{1}{4} \sum_{\langle ij \rangle} J_{ij} \vec{\sigma}_i \cdot R_z(2\gamma_{ij}) \cdot \vec{\sigma}_j, \tag{2.9}$$

where the tilt in quantization axis results in an anisotropic exchange interaction, with $R_z(2\gamma_{ij})$ a rotation around the z-axis by an angle $2\gamma_{ij}$. Note that this difference in quantization axes has been recently measured and exploited to realized single-qubit gates with Ge/SiGe quantum dots [52, 53]. This anisotropy in the exchange interaction has also been recently characterized in literature for holes in Ge/SiGe [54] and Si [55].

2.2.5. DECOHERENCE AND RESILIENCE TO ERRORS

The quantum mechanical systems we use for computation and simulation are not closed: their constituents naturally couple to their environment. Some of that coupling is necessary: the experimentalist needs to be able to address the system in order to initialize, manipulate and read out its state. However, the residual, unwanted coupling to the surroundings causes a gradual loss of quantum information from the system to the environment, a process called **decoherence**. The time during which a quantum mechanical object can store a quantum state before it is lost is called the coherence time [56].

Decoherence in quantum dot devices mainly stems from two sources: coupling to nuclear spins (**hyperfine noise**) and coupling to fluctuating charges (**charge noise**). Hyperfine noise is caused by the random fluctuation of the state of nuclear spins, which

couple to the electron or hole spins the via the hyperfine interaction. This effect can be mitigated for group-IV semiconductor devices using isotopic purification of the material stack [57], removing the naturally occurring odd-number Ge and Si isotopes. While so far only Si is routinely purified, Ge/SiGe with purified Ge have been demostrated [58]. Furthermore, the p-type character of holes in germanium results in a vanishing hyperfine coupling for in-plane magnetic fields. At this so-called sweet-spot, the coherence time of hole spins can be enhanced [45].

In contrast, charge noise refers to the electrical fluctuations caused by charges in the material stack. For quantum dot devices, a typical model assumes these to be two-level fluctuators, where charges trapped in the heterostructure and gate stack can jump from one potential well to another. An ensemble of these two-level fluctuators with a log-uniform distribution of switching frequencies causes a typical charge noise spectral density with a $1/f$ frequency dependence [59], with f the noise frequency. In systems with strong spin-orbit coupling or inhomogeneous magnetic fields, which so far have been presented as advantageous to enable spin control, charge noise can efficiently couple to the spins, thereby causing decoherence. Strategies to mitigate charge noise include the development of cleaner oxide layers, where typically most charge traps are located; a placement of the quantum well far away from the gate stack; or by improvements in the material stack [59–61]. Note that deeper quantum wells also result in a reduced coupling of the spins to gate voltages.

Retaining a high level of system coherence is of paramount importance to the development of quantum computing and simulations. Since perfect quantum gates with arbitrary precision or perfect tuning of Hamiltonian parameters are infeasible, the resulting computational errors need to be characterized and, ideally, corrected for. For digital quantum computers, there exist protocols to detect, mitigate and correct for errors emerging during a quantum algorithm. These error correction protocols [62] require an overhead in physical qubit numbers. Standard error correction algorithms require qubit counts reaching the millions [63] before fault-tolerance is enabled. For semiconductor spin qubits, only a handful of error correction codes have been experimentally demonstrated in the literature [64, 65], while more mature quantum computing platforms have demonstrated more advanced error correction schemes [66].

For analog quantum simulators, to my knowledge, no clear error correction strategies exist. While analog simulators are also naturally subjected to decoherence, it has been theoretically shown that these systems should be more resilient to errors [67] than their digital counterparts [68].

2.3. QUANTUM DOTS FOR QUANTUM COMPUTATION

A wide range of research groups working with semiconductor quantum dot arrays aim to use these systems as quantum processors for gate-based quantum computing. Concretely, the coherent control of their spin degree of freedom has sparked excitement due to the system's coherence times, tunabilty, and promises of scalability. While this thesis' main focus is analog quantum simulations, we borrow many methods envisioned and developed in the context of digital quantum computing. These are best explained by outlining four different types of qubits, from which we use either spectroscopic tools or gate-based methods. Especially in chapter 6, digital and analog methods are explicitly

joined together in an analog-digital framework, using tools from both single-spin and singlet-triplet qubit initialization, control and readout.

2.3.1. CHARGE QUBITS

Charge qubits are among the early types of qubits proposed for quantum dot systems. A charge qubit consists of a double quantum dot, where the two logical states can be defined as the charge being on the left ($|0\rangle = |L\rangle$) or right ($|1\rangle = |R\rangle$) quantum dot. The charge qubit Hamiltonian H_{CH} can be written in the basis $\{|L\rangle, |R\rangle\}$ as [69]:

$$H_{\mathrm{CQ}} = \frac{1}{2}\varepsilon\sigma_z + t\sigma_x, \tag{2.10}$$

with σ_x and σ_z the corresponding Pauli matrices. The energy spectrum of such a charge qubit can be seen in Fig. 2.3c and d for two values of t. Charge qubits have been coherently probed in GaAs [69–71] and Si/SiGe [72, 73]. While conceptually straightforward and fast to operate, these qubits suffer from very low coherence times, typically in the nanosecond range, due to their coupling to charge noise (see section 2.2.5). Nonetheless, electron charge qubits with close to 100 µs coherence time have been recently demonstrated on solid neon [74].

In chapter 4, we use a continuous microwave drive to drive transitions between the two energy branches, which occur when the energy of the photons $h\nu$ match the energy level splitting. This is a process known as **photon-assisted tunneling** [75]. The resulting signal as a function of microwave frequency and detuning can be fitted to a hyperbolic function of the shape $E = \sqrt{\varepsilon^2 + 4t^2}$. From the fit, one can to extract two relevant quantities for quantum dot experiments: the tunnel coupling t and the **lever arm** α. The latter connects a difference in gate voltage $\delta \mathrm{p}_i$ (in mV) to its corresponding change in electrochemical potential $\delta\mu_i$ (in meV) as $\delta\mu_i = \alpha \mathrm{p}_i$, and is an important quantity to extract the energy scales of the system.

2.3.2. SINGLE-SPIN QUBITS

Single-spin or Loss-Di Vincenzo qubits were proposed as a quantum computing platform over 25 years ago [76]. The logical states are encoded in the two spin states of a spin-$\frac{1}{2}$ system: $|0\rangle = |\uparrow\rangle$ and $|1\rangle = |\downarrow\rangle$. Both states are split in energy by applying an external magnetic field B, which results in a Zeeman energy splitting $E_z = \hbar\omega_0$, with ω_0 the Larmor frequency. Rotations around the single-qubit Bloch sphere are enabled using resonant electric or magnetic fields of frequency ω_{MW} and amplitude $\hbar\Omega$. The phase of this microwave tone ϕ can also be adjusted to enable arbitrary single-qubit rotations around the Bloch sphere. The effective two-level Hamiltonian describing a Loss-Di Vincenzo spin qubit reads [77]:

$$H_{\mathrm{LD}} = \frac{1}{2}\hbar\Delta\sigma_z + \frac{1}{2}\hbar\Omega\left(\cos(\phi)\sigma_x + \sin(\phi)\sigma_y\right), \tag{2.11}$$

with the detuning $\Delta = \omega_0 - \omega_{\mathrm{MW}}$ between the microwave frequency and the Larmor frequency. Note that this Hamiltonian cancels higher-order rotation terms through the so-called rotating wave approximation, which is valid close to the resonant condition and with weak driving amplitude $\Omega \ll \omega_0$. Single-spin qubits have been realized in GaAs

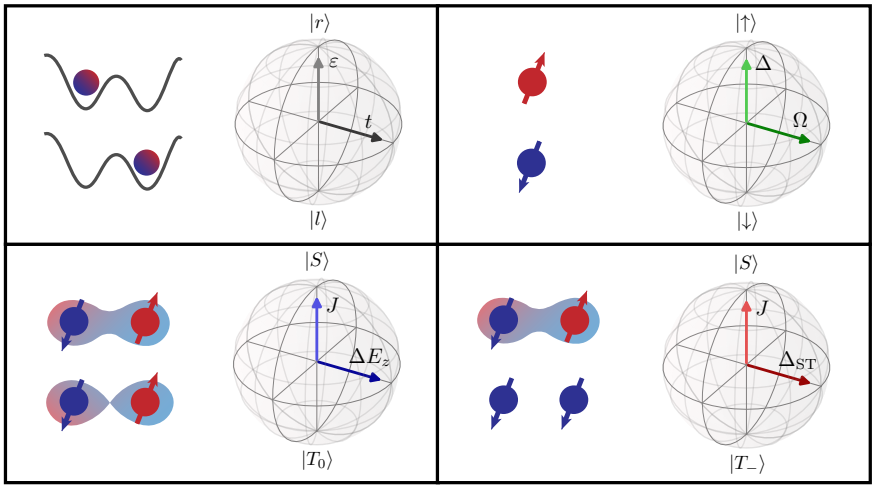

Figure 2.5: Four types of qubits are encountered in this thesis: (a) charge qubits, (b) single-spin qubits, (c) S-T^0 qubits, and (d) S-T^- qubits.

[26, 27], SiMOS [22, 28] and Si/SiGe [29, 30, 78]. In recent years, single-spin qubits have also been demonstrated in a wide range of experiments using Ge/SiGe quantum dots [41, 43, 79]. The single-qubit driving mechanism was discussed in section 2.2.3. In chapter 6, we use resonant microwave driving as a means to characterize the Zeeman energy of each individual single-spin qubit. Here, we do not aim at performing high-fidelity qubit rotations but use microwave driving as a spectroscopic tool.

In addition to single qubit control, two-qubit gates between single-spin qubits are enabled by activating the exchange interaction between neighboring spins. While most high-fidelity two-qubit gate demonstrations [31, 53, 80] rely on exchange interaction strengths smaller than the Zeeman energy difference ($J \ll \Delta E_z$), in chapter 6 we utilize SWAP gates for initialization and readout, which require strong exchange ($J \gg \Delta E_z$) and are suitable for low magnetic field operation.

2.3.3. SINGLET-TRIPLET QUBITS

Encoding the quantum state of a qubit over two or more quantum dots has several potential advantages, typically related to relaxed constraints in qubit control or simplified device layouts. Concretely, the singlet-triplet qubit encoding plays an important role in this thesis, where we exploit elements of qubit initialization, control and readout.

THE S-T_0 QUBIT

Restricting ourselves to the $S_z = 0$ subspace of the two-spin Heisenberg Hamiltonian of Eq. 2.2 yields the effective Hamiltonian for an S-T_0 qubit:

$$H_{\mathrm{ST_0}} = \frac{J}{2}\sigma_z + \frac{\Delta E_z}{2}\sigma_x, \tag{2.12}$$

written in the $\{S, T_0\}$ basis, and assuming a non-zero difference in Zeeman energies ΔE_z. Experimentally, single-qubit X gates are achieved when the exchange interaction

is switched off ($J \ll \Delta E_z$), leading to S-T_0 rotations. Approximate Z rotations are enabled at high J ($J \gg \Delta E_z$). A combination of high-J and low-J pulses allows for two-axis control, enabling arbitrary rotations around the S-T_0 Bloch sphere [44]. Also here, two-qubit gates can be performed by activating the exchange interaction between neighboring qubits. Singlet-triplet qubits have been shown for electrons in GaAs [25, 81] and Si/SiGe [82, 83], as well for holes in SiMOS [84] and Ge/SiGe [44, 85].

THE S-T_- QUBIT

In systems with spin-orbit coupling, one can additionally exploit the resulting anticrossing between the singlet and T_- branches as a means to perform coherent spin rotations outside of the spin-preserving subspace of the Heisenberg Hamiltonian. This enables a further type of singlet-triplet qubit: the S-T_- qubit. The corresponding Hamiltonian near the anticrossing reads:

$$H_{\mathrm{ST}_-} = \frac{\bar{E}_z - J}{2}\sigma_z + \frac{\Delta_{\mathrm{ST}}}{2}\sigma_x, \tag{2.13}$$

with the parameters Δ_{ST} the size of the spin-orbit-induced S-T_- anticrossing. In a recent work, universal control of four S-T_- qubits in a chain was demonstrated [86].

In the context of this thesis, chapter 6 explores an extension of the Hamiltonians of Eqs. 2.12 and 2.13 to coupled, multi-site arrays. Concretely, the two-spin Hamiltonian in Eq. 2.12 showcases two competing terms: an exchange interaction term which favors propagation of individual spin excitations of **magnons**, and a difference in Zeeman energies which promotes localization. In the context of an extended array of spins, the competition of these terms can lead to non-thermalizing phases of matter such as many-body localization [13]. As for Eq. 2.13, we exploit the singlet-triplet control enabled by Eq. 2.13 to explore the dynamics of two-spin excitations or **triplons** in an array of coupled S-T_- qubits. It is a combination of the experimental toolbox developed for the control of single-spin and singlet-triplet qubits, together with an extension of these methods to an analog quantum simulation framework, which enables the experiments outlined in chapter 6.

BIBLIOGRAPHY

[1] F. Bloch. "Über die Quantenmechanik der Elektronen in Kristallgittern". *Zeitschrift für Physik* 52.7 (1929), pp. 555–600.

[2] W. Heitler and F. London. "Wechselwirkung neutraler Atome und homöopolare Bindung nach der Quantenmechanik". *Zeitschrift für Physik* 44.6 (1927), pp. 455–472.

[3] J. H. d. Boer and E. J. W. Verwey. "Semi-conductors with partially and with completely filled 3d-lattice bands". *Proceedings of the Physical Society* 49.4S (1937), p. 59.

[4] J. Hubbard. "Electron correlations in narrow energy bands". *Proc. Roy. Soc. (London), Ser. A* Vol: 276 (1963).

[5] M. C. Gutzwiller. "Effect of Correlation on the Ferromagnetism of Transition Metals". *Physical Review Letters* 10.5 (1963), pp. 159–162.

[6] J. Kanamori. "Electron Correlation and Ferromagnetism of Transition Metals". *Progress of Theoretical Physics* 30.3 (1963), pp. 275–289.

[7] D. P. Arovas et al. "The Hubbard Model". *Annual Review of Condensed Matter Physics* 13.Volume 13, 2022 (2022), pp. 239–274.

[8] E. H. Lieb and F. Y. Wu. "Absence of Mott Transition in an Exact Solution of the Short-Range, One-Band Model in One Dimension". *Physical Review Letters* 20.25 (1968), pp. 1445–1448.

[9] B. Keimer et al. "From quantum matter to high-temperature superconductivity in copper oxides". *Nature* 518.7538 (2015), pp. 179–186.

[10] C. L. Cleveland and R. Medina A. "Obtaining a Heisenberg Hamiltonian from the Hubbard model". *American Journal of Physics* 44.1 (1976), pp. 44–46.

[11] W. Heisenberg. "Zur Theorie des Ferromagnetismus". *Zeitschrift für Physik* 49.9 (1928), pp. 619–636.

[12] W. Zhu, S.-S. Gong, and D. N. Sheng. "Quantum spin liquids in frustrated Kagome Heisenberg model". *Quantum Frontiers* 4.1 (2025), p. 11.

[13] D. A. Abanin et al. "Colloquium: Many-body localization, thermalization, and entanglement". *Reviews of Modern Physics* 91.2 (2019), p. 021001.

[14] R. Hanson. "Spins in few-electron quantum dots". *Reviews of Modern Physics* 79.4 (2007), pp. 1217–1265.

[15] T. Hensgens et al. "Quantum simulation of a Fermi–Hubbard model using a semiconductor quantum dot array". *Nature* 548.7665 (2017), pp. 70–73.

[16] S. Yang, X. Wang, and S. Das Sarma. “Generic Hubbard model description of semiconductor quantum-dot spin qubits”. *Physical Review B* 83.16 (2011), p. 161301.

[17] P. Barthelemy and L. M. K. Vandersypen. “Quantum Dot Systems: a versatile platform for quantum simulations”. *Annalen der Physik* 525.10-11 (2013), pp. 808–826.

[18] J. Knörzer et al. “Long-range electron-electron interactions in quantum dot systems and applications in quantum chemistry”. *Physical Review Research* 4.3 (2022), p. 033043.

[19] W. G. van der Wiel et al. “Electron transport through double quantum dots”. *Reviews of Modern Physics* 75.1 (2002), pp. 1–22.

[20] C. Volk et al. “Loading a quantum-dot based “Qubyte” register”. *npj Quantum Information* 5.1 (2019), p. 29.

[21] B. van Straaten et al. “QArray: A GPU-accelerated constant capacitance model simulator for large quantum dot arrays”. *SciPost Physics Codebases* (2024), p. 035.

[22] M. Veldhorst et al. “A two-qubit logic gate in silicon”. *Nature* 526.7573 (2015), pp. 410–414.

[23] L. Pfeiffer et al. “Electron mobilities exceeding 10^7 cm2/V s in modulation-doped GaAs”. *Applied Physics Letters* 55.18 (1989), pp. 1888–1890.

[24] J. M. Elzerman et al. “Single-shot read-out of an individual electron spin in a quantum dot”. *Nature* 430.6998 (2004), pp. 431–435.

[25] J. R. Petta et al. “Coherent Manipulation of Coupled Electron Spins in Semiconductor Quantum Dots”. *Science* 309.5744 (2005), pp. 2180–2184.

[26] F. H. L. Koppens et al. “Driven coherent oscillations of a single electron spin in a quantum dot”. *Nature* 442.7104 (2006), pp. 766–771.

[27] K. C. Nowack et al. “Coherent Control of a Single Electron Spin with Electric Fields”. *Science* 318.5855 (2007), pp. 1430–1433.

[28] M. Veldhorst et al. “An addressable quantum dot qubit with fault-tolerant control-fidelity”. *Nature Nanotechnology* 9.12 (2014), pp. 981–985.

[29] T. F. Watson et al. “A programmable two-qubit quantum processor in silicon”. *Nature* 555.7698 (2018), pp. 633–637.

[30] S. G. J. Philips et al. “Universal control of a six-qubit quantum processor in silicon”. *Nature* 609.7929 (2022), pp. 919–924.

[31] X. Xue et al. “Quantum logic with spin qubits crossing the surface code threshold”. *Nature* 601.7893 (2022), pp. 343–347.

[32] Y.-H. Wu et al. *Simultaneous High-Fidelity Single-Qubit Gates in a Spin Qubit Array*. 2025.

[33] G. Scappucci et al. “The germanium quantum information route”. *Nature Reviews Materials* 6.10 (2021), pp. 926–943.

[34] M. Cardona. “Energy-Band Structure of Germanium and Silicon: The k·p Method”. *Physical Review* 142.2 (1966), pp. 530–543.

[35] R. Winkler. *Spin—Orbit Coupling Effects in Two-Dimensional Electron and Hole Systems*. Vol. 191. Springer Tracts in Modern Physics. Berlin, Heidelberg: Springer, 2003. ISBN: 978-3-540-01187-3 978-3-540-36616-4.

[36] L. A. Terrazos. "Theory of hole-spin qubits in strained germanium quantum dots". *Physical Review B* 103.12 (2021).

[37] M. Lodari. "Light effective hole mass in undoped Ge/SiGe quantum wells". *Physical Review B* 100.4 (2019).

[38] F. van Riggelen et al. "A two-dimensional array of single-hole quantum dots". *Applied Physics Letters* 118.4 (2021), p. 044002.

[39] F. Borsoi et al. "Shared control of a 16 semiconductor quantum dot crossbar array". *Nature Nanotechnology* 19.1 (2024), pp. 21–27.

[40] T.-K. Hsiao et al. "Exciton Transport in a Germanium Quantum Dot Ladder". *Physical Review X* 14.1 (2024), p. 011048.

[41] V. John et al. *A two-dimensional 10-qubit array in germanium with robust and localised qubit control*. 2024.

[42] B. Hetényi. "Exchange interaction of hole-spin qubits in double quantum dots in highly anisotropic semiconductors". *Physical Review Research* 2.3 (2020).

[43] N. W. Hendrickx et al. "A four-qubit germanium quantum processor". *Nature* 591.7851 (2021), pp. 580–585.

[44] D. Jirovec et al. "A singlet-triplet hole spin qubit in planar Ge". *Nature Materials* 20.8 (2021), pp. 1106–1112.

[45] N. W. Hendrickx et al. "Sweet-spot operation of a germanium hole spin qubit with highly anisotropic noise sensitivity". *Nature Materials* 23.7 (2024), pp. 920–927.

[46] M. Pioro-Ladrière et al. "Electrically driven single-electron spin resonance in a slanting Zeeman field". *Nature Physics* 4.10 (2008), pp. 776–779.

[47] B. Martinez. "Hole spin manipulation in inhomogeneous and nonseparable electric fields". *Physical Review B* 106.23 (2022).

[48] Z. György. "Limitations of the g-tensor formalism of semiconductor spin qubits". *Physical Review B* 112.4 (2025).

[49] J. Danon. "Pauli spin blockade in the presence of strong spin-orbit coupling". *Physical Review B* 80.4 (2009).

[50] P. M. Mutter. "All-electrical control of hole singlet-triplet spin qubits at low-leakage points". *Physical Review B* 104.19 (2021).

[51] K. Ono et al. "Current Rectification by Pauli Exclusion in a Weakly Coupled Double Quantum Dot System". *Science* 297.5585 (2002), pp. 1313–1317.

[52] F. van Riggelen-Doelman et al. "Coherent spin qubit shuttling through germanium quantum dots". *Nature Communications* 15.1 (2024), p. 5716.

[53] C.-A. Wang et al. "Operating semiconductor quantum processors with hopping spins". *Science* 385.6707 (2024), pp. 447–452.

[54] J. Saez-Mollejo et al. “Exchange anisotropies in microwave-driven singlet-triplet qubits”. *Nature Communications* 16.1 (2025), p. 3862.

[55] S. Geyer et al. “Anisotropic exchange interaction of two hole-spin qubits”. *Nature Physics* 20.7 (2024), pp. 1152–1157.

[56] M. A. Nielsen and I. L. Chuang. *Quantum Computation and Quantum Information: 10th Anniversary Edition*. 2010.

[57] K. Eng et al. “Isotopically enhanced triple-quantum-dot qubit”. *Science Advances* 1.4 (2015), e1500214.

[58] O. Moutanabbir et al. “Nuclear Spin-Depleted, Isotopically Enriched 70Ge/28Si70Ge Quantum Wells”. *Advanced Materials* 36.8 (2024), p. 2305703.

[59] M. Lodari et al. “Low percolation density and charge noise with holes in germanium”. *Materials for Quantum Technology* 1.1 (2021), p. 011002.

[60] B. Paquelet Wuetz et al. “Reducing charge noise in quantum dots by using thin silicon quantum wells”. *Nature Communications* 14.1 (2023), p. 1385.

[61] L. E. A. Stehouwer et al. “Exploiting strained epitaxial germanium for scaling low-noise spin qubits at the micrometre scale”. *Nature Materials* (2025), pp. 1–7.

[62] J. Roffe. “Quantum error correction: an introductory guide”. *Contemporary Physics* 60.3 (2019), pp. 226–245.

[63] E. T. Campbell, B. M. Terhal, and C. Vuillot. “Roads towards fault-tolerant universal quantum computation”. *Nature* 549.7671 (2017), pp. 172–179.

[64] F. van Riggelen et al. “Phase flip code with semiconductor spin qubits”. *npj Quantum Information* 8.1 (2022), p. 124.

[65] K. Takeda et al. “Quantum error correction with silicon spin qubits”. *Nature* 608.7924 (2022), pp. 682–686.

[66] E. Campbell. “A series of fast-paced advances in Quantum Error Correction”. *Nature Reviews Physics* 6.3 (2024), pp. 160–161.

[67] R. Trivedi, A. Franco Rubio, and J. I. Cirac. “Quantum advantage and stability to errors in analogue quantum simulators”. *Nature Communications* 15.1 (2024), p. 6507.

[68] G. González-García, R. Trivedi, and J. I. Cirac. “Error Propagation in NISQ Devices for Solving Classical Optimization Problems”. *PRX Quantum* 3.4 (2022), p. 040326.

[69] K. D. Petersson et al. “Quantum Coherence in a One-Electron Semiconductor Charge Qubit”. *Physical Review Letters* 105.24 (2010), p. 246804.

[70] T. Hayashi et al. “Coherent Manipulation of Electronic States in a Double Quantum Dot”. *Physical Review Letters* 91.22 (2003), p. 226804.

[71] G. Cao et al. “Ultrafast universal quantum control of a quantum-dot charge qubit using Landau–Zener–Stückelberg interference”. *Nature Communications* 4.1 (2013), p. 1401.

[72] Z. Shi et al. “Coherent quantum oscillations and echo measurements of a Si charge qubit”. *Physical Review B* 88.7 (2013), p. 075416.

[73] D. Kim et al. “Microwave-driven coherent operation of a semiconductor quantum dot charge qubit”. *Nature Nanotechnology* 10.3 (2015), pp. 243–247.

[74] X. Zhou et al. “Electron charge qubit with 0.1 millisecond coherence time”. *Nature Physics* 20.1 (2024), pp. 116–122.

[75] T. H. Oosterkamp et al. “Microwave spectroscopy of a quantum-dot molecule”. *Nature* 395.6705 (1998), pp. 873–876.

[76] D. Loss and D. P. DiVincenzo. “Quantum computation with quantum dots”. *Physical Review A* 57.1 (1998), pp. 120–126.

[77] E. Kawakami. “Characterization of an electron spin qubit in a Si/SiGe quantum dot”. Dissertation (TU Delft). 2016.

[78] E. Kawakami et al. “Electrical control of a long-lived spin qubit in a Si/SiGe quantum dot”. *Nature Nanotechnology* 9.9 (2014), pp. 666–670.

[79] N. W. Hendrickx et al. “A single-hole spin qubit”. *Nature Communications* 11.1 (2020), p. 3478.

[80] A. Noiri et al. “Fast universal quantum gate above the fault-tolerance threshold in silicon”. *Nature* 601.7893 (2022), pp. 338–342.

[81] C. Barthel et al. “Rapid Single-Shot Measurement of a Singlet-Triplet Qubit”. *Physical Review Letters* 103.16 (2009), p. 160503.

[82] B. M. Maune et al. “Coherent singlet-triplet oscillations in a silicon-based double quantum dot”. *Nature* 481.7381 (2012), pp. 344–347.

[83] X. Wu et al. “Two-axis control of a singlet–triplet qubit with an integrated micromagnet”. *Proceedings of the National Academy of Sciences* 111.33 (2014), pp. 11938–11942.

[84] S. D. Liles et al. “A singlet-triplet hole-spin qubit in MOS silicon”. *Nature Communications* 15.1 (2024), p. 7690.

[85] D. Jirovec et al. “Dynamics of Hole Singlet-Triplet Qubits with Large g-Factor Differences”. *Physical Review Letters* 128.12 (2022), p. 126803.

[86] X. Zhang et al. “Universal control of four singlet–triplet qubits”. *Nature Nanotechnology* 20.2 (2025), pp. 209–215.

3

EXPERIMENTAL METHODS

In the first two chapters of this thesis, I have introduced many relevant concepts related to the capabilities of quantum dot arrays as quantum processors and simulators. The goal of this chapter is to complement these more theoretical and abstract notions with the actual procedures which are required to experimentally observe the desired phenomena. While briefly, I will touch upon many relevant aspects such as device design, fabrication and testing, as well as the experimental setup and the tuning procedure.

3.1. DEVICE LAYOUT AND FABRICATION

3.1.1. HETEROSTRUCTURE GROWTH AND DEVICE FABRICATION

The device geometry of choice for the experimental results outlined in chapters 4, 5 and 6 is a 2×4 quantum dot array, fabricated on a $Ge/Si_{0.2}Ge_{0.8}$ heterostructure, with the Ge quantum well buried 55 nm below the surface. The heterostructure was grown using chemical vapor deposition starting from a Si substrate. After growing a thick layer of Ge on the substrate, the Si concentration is linearly increased to reach the desired composition. Details about the heterostructure and the growth process can be found in Ref. [1].

The fabrication of the devices used in this thesis was carried out by Stefan D. Oosterhout (TNO). As opposed to single-layer fabrication, common for smaller devices or industrial cleanrooms [2, 3], our quantum dot devices are fabricated in a multi-layer fashion. As a first step, Pt or Al Ohmic contacts are defined using electron-beam lithography. The Ohmics are subsequently annealed, so that they diffuse into the heterostructure and directly contact the quantum well. Due to Fermi level pinning in Ge/SiGe heterostructures [4], carriers in the Ohmic contacts can be directly loaded into the semiconductor without the need for implanted regions and accumulation gates, typical for Si devices [5]. After depositing the Ohmics, three fabrication layers are used to electrostatically define the quantum dots: screening gates, plunger gates and barrier gates. The plunger gates are used to control the chemical potential of each quantum dot; barriers are used to modulate the interaction strength between neighboring dots; and screening gates prevent unwanted charge accumulation around the quantum dot area. The gate material is Ti/Pd with a thickness of 3/17 nm for the first gate layer, 3/27 nm for the second, and 3/37 nm for the third gate layer. Gate layers are separated from each other with 5 nm insulating Al_2O_3 layers, grown with atomic layer deposition (ALD).

3.1.2. LAYOUT AND GATE NAMING

Fig. 3.1 shows two scanning electron microscopy (SEM) images of two 2×4 devices, nominally identical to those used in this thesis. The plunger gates of quantum dots 1-8 are labeled accordingly. The four additional, larger dots on the corners of the device are the **sensing dots** used for measuring the charge state of the quantum dot array (see sec. 3.4.2). For the remainder of this thesis, I will use the following nomenclature for gate voltages: The variable p_i stands for "the voltage on the plunger gate of dot i", while b_{ij} refers to "the voltage on the barrier gate between dots i and j". Specifically for the barrier gates which control the coupling between a quantum dot and its neighboring sensing dot, b_i will be used, leaving out the subscript for the sensor for simplicity. Whenever gate voltages are virtualized to compensate for crosstalk (see e.g. section 3.4.3 or chap-

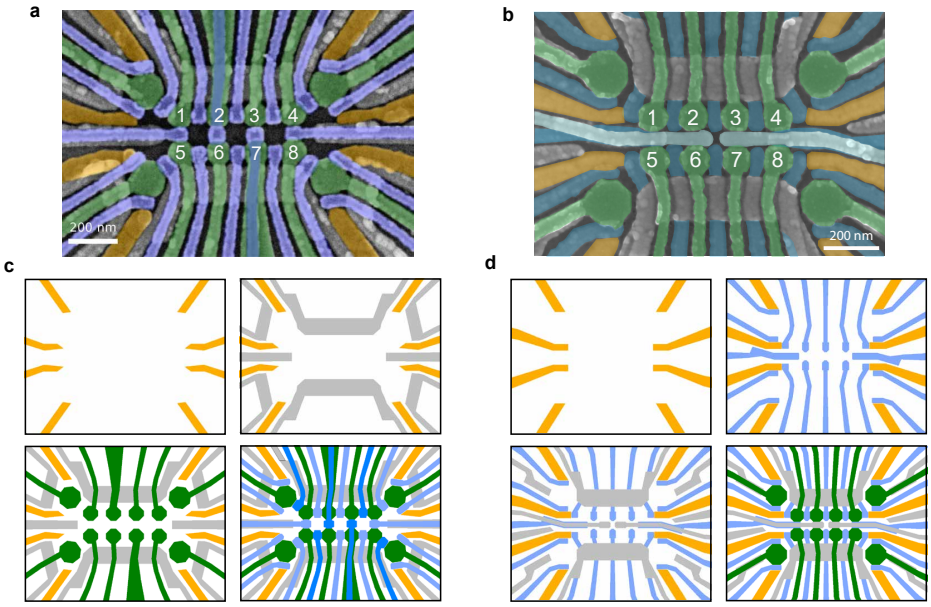

Figure 3.1: (a) Flase-colored scanning electron microscope (SEM) image of a Ge/SiGe 2×4 array, nominally identical to the devices used to measure exciton transport and triplon propagation (chapters 4 and 6). This device will be refered to as device I. (b) SEM of image of a Ge/SiGe 2×4 array, nominally identical to the device used to measure exchange virtualization and magnon propagation (chapters 5 and 6). This device will be refered to as device II. For both SEM images, the Ohmic contacts are color-coded in yellow, the screening gates in gray, the barrier gates in blue and the plunger gates in green. (c) Gate layout corresponding to device I. The order of fabrication is Ohmics-screening-plungers-barriers. (d) Gate layout corresponding to device II. The order of fabrication is Ohmics-barriers-screening-plungers.

ter 5), this will be labeled accordingly with a dash (') or with the letter "v" in front of the corresponding barrier or plunger variable.

The scanning electron microscope (SEM) image of Fig. 3.1a corresponds to the first successful generation of 2×4 devices. Two nominally identical devices from the same batch were used to perform the exciton transport and triplon propagation experiments (chapters 4 and 6, respectively). While performing these experiments, two shortcomings of the gate layout became apparent. First, reducing the tunnel coupling between sensing dots and their neighboring quantum dots, important for quantum dot operation, often led to a poor sensing dot quality. Second, having the barrier gates in the highest fabrication layer resulted in a limited exchange coupling control. These two findings led to the redesigning of a new generation of devices (Fig. 3.1b). In this case, the barrier gates were fabricated in the lowest layer, increasing their impact on the interdot coupling strength. Furthermore, loading of charges to the quantum dot array was designed to happen directly via the Ohmic contacts, suppressing sensor-to-dot tunnel coupling, while only minimally increasing the distance between sensing dot and quantum dots. Fig. 3.1c and d show the corresponding gate layouts for devices I and II, respectively, as drawn and designed using the software KLayout.

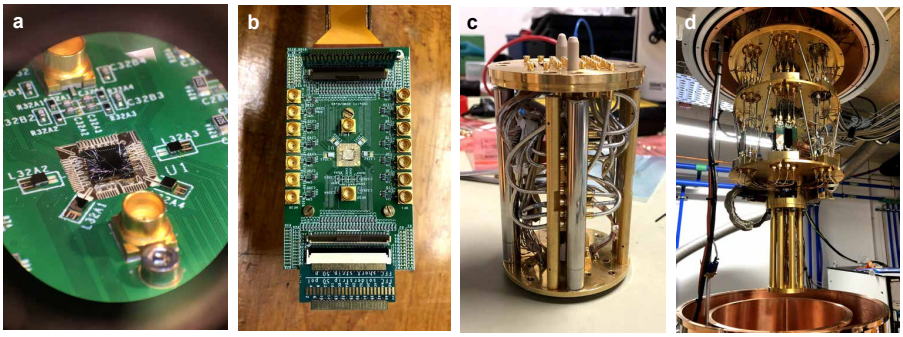

Figure 3.2: (a) Picture of a 4×4 mm chip containing a 4×2 device, imaged under an optical microscope. The device is glued and bonded on a printed circuit board (PCB) which was designed in house. Additionally, four off-chip NbTiN inductors are visible, which are used for RF readout. (b) Picture of a PCB with a wire bonded sample. This PCB allows for up to 100 DC lines for electrostatic control. Two groups of 50 DC lines each are routed to the top and bottom parts of the PCB, where they can be connected to flat flexible cables (FFC). Additionally, bias-tees are used to connect AC lines to some gates, enabling fast control for up to 32 lines. Each fast line is routed to an individual SMP connector, 15 on each side of the PCB, with the remaining two connectors in the center. (c) Image of a puck containing a PCB with a sample, before loading to the fridge and with the outer shield removed. In addition to FFCs for DC wiring, several hand-formable coaxial cables are used to connect each RF line to the top part of the puck, which can be connected to the mixing chamber plate of the fridge. (d) Image of the open Oxford Instruments Triton dilution refrigerator used for the experiments in this thesis. When the fridge is closed, the puck with the sample can be exchanged without opening the fridge using a bottom-loading system.

3.2. DEVICE SCREENING: 4 K MEASUREMENTS

3.2.1. FAILURE MODES AND FIRST SCREENING

Each fabrication round usually yields a batch of eight 4×4 mm chips. Given the complex gate pattern and multi-layer fabrication process, there are many failure modes that can render a device unusable. For instance, bad quality oxide can result in contact between gates of different layers, resulting in gate-to-gate leakage. Having too many overlapping gates or gates too close to each other often causes gate delamination. Unsafe handling of devices can lead to electrostatic discharge (ESD). Additionally, we observed that unwanted contact to the two-dimensional hole gas (2DHG) under the bonding pads can result in gates shorted to ground. These failure modes often lead to low device yields. In order to identify these failure modes before the tuning stage, a device screening routine allows for fast device characterization before cooling down devices to millikelving temperatures. A useful first step is device imaging with an atomic-force microscope (AFM), which is non-invasive and typically allows to identify major device failure modes such as gate delamination or ESD.

3.2.2. GLUEING AND PCB DESIGN

The devices which pass the AFM inspection are then bonded and glued onto custom-built printed circuit boards (PCB) using GE varnish. An image of a bonded 2×4 device under the optical microscope can be seen in Fig. 3.2a, while Fig. 3.2b shows an image of

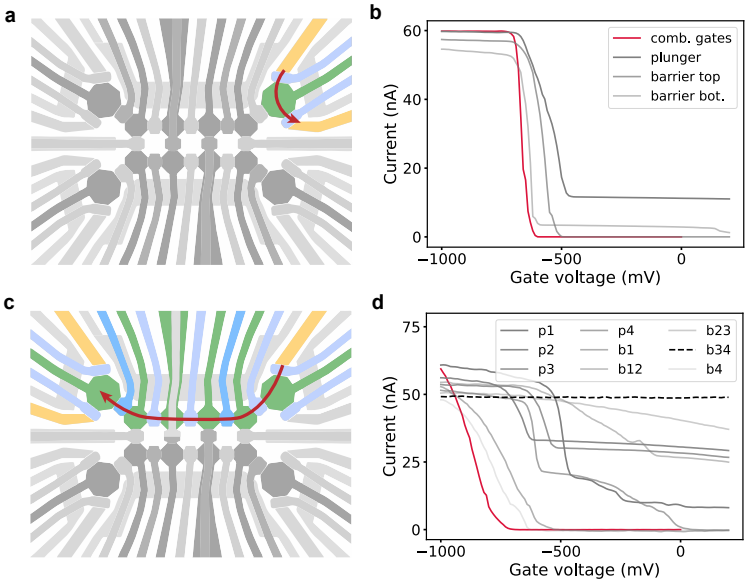

Figure 3.3: Characterization of devices at 4 K. (a) Gate layout of a tested 4×2 device. A source-drain bias is applied across the two Ohmic contacts on the top right sensing dot. The current passing through the sensor (red arrow) is acquired as a function of voltage applied to all gates highlighted in color. (b) Red: Turn-on curve as a function of all gate voltages, scanned simultaneously. Gray: Individual pinch-off curves, where all gate voltages are kept at −1000 mV, and a single gate is scanned to positive voltages. (c) A source-drain bias is applied across the Ohmics on the top quantum dot channel. The current passing through the channel (red arrow) is acquired as a function of voltage applied to all gates highlighted in color. (b) Red: Turn-on curve as a function of all gate voltages, scanned simultaneously. Gray: Individual pinch-off curves. For this device, gate b_{34} (black dashed line) showed no effect.

a PCB with a wire bonded device in the center. This type of PCB supports up to 100 DC lines, which can be connected using two 50-line flat flexible (FFC) cables. Additionally, we use bias-tees with resistor-capacitor time constants of 100 ms, orders of magnitude longer than the duration of each single experimental shot, to simultaneously enable for fast RF control for a subset of 32 lines. Each fast line is individually routed to a sub-miniature push-on (SMP) connector.

One of the two center SMP pins is multiplexed with four different RF lines to enable simultaneous readout of up to four charge sensors (see sec. 3.4.1).

3.2.3. DIPSTICK TEST

We typically screen devices using a variable temperature insert (VTI) or **dipstick** setup, where devices are quickly cooled down to liquid helium temperatures. In a typical dipstick test, all DC lines are connected to a custom-built matrix module and serial peripheral interface (SPI) DAC modules, which allow us to set and scan DC voltages for all gates. During the test, using a ground lifting scheme, we typically apply a source-drain bias V_{SD} to an Ohmic contact and measure the current passing through another Ohmic while a combination of gate voltages are scanned. At 4 K, the 2DHG is fully depleted at zero gate

voltage. Like in the case of transistors, when a certain **turn-on** voltage is applied to the gates, conduction through the device is enabled, resulting in a measurable current. Conversely, when the channel is accumulated and a single gate is scanned to more positive voltages until the current is stopped, the channel is said to be **pinched off**.

We first measure the turn-on and pinch-off curves through the four sensing dots, as exemplarily shown for the top right sensor in Figs. 3.3a and b. In this particular case, we measure the current between the two top right Ohmics with a source-drain bias of V_{SD} =1 mV. We first scan all relevant gate voltages, i.e. the sensing dot plunger and both sensing dot barriers all the way to V_{gates} =−1000 mV. We observe a channel turn-on at about −600 mV (red curve in Fig. 3.3b). After we reach this value, all gate voltages are left at −1000 mV, and the individual gates are scanned back to zero volts and back. For each gate, we observe their pinch-off behavior and we can extract the individual pinch-off voltages. Note that, for this particular example, both the plunger and the bottom barrier cannot fully pinch off the channel, leading to a finite current at zero gate voltage. However, this is often of little relevance in quantum dot experiments, where DC voltages are kept at smaller absolute values, below their pinch-off voltage. Another observation is that the maximum current value shifts down for gates scanned at a later time, owing to device drifts. These drifts are typically caused by accumulation of charges at the interface between heterostructure and dielectric [6]. These charges increasingly screen gate voltages over time, leading to a hysteretic behavior. At millikelvin temperatures, where fewer charge traps are thermally activated compared to 4 K temperatures, we have often observed that these drifts are typically mitigated.

We further test the gate voltages of the quantum dot array by repeating the same procedure, but this time measuring between the top right and top left Ohmics, as depicted in Fig. 3.3c. Fig. 3.3d shows the channel turn-on curve (in red) and individual pinch-off curves (in gray) for all channel gates. In this particular case, almost all gates show an effect on the current passing through the channel. However, gate b_{34}, shown as a black dashed line, seems to have no effect. In this particular case, we would deem the device unusable and discard it.

3.3. SETUP

After a suitable device is found, it is mounted on a puck (Fig. 3.2c), where both DC and AC lines are connected using FFC and hand-formable coaxial cables, respectively. Most experiments in this work are carried out in an Oxford Instruments Triton dilution refrigerator with base temperatures of around 10 mK (Fig. 3.2d). When the fridge is cooled down, the puck can be introduced and connected to the refrigerator's mixing chamber plate using a bottom-loading system. This allows for a fast sample exchange without the need to open or warm up the refrigerator.

A schematic view of the experimental setup is depicted in Fig. 3.4. Inside of the dilution refrigerator, the routing of both RF and DC lines is shown. RF lines are attenuated and thermally anchored to each dilution refrigerator plate using cryogenic attenuators, with total attenuation of the lines ranging from 23 to 27 dB. Additionally, these lines are filtered using common-mode ferrite chokes at room temperature to filter out low-frequency noise. Having been upgraded several times over the years, this refrigerator has a capacity for up to 28 RF lines, which limits the size of the quantum dot arrays that

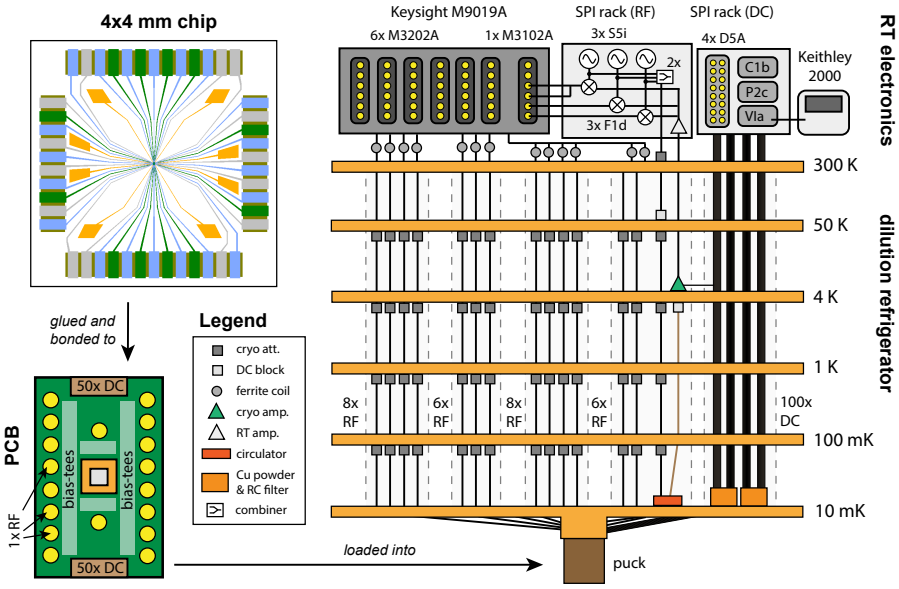

Figure 3.4: Schematics of the measurement setup. A 4×4 millimeter chip containing a 2×4 quantum dot array is glued and bonded on a PCB with capacity for 100 DC and 32 AC lines. The PCB is connected and mounted into a puck, which sits at the mixing chamber plate of an Oxford Instruments Triton dilution refrigerator. The refrigerator itself contains five stages with varying temperatures and is equipped with 100 DC and 28 AC lines, routed all the way from the puck to room temperature and thermally anchored to each stage. The DC lines are grouped in bundles of 24 lines (12 twisted pairs). At 10 mK, high-frequency noise is filtered using copper powder and RC filters. The RF lines are organized in four columns of 6 or 8 lines each. The noise from room temperature instrumentation on each RF line is mitigated using cryogenic attenuators. The typical total attenuation of the lines ranges from 23 to 27 dB. Additionally, the two lines used for RF reflectometry readout are connected to the same PCB line using a circulator on the mixing chamber plate. The signal of the output readout line is amplified using both a cryogenic and a room temperature (RT) amplifier. At room temperature, all RF and DC lines are connected to the corresponding electronics: a Keysight arbitrary waveform generator (AWG) for fast pulsing; RF sources and demodulators for reflectometry readout; and DC electronics to set voltages and read out currents.

could be operated in this refrigerator to about 10 spins, depending on connectivity.

At room temperature, all RF lines are connected to Keysight M3202A arbitrary waveform generators (AWG) with a sampling rate of 1 GSa/s, allowing for baseband pulse control of the device's plunger and barrier gate voltages. Two additional RF lines allow for fast charge and spin readout using RF reflectometry (see sec. 3.4.1 below). At room temperature, two homemade RF sources are used to generate the carrier signals, which are combined and sent through an input line which is multiplexed to up to four tank circuits using bias-tees on the PCB. A circulator on the mixing chamber plate allows to retrieve the reflected signal through the readout RF line. This signal is amplified both at 4 K and at room temperature using a cryogenic and a room temperature amplifier, and then demodulated and read out with an M3102A module.

For the DC lines, high-frequency noise is filtered using resistor-capacitor filters and

copper-powder filters at the mixing chamber plate, depicted in orange. At room temperature, each DC line is connected to the ports of home-built serial peripheral interface (SPI) DAC modules to individually set DC voltages. If necessary, a Keithley 2000 multimeter is used to read out the DC current.

3.4. DEVICE TUNING

Tuning up a multi-dot quantum dot array to the point where one can start exploring physics with it is perhaps the most time-consuming experimental task. Using a double quantum dot as an example, the following paragraphs will go through the most important tuning steps, starting from the moment a device is cooled down all the way to performing spin readout.

3.4.1. SENSOR TUNING AND RF REFLECTOMETRY

At the start of a typical tuning routine, DC gate voltages are set close to the expected accumulation voltages for sensors and quantum dots, as roughly extracted from the turn-on values from the dipstick tests. As a next step, we tune up the device's charge sensors. The goal is to obtain regular **Coulomb peaks** or Coulomb oscillations [7]: a non-linear modulation of the current between Ohmics, resulting from the quantum dot's electrochemical potential levels being inside (current) or outside (no current) of the source-drain voltage window. Starting from the turn-on voltages for each sensing dot, the barrier voltages to the reservoirs are iteratively lowered and adjusted, until a more or less regular pattern of Coulomb peaks is obtained (Fig. 3.5a). Typically, sharp and regular Coulomb peaks are an indication of a well-tuned sensing dot. However, in practice, only a single, sharp Coulomb peak is required to perform measurements. Once this Coulomb peak is found, the DC voltage of the sensing dot plunger is set to one of its flanks. At this voltage point the current through the sensing dot is particularly sensitive to the change in charge state of nearby quantum dots, as a result of capacitive coupling. This measurable change in current is used to perform charge state readout.

For subsequent tuning steps, reading out the current in a DC fashion is typically too slow. Instead, the state of the sensors can be also read out using **radiofrequency (RF) reflectometry** [8]. This method requires an extra inductor to be bonded to one of the two Ohmic contacts. In this case we use homemade off-chip NbTiN inductors (see also Fig. 3.2a). Together with the bond wire to the sensing dot, this forms an inductor-capacitor (LC) tank circuit, with a resonance frequency $\omega_i \sim \frac{1}{\sqrt{L_i C_i}}$, with L_i the inductance of each resonator and C_i the total capacitance. Then, changes in the resistance of the sensing dot channel embedded in the tank circuit result in differences in the RF signal reflected by the circuit, which can be measured.

Every inductor is fabricated to have a different inductance by means of changing their length or width. This results in a different resonance frequency for each tank circuit, such that the readout circuit can be multiplexed to a single RF readout line. This allows for simultaneous readout of all sensors, together with modulation and demodulation measurements using custom-built SPI RF generators and in-phase and quadrature (IQ) demodulators (see Fig. 3.4). Typical resonance frequencies of about 100 MHz allow for high-speed readout, with typical 2D scans taking only a fraction of a second,

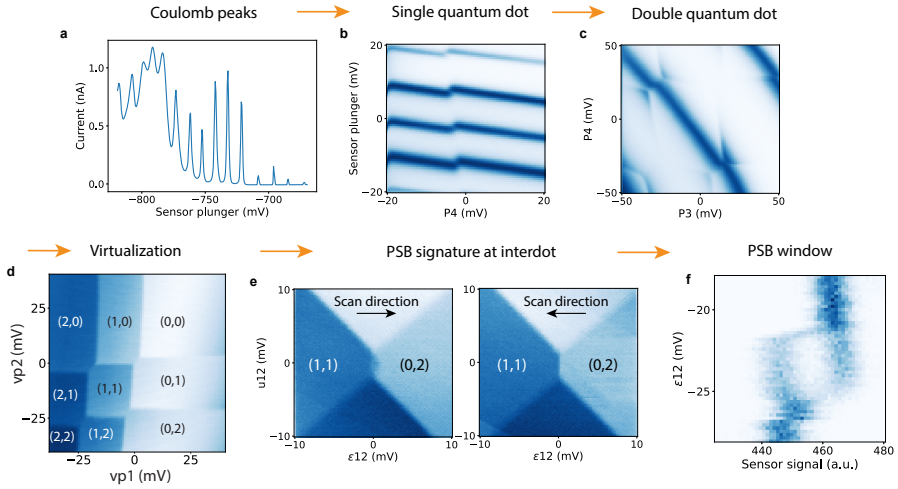

Figure 3.5: Tuning of a double quantum dot: from Coulomb peaks to PSB. (a) Sensing dot Coulomb peaks measured in transport, as a function of plunger gate voltage. (b) Sensing dot Coulomb peaks measured with RF reflectometry, as a function of the voltage on the sensor plunger and quantum dot gate p_4. The first addition line of quantum dot 4 is visible as a shift of the Coulomb peaks. (c) Sensing dot signal as a function of gate voltages p_3 and p_4. The addition lines of quantum dots 3 and 4 are visible near the sensing dot Coulomb peaks. (d) Sensing dot signal as a function of virtual gate voltages vp_1 and vp_2, which compensate for crosstalk to the sensor and between quantum dots. (e) Sensing dot signal around the (1,1)-(0,2) transition as a function of detuning ε_{12} and global chemical potential u_{12}. In the forward scan direction, the characteristic signature of PSB is visible as a fuzzy triangular region. (f) Histogram of sensor signal as a function of detuning ε_{12}. At the PSB region (center of the plot), two peaks are clearly visible, which correspond to two different spin states.

which significantly eases the further tuning procedure. In fact, this allows to tune up charge stability diagrams (see below) in "real time" by quickly generating and plotting measurement data as parameters are swept. We refer to this process as **video mode** tuning.

3.4.2. CHARGE SENSING AND CHARGE STABILITY DIAGRAMS

Changes of the charge state of nearby quantum dots will result in shifts of the sensing dot's electrochemical potential levels. In Fig. 3.5b, the voltage of the top right sensor plunger p_{TR} is scanned against the voltage of p_4, the plunger gate of the closest quantum dot. Note that the "zero" point does not represent zero voltage, but the relative voltage away from the set DC values. Along the y-axis, the expected modulation of Coulomb peaks is observed. A sudden jump of the sensing dot as a function of the voltage p_4 is consistent with the change of the charge state of quantum dot 4 by 1. Additionally, the cross-capacitance between gate voltages and quantum dots results in both the addition line and the sensing dot Coulomb peaks to be slanted.

Scanning gate voltages p_3 against p_4, one can observe the characteristic double-dot pattern of a charge stability diagram in Fig. 3.5c (compare with Fig. 2.2). The lack of crosstalk compensation results in an oscillating sensor signal and slanted transition lines.

3.4.3. CROSSTALK COMPENSATION

Tuning up a multi-dot array benefits heavily from crosstalk compensation. This is routinely done through the process of **virtualization** of the gate voltages. In particular, the voltage crosstalk to all quantum dot's chemical potentials is linear [9]. This linearity can be seen exemplarily in Figs. 3.5b and c, resulting in a slope of the Coulomb peaks and of both quantum dot's addition lines. These slopes can be extracted to obtain the crosstalk elements α_{ij} between gate voltage p_i and quantum dot j (per definition, we set $\alpha_{ii} = 1$). This allows for an efficient transformation between real voltages and a set of virtual gate voltages $vp_i = \sum_j \alpha_{ij} p_j$, which then control the individual chemical potentials. All crosstalk values can be extracted from measurements such as in Figs. 3.5b and c, and inputted as elements of a single virtualization matrix, a transformation matrix between real and virtual gate space.

For a double quantum dot, one can then obtain charge stability diagrams like in Fig. 3.5d, as a function of gate voltages vp_1 and vp_2, where each charge state has a distinct charge sensor signal, and the addition lines of dot i are independent of the voltage on virtual gate vp_j. Each quantum dot charge state can then be labeled as (n_i,n_j), as seen in the Figure. Note that barrier-to-plunger compensation can also be performed in the same fashion, tracking each addition line as a function of barrier voltage. However, barrier-to-barrier compensation, which is relevant to be able to dial in tunnel couplings independently of each other, is typically a more challenging task. This is the subject of chapter 5.

3.4.4. PAULI SPIN BLOCKADE TUNING

As discussed in section 2.2.4, spin-to-charge conversion via Pauli spin blockade (PSB) allows for the charge sensor to distinguish between two spin states, which yield a blocked and an unblocked signal. For a pair of quantum dots, their PSB readout window is typically found as a triangular region next to the interdot line between the (1,1) and (0,2) charge states. The left panel of Fig. 3.5e shows a typical 2D plot around this PSB region, showing the expected "fuzziness" next to the interdot line. This signal results from averaging over many realizations and with both spins being likely in a mixed state, since no particular initialization scheme is used here (as outlined e.g. in section 2.2.4). Note that, for this plot, the scan axes are not the individual chemical potentials, but the detuning $\varepsilon_{12} = \frac{1}{2}(vp_1 - vp_2)$ and the global electrochemical potential $u_{12} = vp_1 + vp_2$.

It is worth noting that, at small tunnel couplings, a similar fuzzy signal is expected at the interdot line because of latching, where tunneling between quantum dots is slow due to the low tunneling rates. A key signature to distinguish latching from PSB is the absence of fuzziness when reversing the scan direction for PSB, as shown in the right panel of 3.5f. This is because Pauli exclusion principle allows for the (0,2) to (1,1) transition, irrespectively of the spin state. To further quantify the PSB window, one can plot a histogram of the sensor signal as a function of detuning, shown in Fig. 3.5f. In the center of the plot, two distinct peaks emerge, corresponding to the two different spin states. Ultimately, the clearest test to prove that readout is properly tuned up is the measurement of spin-dependent phenomena like the position of the ST^- anticrossing, singlet-triplet oscillations or single-spin resonances.

BIBLIOGRAPHY

[1] M. Lodari et al. “Low percolation density and charge noise with holes in germanium”. *Materials for Quantum Technology* 1.1 (2021), p. 011002.

[2] X. Xue et al. “Quantum logic with spin qubits crossing the surface code threshold”. *Nature* 601.7893 (2022), pp. 343–347.

[3] H. C. George et al. “12-Spin-Qubit Arrays Fabricated on a 300 mm Semiconductor Manufacturing Line”. *Nano Letters* 25.2 (2025), pp. 793–799.

[4] A. Dimoulas et al. “Fermi-level pinning and charge neutrality level in germanium”. *Applied Physics Letters* 89.25 (2006), p. 252110.

[5] S. G. J. Philips et al. “Universal control of a six-qubit quantum processor in silicon”. *Nature* 609.7929 (2022), pp. 919–924.

[6] M. Meyer et al. “Electrical Control of Uniformity in Quantum Dot Devices”. *Nano Letters* 23.7 (2023), pp. 2522–2529.

[7] R. Hanson. “Spins in few-electron quantum dots”. *Reviews of Modern Physics* 79.4 (2007), pp. 1217–1265.

[8] Y.-Y. Liu et al. “Radio-Frequency Reflectometry in Silicon-Based Quantum Dots”. *Physical Review Applied* 16.1 (2021), p. 014057.

[9] C. Volk et al. “Loading a quantum-dot based “Qubyte” register”. *npj Quantum Information* 5.1 (2019), p. 29.

4

EXCITON TRANSPORT IN A GERMANIUM QUANTUM DOT LADDER

Quantum systems with engineered Hamiltonians can be used to study many-body physics problems to provide insights beyond the capabilities of classical computers. Semiconductor gate-defined quantum dot arrays have emerged as a versatile platform for realizing generalized Fermi-Hubbard physics, one of the richest playgrounds in condensed matter physics. In this work, we employ a germanium 4×2 quantum dot array and show that the naturally occurring long-range Coulomb interaction can lead to exciton formation and transport. We tune the quantum dot ladder into two capacitively-coupled channels and exploit Coulomb drag to probe the binding of electrons and holes. Specifically, we shuttle an electron through one leg of the ladder and observe that a hole is dragged along in the second leg under the right conditions. This corresponds to a transition from single-electron transport in one leg to exciton transport along the ladder. Our work paves the way for the study of excitonic states of matter in quantum dot arrays.

This chapter has been published as: Tzu-Kan Hsiao, **Pablo Cova Fariña**, Stefan D. Oosterhout, Daniel Jirovec, Xin Zhang, Cornelis Jacobus van Diepen, William I. L. Lawrie, Chien-An Wang, Amir Sammak, Giordano Scappucci, Menno Veldhorst, Eugene Demler, and Lieven M. K. Vandersypen, "Exciton transport in a germanium quantum dot ladder", Physical Review X, **14**, 011048 (2024).

4.1. INTRODUCTION

Quantum systems with well-controlled interaction parameters can shed light on the physics of strongly-correlated many-body quantum systems [1, 2]. Electrostatically-defined semiconductor quantum dot arrays, owing to their in-situ tunability of electrochemical potentials and relevant energy scales which can far exceed the thermal energy, have become an attractive platform for studying a wide variety of fermionic systems [3–6]. Over the past few years, the techniques for control and probing of quantum dot simulators has progressed significantly. This platform and closely related donor arrays have been used as a small-scale simulator of Mott-Hubbard physics [7–9], Nagaoka ferromagnetism [10], Heisenberg antiferromagnetic spin chains [11], resonating valence bond states [12], and the Su–Schrieffer–Heeger model [13].

The charge carriers confined in quantum dot arrays exhibit an intrinsic long-range Coulomb interaction which is essential for a wide range of interesting phenomena. The long-range interaction induces spontaneous ordering of charges in a flat potential landscape to form a Wigner crystal [14, 15]. Similar spontaneous charge ordering occurs in lattice potentials that are fractionally-filled [16, 17]. Also pair density wave states crucially rely on non-local interactions [18]. When particles of opposite charge are involved, the long-range Coulomb interaction is attractive instead of repulsive, and composite particles can be formed. The attractive interaction between electrons and holes is the essential ingredient for exciton formation [19], excitonic insulators [20] and exciton condensates [21]. In lattices that are close to fractional filling, a charge-transfer exciton can bind one or two holes, giving rise to a polariton or trimer [22]. It has been suggested that this trimer can give rise to unconventional superconductivity [23].

The long-range Coulomb interaction combined with the precise control of the lattice filling, inter-dot charge tunneling and the spin degree of freedom thus allow quantum dot systems access to a wealth of interesting many-body phenomena in Coulomb-mediated states of matters. In ultra-cold atoms systems, combining tunneling with long-range interactions has only recently been achieved [24, 25], and remains challenging. For ultracold atoms in optical lattices, the Hamiltonian is usually limited to on-site interactions and tunneling [26, 27]. Conversely, for atoms with a large magnetic moment or dipolar molecules in optical lattices, long-range dipolar interactions exist, but tunneling is generally absent [28, 29]. In such platforms as well as for Rydberg atoms trapped by optical tweezers, the focus has therefore been on studying various spin models [30–32].

In low-dimensional solid-state systems, a clear manifestation of long-range Coulomb interactions is Coulomb-drag. In a two-channel system, a current imposed by a voltage bias across one channel (the drive channel) leads to a current or voltage across a second channel (the drag channel) [33]. Coulomb drag can take two forms. “Positive" Coulomb drag occurs when an electron in the drive channel pushes electrons in the drag channel forward due to Coulomb-mediated momentum transfer [34]. “Negative" Coulomb drag can result from Wigner-crystal physics [35] or from exciton formation [33, 36], in which the motion of a charge carrier in the drive channel pulls along a charge carrier of opposite sign in the drag channel. The negative Coulomb drag effect from exciton formation has been observed in double quantum wells in the quantum hall regime [33, 37, 38], double quantum wires [39] and 2D materials [40–42]. In these works, the negative Coulomb drag is interpreted as resulting from inter-channel exciton transport. Whereas

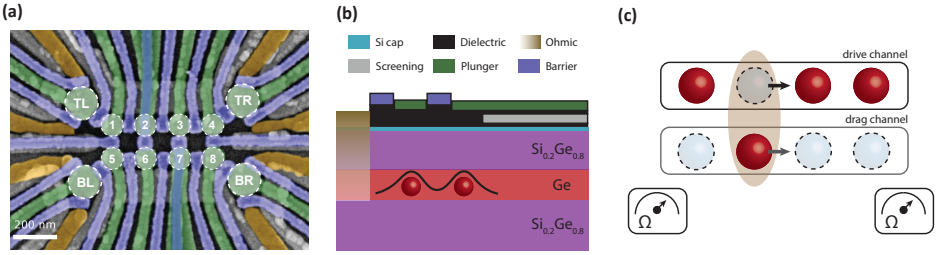

Figure 4.1: (a) A false-color scanning electron microscope image of a device nominally identical to the one used in this work. The dashed white circles indicate the intended positions of the 4×2 dot array and sensing dots. (b) Schematic cross-section of the gate stack and a germanium quantum well heterostructure. Holes are confined in the 55 nm-deep quantum well. Gate layers with different functions are drawn in colors shown in the legend. (c) Schematics illustrating the Coulomb drag of a hole in the bottom channel by the (imposed) motion of an electron (missing hole) in the top channel of a 4×2 quantum dot array. The bound state of an electron and hole (an exciton) arises from the inter-channel Coulomb interaction. Two charge sensors, located at the bottom-left and bottom-right corners, are used to probe the charge configuration in the two array.

Coulomb drag can arise from interactions between classical charges, in the quantum dot platform, the motion of charges and excitons occurs by tunneling and co-tunneling respectively, which are intrinsically quantum mechanical processes. Coulomb drag then serves as a precursor for exciton condensation and excitonic insulator phases.

Excitonic states can be described theoretically using a two-channel Hubbard model with $N \times 2$ sites [43–45],

$$\begin{aligned} H = &- t \sum_{\langle i,j\rangle,\sigma} c^{\dagger}_{i\sigma} c_{j\sigma} + U \sum_{i} \frac{n_i(n_i-1)}{2} \\ &+ U' \sum_{\langle i,j\rangle} n_i n_j + V \sum_{i\in\alpha, j\in\beta} n_i n_j \\ &+ V' \sum_{i\in\alpha, j\in\beta} n_i n_j, \end{aligned} \tag{4.1}$$

where $c_{i\sigma}$ denotes the annihilation operator of a spin-1/2 fermion with spin $\sigma \in \{\uparrow, \downarrow\}$ at site i of a two-channel system where site 1 to N are located in channel α and site $(N+1)$ to $2N$ are part of channel β, and $\langle i, j\rangle$ sums over neighboring sites in the same channel. The number operator is given by $n_i = c^{\dagger}_{i\uparrow} c_{i\uparrow} + c^{\dagger}_{i\downarrow} c_{i\downarrow}$, t is the tunnel coupling within the same channel, U the on-site Coulomb interaction, U' is the nearest-neighbor Coulomb interaction within the same channel, V is the nearest-neighbor inter-channel Coulomb interaction, and V' is the diagonal inter-channel Coulomb interaction. When the two channels are occupied by charge carriers of opposite sign, the inter-channel interactions are attractive. Note that we consider systems without hopping between the two channels and interaction terms beyond nearest-neighbor or diagonal sites are neglected. Furthermore, in Eq. 4.1 we assume homogeneous tunnel couplings and Coulomb interactions. To describe systems with inhomogeneous couplings, we will use t_{ij} and V_{ij} to denote the tunnel coupling and inter-channel Coulomb interaction between site i and j.

This model can describe the conduction band and valence band in a material, and

also two capacitively-coupled channels. Earlier works have reported on arrays of metallic or superconducting tunnel junctions [46–48], and small quantum-dot arrays [49]. However, these systems lack the control knobs for individual interaction parameters and the probes for the quantum state at each site. In comparison, when a N×2 quantum dot ladder is tuned to host electrons in one channel and holes in the other channel, thanks to the advanced control and probing capabilities, it can be used as a versatile platform for studying excitonic physics.

Many years of work on quantum dot systems have led to steady scaling of linear arrays [50–52]. Furthermore, several reports on two-dimensional quantum dot arrays have appeared using GaAs [10, 53], silicon [54, 55] and germanium [56] as the host material. Among the various host materials, germanium is particularly promising to scale to large arrays thanks to the low disorder and light effective mass [57, 58]. Even a 4×4 Ge quantum dot array has been realized [59], albeit with shared-controlled electrochemical potentials and tunnel couplings.

In this work we use a 4×2 Ge quantum dot ladder as an excitonic system, doubling the size of fully controlled Ge quantum dot arrays [56]. We activate hopping along the legs of the ladder but suppress hopping between the legs. In this way, two capacitively-coupled channels of quantum dots are formed. The charge carriers in this platform are holes arising from the valence band. A missing hole on top of a singly-occupied background of holes effectively defines an electron. We control the electrochemical potentials of the array such that the top channel hosts an electron and the bottom channel can host a hole. To explore the formation of excitons, we use real-time charge sensing to study under what conditions the imposed motion of an electron through the top channel drags along a hole in the bottom channel through the long-range Coulomb-interaction.

4.2. DEVICE AND EXPERIMENTAL APPROACH

The experiment is carried out in an electrostatically-defined 4×2 hole quantum dot array, which is fabricated in a Ge/SiGe quantum well heterostructure [60]. Fig. 4.1(a) shows a device image, with the positions of the dots and charge sensors as indicated by the labeled circles. Fig. 4.1(b) shows a schematic gate stack of the device. Screening gates, plunger gates and barrier gates were fabricated in successive lithography steps (see the Appendix for details), using a device design that can be easily extended to longer bilinear quantum dot ladders. We refer to the path from dot 1 to dot 4 as the top channel (drive channel) and to the path from dot 5 to dot 8 as the bottom channel (drag channel). Quantum dots are formed by applying negative DC voltages on a set of plunger gates, P, and barrier gates, B, to accumulate and confine holes in the quantum well in the area between the screening gates. The charge occupation of the 4×2 array is denoted $\begin{pmatrix} O_1 & O_2 & O_3 & O_4 \\ O_5 & O_6 & O_7 & O_8 \end{pmatrix}$, where O_i represents the number of holes in dot i. The structure allows for individual control of all ten nearest-neighbor tunnel couplings. Plunger gates and barrier gates are additionally connected to high-frequency lines via bias tees to allow fast control of electrochemical potentials and tunnel couplings.

In this experiment the plunger and barrier gates are virtualized such that changing a virtual plunger P'_i independently controls the electrochemical potential, μ_i, of dot i and changing a virtual barrier B'_{ij} mainly modulates the tunnel coupling, t_{ij}, between neigh-

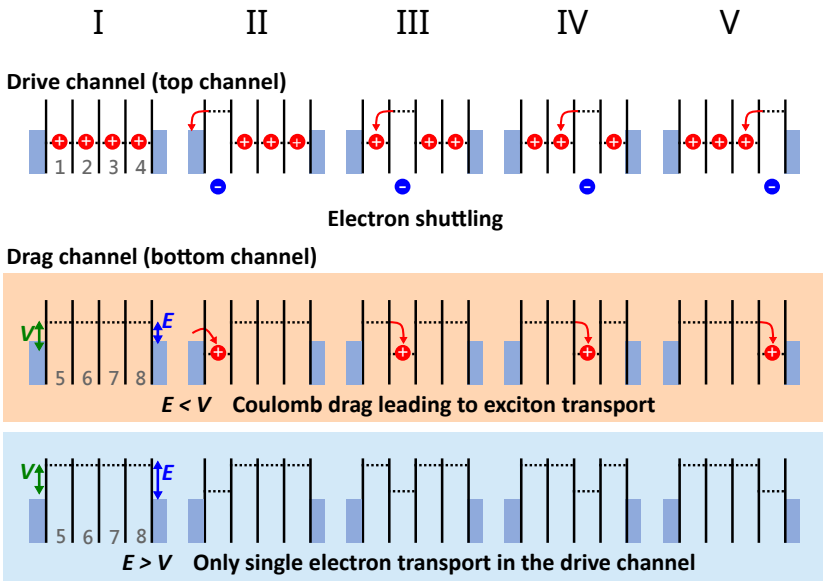

Figure 4.2: Schematics illustrating the experimental scheme for probing exciton formation through Coulomb drag. The first row shows the ladder diagrams of the drive channel. The vertical axis is an energy axis, the horizontal axis is space. Vertical black lines indicate tunnel barriers, the blue shaded region represents the reservoir, which is filled up to the Fermi level. Phase I: Each dot is filled with one hole and the dot potentials are aligned. Phase II: The leftmost hole is pushed out by raising μ_1, which can be viewed as loading an electron in dot 1. Phase III: μ_1 is lowered and μ_2 is raised. The electron moves to dot 2. Phase IV: μ_2 is lowered and μ_3 is raised. The electron moves to dot 3. Phase V: μ_3 is lowered and μ_4 is raised. The electron moves to dot 4. The second and the third rows compare the ladder diagrams of the drag channel with and without Coulomb drag effect, respectively. The second row is the exciton transport regime ($E < V_{ij}$), in which the presence of a drive-channel electron lowers the dot potentials in the drag channel sufficiently for a hole to be loaded in the bottom channel. The hole will then be bound to the electron and travel along with the electron, i.e. an exciton is formed. The third row is the single-electron transport regime ($E > V_{ij}$), in which the charge state in the drag channel is not affected by the drive-channel electron. Note that for simplicity we assume homogeneous $V_{ij} = V$, and the intra-channel and diagonal Coulomb interactions are ignored in the schematics. Also note that while electrons have been added to the first row to make the underlying particle-hole transformation clear, our device can only host holes.

boring dots i and j without influencing the dot potentials. In this device four charge sensors (BL, BR, TL and TR) can be formed at the four corners of the array. They serve both as detectors for the charge occupation and as reservoirs. In this experiment we use only the BL and BR sensors for charge sensing, with multiplexed RF reflectometry (TL and TR are used as reservoirs.). The plunger gates for the BL and BR sensors are also included in the gate virtualization, such that sweeping a plunger gate in the array does not shift the sensor peak position. Therefore, the sensors are mostly sensitive to changes of the charge occupation in the array. While jumps in the charge sensor peak position could in principle affect the loading fidelity, the Coulomb peaks are broad enough such that this effect is negligible for the experiments described below. Thus, we can simultaneously use them as charge sensors and reservoirs without a measurable impact in loading fidelity.

To study exciton formation via the Coulomb drag effect, we will aim to initialize the device in the $\left(\begin{smallmatrix}1&1&1&1\\0&0&0&0\end{smallmatrix}\right)$ charge state, where each top-channel dot is occupied by one hole and the bottom channel is empty. Because the charge carriers in the array are holes originating from the valence band, removing a hole in the top channel amounts to adding an electron relative to the singly-filled background of holes (see Fig. 4.2). We can thus load an electron to the top channel by emptying a dot (e.g. pulsing to the (0111) charge state in the top channel). The electrochemical potentials of the bottom dots in the $\left(\begin{smallmatrix}1&1&1&1\\0&0&0&0\end{smallmatrix}\right)$ configuration are aligned with each other, such that loading a hole from the reservoir to the bottom channel costs the same energy regardless of its position. We label this energy cost E (Fig. 4.2). When E is lower than the nearest-neighbor inter-channel Coulomb interaction V_{ij}, a hole will be attracted in the bottom channel by the top-channel electron, reaching e.g. the charge state $\left(\begin{smallmatrix}0&1&1&1\\1&0&0&0\end{smallmatrix}\right)$. An electron-hole pair is thus formed bound by V_{ij}, which constitutes an inter-channel exciton (strictly speaking, V_{ij} must here be corrected by intra-channel and diagonal Coulomb interactions; we will neglect these corrections to simplify the discussion but they are included when aligning the bottom dot potentials). Furthermore, if the system Hamiltonian favors an exciton ground state, pushing the electron (the missing hole) through the top channel will cause the hole in the bottom to move together with the electron (Fig. 4.1(c) and Fig. 4.2).

4.3. QUANTUM DOT LADDER FORMATION AND TUNE-UP

Figure 4.3(a) shows charge stability diagrams for the inter-channel dot pair 1-5 near the $\left(\begin{smallmatrix}1&1&1&1\\0&0&0&0\end{smallmatrix}\right)$ charge configuration (see the Appendix for the other inter-channel pairs). The virtualized sensors result in a gradient-free signal within each charge state region. The inter-channel Coulomb interactions V_{ij} between dot i and j are extracted from the size of the anti-crossing for an inter-dot transition. The obtained inter-channel Coulomb interaction strengths are $V_{15} = 220\,\mu\text{eV}$, $V_{26} = 260\,\mu\text{eV}$, $V_{37} = 315\,\mu\text{eV}$, and $V_{48} = 213\,\mu\text{eV}$. The diagonal Coulomb interactions V' are smaller than $100\,\mu\text{eV}$.

Figure 4.3(b) shows the sensor signal as a function of the detuning of dots 1 and 2, $\delta(P'_1 - P'_2)$, and the detuning of dots 5 and 6, $\delta(P'_5 - P'_6)$, near their respective inter-dot transitions. If we sweep $\delta(P'_1 - P'_2)$ and keep $\delta(P'_5 - P'_6)$ fixed near the 5-6 transition, as indicated by the black arrow in Fig. 4.3(b), a transition is made from $\left(\begin{smallmatrix}0&1&1&1\\1&0&0&0\end{smallmatrix}\right)$ to $\left(\begin{smallmatrix}1&0&1&1\\0&1&0&0\end{smallmatrix}\right)$ whereby a charge tunnels from dot 2 to dot 1 and simultaneously a charge moves from dot 5 to dot 6, thanks to the inter-channel Coulomb interactions V_{15} and V_{26}. This co-

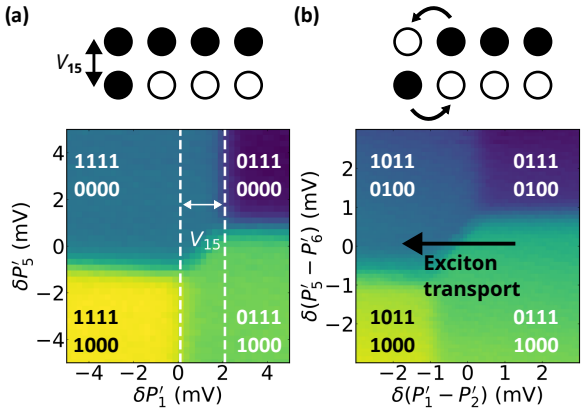

Figure 4.3: Charge occupation control of the 4×2 dot array in the single-hole regime. (a) Charge stability diagram of an inter-channel dot pair 1-5. $\delta P_i'$ refers to the change in P_i' relative to a baseline DC voltage. The inter-channel Coulomb interaction V_{15}, as illustrated in the schematic above, can be determined by measuring the size of the anti-crossing (the distance between the white dashed lines) in the charge stability diagrams. The Coulomb interaction strengths are converted from voltage to energy using lever arms. See appendix for the charge-stability diagrams of all nearest-neighbor dot pairs, for all inter-channel Coulomb interaction measurements and for the extraction of lever arms. (b) Charge stability diagram as a function of 1-2 detuning $\delta(P_1' - P_2')$ and 5-6 detuning $\delta(P_5' - P_6')$. Along the black arrow an exciton moves in the dot array due a co-tunneling process depicted in the schematic.

tunneling process [49] results in an exciton moving in the ladder array, and is the dominant exciton transport process since it happens before sequential tunneling is energetically allowed (see the path along the black line in Fig. 4.3.

Efficient exciton transport requires strong intra-channel tunnel couplings in order to obtain large intra-channel co-tunneling couplings, and weak inter-channel tunnel couplings. Strong inter-channel tunneling exceeding the channel detuning would allow the charge carriers to hybridize between the two channels, in which case we can no longer speak of a distinct electron and hole which are bound by long-range Coulomb interaction.

Using the gate voltages, we can control both the inter-channel and intra-channel tunnel couplings. The tunnel couplings are characterized by fitting inter-dot transition sensor signals to a model described in [61]. Figures 4.4(a-b) show the control of t_{12} and t_{15}. Due to fabrication procedure, some barrier gates exhibit a weaker response than others, meaning that larger voltage swings are required for modulating the corresponding tunnel couplings (see appendix for details). Note that in the virtualized B' we do not compensate for tunnel coupling crosstalk [62, 63] since the present experiment only requires setting the tunnel couplings once and furthermore is robust to small variations in tunnel couplings.

We here set all intra-channel tunnel couplings to 30–40 μeV. For the inter-channel tunnel couplings we target values ideally below 1 μeV. However, it is challenging to quantify such small tunnel couplings by fitting the inter-dot sensor signal, given that the thermal energy based on the effective electron temperature is about 20 μeV in this experiment. Instead of the tunnel couplings, we measure the inter-dot tunnel rates by

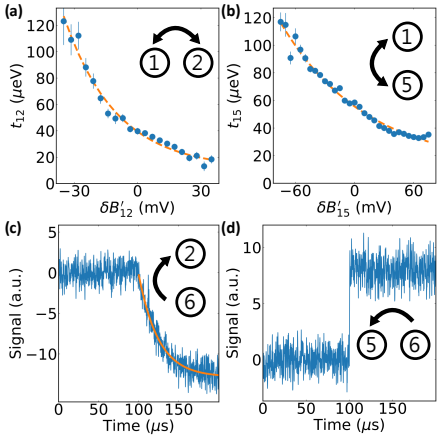

Figure 4.4: Tunnel coupling control of the 4×2 dot array in the single-hole regime. (a-b) Measurements of (a) intra-channel tunnel coupling t_{12} and (b) inter-channel tunnel coupling t_{15} as a function of B'_{12} and B'_{15}, respectively. The orange dashed lines show exponential fits to the data. (c) Measurement of tunneling rate Γ_{26} between dot 2 and dot 6 when t_{26} is suppressed. A hole is initialized in dot 6 ($\mu_6 < \mu_2$) and at 100μs we abruptly align the electrochemical potentials ($\mu_6 = \mu_2$) using a gate voltage pulse. From this moment, the hole can tunnel from dot 6 to dot 2. The plot shows the time averaged charge sensor response. As expected, we see an exponential trend in the sensor response, since the tunnel time should obey Poisson statistics. The exponential fit yields $\Gamma_{26} = 40$ kHz, which gives a rough estimate of $t_{26} = 0.03$ μeV. (d) same as (c) but for Γ_{56} when $t_{56} = 46$ μeV. Γ_{56} is higher than the measurement bandwidth of 1 MHz.

abruptly aligning the dot potentials using a gate voltage pulse. The relation between tunnel coupling and tunnel rate can be expressed as [64]

$$\Gamma_{ij} = 2T_2 t_{ij}^2 \tag{4.2}$$

where Γ_{ij} and t_{ij} are the tunnel rate and tunnel couplings between dot i and j, and T_2 is the charge dephasing time ($T_2 \geq 0.3$ ns extracted from photon-assisted-tunneling measurement [65], see appendix for details). Figure 4.4(c) shows the tunnel rate measurement between dot 2 and dot 6. The fit yields $\Gamma_{26} = 40$ kHz. Using Eq. (4.2) we obtain $t_{26} \leq 0.03$ μeV. For comparison, Fig. 4.4(d) shows the measurement of Γ_{56} when $t_{56} = 46$ μeV. In this case the decay appears instantaneous owing to the fast tunneling between the dots. Using the inter-channel barrier voltages, all inter-channel tunnel couplings can be suppressed below 0.1 μeV (see appendix), with all inter-channel Coulomb interactions > 150 μeV. However, we ideally want homogeneous inter-channel Coulomb interactions of about 200-300 μeV, in order to have a large window for Coulomb drag. Since V_{15} is only 166 μeV when $t_{15} = 0.07$ μeV, we bring dot 1 and dot 5 closer together to increase V_{15} to 220 μeV, at the expense of a higher $t_{15} \sim 25$ μeV [1].

[1] We note that although t_{15} is higher than other inter-channel tunnel couplings, since electron-hole pair transport is a co-tunneling process and since t_{26} remains below 1μeV, the correlated hopping of an electron-hole pair across the channels is still three orders of magnitude smaller than the hopping along the channel direction.

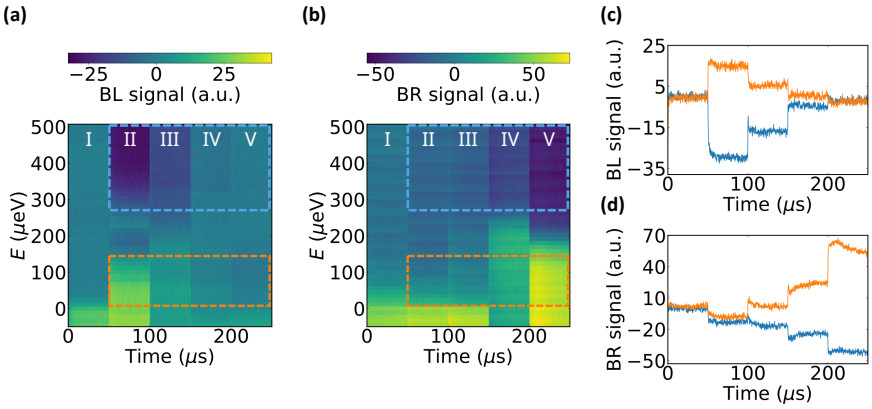

Figure 4.5: Coulomb drag and exciton transport measurements. (a) BL and (b) BR processed (see appendix) sensor signals as a function of time and E. In the time domain the dot potentials in the top channel are pulsed from phase I to V as described in Fig. 4.2. A positive (negative) charge causes a positive (negative) sensor signal. The regions enclosed by a blue dashed rectangle correspond to the single-electron transport regime, in which only a negative charge moves from the left to the right in the top channel. The regions enclosed by a orange dashed rectangle indicate the exciton transport regime, in which an additional positive charge is loaded and travels with the top-channel electron. Since the BL and BR sensors are more sensitive to charges in the bottom channel than in the top channel, the sensor signals change sign in the exciton transport regime compared to those in the single-electron transport regime. (c) 1D line cuts of the BL sensor signal in the single-electron transport regime ($E \simeq 500\,\mu$eV, blue trace) and in the exciton transport regime ($E \simeq 100\,\mu$eV, orange trace). (d) Same as (c) but for the BR sensor signal. The small drop in the BR signal between 50 μs and 100 μs is caused by imperfect virtualization of the BR sensor with respect to P_1'. The slight bending of the BR signal is possibly caused by charging/discharging of the 2DHG near the BR sensor. Additionally, we understand the broadening of the transition line in phase II as a result of strong dot-reservoir coupling.

4.4. COULOMB DRAG AND EXCITON FORMATION

The experiment scheme for measuring exciton formation and transport is illustrated in Fig. 4.2. In phase I, the 4×2 dot array is set to the $\left(\begin{smallmatrix}1&1&1&1\\0&0&0&0\end{smallmatrix}\right)$ charge occupation in which the dot potentials in the top channel (drive channel) are aligned and are placed ~ 200 μeV below the Fermi level. The potentials in the bottom channel (drag channel) are aligned as well, and positioned above the Fermi level by an energy offset, E. From phase II to V, the respective top-channel dot potentials are consecutively raised and then lowered by 6 mV (~ 670 μeV) to load and shuttle an electron from left to right. If $E < V_{ij}$, the top-channel electron capacitively lowers the bottom-channel potential on the opposite site below the Fermi level. As a consequence a hole is loaded in the bottom channel. Due to the inter-channel Coulomb interaction, the hole is dragged along with the electron, i.e. the electron and hole move together as an exciton along the channel throughout the pulse sequence. In contrast, if $E > V_{ij}$, the top-channel electron moves alone without dragging along a hole. Therefore, a transition between exciton transport and single electron transport is expected to occur at $E \sim V_{avg} = \langle V_{ij} \rangle$. In this work, the average inter-channel Coulomb interaction V_{avg} is 252 μeV. We note that for a system with inhomogeneous V_{ij}, the range of E where Coulomb drag can occur is limited by the smallest V_{ij}.

In the measurements shown in Fig. 4.5, the top-channel dot potentials are pulsed from phase I to V in the time domain while the bottom-channel potentials are fixed at E [2]. Figs. 4.5(a) and (b) show the BL and BR sensor signals as a function of time and E. The sensor signals corresponding to the $\left(\begin{smallmatrix}1&1&1&1\\0&0&0&0\end{smallmatrix}\right)$ charge state (phase I when $E > 0$) are assigned a reference value of 0. An increasing (decreasing) signal indicates a positive (negative) charge moves closer to the corresponding sensor. In the region enclosed by the blue dashed rectangle, from phase II to V, the BL (BR) sensor signal is increasingly (less and less) negative. As E is reduced, the sensor signals first pass through a transition region around $E \sim 200$ μeV and then reach a region enclosed by the orange rectangle, where the BL (BR) sensor signal is less and less (increasingly) positive from phase II to V.

The data in Fig. 4.5(a) and (b) can be understood as follows. In the blue-dashed region, the system is in the single-electron regime in which a top-channel electron is moving away from BL and towards BR. Hence, the magnitude of the negative signal decreases (increases) over time for BL (BR). In contrast, in the orange-dashed region, the system enters the exciton transport regime in which an inter-channel exciton moves to the right. Because the BL and BR sensors are more sensitive to the bottom-channel hole than to the top-channel electron, the net signal induced by the exciton is positive and the magnitude of this positive signal decreases (increases) over time for BL (BR). See Fig. 4.5(c) and (d) for a further comparison between the signals in the single-electron-transport regime and the exciton transport regime. In Fig. 4.5(a) and (b) the transition between the single-electron regime and the exciton transport regime occurs around $E \sim 200$ μeV, which is consistent with the predicted transition point $E \sim V_{avg} = 252$ μeV. The width of the transition regime depends on the level of disorder in the dot potentials ($\delta\mu \leq 50$ μeV, which is the accuracy of the automated calibration) and variations in inter-channel V_{ij} (standard deviation in V_{ij} of ~ 40 μeV). Note that when $E < 0$ μeV, the signals in phase I

[2] In the experiment we apply a global virtual gate voltage on the bottom channel and convert the global voltage to a global energy offset using an averaged bottom-channel lever arm 112 μeV/mV

increase because the bottom channel starts loading holes from the reservoirs, even if no electron is loaded in the top channel.

Finally, since the transport of an inter-channel exciton involves a co-tunneling process, it is possible in principle that either the electron or the hole or the entire exciton are not successfully transferred from one site to another. In the data of Fig. 4.5, no such failed charge transfers are observed. This is expected since the 50 µs duration of the pulse segments by far exceeds both the single-particle tunneling rates and the co-tunneling rates (in the Appendix, we estimate the probability of successful adiabatic charge transfer to be about 99.2%).

4.5. CONCLUSION AND OUTLOOK

In summary, we have fabricated a germanium 4×2 quantum dot ladder and use it to study exciton formation and transport. To engineer the system Hamiltonian, we tune the full array into the single-hole regime and independently control all the on-site potentials and interdot tunnel couplings. We find strong inter-channel Coulomb interaction while the tunneling between channels is suppressed, which is essential for realizing excitonic physics. To probe exciton formation by means of Coulomb drag, we drive an electron through the top channel and measure the charge sensor signals as a function of the bottom channel potential. The measured signals are in good agreement with the picture of a transition from single-electron transport to exciton transport resulting from the inter-channel Coulomb interaction. An interesting next step possible with the present sample is to create and study an engineered excitonic insulator [20].

Whereas tunneling and Coulomb-mediated co-tunneling of charges between the dots along each leg of the ladder are quantum mechanical effects, the present experiments on exciton formation and transport can be understood in terms of classical long-range Coulomb interactions without invoking quantum effects (see Section 11 of the appendix). In the future, we envision that with sufficiently homogeneous interaction energies and co-tunnel couplings in longer ladders, excitons can delocalize over the array, show coherent dynamics in the time domain, and exciton quasi-condensation [3]. Already, coherent delocalization of individual charges as well as coherent oscillations of charges in the time domain have been observed previously in quantum dot arrays [10, 64, 67–71]. Also spin coherence was shown to extend over quantum dot arrays [11, 12, 63], including across a 4x2 quantum ladder using a nominally identical device to the one used here [72].

It is useful to point out an enhanced symmetry in bilinear quantum dot arrays as described by Eq. 4.1, which should play an important role in the nature of the ground state in the thermodynamic limit. As there is no tunnelling between the channels, one can define separate SU(2) symmetries for each channel [4]. The full Hamiltonian is symmetric with respect to both of them, and the full symmetry of the system is SO(4) ≃ SU(2) ⊗ SU(2)[73]. Excitonic condensation in this system would require spontaneous symmetry breaking of the SO(4) symmetry. For non-Abelian symmetries such as SO(4), the Hohenberg-Mermin-Wagner theorem shows that only exponentially decaying correla-

[3] Strictly speaking, exciton condensation does not occur in 1D or 2D at finite temperature. However, for real experimental systems we can have quasi-condensation when the correlation length exceeds the system size [66]

[4] Holes in strained germanium have spin-3/2, but the large heavy-hole light-hole splitting leads to an effective two-level system.

tions are allowed even at zero temperature, due to the abundance of possible fluctuations of the order parameter. This should be contrasted to the excitonic states of spinless fermions, for which condensation corresponds to the Abelian U(1) symmetry and thus the system can exhibit quasi-long range at zero temperature in one dimensional systems.

Interestingly, two excitons can together form a SO(4) singlet. Such singlets can exhibit quasi-long range order at zero temperature in one dimensional systems, analogously to spinless bosons. This suggests our system can exhibit unusual types of ground states in the thermodynamic limit, such as quasi-condensates of composite particles or states with broken translational symmetry. Analogous phenomena have been discussed in the context of spinor condensates of cold atoms in one-dimensional systems[74, 75].

One can also break the SO(4) symmetry by introducing extra terms to the Hamiltonian. When breaking SO(4) symmetry with a magnetic field, $S_z = 1$ excitons are favored and can form a (quasi-)condensate, which is not usually seen in optical spectroscopy since these excitons are dark. In addition, the spin-orbit coupling present in germanium quantum wells, while not breaking time reversal symmetry [76], can also hybridize singlet and triplet states, lifting their degeneracy [77, 78], which may lead to condensation at zero magnetic field.

Owing to the in-situ tunability of device parameters, the quantum dot platform offers access to a wide variety of regimes. For instance, a transition from semiconductor to excitonic insulator can be observed by changing the detuning between two channels. The BCS-BEC crossover might be realized by increasing the exciton density while fixing the Coulomb interaction strength [79]. Moreover, one may create and manipulate charged excitons (trions) by introducing imbalanced electron and hole numbers in the channels. Another important regime for the SO(4) physics in 1D systems is the so-called “incoherent Luttinger liquid" regime [80], where the temperature is below the charge (exciton in our case) binding energy but above the spin interaction energy. In this case, we expect Luttinger liquid power-law correlations in the “exciton number" but short range correlations in the spin sector.

4.6. SUPPLEMENTARY MATERIAL

4.6.1. DEVICE FABRICATION AND EXPERIMENT SETUP

The device was fabricated on a Ge/SiGe heterostructure featuring a strained Ge quantum well positioned 55 nm below the semiconductor-dielectric interface, as described in [60]. The fabrication started by defining ohmic contacts, which were made by electron beam lithography, etching of the native oxide with buffered HF, and electron beam deposition of 30 nm of Al. An insulating layer of 7 nm Al_2O_3 was grown with atomic layer deposition, also annealing the device and diffusing the aluminum into the heterostructure during the process. Subsequently, the screening gates (3/17 nm Ti/Pd), plunger gates (3/27 nm Ti/Pd), and barrier gates (3/37 nm Ti/Pd) were made in three metalization layers, which are all separated by 5 nm thick layers of Al_2O_3. Note that for easing the lift-off of the compact barrier gates, we made the barrier gates in two steps, in which the barrier gates were distributed in two lithography/evaporation/lift-off processes without a Al_2O_3 layer in between. The fabrication procedure is summarized in Fig. 4.6. The chosen device design provides a scalable path to longer bilinear quantum dot arrays with full control over

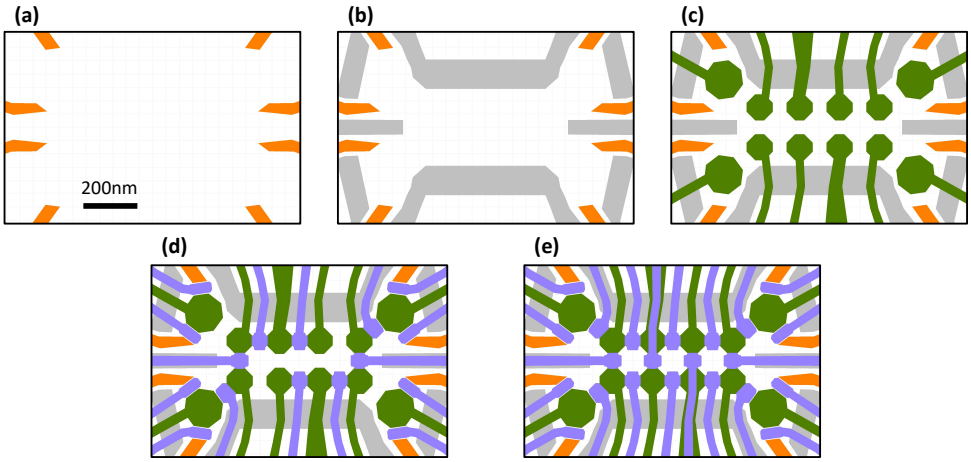

Figure 4.6: Fabrication steps for the 4×2 Ge quantum dot ladder, showing the design of each patterned layer. (a) Ohmic contact layer for contacting the Ge quantum well. (b) Screening gate layer for defining the active region in which holes are confined. (c) Plunger gate layer for charge accumulation and electrochemical potential control. (d) and (e) are the first and second barrier layer used for shaping the quantum dot potentials and for tunnel coupling control. The layers in (a)-(d) are separated by Al_2O_3 insulating layers. The barrier gates in (d) and (e) are realized in two separate metalization steps (with no insulating layer in between) to ease the lift-off process.

all dot potentials and interdot tunnel couplings. Charge sensing can be accomplished dispersively or with sensors integrated alongside the ladder instead of at the extremities only.

The measurement was performed in a Oxford Instruments Triton dilution refrigerator with a nominal base temperature of 6 mK. The device was mounted on a custom-made sample PCB. DC voltages from homebuilt SPI DAC modules and pulses from a Keysight M3202A AWG are combined using on-PCB bias-tees. RF reflectometry for charge sensing was done using SPI IQ-demodulation modules and on-PCB LC tank circuits. The demodulated signals were recorded by a Keysight M3102A digitizer.

4.6.2. SINGLE-HOLE REGIME OF THE 4×2 ARRAY

The charge state tunability of the 4×2 ladder is displayed in Fig. 4.7, where we show charge stability diagrams for all dot pairs down to the single-hole regime. The area on the top right corner of the plots corresponds to the zero-charge state. The effect of gate voltage crosstalk is compensated using virtual gates P'. All ten plots are obtained using charge sensing using the bottom right and bottom left sensors.

Additionally, in Fig. 4.8, we show global charge state control of full the 4×2 array by sweeping two virtual gates, corresponding to the top and bottom channel energies (P_T and P_B, respectively). Every vertical or horizontal addition line reflects a single charge being added to either the top or the bottom channel. Lines are spaced apart by the long-range Coulomb interaction. The starting charge occupation for the Coulomb drag experiment corresponds to the top left of this plot, with 4 charges in the top channel and none in the bottom.

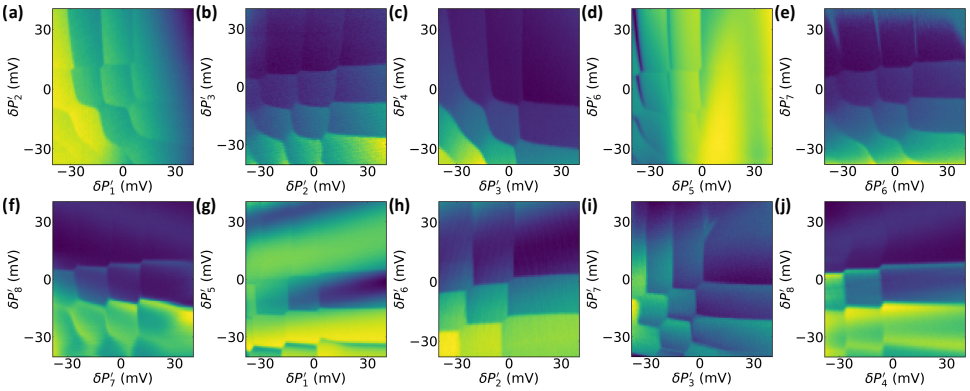

Figure 4.7: Charge stability diagrams of all neighbouring dot pairs, showing the left or right bottom sensor signal as a function of two virtual plunger gate voltages. (a)-(f) Dot pairs along the top or bottom channel. (g)-(j) Dot pairs across the channel. The top right corner of each figure corresponds to the zero-charge state. Note that at this tuning stage, there existed a strong coupling between dot 5 and BL sensor, which resulted in an improper virtualization and reduced sensitivity when dot 5 was empty. However, this problem was solved with further tuning. See Fig. 4.3, where all relevant addition and interdot lines as well as the proper sensor virtualization are clearly visible for dots 1 and 5.

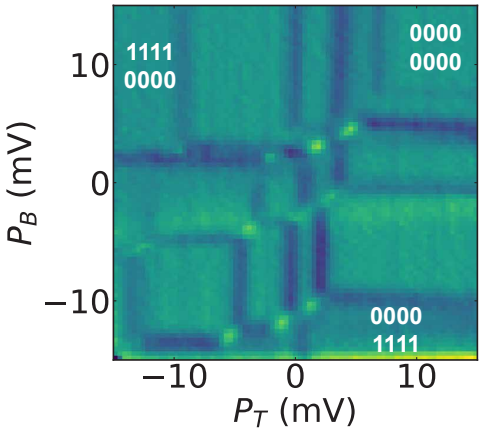

Figure 4.8: Charge stability diagram depicting the global charge state tunability of the 4x2 array. The scanned gates are the top and bottom channel virtual voltage $P_T = P'_1 + P'_2 + P'_3 + P'_4$ and $P_B = P'_5 + P'_6 + P'_7 + P'_8$. Every vertical (horizontal) charge transition corresponds to adding a single charge to the top (bottom) channel. We plot the gradient of the sensor signal for better resolution of the transition lines. The top left region of this plot corresponds to a filled top channel and an empty bottom channel, which is the starting charge configuration for the Coulomb drag experiment.

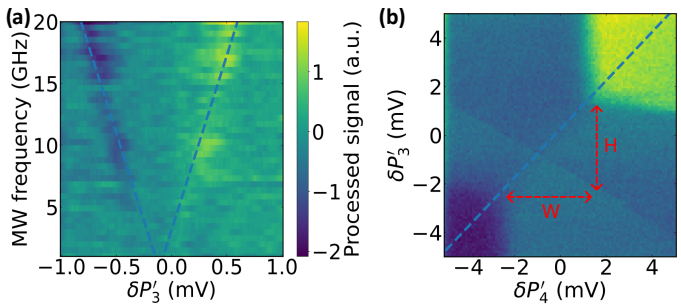

Figure 4.9: Example of lever arm measurements. (a) PAT measurement showing the processed sensor signal as a function of frequency and detuning at the inter-dot transition between dot 3 and dot 7. The blue dashed line is a fit of the form $hf = \sqrt{\delta\mu_3^2 + 4t_{37}^2}$, where $\delta\mu_3 = L_3\delta P_3'$. The linewidth is about 0.1 mV (11.7 µeV), from which we estimate a charge coherence time $T_2 \geq 0.3$ ns. (b) The charge stability diagram at the inter-dot transition between dot 3 and dot 4. The blue dashed line shows the inter-dot transition line with a slope $S = H/W = L_4/L_3$ where H is the height and W is the width of the transition line.

L_i	Value (µeV/mV)	Method
L_1	111	Inter-dot slope
L_2	104	PAT
L_3	117	PAT
L_4	117	Inter-dot slope
L_5	115	Inter-dot slope
L_6	113	PAT
L_7	112	PAT
L_8	111	Inter-dot slope

Table 4.1: The values and measurement methods for each lever arm L_i.

4.6.3. LEVER ARM MEASUREMENT

The conversion between a virtual gate voltage P_i' and electrochemical potential μ_i is described by $\delta\mu_i = L_i\delta P_i'$, where L_i is the lever arm for dot i. The lever arms can be characterized using photon-assisted tunneling (PAT) [65]. In Fig. 4.9(a), the signal is fitted to $hf = \sqrt{\delta\mu_3^2 + 4t_{37}^2}$. From the fit a lever arm $L_3 = 117$ µeV/mV is extracted. In addition, the ratio between two lever arms can be determined from the slope, S, of an inter-dot charge transition line based on the fact that $V_{ij} = V_{ji}$. For instance, in Fig. 4.9(b), $V_{34} = L_3H = V_{43} = L_4W$. Therefore, $S = H/W = L_4/L_3$. So, L_4 can be estimated from L_3 and S. We obtain $L_4 = 117$ µeV/mV with $L_3 = 117$ µeV/mV and S =1.0. Similarly, based on PAT measurements and inter-dot slopes, all lever arms are estimated. The results are summarized in table 4.1. All lever arms have similar value ~ 110 µeV/mV with a standard deviation of 4 µeV/mV.

4.6.4. INTER-CHANNEL COULOMB INTERACTION MEASUREMENT

Figure 4.10(a)-(d) shows the measurements of inter-channel Coulomb interactions, which are responsible for the excitonic Coulomb drag effect. As in Figure 4.3(a), the Coulomb

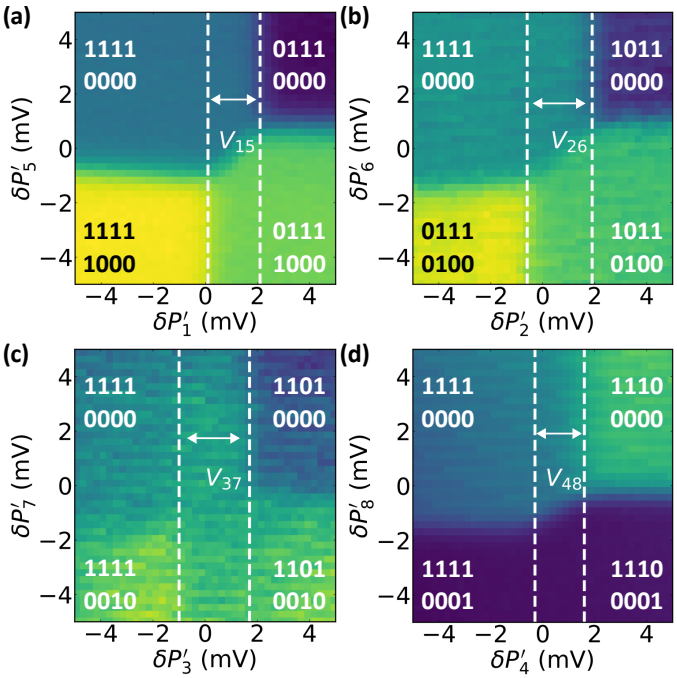

Figure 4.10: Measurements of inter-channel Coulomb interactions (a) V_{15} (replotted from Fig. 4.3a), (b) V_{26}, (c) V_{37} and (d) V_{48}.

interactions are characterized by finding the sizes of the anti-crossings and converting them into energies through lever arms. From Fig. 4.10(a)-(d) we obtain $V_{15} = 220\,\mu\text{eV}$, $V_{26} = 260\,\mu\text{eV}$, $V_{37} = 315\,\mu\text{eV}$, and $V_{48} = 213\,\mu\text{eV}$.

4.6.5. TUNNEL COUPLING CONTROL

Figure 4.11 shows control of all nearest-neighbour tunnel couplings t_{ij} using the corresponding virtual barrier gates B'_{ij}. The tunnel coupling dependency is fitted by an exponential function $A\exp(-\gamma_{ij}B'_{ij})+C$, from which the barrier lever arm γ_{ij} is extracted. The γ_{ij} are summarized in table 4.2. Roughly, the barrier lever arms can be separated into two groups, corresponding to the two steps in which the barriers were fabricated. Notably, the barrier gates patterned in the first fabrication step display a stronger lever arm than those patterned in the second step, despite the absence of an ALD layer between the two barrier metalization layers. The reasons for this discrepancy requires further investigation, but might be caused by the device design or residual resist under the second barrier gate layer. Nonetheless, all barriers display a reasonable level of tunnel coupling control, which allows us to tune the tunnel couplings to the values required to perform the excitonic Coulomb drag experiment.

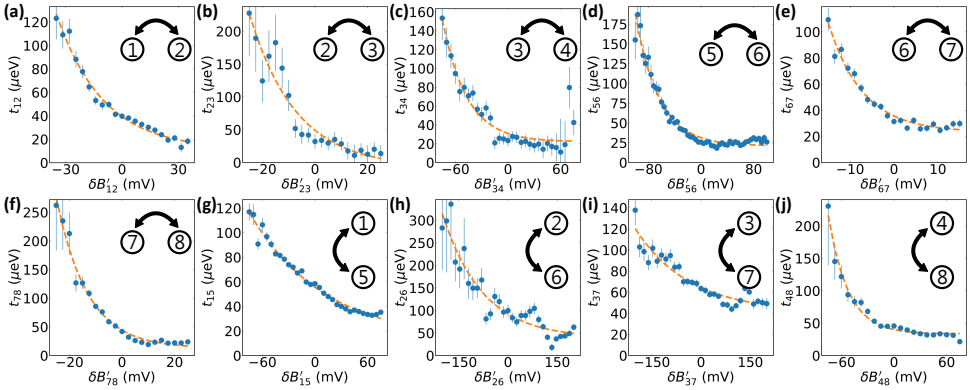

Figure 4.11: Control of all nearest-neighbour tunnel couplings. (a)-(f) Measured intra-channel tunnel coupling t_{ij} as a function of virtual barrier gates B'_{ij}. (g)-(j) Measured inter-channel tunnel coupling t_{ij} as a function of virtual barrier gates B'_{ij}. The orange dashed lines are exponential fits to the data.

γ_{ij}	Value (1/mV)	Barrier fabrication step
γ_{12}	0.040	1st
γ_{23}	0.057	1st
γ_{34}	0.036	2nd
γ_{56}	0.028	2nd
γ_{67}	0.128	1st
γ_{78}	0.085	1st
γ_{15}	0.012	1st
γ_{26}	0.008	2nd
γ_{37}	0.006	2nd
γ_{48}	0.044	1st

Table 4.2: The values and corresponding barrier fabrication steps for each tunnel barrier lever arm γ_{ij}.

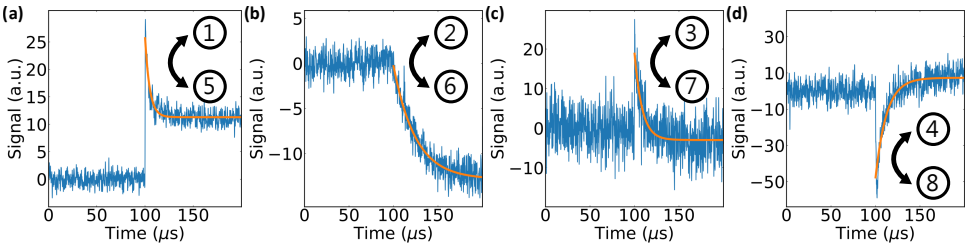

Figure 4.12: Tunnel rate measurements for (a) Γ_{15}, (b) Γ_{26}, (c) Γ_{37}, and (d) Γ_{48}. The orange curves are exponential fits to the data.

4.6.6. TUNNEL RATE MEASUREMENT

Tunnel coupling extraction via fitting of the inter-dot transition signals allows us to reliably obtain tunnel coupling values of the order of tens of μeV, larger than or comparable to the electron temperature. As t_{ij} becomes much smaller than the electron temperature, this fit becomes unreliable. When the hopping between channels is suppressed, we estimate the inter-channel t_{ij} from the inter-channel tunnel rates Γ_{ij} as described in the main text. Figure 4.12 (a)-(d) show the tunnel rate measurements, from which we obtain $\Gamma_{15} = 208\,\text{kHz}$, $\Gamma_{26} = 40\,\text{kHz}$, $\Gamma_{37} = 118\,\text{kHz}$, and $\Gamma_{48} = 81\,\text{kHz}$. Since we estimate $T_2 \geq 0.3\,\text{ns}$ (lower limit) from the linewidth of the PAT in Fig. 4.9(a), by using Eq. 4.2 we can then estimate $t_{15} \leq 0.07\,\mu\text{eV}$, $t_{26} \leq 0.03\,\mu\text{eV}$, $t_{37} \leq 0.06\,\mu\text{eV}$, and $t_{48} \leq 0.05\,\mu\text{eV}$ in the target regime where the inter-channel hopping is suppressed.

4.6.7. AUTOMATED CALIBRATION ROUTINE

Slow changes in the electrostatic environment of the device lead to inevitable drift of dot electrochemical potentials. To compensate for this low frequency drift, we implement a fast automated calibration routine to keep the electrochemical potentials fixed relative to the Fermi level. Our target is to set the level of dot i with an offset $P'_{i,target}$ from the Fermi level. In this experiment $P'_{1,target}$ to $P'_{8,target}$ are initially [2, 2, 2, 2, -4, -4, -4, -4] mV, which places the device in the $\left(\begin{smallmatrix}1&1&1&1\\0&0&0&0\end{smallmatrix}\right)$ charge state. For the first instance of the calibration, we manually tune the device to a baseline DC voltage V_{base} close to the target condition (within a tolerance of a few mV). The calibration routine starts with optimizing the sensor signals, which is done by scanning sensor plunger gates and locating the optimal sensing positions, as shown in Fig. 4.13(a) and (f). The voltage drift of dot i is measured by scanning P'_i centered at $V_{base} + P'_{i,target}$ and fitting the signal to a charge addition line to locate the Fermi level, as shown in Fig. 4.13 (b)-(e) and (g)-(j). V_{base} is subsequently shifted by the deviation of the addition lines from the centers of the scans to compensate for the voltage drift. The entire automated calibration routine takes about 10 seconds and offers a valuable tool for the efficient adjustment of dot potentials in multi-dot devices.

4.6.8. EXCITON TUNNEL COUPLING

The tunneling of excitons entails a co-tunneling process of two charges in the ladder array. Here we take the tunneling between $\left(\begin{smallmatrix}1&0&1&1\\0&1&0&0\end{smallmatrix}\right)$ and $\left(\begin{smallmatrix}1&1&0&1\\0&0&1&0\end{smallmatrix}\right)$ as an example. The relevant

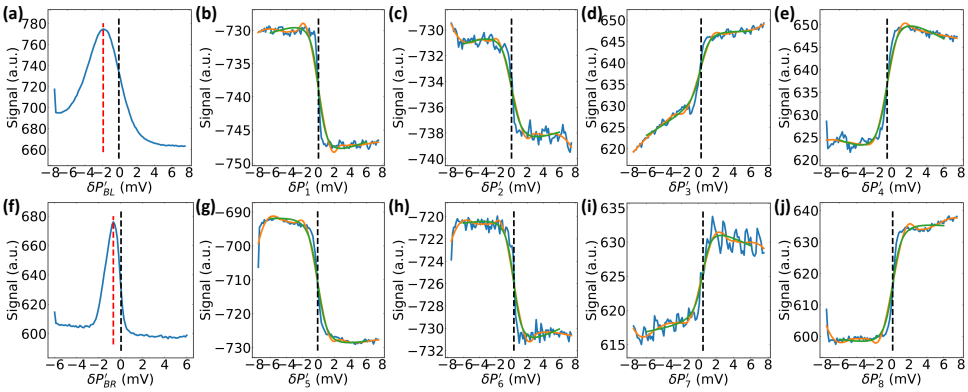

Figure 4.13: Fast automated calibration routine. (a) and (f) show the sensor signals as a function of sensor plunger gates P'_{BL} (BL sensor) and P'_{BL} (BR sensor). The red dashed lines indicate the sensor peak positions and the black dashed lines indicate the optimal sensing positions (where the slope is steepest). P'_{BL} and P'_{BL} are subsequently moved to the optimal sensing positions. (b)-(e) and (g)-(j) are the sensor signals for dot 1 to 8, near the addition lines for the first hole of each dot. The black dashed lines show the voltages at which μ_i aligns with the Fermi level. Note that (b)-(e) and (g)-(j) are not centered at the same DC voltages. Instead, each addition line is taken with an added offset $\Delta P'_{i,target}$ from the original DC voltage V_{base}. V_{base} is then adjusted according to the deviation of the black dashed lines from the centers of the scans. Each scan takes approximately 1 second and the whole calibration routine takes about 10 seconds.

charge states are $|0\rangle = \left(\begin{smallmatrix}1&0&1&1\\0&1&0&0\end{smallmatrix}\right)$, $|1\rangle = \left(\begin{smallmatrix}1&1&0&1\\0&0&1&0\end{smallmatrix}\right)$, $|2\rangle = \left(\begin{smallmatrix}1&1&0&1\\0&1&0&0\end{smallmatrix}\right)$, $|3\rangle = \left(\begin{smallmatrix}1&0&1&1\\0&0&1&0\end{smallmatrix}\right)$, $|4\rangle = \left(\begin{smallmatrix}1&1&1&1\\0&0&0&0\end{smallmatrix}\right)$, and $|5\rangle = \left(\begin{smallmatrix}1&0&0&1\\0&1&1&0\end{smallmatrix}\right)$. The Hamiltonian in this basis is

$$H = \begin{pmatrix} E_0 & 0 & -t_{23} & -t_{67} & -t_{26} & -t_{37} \\ 0 & E_1 & -t_{67} & -t_{23} & t_{37} & t_{26} \\ -t_{23} & -t_{67} & E_2 & 0 & 0 & 0 \\ -t_{67} & -t_{23} & 0 & E_3 & 0 & 0 \\ -t_{26} & t_{37} & 0 & 0 & E_4 & 0 \\ -t_{37} & t_{26} & 0 & 0 & 0 & E_5 \end{pmatrix} \tag{4.3}$$

where

$$\begin{aligned} E_0 &= -\mu_3 - \mu_6 + V + 2V' - \mu_1 - \mu_4 \\ E_1 &= -\mu_2 - \mu_7 + V + 2V' - \mu_1 - \mu_4 \\ E_2 &= -\mu_2 - \mu_6 + 2V + V' - \mu_1 - \mu_4 \\ E_3 &= -\mu_3 - \mu_7 + 2V + V' - \mu_1 - \mu_4 \\ E_4 &= -\mu_2 - \mu_3 + 3V - \mu_1 - \mu_4 \\ E_5 &= -\mu_6 - \mu_7 + V + 2V' - \mu_1 - \mu_4 \end{aligned} \tag{4.4}$$

V the nearest-neighbor Coulomb interaction and V' the diagonal Coulomb interaction (for simplicity we assume homogeneous V and V' in the ladder array). Near a symmetric exciton tunneling condition in which $\mu_2 \approx \mu_3 = \mu + \Delta$, $\mu_6 \approx \mu_7 = \mu$, and $(V - V'), \Delta \gg t_{23}, t_{67}, t_{26}, t_{37}$, Eq. 4.4 becomes

$$
\begin{aligned}
E_0 &= -2\mu - \Delta + V + 2V' + \delta E_0 \\
E_1 &= -2\mu - \Delta + V + 2V' + \delta E_1 \\
E_2 &= -2\mu - \Delta + 2V + V' + \delta E_2 \\
E_3 &= -2\mu - \Delta + 2V + V' + \delta E_3 \\
E_4 &= -2\mu - 2\Delta + 3V + \delta E_4 \\
E_5 &= -2\mu + V + 2V' + \delta E_5
\end{aligned}
\tag{4.5}
$$

where δE_i is a small perturbation of E_i near the symmetric exciton tunneling condition. We then express Eq. 4.3 in the eigenbasis of the first-order perturbation $H' \simeq U^\dagger H U$ in which

$$
U = \begin{pmatrix}
1 & 0 & -\frac{t_{23}}{V-V'} & -\frac{t_{67}}{V-V'} & -\frac{t_{26}}{2V-2V'-\Delta} & -\frac{t_{37}}{\Delta} \\
0 & 1 & -\frac{t_{67}}{V-V'} & -\frac{t_{23}}{V-V'} & \frac{t_{37}}{2V-2V'-\Delta} & \frac{t_{26}}{\Delta} \\
\frac{t_{23}}{V-V'} & \frac{t_{67}}{V-V'} & 1 & 0 & 0 & 0 \\
\frac{t_{67}}{V-V'} & \frac{t_{23}}{V-V'} & 0 & 1 & 0 & 0 \\
\frac{t_{26}}{2V-2V'-\Delta} & -\frac{t_{37}}{2V-2V'-\Delta} & 0 & 0 & 1 & 0 \\
\frac{t_{37}}{\Delta} & -\frac{t_{26}}{\Delta} & 0 & 0 & 0 & 1
\end{pmatrix}
\tag{4.6}
$$

Neglecting terms of more than second order in $\frac{t_{ij}}{V-V'}$, $\frac{t_{ij}}{2V-2V'-\Delta}$ or $\frac{t_{ij}}{\Delta}$ the effective Hamiltonian H' for the perturbed states $|0'\rangle$ and $|1'\rangle$ becomes

$$
H' = \begin{pmatrix} E_{0'} & -t_{co} \\ -t_{co} & E_{1'} \end{pmatrix}
\tag{4.7}
$$

where $E_{0'} = E_0 - \frac{t_{23}^2}{V-V'} - \frac{t_{67}^2}{V-V'} - \frac{t_{26}^2}{2V-2V'-\Delta} - \frac{t_{37}^2}{\Delta}$, $E_{1'} = E_1 - \frac{t_{23}^2}{V-V'} - \frac{t_{67}^2}{V-V'} - \frac{t_{37}^2}{2V-2V'-\Delta} - \frac{t_{26}^2}{\Delta}$, and $t_{co} = 2\frac{t_{23}t_{67}}{V-V'} - \frac{t_{26}t_{37}}{2V-2V'-\Delta} - \frac{t_{26}t_{37}}{\Delta}$ [64]. From Eq. 4.7 we see that the tunneling of exciton states is determined by t_{co}, which has a term proportional to the product of intra-channel tunnel couplings and a term proportional to the product of inter-channel tunnel couplings. In the present experiment, the former is much larger than the latter by at least three orders of magnitude. Therefore, t_{co} is predominantly caused by the co-tunneling of charges in the intra-channel direction.

4.6.9. ADIABATIC EXCITON TRANSFER PROBABILITY

We estimate the probability that an exciton adiabatically transitions between neighbouring sites in the quantum dot ladder. When this transition does not occur adiabatically, the exciton initially stays where it was. Afterwards, either the electron or the hole may tunnel, leaving the other particles behind, and eventually the entire exciton may still transition, but at least for a brief moment in time the intended exciton transport does not take place. For instance, the transition from $\left(\begin{smallmatrix}1&0&1&1\\0&1&0&0\end{smallmatrix}\right)$ to $\left(\begin{smallmatrix}1&1&0&1\\0&0&1&0\end{smallmatrix}\right)$ might instead end with $\left(\begin{smallmatrix}1&0&1&1\\0&1&0&0\end{smallmatrix}\right)$ (the pair is not transferred) or $\left(\begin{smallmatrix}1&1&0&1\\0&1&0&0\end{smallmatrix}\right)$ (a hole lags behind). Using the Landau-

Zener formula [81, 82], we obtain

$$\begin{aligned} P_{dia} &= \exp\left(-2\pi \frac{t_{co}^2}{\hbar V_E}\right) \\ t_{co} &= \frac{2t^2}{V - V'} \\ V_E &= \frac{\Delta E}{\Delta T_r} \end{aligned} \tag{4.8}$$

where P_{dia} is the diabatic transition probability for the transition from $\left(\begin{smallmatrix}1&0&1&1\\0&1&0&0\end{smallmatrix}\right)$ to $\left(\begin{smallmatrix}1&1&0&1\\0&0&1&0\end{smallmatrix}\right)$, t_{co} is the intra-channel co-tunneling of the electron-hole pair, V_E is the energy level velocity, t is the intra-channel tunnel coupling, V is the inter-channel Coulomb interaction, V' is the diagonal Coulomb interaction, ΔE is the energy difference between the $\left(\begin{smallmatrix}1&0&1&1\\0&1&0&0\end{smallmatrix}\right)$ and $\left(\begin{smallmatrix}1&1&0&1\\0&0&1&0\end{smallmatrix}\right)$ charge states, and ΔT_r is the rise time of the pulse. Note that we do not include the inter-channel co-tunneling processes in the analysis because they are at least three orders of magnitude smaller than that of the intra-channel co-tunneling process, as discussed before. Entering the experimental parameters, we obtain $P_{dia} \simeq 0.8\%$. Therefore, during Coulomb drag the inter-channel exciton is transported adiabatically with an estimated fidelity of 99.2%.

At this point, it is worth mentioning the effect of electron temperature to the exciton transfer fidelity. While the measured temperature of 20 μeV is much larger than the inter-channel tunnel coupling, it is still an order of magnitude smaller than the exciton transport window of about 200 μeV. Operation in the exciton transport regime is possible by choosing a global detuning point which is substantially far away from any transition line (see Fig. 4.5 (c) and (d), line cuts taken at a distance of 100 μeV from the Fermi energy). Additionally, the inter-channel tunnel rates extracted from Fig.4.12 naturally include the effect of thermal excitations. Therefore, when the two channels are aligned, the thermal hopping strength is at least below the extracted tunnel rates of below 210 kHz. This translates to an interdot tunnel coupling strength of below 0.1 μeV, which is much weaker than all other tunneling and co-tunneling coupling strengths

4.6.10. COULOMB DRAG DATA PROCESSING

In Fig. 4.5 the raw data of the BR sensor signal is inverted such that an increasing (decreasing) signal corresponds to a positive (negative) charge. In addition, residual crosstalk from the bottom virtual gates to the sensor signals leads to a small gradient along E (y axis) in phase I of Fig. 4.5(a) and (b). We remove this residual crosstalk by fitting the signals in phase I to a linear background signal and subtracting this background from the data of the entire panel. The scripts for data processing can be found in the data repository.

4.6.11. NUMERICAL SIMULATION OF EXCITON TRANSPORT

We perform numerical simulations to compare with the measured exciton transport data in Fig. 4.5(a) and (b). To this end, we compute the ground state charge configuration of a classical Fermi-Hubbard Hamiltonian:

$$H = \sum_i \mu_i n_i + U \sum_i \frac{n_i(n_i-1)}{2} + U' \sum_{\langle i,j \rangle} n_i n_j + \sum_{i\in\alpha, j\in\beta} V_{ij} n_i n_j + V' \sum_{i\in\alpha, j\in\beta} n_i n_j \tag{4.9}$$

Compared to Eq. 4.1, we have set $t = 0$ to facilitate the computation. We further include the electrochemical potentials $\{\mu_i\}$ and account for the experimentally observed differences in inter-channel Coulomb repulsion V_{ij}.

Due to the absence of tunnel coupling terms, this simple Hamiltonian is already diagonal. Finding its ground state charge configuration becomes therefore a straight-forward energy minimization problem. Since $U \gg V_{ij}, U'$, double occupations are always high in energy and it suffices to input homogeneous charging energies $U \sim 2\,\text{meV}$ as extracted from charge stability diagrams in Fig. 4.7. To capture the observed variations of the exciton transport windows, it is necessary to input the measured inter-channel Coulomb interaction parameters V_{ij} as specified in the main text (see section 4.3, neglecting diagonal interactions). Furthermore, for the intra-channel Coulomb interaction, we assume homogeneous interaction terms $U' \sim 400\,\mu\text{eV}$.

Figure 4.14 shows the simulated charge ground state variation as a function of the electrochemical potentials $\{\mu_i\}$. These are varied in the same way as in the experiment: The bottom (drag) channel detuning E is swept from 500 µeV to past the Fermi energy, while the individual top channel potentials are raised and lowered by 670 µeV, corresponding to the charge shuttling sequence specified in section IV. The charge states are converted to charge sensor signal by inputting the sensor-to-dot distances $\{r_i\}$ and assuming $\frac{1}{r^2}$ decay of Coulomb interactions and a linear response of the sensors. The numerical simulations show good agreement with the measured data. We point out that for each dot pair, the exciton transport window is equal to the inter-channel Coulomb interaction V_{ij}, as highlighted in the main text. The faster vanishing response of the measured data as opposed to the numerical simulations can be explained by a decay of Coulomb interactions faster than $\frac{1}{r^2}$, as previously observed in other work [83].

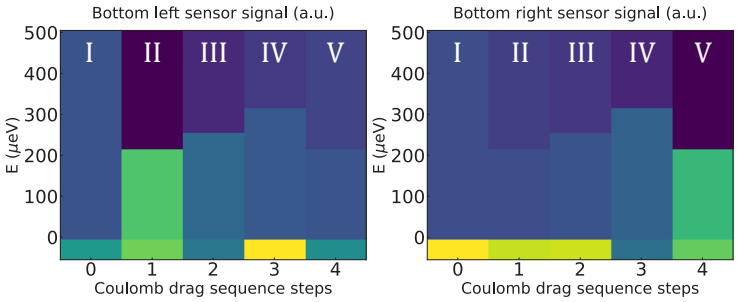

Figure 4.14: Numerical simulation of exciton transport measurements. The simulation calculates the ground state charge configuration as a function of electrochemical potentials $\{\mu_i\}$. At every Coulomb drag step, the corresponding dot potential is pulsed by 670 µeV as specified in the main text. The simulation uses the measured V_{ij} and assumes slightly larger intra-channel Coulomb interaction terms of 400 µeV. Further we input $U_i = 2000$ µeV and neglect next-nearest neighbour interactions. The calculated charge state is transformed to sensor signal assuming a linear sensor response and a $\frac{1}{r^2}$ decay of interactions over distance. The simulation data is in good agreement with the measured data (Fig. 4.5a).

BIBLIOGRAPHY

[1] J. I. Cirac and P. Zoller. “Goals and opportunities in quantum simulation”. *Nature Physics* 8.4 (2012), pp. 264–266.

[2] I. M. Georgescu, S. Ashhab, and F. Nori. “Quantum simulation”. *Reviews of Modern Physics* 86.1 (2014), pp. 153–185.

[3] P. Barthelemy and L. M. K. Vandersypen. “Quantum Dot Systems: a versatile platform for quantum simulations”. *Annalen der Physik* 525.10-11 (2013), pp. 808–826.

[4] E. Manousakis. “A Quantum-Dot Array as Model for Copper-Oxide Superconductors: A Dedicated Quantum Simulator for the Many-Fermion Problem”. *Journal of Low Temperature Physics* 126.5 (2002), pp. 1501–1513.

[5] T. Byrnes et al. “Quantum simulation of Fermi-Hubbard models in semiconductor quantum-dot arrays”. *Physical Review B* 78.7 (2008), p. 075320.

[6] S. Yang, X. Wang, and S. Das Sarma. “Generic Hubbard model description of semiconductor quantum-dot spin qubits”. *Physical Review B* 83.16 (2011), p. 161301.

[7] T. Hensgens et al. “Quantum simulation of a Fermi–Hubbard model using a semiconductor quantum dot array”. *Nature* 548.7665 (2017), pp. 70–73.

[8] A. Singha et al. “Two-Dimensional Mott-Hubbard Electrons in an Artificial Honeycomb Lattice”. *Science* 332.6034 (2011), pp. 1176–1179.

[9] J. Salfi et al. “Quantum simulation of the Hubbard model with dopant atoms in silicon”. *Nature Communications* 7.1 (2016), p. 11342.

[10] J. P. Dehollain et al. “Nagaoka ferromagnetism observed in a quantum dot plaquette”. *Nature* 579.7800 (2020), pp. 528–533.

[11] C. J. van Diepen et al. “Quantum Simulation of Antiferromagnetic Heisenberg Chain with Gate-Defined Quantum Dots”. *Physical Review X* 11.4 (2021), p. 041025.

[12] C.-A. Wang et al. “Probing resonating valence bonds on a programmable germanium quantum simulator”. *npj Quantum Information* 9.1 (2023), p. 58.

[13] M. Kiczynski et al. “Engineering topological states in atom-based semiconductor quantum dots”. *Nature* 606.7915 (2022), pp. 694–699.

[14] E. Abrahams, S. V. Kravchenko, and M. P. Sarachik. “Metallic behavior and related phenomena in two dimensions”. *Reviews of Modern Physics* 73.2 (2001), pp. 251–266.

[15] Y. Zhou et al. “Bilayer Wigner crystals in a transition metal dichalcogenide heterostructure”. *Nature* 595.7865 (2021), pp. 48–52.

[16] Y. Xu et al. “Correlated insulating states at fractional fillings of moiré superlattices”. *Nature* 587.7833 (2020), pp. 214–218.

[17] H. Li et al. “Imaging two-dimensional generalized Wigner crystals”. *Nature* 597.7878 (2021), pp. 650–654.

[18] D. F. Agterberg et al. “The Physics of Pair-Density Waves: Cuprate Superconductors and Beyond”. *Annual Review of Condensed Matter Physics* 11.Volume 11, 2020 (2020), pp. 231–270.

[19] J. Frenkel. “On the Transformation of light into Heat in Solids. I”. *Physical Review* 37.1 (1931), pp. 17–44.

[20] D. Jérome, T. M. Rice, and W. Kohn. “Excitonic Insulator”. *Physical Review* 158.2 (1967), pp. 462–475.

[21] W. KOHN and D. SHERRINGTON. “Two Kinds of Bosons and Bose Condensates”. *Reviews of Modern Physics* 42.1 (1970), pp. 1–11.

[22] K. Slagle and L. Fu. “Charge transfer excitations, pair density waves, and superconductivity in moir\’e materials”. *Physical Review B* 102.23 (2020), p. 235423.

[23] V. Crépel and L. Fu. “New mechanism and exact theory of superconductivity from strong repulsive interaction”. *Science Advances* 7.30 (2021), eabh2233.

[24] E. Guardado-Sanchez et al. “Quench Dynamics of a Fermi Gas with Strong Nonlocal Interactions”. *Physical Review X* 11.2 (2021), p. 021036.

[25] L. Su et al. “Dipolar quantum solids emerging in a Hubbard quantum simulator”. *Nature* 622.7984 (2023), pp. 724–729.

[26] I. Bloch, J. Dalibard, and W. Zwerger. “Many-body physics with ultracold gases”. *Reviews of Modern Physics* 80.3 (2008), pp. 885–964.

[27] J. Argüello-Luengo et al. “Analogue quantum chemistry simulation”. *Nature* 574.7777 (2019), pp. 215–218.

[28] A. M. Kaufman and K.-K. Ni. “Quantum science with optical tweezer arrays of ultracold atoms and molecules”. *Nature Physics* 17.12 (2021), pp. 1324–1333.

[29] L. Chomaz et al. “Dipolar physics: a review of experiments with magnetic quantum gases”. *Reports on Progress in Physics* 86.2 (2022), p. 026401.

[30] B. Yan et al. “Observation of dipolar spin-exchange interactions with lattice-confined polar molecules”. *Nature* 501.7468 (2013), pp. 521–525.

[31] H. Bernien et al. “Probing many-body dynamics on a 51-atom quantum simulator”. *Nature* 551.7682 (2017), pp. 579–584.

[32] G. Semeghini et al. “Probing topological spin liquids on a programmable quantum simulator”. *Science* 374.6572 (2021), pp. 1242–1247.

[33] D. Nandi et al. “Exciton condensation and perfect Coulomb drag”. *Nature* 488.7412 (2012), pp. 481–484.

[34] T. J. Gramila et al. “Mutual friction between parallel two-dimensional electron systems”. *Physical Review Letters* 66.9 (1991), pp. 1216–1219.

[35] M. Yamamoto et al. “Negative Coulomb Drag in a One-Dimensional Wire”. *Science* 313.5784 (2006), pp. 204–207.

[36] B. N. Narozhny and A. Levchenko. “Coulomb drag”. *Reviews of Modern Physics* 88.2 (2016), p. 025003.

[37] M. Kellogg et al. “Observation of Quantized Hall Drag in a Strongly Correlated Bilayer Electron System”. *Physical Review Letters* 88.12 (2002), p. 126804.

[38] E. Tutuc, M. Shayegan, and D. A. Huse. “Counterflow Measurements in Strongly Correlated GaAs Hole Bilayers: Evidence for Electron-Hole Pairing”. *Physical Review Letters* 93.3 (2004), p. 036802.

[39] D. Laroche et al. “Positive and negative Coulomb drag in vertically integrated one-dimensional quantum wires”. *Nature Nanotechnology* 6.12 (2011), pp. 793–797.

[40] R. V. Gorbachev et al. “Strong Coulomb drag and broken symmetry in double-layer graphene”. *Nature Physics* 8.12 (2012), pp. 896–901.

[41] J. I. A. Li et al. “Excitonic superfluid phase in double bilayer graphene”. *Nature Physics* 13.8 (2017), pp. 751–755.

[42] X. Liu et al. “Quantum Hall drag of exciton condensate in graphene”. *Nature Physics* 13.8 (2017), pp. 746–750.

[43] B. Pandey, G. Alvarez, and E. Dagotto. “Excitonic wave-packet evolution in a two-orbital Hubbard model chain: A real-time real-space study”. *Physical Review B* 104.22 (2021), p. L220302.

[44] T. Kaneko, K. Seki, and Y. Ohta. “Excitonic insulator state in the two-orbital Hubbard model: Variational cluster approach”. *Physical Review B* 85.16 (2012), p. 165135.

[45] D. Vu and S. Das Sarma. “Excitonic phases in a spatially separated electron-hole ladder model”. *Physical Review B* 108.23 (2023), p. 235158.

[46] D. V. Averin, A. N. Korotkov, and Y. V. Nazarov. “Transport of electron-hole pairs in arrays of small tunnel junctions”. *Physical Review Letters* 66.21 (1991), pp. 2818–2821.

[47] M. Matters, J. J. Versluys, and J. E. Mooij. “Electron-Hole Transport in Capacitively Coupled 1D Arrays of Small Tunnel Junctions”. *Physical Review Letters* 78.12 (1997), pp. 2469–2472.

[48] H. Shimada and P. Delsing. “Current Mirror Effect and Correlated Cooper-Pair Transport in Coupled Arrays of Small Josephson Junctions”. *Physical Review Letters* 85.15 (2000), pp. 3253–3256.

[49] G. Shinkai et al. “Bidirectional Current Drag Induced by Two-Electron Cotunneling in Coupled Double Quantum Dots”. *Applied Physics Express* 2.8 (2009), p. 081101.

[50] D. M. Zajac et al. “Scalable Gate Architecture for a One-Dimensional Array of Semiconductor Spin Qubits”. *Physical Review Applied* 6.5 (2016), p. 054013.

[51] S. G. J. Philips et al. “Universal control of a six-qubit quantum processor in silicon”. *Nature* 609.7929 (2022), pp. 919–924.

[52] W. Ha et al. “A Flexible Design Platform for Si/SiGe Exchange-Only Qubits with Low Disorder”. *Nano Letters* 22.3 (2022), pp. 1443–1448.

[53] P.-A. Mortemousque et al. “Enhanced Spin Coherence while Displacing Electron in a Two-Dimensional Array of Quantum Dots”. *PRX Quantum* 2.3 (2021), p. 030331.

[54] E. Chanrion et al. “Charge Detection in an Array of CMOS Quantum Dots”. *Physical Review Applied* 14.2 (2020), p. 024066.

[55] F. K. Unseld et al. “A 2D quantum dot array in planar 28Si/SiGe”. *Applied Physics Letters* 123.8 (2023), p. 084002.

[56] N. W. Hendrickx et al. “A four-qubit germanium quantum processor”. *Nature* 591.7851 (2021), pp. 580–585.

[57] M. Lodari. “Light effective hole mass in undoped Ge/SiGe quantum wells”. *Physical Review B* 100.4 (2019).

[58] G. Scappucci et al. “The germanium quantum information route”. *Nature Reviews Materials* 6.10 (2021), pp. 926–943.

[59] F. Borsoi et al. “Shared control of a 16 semiconductor quantum dot crossbar array”. *Nature Nanotechnology* 19.1 (2024), pp. 21–27.

[60] M. Lodari et al. “Low percolation density and charge noise with holes in germanium”. *Materials for Quantum Technology* 1.1 (2021), p. 011002.

[61] C. J. van Diepen et al. “Automated tuning of inter-dot tunnel coupling in double quantum dots”. *Applied Physics Letters* 113.3 (2018), p. 033101.

[62] T.-K. Hsiao et al. “Efficient Orthogonal Control of Tunnel Couplings in a Quantum Dot Array”. *Physical Review Applied* 13.5 (2020), p. 054018.

[63] H. Qiao et al. “Coherent Multispin Exchange Coupling in a Quantum-Dot Spin Chain”. *Physical Review X* 10.3 (2020), p. 031006.

[64] F. R. Braakman et al. “Long-distance coherent coupling in a quantum dot array”. *Nature Nanotechnology* 8.6 (2013), pp. 432–437.

[65] T. H. Oosterkamp et al. “Microwave spectroscopy of a quantum-dot molecule”. *Nature* 395.6705 (1998), pp. 873–876.

[66] D. S. Petrov, G. V. Shlyapnikov, and J. T. M. Walraven. “Regimes of Quantum Degeneracy in Trapped 1D Gases”. *Physical Review Letters* 85.18 (2000), pp. 3745–3749.

[67] M. Sigrist et al. “Coherent Probing of Excited Quantum Dot States in an Interferometer”. *Physical Review Letters* 98.3 (2007), p. 036805.

[68] S. Gustavsson et al. “Time-Resolved Detection of Single-Electron Interference”. *Nano Letters* 8.8 (2008), pp. 2547–2550.

[69] G. Shinkai et al. “Correlated Coherent Oscillations in Coupled Semiconductor Charge Qubits”. *Physical Review Letters* 103.5 (2009), p. 056802.

[70] H.-O. Li et al. “Controlled Quantum Operations of a Semiconductor Three-Qubit System”. *Physical Review Applied* 9.2 (2018), p. 024015.

[71] K. D. Petersson et al. “Quantum Coherence in a One-Electron Semiconductor Charge Qubit”. *Physical Review Letters* 105.24 (2010), p. 246804.

[72] X. Zhang et al. “Universal control of four singlet–triplet qubits”. *Nature Nanotechnology* 20.2 (2025), pp. 209–215.

[73] C. N. Yang and S. Zhang. “So4 symmetry in a hubbard model”. *Modern Physics Letters B* 04.11 (1990), pp. 759–766.

[74] M. Rizzi et al. “Phase Diagram of Spin-1 Bosons on One-Dimensional Lattices”. *Physical Review Letters* 95.24 (2005), p. 240404.

[75] G. V. Shlyapnikov and A. M. Tsvelik. “Polar phase of one-dimensional bosons with large spin”. *New Journal of Physics* 13.6 (2011), p. 065012.

[76] R. Winkler. *Spin—Orbit Coupling Effects in Two-Dimensional Electron and Hole Systems*. Vol. 191. Springer Tracts in Modern Physics. Berlin, Heidelberg: Springer, 2003. ISBN: 978-3-540-01187-3 978-3-540-36616-4.

[77] L. P. Gor’kov and E. I. Rashba. “Superconducting 2D System with Lifted Spin Degeneracy: Mixed Singlet-Triplet State”. *Physical Review Letters* 87.3 (2001), p. 037004.

[78] V. N. Golovach, A. Khaetskii, and D. Loss. “Spin relaxation at the singlet-triplet crossing in a quantum dot”. *Physical Review B* 77.4 (2008), p. 045328.

[79] C. Comte and P. Nozières. “Exciton Bose condensation : the ground state of an electron-hole gas - I. Mean field description of a simplified model”. *Journal de Physique* 43.7 (1982), pp. 1069–1081.

[80] G. A. Fiete. “Colloquium: The spin-incoherent Luttinger liquid”. *Reviews of Modern Physics* 79.3 (2007), pp. 801–820.

[81] L. D. Landau. “Zur Theorie der Energieübertragung. II”. *Physics of the Soviet Union,* 2 (1932), pp. 46–51.

[82] C. Zener and R. H. Fowler. “Non-adiabatic crossing of energy levels”. *Proceedings of the Royal Society of London. Series A, Containing Papers of a Mathematical and Physical Character* 137.833 (1997), pp. 696–702.

[83] J. Knörzer et al. “Long-range electron-electron interactions in quantum dot systems and applications in quantum chemistry”. *Physical Review Research* 4.3 (2022), p. 033043.

5

MITIGATION OF EXCHANGE CROSSTALK IN DENSE QUANTUM DOT ARRAYS

Coupled spins in semiconductor quantum dots are a versatile platform for quantum computing and simulations of complex many-body phenomena. However, on the path of scale-up, crosstalk from densely packed electrodes poses a severe challenge. While crosstalk onto the dot potentials is nowadays routinely compensated for, crosstalk on the exchange interaction is much more difficult to tackle because it is not always directly measurable. Here we propose and implement a way of characterizing and compensating crosstalk on adjacent exchange interactions by following the singlet-triplet avoided crossing in Ge. We show that we can easily identify the barrier-to-barrier crosstalk element without knowledge of the particular exchange value in a 2×4 quantum dot array. We uncover striking differences among these crosstalk elements which can be linked to the geometry of the device and the barrier gate fan-out. We validate the methodology by tuning up four-spin Heisenberg chains. The same methodology should be applicable to longer chains of spins and to other semiconductor platforms in which mixing of the singlet and the lowest-energy triplet is present or can be engineered. Additionally, this procedure is well suited for automated tuning routines as we obtain a stand-out feature that can be easily tracked and directly returns the magnitude of the crosstalk.

This chapter has been published as: Daniel Jirovec, **Pablo Cova Fariña**, Stefano Reale, Stefan D. Oosterhout, Xin Zhang, Sander de Snoo, Amir Sammak, Giordano Scappucci, Menno Veldhorst & Lieven M. K. Vandersypen, "Mitigation of exchange crosstalk in dense quantum dot arrays", Phys. Rev. Applied **24**, 034051 (2025).

5.1. INTRODUCTION

Spin qubits in gate defined semiconductor quantum dots constitute a versatile platform for quantum computation owing to their long coherence times, demonstrated high fidelity single- and two-qubit gates as well as their small footprint [1, 2]. Also, they find applications in quantum simulations due to the inherent tunability of most Hamiltonian parameters which allows to explore different limits of the Fermi-Hubbard and the Heisenberg model [3]. A challenge in scaling up, however, is crosstalk from the gates defining the potential landscape as sketched in Fig. 5.1a. Several approaches for crosstalk management exist and rely on defining a set of virtual gates designed to control the energy scale of choice, be it the on-site potential, tunnel coupling, or the exchange interaction [4–8]. Virtual plunger gates controlling the on-site potential are nowadays routinely used in experiments (Fig. 5.1b), but methods for barrier-to-barrier crosstalk compensation are typically overlooked (Fig. 5.1c) and only rarely implemented [9, 10].

Digital spin qubit experiments so far circumvent the problem by avoiding the simultaneous activation of adjacent exchange couplings [11, 12] or by populating quantum dot arrays only sparsely [13–15]. When only one exchange interaction is activated at a time, any crosstalk to other exchanges will not induce a detrimental effect, because the exponential dependence of exchange strength on barrier voltage leads to a wide voltage range over which the other interactions are effectively switched 'off'. However, implementations of three-qubit gates have been shown and do require require simultaneously activated adjacent exchange couplings [16, 17]. Moreover, quantum simulation of the rich variety of physical phenomena described by the Fermi-Hubbard model [18–27] does require dense arrays of quantum dots with precise, and ideally orthogonal control not only of the on-site potentials but also of the nearest-neighbor exchange interactions or tunnel couplings.

To appreciate why this is not straightforward, we note that once three or more spins are coupled together, the resulting energy spectrum and, hence, the oscillation frequencies are typically a combination of all the exchanges involved, hindering independent calibration of the exchange couplings. Furthermore, whereas the local electrochemical potentials vary linearly in the gate voltages, the tunnel coupling and exchange interaction depend exponentially on gate voltage. To realize crosstalk compensation in the face of this exponential dependence, references [6, 28] assumed that barrier-to-barrier crosstalk can be compensated by a linear combination of voltages in the *argument* of the exponential function, reducing crosstalk compensation between barriers to a linear problem nonetheless. In both cases, the virtualization methods required repeated measurements of either the tunnel coupling or exchange oscillations. crosstalk was then extracted from exponential fits resulting in an indirect, laborious, and potentially error-prone measure. It is therefore desirable to obtain a measure of the crosstalk in a direct way similar to reservoir addition lines used to virtualize plunger gates.

Here we demonstrate a way of characterizing barrier-to-barrier crosstalk to allow individual control of exchange interactions in a dense array of quantum dots. The method consists of tracking the position of the singlet-triplet anti-crossing in the multi-dimensional voltage space spanned by the confining barrier gates. Such a feature can be induced by a suitable intrinsic spin-orbit interaction, local magnetic field gradients or differences in the g-tensors, and determines a point of constant exchange that is fast to measure and

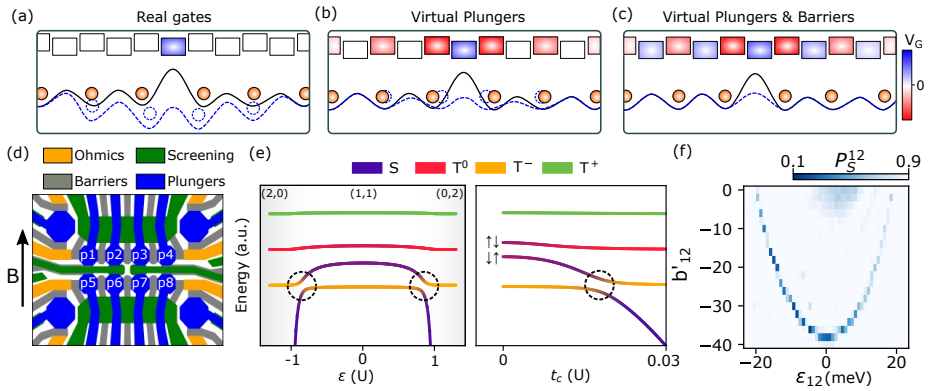

Figure 5.1: (a) Schematics of the confinement potential for a chain of charges defined by the top gates in real voltage space (black solid line). A negative voltage pulse on the central barrier gate causes not only the middle tunnel barrier to be lowered but also shifts the electrochemical potentials of the nearby dots and the height of adjacent tunnel barriers (blue dashed line). (b) Commonly used virtual plunger gates work by applying a linear combination of gate voltages that keeps the electrochemical potentials of all other dots fixed. However, adjacent tunnel barrier heights are still affected and lateral shifts of charges are still present, although they might be slightly reduced. (c) If also the barriers are virtualized, a pulse on the middle barrier gate is compensated by suitable pulses on other barrier gates to keep the other tunnel barriers fixed and, ideally, counteract the lateral shifts of charges. In practice, however, only the combined effect of lateral shifts and tunnel barrier alterations can be compensated. A correct virtualization should allow orthogonal control of exchange interactions and enable a straightforward tuning of multi-spin chains. (d) Schematic of the 2×4 dot array we use in this experiment. The dot plungers are labeled as p_i. Barriers b_{ij} separate dots i and j. The external magnetic field B is applied in an in-plane direction marked by the arrow. (e) Energy level diagram of a two-spin system in a double quantum dot as a function of detuning ϵ (left) and tunnel coupling t_c (right). The dashed circles mark the spin-orbit induced avoided crossings. At $|\epsilon| > U$ the two charges occupy the same dot ((2,0) and (0,2) charge regions). For $|\epsilon| < U$ the charges are shared between the two adjacent dots and the energy splittings are determined by the respective Zeeman energies and the exchange interaction. The position of the avoided crossing can be influenced by ϵ and t_c. (f) Measurement of the avoided crossing as a function of detuning and barrier voltage of Q_{12}, as described in the main text. The avoided crossing always occurs when $J = E_{T^-}$ constituting a constant-exchange feature which we are able to follow as a sharp reduction in singlet return probability P_S^{12}. At more positive values of b'_{12}, $S-T^0$ oscillations cause a reduced singlet return probability as well. As the barrier gets more negative, the exchange increases pushing the avoided crossing feature to smaller ϵ_{12}. At $\epsilon_{12} = 0$ all the exchange is induced by the barrier voltage b'_{12}.

easy to identify. This is especially useful because it isolates the effect of the exchange interaction of interest and could also be adapted for automated optimizations [7]. We empirically find how the gate architecture affects the crosstalk in the device. Finally, we apply this method to the tuning of four-spin Heisenberg chains in different configurations to test its validity and limitations.

5.2. DEVICE AND ENERGY DIAGRAM

The device consists of a 2x4 array of gate-defined quantum dots in a Ge/SiGe heterostructure [29] (Fig. 5.1d and further details can be found in the Appendix section 5.7.1). Four sensors at the corners of the device enable fast charge sensing via radio-frequency (RF) tank circuits (the inductors are off-chip NbTiN coils while the capacitance stems from parasitic capacitances) bonded directly to one of the ohmic contacts of the respective

sensor [30]. The potential landscape is tuned by means of DC voltages to form eight quantum dots, each containing a single hole, under the plunger gates p_i, with $i \in [1,8]$, except for dot 2 where, for practical reasons, we confine three holes. The interdot barrier gates b_{ij} separate dots i and j. Dots 1, 4, 5 and 8 have additional barriers to the reservoirs. Except for b_{26} and b_{37} all the barriers are deposited in the first gate layer allowing strong exchange tunability, unlike in previous experiments on 2x4 Ge/SiGe quantum dot arrays [31, 32] (see Appendix section 5.7.7). Importantly, since the charge carriers are holes, accumulation voltages are negative. A typical DC voltage configuration of the tuned up device is reported in Appendix Fig. 5.7. All the plunger gates and interdot barrier gates are connected also to an arbitrary waveform generator (AWG), via bias-tees and attenuated coaxial transmission lines, to allow fast pulsing away from the DC voltage configuration. In all measurements, the reported voltage amplitudes are the attenuated AWG amplitudes at the gates, without the DC component.

Throughout the experiments we work with virtualized plunger gates (p'_i) which are designed to vary the electrochemical potential of dot i while keeping the electrochemical potential of all other dots fixed [4, 7]. The barrier gates are at first virtualized against the electrochemical potentials only and we denote them as b'_{ij}. This ensures that a pulse on a virtual barrier keeps the dot potentials unchanged (see Fig. 5.1a,b). We further define a detuning axis $\epsilon_{ij} = ap'_i - bp'_j$ and an electrochemical potential axis $\mu_{ij} = cp'_i + dp'_j$, with a, b, c, d experimentally determined coefficients (see Appendix section 5.7.2 for details on the transformations between real and virtual gate voltages). Every double dot is capable of hosting a singlet-triplet ($S-T$) qubit [33–35] which we label Q_{ij} with i and j (we choose $i < j$) denoting the first and second dot in the pair, respectively. To operate $S-T$ qubits, precise control of the exchange interaction J_{ij} is required (in the following discussion we omit the indices ij and reintroduce them when necessary). In quantum dots systems, J originates from the wave-function overlap of and the Coulomb repulsion between neighboring spins [6, 36] and can be controlled by means of ϵ and tunnel coupling t_c taking the form:

$$J(\epsilon, b') = \frac{4t_c^2(b')U}{(U^2 - \epsilon^2)},$$

for $J \ll U$, where U is the charging energy [37]. The tunnel coupling is itself a function of the barrier voltage, and because of crosstalk, also of the voltage on neighboring barriers. This crosstalk we will seek to compensate for in section 5.4 to obtain orthogonal control of exchange interactions. We point out we will not attempt to compensate for the effect of plunger voltages on the exchange, as the interdot detuning is an explicit and desired control knob for the exchange strength, especially during readout and initialization.

A typical energy diagram as a function of ϵ with finite t_c of an $S-T$ qubit is depicted in the left panel of Fig. 5.1e. Unless indicated otherwise, we operate every qubit at its symmetry point $\epsilon = 0$ where the exchange reduces to $J(b') = \frac{4t_c^2(b')}{U}$ and is, therefore, only controlled by the barrier voltage [38]. The energy diagram in this case is depicted in the right panel of Fig. 5.1e.

Contrary to previous works [31], here we do not measure t_c and U, rather, we assume an empirical dependence of J on the designated barrier:

$$J(b') = J_0 \exp(k(b' - b'_0)),$$

where $J_0 = 1\,\text{MHz}$, k represents the exponential lever arm of the barrier and b'_0 is an offset which depends on the particular DC voltage configuration. The DC configuration of the barriers is tuned in a way that ensures b'_0 to be relatively small such that the voltage pulses from the AWG are capable of inducing a considerable on-off ratio for each exchange (in general we find $|b'_0| < 40\,\text{mV}$, see Appendix section 5.7.7). Assuming zero residual exchange at the symmetry point the four eigenstates are the polarized triplets $|T^-\rangle = |\downarrow\downarrow\rangle$, $|T_+\rangle = |\uparrow\uparrow\rangle$ with energies $E_{T^\pm} = \pm\sum E_Z = \pm\sum g\mu_B B$, and the anti-parallel states $|\uparrow\downarrow\rangle$, $|\downarrow\uparrow\rangle$ with energies $E_{AP} = \pm\frac{\Delta E_Z}{2} = \pm\frac{\Delta g\mu_B B}{2}$. g is the effective g-factor of each of the dots which we measure to take values between 0.3 and 0.45 in the in-plane magnetic field direction, consistent with previously reported values for holes in Ge [16]. μ_B is the Bohr magneton and $B = 10\,\text{mT}$ is the external magnetic field approximately applied in the in-plane direction. At large exchange J, the antiparallel states are no longer eigenstates of the Hamiltonian being replaced by $|S\rangle = \frac{|\uparrow\downarrow\rangle - |\downarrow\uparrow\rangle}{\sqrt{2}}$ and $|T^0\rangle = \frac{|\uparrow\downarrow\rangle + |\downarrow\uparrow\rangle}{\sqrt{2}}$. Finally, the spin-orbit spin-flip term Δ_{SO} couples $|S\rangle$ and $|T^-\rangle$ as highlighted by the dashed circles in Fig. 5.1e [39, 40]. At these avoided crossings, coherent $S - T^-$ oscillations can be induced [32, 41].

In the (2,0) charge configuration, the energy splitting between $|S(2,0)\rangle$ and $|T(2,0)\rangle$ well exceeds the thermal energy, enabling fast initialization in the singlet ground state. The different energy scales of the system then allow us to initialize target eigenstates by appropriately choosing the ramp-time from the (2,0) to the (1,1) charge symmetry point (see Appendix section 5.7.5). For read-out, we rely on Pauli spin blockade (PSB). The rather small external magnetic field ensures that only the singlet state is unblocked in the PSB region, as opposed to parity readout where both anti-parallel spin states are typically unblocked [42]. This enables the discrimination of $|S\rangle$ from the triplets by monitoring the charge sensor in single-shot readout.

In Fig. 5.1f we experimentally map out the ST^- avoided crossing as a function of ϵ_{12} and b'_{12} by initializing $|S\rangle$ in Q_{12} and recording the probability to retrieve $|S\rangle$. In between, we rapidly pulse to (1,1), let the system evolve for 50 ns, corresponding approximately to flipping the initial $|S\rangle$ to $|T^-\rangle$ at the avoided crossing, and pulse back to (2,0) for read-out. We can identify the position of the ST^- avoided crossing by a sharp reduction in P_S. Since at these positions $J(\epsilon, b') = E_{T^-}$, the avoided crossing constitutes a constant-exchange feature. The symmetric U-shape is a confirmation that the virtualization of b'_{12} against the plunger gates is accurate as we would otherwise find a skewed shape [32] (see Appendix Fig. 5.10). For more positive barrier voltages we also observe a reduction of P_S which can be attributed to $S - T^0$ oscillations at low J. Importantly, around the avoided crossing, there is no other feature present which allows for a precise identification of its location.

5.3. EXCHANGE CROSSTALK

Before discussing how to correct for crosstalk, we want to elucidate how exchange interactions are affected by nearby barrier voltages. As an example, consider the left side of the device. Fig. 5.2a shows exchange oscillations in Q_{56} as a function of b'_{15}, with b'_{56} kept at a constant, negative value (see sketch in Fig. 5.2c). We initialize Q_{56} in $|\downarrow\uparrow\rangle$ and Q_{12} in $|\downarrow\downarrow\rangle$ and record the final state probability $P^{56}_{\downarrow\uparrow}$ as a function of dwell time τ. At first, b'_{56} is

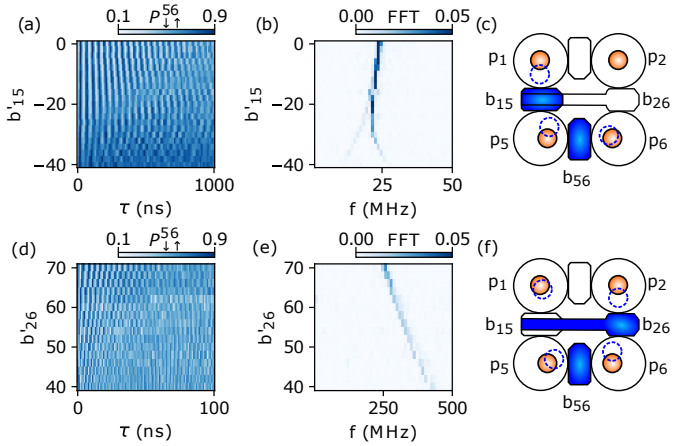

Figure 5.2: (a) Exchange oscillations in Q_{56} as a function of b'_{15} and dwell time τ, as explained in the main text. (b) FFT of (a). We clearly see that the main frequency is reduced and for more negative values of b'_{15} a second oscillation frequency appears. The frequency reduction is a sign of crosstalk, the appearance of a second frequency is due to a finite J_{15}. (c) Sketch of the experiment in (a). The orange circles depict the approximate charge positions when only b'_{56} induces exchange. The blue dashed circles represent the shifted dot positions as we open b'_{15}. (d) Exchange oscillations in Q_{56} as a function of b'_{26} and dwell time τ. (e) FFT of (d). We see a change in frequency of about 60% over only 30 mV, indicating strong crosstalk. (f) Sketch of the experiment in (d) similar to (c). The fan-out of b_{26} leads to a much larger crosstalk than for b_{15} and may affect the position of all the nearby charges.

5

the only gate inducing exchange between the spins in dot 5 and 6 leading the oscillation seen in the top part of Fig. 5.2a. As we pulse b'_{15} more negative, we first see the frequency of the oscillations reduce, a clear example of crosstalk. Furthermore, we also see another frequency appearing below $b'_{15} = -20$ mV (see also the FFT in Fig. 5.2b). This is an indication that b'_{15} now induces exchange between dots 5 and 1. In such a situation it is not clear which of the measured frequency shifts can be attributed to the activation of J_{15} or to crosstalk on J_{56}. Without further modeling, it is, therefore, not possible to quantify the effect of b'_{15} on J_{56} in this voltage range. We can only reliably extract the crosstalk for values $b'_{15} > -20$ mV, e.g. before we induce any measurable exchange J_{15}.

A similar experiment is plotted in Fig. 5.2d-f. However, in this case we pulse on b'_{26} (b'_{56} is more negative than in Fig. 5.2a leading to much faster oscillations). While here we do not see another frequency appear because we do not apply a large enough pulse on b'_{26}, we observe a change in frequency of about 60% in a range of only 30 mV, indicating very strong crosstalk. This might be due to the fan-out of b_{26} as highlighted in the sketch in Fig. 5.2f. While this measurements reveals the crosstalk from b'_{26} onto J_{56}, it doesn't tell us how to compensate for it. In the next section we show how exchange crosstalk can be extracted directly and compensated.

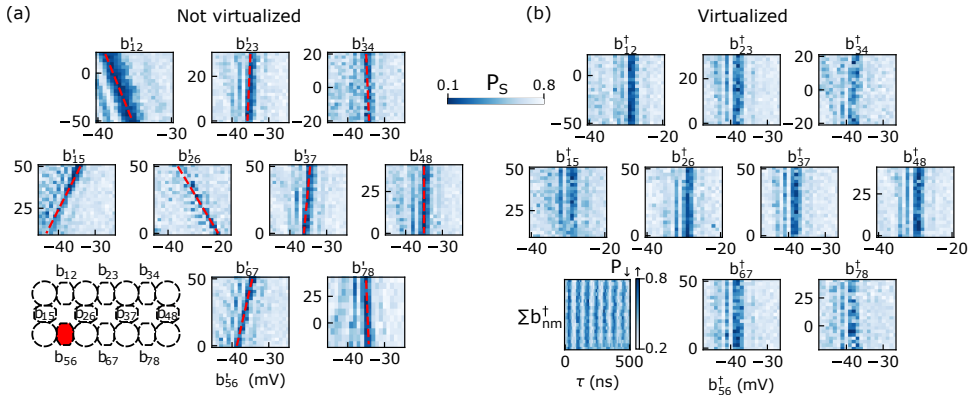

Figure 5.3: (a) ST^- avoided crossing of Q_{56} as a function of b'_{56} on the horizontal axis and all the other barriers on the respective vertical axis. The plots are ordered to reflect the geometric location of the stepped gate. The position of the avoided crossing is reflected by a sharp decrease of the singlet return probability (see main text). From the fitted red dashed lines we extract the crosstalk elements α^{mn}_{56}. The fact that we can fit all crosstalk features with a linear function confirms the assumption of linear barrier crosstalk. (b) ST^- avoided crossing of Q_{56} as a function of $b^\dagger_{56}$ on the horizontal axis and all the other virtual barriers on their respective vertical axis. After the virtualization process the ST^- avoided crossing position is only controlled by $b^\dagger_{56}$ as intended. To further verify that the exchange remains stable we plot exchange oscillations of Q_{56} in the bottom left. We vary all the virtual barriers except $b^\dagger_{56}$ together in the same range as in the individual plots. As desired, the exchange oscillations do not change in the ranges considered here. We repeat the same procedure on the other barrier gates (see Appendix section 5.7.4) and successively fill in the values for α^{mn}_{ij}.

5.4. CHARACTERIZATION OF EXCHANGE VIRTUALIZATION PARAMETERS

We now show how we can leverage the $S-T^-$ avoided crossing to directly extract the crosstalk matrix element for barrier to barrier crosstalk compensation. At the avoided crossing, with $\epsilon_{ij}=0$, all the exchange is induced by the virtual barrier gate voltage b'_{ij} satisfying $|J(b'_{ij})| = |E_{T^-_{ij}}|$ and is to first order insensitive to small variations of ϵ_{ij}. Moreover, any unintentional variation in ϵ_{ij} will only increase J_{ij}, but never decrease it as in the case of lateral shifts of the dot positions. To compensate exchange crosstalk we introduce a second layer of virtualization and define new virtual barrier voltages as $b^\dagger_{ij}$. As in previous works[6, 28] we assume a linear barrier crosstalk and an exponential dependence of J on the new virtual barrier: $J_{ij} = J_0 \exp(k(b^\dagger_{ij} - b^\dagger_{0ij}))$, $b^\dagger_{ij} = \sum_{mn} \alpha^{mn}_{ij} b'_{mn}$, where nm are all the tuples corresponding to adjacent spins and $\alpha^{mn}_{ij} = \frac{\delta J_{ij}}{\delta b'_{mn}} / \frac{\delta J_{ij}}{\delta b'_{ij}}$. The term $b^\dagger_{0ij}$ is an offset in $b^\dagger_{ij}$ that we need to quantify only when calibrating the dependence of J on $b^\dagger_{ij}$. For crosstalk compensation, we therefore need to determine all the values α^{mn}_{ij}, where by definition $\alpha^{ij}_{ij}=1$. Since the avoided crossing constitutes a constant-exchange feature, we can track its position as a function of b'_{mn} and b'_{ij} and extract a slope returning $-\alpha^{mn}_{ij}$ directly, without the need to extract $\frac{\delta J_{ij}}{\delta b'_{mn}}$ with exponential

fits through a series of datapoints. This is the main advantage of the method presented here.

Fig. 5.3a shows measurements of the avoided crossing of Q_{56} as a function of b'_{56} and all other b'_{mn}. The position of the avoided crossing is reflected by a sharp reduction in P_S. In all plots we can follow this stand-out feature with Gaussian fits and extract the red dashed lines (see Appendix). The linear slopes confirm the assumption that barrier gate crosstalk is linear, at least in this regime. The value of the slope $\frac{\delta b'_{56}}{\delta b'_{mn}}$ directly returns the crosstalk element α_{56}^{mn}.

By plugging α_{56}^{mn} in the correction matrix and repeating the measurement of Fig. 5.3a as a function of $b_{56}^{\dagger}$ and $b_{mn}^{\dagger}$ (Fig. 5.3b), we now observe completely vertical constant-exchange features, controlled exclusively by $b_{56}^{\dagger}$, as intended. The bottom left panel in Fig. 5.3b further confirms that the crosstalk is compensated as we record exchange oscillations of Q_{56} as a function of all the $b_{mn}^{\dagger}$ except $b_{56}^{\dagger}$ and observe no change in frequency for the voltage ranges considered here. Note that the voltage range of $b_{12}^{\dagger}$ we scan here corresponds to an on-off ratio of J_{12} of > 100. Similar ratios apply to J_{23}, J_{34}, J_{48}, and J_{78} and their respective virtual barrier gates. This shows that for non-adjacent exchange interactions, the gate crosstalk can be efficiently compensated over at least two orders of magnitude. The virtual barriers $b_{15}^{\dagger}$, $b_{26}^{\dagger}$, and $b_{67}^{\dagger}$ are scanned over a range chosen as to not induce any exchange, since this would alter the position of the avoided crossing even without crosstalk (recall Fig. 5.2). We will show in section 5.5 how to test whether the virtualization remains effective also when adjacent exchanges are turned on.

We find correction factors for every gate where we were able to induce exchange, always taking care that nearest-neighbor gates do not induce any exchange. For practical reasons we did not characterize virtualization of $b_{26}^{\dagger}$, $b_{37}^{\dagger}$ and $b_{67}^{\dagger}$ but only their effect on other gates. In fact, the fan-out of b_{26} and b_{37} affects the charge sensors and result in a loss of the read-out signal, while a too negative voltage in b_{67} accumulates spurious dots that couple to the spins in dots 5 and 6. These problems will be addressed in future device generations.

Fig. 5.4a color codes the extracted crosstalk elements and shows their geometrical distribution with respect to the gate which is being virtualized (highlighted by the bright green color).

We clearly observe a decay of $|\alpha_{ij}^{mn}|$ with distance as expected. We note that crosstalk between barriers that are side by side along the legs of the ladder is negative, similar to previous works [5, 6]. In contrast, crosstalk between barriers oriented orthogonal to each other can also be positive, which is an indication that lateral shifts of the dot positions are less important. Finally, many α_{ij}^{26} and α_{ij}^{37} are relatively large, sometimes exceeding 30% (see Fig. 5.4b), which suggests that the fan-out of their respective gates, b_{26} and b_{37}, can induce considerable crosstalk (see Fig. 5.1d and Appendix Fig. 5.6). This fact should be taken into account when designing future devices.

In the crosstalk extraction we have not considered g-factor modulation due to detuning and barrier gate voltages [43]. Moreover, we note that occasionally we have to slightly correct the initially extracted virtualization matrix element (Fig. 5.4b) to obtain an accurate crosstalk compensation.

Finally, we note that this method is suitable when exchange values are of the same

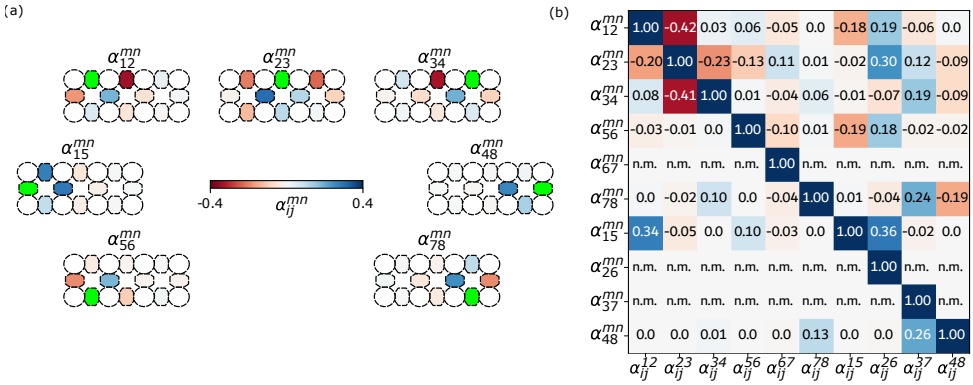

Figure 5.4: (a) Summary of the exchange crosstalk elements α_{ij}^{mn} extracted for the barriers highlighted in bright green. We clearly see a reduction of crosstalk with distance as we expect for capacitive crosstalk. Positive (negative) crosstalk elements imply that an adjacent barrier gate enhances (reduces) a given exchange coupling. (b) Virtual gate matrix for the barrier gates showing the α_{ij}^{mn}, summarizing the results from (a). Except for α_{26}^{mn}, α_{37}^{mn}, and α_{67}^{mn}, all the elements α_{ij}^{mn} are measured. In the experiment the elements labeled 'n.m.' are replaced by 0. To be clear, this matrix reports how much each b'_{ij} affects the various $b_{mn}^{\dagger}$. The barrier gate voltages b'_{ij} needed to orthogonally control the respective exchange interactions via $b_{mn}^{\dagger}$ are obtained from the inverse of this matrix.

order as the Zeeman energy. For $|J| \ll |E_T - |$, which is the case for high external magnetic field operation, there is no avoided crossing to follow. To circumvent this, one could determine the crosstalk elements at low external field and then perform the desired experiments at higher field. Alternatively, it might be possible to use microwave driving to track the dependence of the spin resonance frequency. Indeed, the resonance frequency of a spin is modified by the exchange interaction, so it would be possible to fix the applied microwave tone and scan the desired barrier against all other barriers and extract α_{ij}^{mn} in the same way we did here.

In the following we explore whether α_{ij}^{mn} is stable even when nearest-neighbor exchanges are turned on. This is a crucial question as it would allow to extend spin chains indefinitely after locally mitigating crosstalk.

5.5. VALIDATION OF THE VIRTUALIZATION IN EXTENDED SPIN-CHAINS

In order to test if the virtualization parameters are still valid in a regime where nearest-neighbor exchanges are turned on, we proceed to couple four spins into a chain and observe the resulting oscillation dynamics. As shown in Fig. 5.2a,b, activated nearest-neighbor interactions result in a highly non-trivial time evolution with multiple visible oscillation frequencies. However, preparing special states and evolving them at special voltage points results in a single visible oscillation frequency which we use here to validate the virtualization. For a chain of coupled spins, the Hamiltonian describing the

system can be approximated as

$$H = \sum_i g_i \mu_B B S_{z,i} + \sum_i \Delta_{SO,i} S_{x,i} + \sum_{<i,j>} J_{ij} \left(\boldsymbol{S_i S_j} - \frac{1}{4} \right) \tag{5.1}$$

where $\mathbf{S} = (S_x, S_y, S_z) = \hbar/2(\sigma_x, \sigma_y, \sigma_z)$ is the vector of spin operators with the Pauli matrices $\sigma_{x,y,z}$ for each spin and the indeces i, j run over nearest neighbors, and we set $\hbar = 1$. The additional term Δ_{SO} stems from intrinsic spin-orbit interaction and the anisotropic g-tensors [32]. Ignoring the spin-orbit term and considering four adjacent spins, Eq. 5.1 can be conveniently written in the reduced basis $\{|S_{ij}S_{kl}\rangle, |S_{ij}T^-_{kl}\rangle, |T^-_{ij}S_{kl}\rangle, |T^-_{ij}T^-_{kl}\rangle\}$ as $H = H_Q =$

$$\begin{pmatrix} -J_{ij} - J_{kl} & 0 & 0 & 0 \\ 0 & -J_{ij} - \overline{E}_{z,kl} & -\frac{J_{jk}}{2} & 0 \\ 0 & -\frac{J_{jk}}{2} & -\overline{E}_{z,ij} - J_{kl} & 0 \\ 0 & 0 & 0 & -\overline{E}_{z,ijkl} + \frac{J_{jk}}{2} \end{pmatrix}$$

We want to draw attention to the matrix elements that involve $|S_{ij}T^-_{kl}\rangle$ and $|T^-_{ij}S_{kl}\rangle$. When $|J_{ij} - \overline{E}_{z,ij}| = |J_{kl} - \overline{E}_{z,kl}|$, the diagonal elements are equal and the resulting degeneracy is lifted by the off-diagonal elements $-J_{jk}/2$. We call this the resonant ST^- condition. Initializing one of the two states $|S_{ij}T^-_{kl}\rangle$ or $|T^-_{ij}S_{kl}\rangle$, and letting the system evolve at this special point, results in $|ST^-\rangle \leftrightarrow |T^-S\rangle$ oscillations with a frequency $hf = J_{jk}$. This convenient feature was exploited in [32] to implement a two-qubit gate for singlet-triplet qubits and in [26] to estimate the exchange interaction in a four-qubit plaquette. Similar arguments hold for the $\{|S_{ij}S_{kl}\rangle, |S_{ij}T^0_{kl}\rangle, |T^0_{ij}S_{kl}\rangle, |T^0_{ij}T^0_{kl}\rangle\}$ subspace where the resonant condition appears when $\sqrt{J^2_{ij} + \Delta E^2_{z,ij}} = \sqrt{J^2_{kl} + \Delta E^2_{z,kl}}$. We utilize these resonant conditions to verify whether the virtualization obtained with nearest-neighbor couplings switched off is still valid when nearest-neighbor interactions are turned on. This test relies on the fact that the position of the resonant condition depends on both $J_{ij}(b^\dagger_{ij})$ and $J_{kl}(b^\dagger_{kl})$ (as well as the Zeeman energies), while the oscillation frequency depends on $J_{jk}(b^\dagger_{jk})$. Hence, we can test whether we find the resonant condition at the correct location and whether the oscillation frequency matches our expectations (more details can be found in Appendix section 5.7.8).

We study three implementations of a four-spin chain with nearest-neighbor couplings: chain 3-4-8-7, chain 2-1-5-6, and chain 1-2-3-4. In the first two cases, the chains are curved around the right and left edges of the device, respectively, while in the last case the dots forming the chain are assembled linearly. The latter situation was previously studied in GaAs devices in [6, 28].

We first consider the chain 3-4-8-7. After having extracted the crosstalk coefficients α^{mn}_{34}, α^{mn}_{48}, and α^{mn}_{78} we measure exchange oscillations for Q_{34}, Q_{48}, and Q_{78} as a function of $b^\dagger_{34}$, $b^\dagger_{48}$, and $b^\dagger_{78}$, respectively, to extract the dependence $J_{ij}(b^\dagger_{ij})$. For these measurements, the other exchange interactions are turned off such that the oscillation frequency only depends on the exchange interaction of interest. We then fit the oscillation fre-

quency to

$$f_{ij}(b_{ij}^{\dagger}) = \sqrt{\left(J_0 \exp k_{ij}(b_{ij}^{\dagger} - b_{0,ij}^{\dagger})\right)^2 + \Delta E_{Z,ij}^2} \tag{5.2}$$

with k_{ij}, $b_{0,ij}^{\dagger}$, and $\Delta E_{Z,ij}$ as free parameters (see Appendix Fig. 5.20). With the knowledge of these exchange dependencies as well as the Zeeman energies, we are able to predict at which voltage points $(b_{34}^{\dagger}, b_{78}^{\dagger})$ the resonant conditions should appear. Fig. 5.5a shows the resonant ST^- condition as a function of $(b_{34}^{\dagger}, b_{78}^{\dagger})$ with the exchange in between set to $J_{48} \approx 2\,\mathrm{MHz}$ through $b_{48}^{\dagger}$. We initialize $|S_{78}T_{34}^-\rangle$ and let the system evolve for $\tau = 380\,\mathrm{ns}$ at each voltage point which ensures an approximate population inversion to $|T_{78}^- S_{34}\rangle$ at the resonant condition as long as J_{48} remains unaffected by $b_{34,78}^{\dagger}$. We identify the resonant condition as a sharp change in return probability. We do not record the joint probability of measuring $|S_{34}T_{78}^-\rangle$ but rather choose to measure only P_S^{34}. By operating in regimes where leakage outside the $|ST^-\rangle, |T^-S\rangle$ subspace is suppressed, we still recover the desired information. The red dotted line is the predicted location of the resonant condition based on the extracted exchange dependencies and the Zeeman energies, which agrees well with the data. Numerical simulations of P_S^{34} resulting from the full system dynamics also match the experimental data very well (Appendix Fig. 5.23a). This suggests that $J_{34}(b_{34}^{\dagger})$ and $J_{78}(b_{78}^{\dagger})$ are still well virtualized even when J_{48} is activated.

To extract the value of J_{48} at a given voltage point, we can record the dynamics at the resonant condition. To do this, we choose any point along the resonant condition, away from any leakage features, and sweep $b_{34}^{\dagger}$ ($b_{78}^{\dagger}$) by $\pm 5\,\mathrm{mV}$ ($\mp 5\,\mathrm{mV}$), here resulting in the black dashed line in Fig. 5.5a, as a function of dwell time. In 5.5b we clearly see a chevron pattern with a maximum in amplitude, corresponding to the resonant condition, oscillating at a frequency given by J_{48}. This frequency agrees well with the corresponding frequency seen in numerical simulations (Appendix Fig. 5.23 b), providing evidence that also $b_{48}^{\dagger}$ is properly virtualized.

Finally, in Fig. 5.5c we report coherent $|S_{78}T_{34}^-\rangle \leftrightarrow |T_{78}^- S_{34}\rangle$ oscillations as a function of $b_{48}^{\dagger}$ at the resonant condition, while recording P_S^{78} this time. Fig. 5.5d is the FFT of (c) and the red dashed line is the exchange dependence $J_{48}(b_{48}^{\dagger})$ we extracted from the isolated Q_{48} measurements. Since also here we find good agreement, we conclude that, in this case, the virtualization of all three barrier gates involved was successful.

We repeat the same procedure for chain 2-1-5-6 (Fig. 5.5e-h). Here we show data that was taken during a different cool-down and where $b_{15}^{\dagger}$ was not virtualized ($b_{12}^{\dagger}$ and $b_{56}^{\dagger}$ were virtualized). However, the crosstalk onto $b_{15}^{\dagger}$ turned out to be relatively weak such J_{15} was only mildly affected by $b_{12}^{\dagger}$ and $b_{56}^{\dagger}$. Moreover, Fig. 5.5g-h pertain to the resonant $|ST^0\rangle$ condition. The red dashed line in Fig. 5.5h is a fit to the data that allows us to extract $J_{15}(b_{15}^{\dagger})$ for this particular voltage configuration. In addition, in Appendix Fig. 5.22 we report further resonant condition plots similar to Fig. 5.5f for different values of $b_{15}^{\dagger}$ and observe that the position of the resonant condition does not change. We therefore conclude that the virtualization of $b_{12}^{\dagger}$ and $b_{56}^{\dagger}$ is correct also in this four-spin chain, and we have full knowledge of the Hamiltonian parameters in this configuration.

For the ultimate test, we consider the same plots as for 3-4-8-7 also for the chain 1-2-3-4 involving b_{23}, which displays the most severe crosstalk elements α_{23}^{mn}. (Fig. 5.5i-l).

Although we find a good theoretical agreement with the data in Fig. 5.5i, to match the oscillation frequencies in 5.5j,k, we needed to adjust the value of $b^{\dagger}_{0,23}$ by −6 mV compared to the values extracted via Eq. 5.2 from the isolated oscillations Q_{23}. This suggests that, while we are able to correct for most of the crosstalk, there might be some non-linear effects which we did not take into account. We have identified a possible cause for this, which was also extensively discussed in ref. [8]. In fact, we observe a nonlinear crosstalk between b'_{23} and p'_3 which we show in Appendix Fig. 5.8. This can lead to a miscalibrated crosstalk and the observed discrepancy between the isolated Q_{23} and the coupled four-spin chain measurement. To correct for such effects, we would require a more sophisticated, non-linear crosstalk compensation scheme which is outside the scope of this work.

In general, we find that we are able to compensate most of the crosstalk and infer the Hamiltonian parameters also in the coupled four-spin chains. All the data is supported by numerical simulations which we report in Appendix section 5.7.10.

5.6. DISCUSSION

In this work, we have proposed and demonstrated a way of directly extracting barrier-to-barrier crosstalk by tracking the constant-exchange feature given by the ST^- avoided crossing in Ge. While the effects generally vary from gate to gate, we were able to observe a few trends. In fact, electrodes featuring a fan-out in proximity to other gates typically display large crosstalk to other exchanges. For two-dimensional quantum dot arrays, these lateral fan-outs can be avoided through a vertical fan-out with vias [44–46]. Perfecting the gate layout and oxide composition can also contribute to reduced crosstalk as demonstrated recently [10]. On the other hand, barrier gates oriented perpendicularly to each other and with no proximal fan-out, typically show much less crosstalk which seems easier to mitigate. This suggests that, for 1D chains, a zigzag alignment of quantum dots could be favorable over a strictly linear placement.

An important verification tool in our work is the construction of four-spin chains and their time evolution at the resonant ST^- or ST^0 condition. It allowed us to confirm that the crosstalk extracted in the isolated two-qubit regime also mostly carries over to the regime of coupled four-spin chains. This important observation might enable the construction of longer spin-chains with only local crosstalk calibration.

Finally, we want to emphasize also some of the limitations of this method. If we want to utilize the ST^- avoided crossing, we can only calibrate the crosstalk reliably in the isolated two-spin regime and only for $J \approx E_{T^-}$. Other methods for direct crosstalk extraction can be utilized and also rely on following a constant-exchange feature, but are still limited to the isolated two-spin regime. For example, to extract the crosstalk elements α^{mn}_{23} we made use of exchange oscillations at a fixed time evolution (see Appendix Fig. 5.13) as we did not calibrate $|S\rangle$ initialization and direct PSB readout due to the distance from the sensing dots. This method is more versatile as it doesn't require spin-orbit interactions, making it suitable also for GaAs or silicon quantum dot devices. Nonetheless, we found that the ST^- avoided crossing is a feature that is typically robust and easy to measure without knowledge of the particular Hamiltonian parameters like the exchange dependence on any barrier nor any lever arms. This information was crucial in earlier works on virtualization [5, 6]. In practice the method presented here is, therefore, preferable as

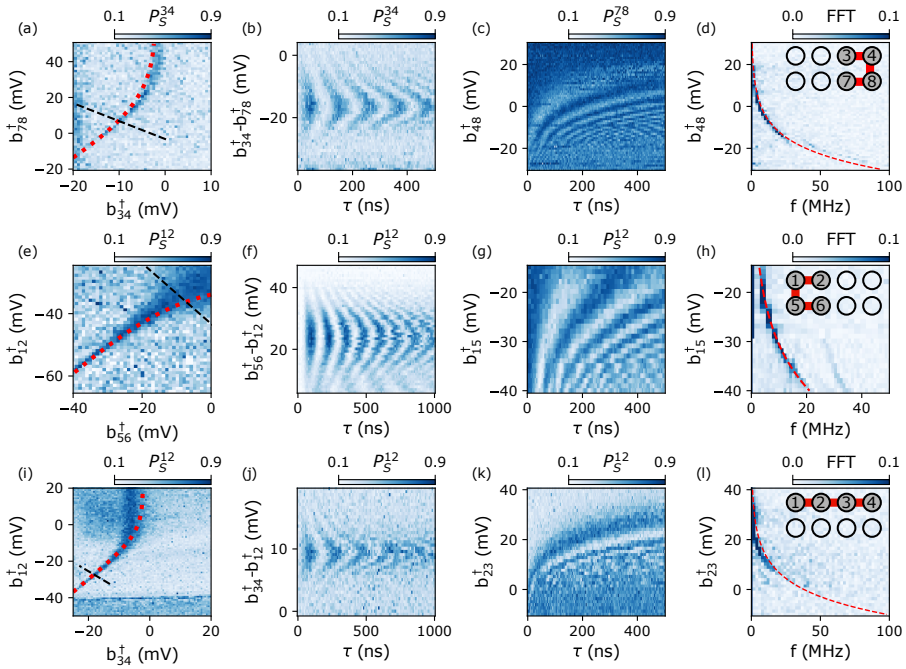

Figure 5.5: (a) Resonant $|S_{78}T_{34}^-\rangle \leftrightarrow |T_{78}^-S_{34}\rangle$ condition as a function of $b_{34}^\dagger$ and $b_{78}^\dagger$ with an exchange $J_{48} \approx 2\,\mathrm{MHz}$ induced by $b_{48}^\dagger$. We record the probability of measuring $|S_{34}\rangle$ after initializing $|S_{78}T_{34}^-\rangle$ and letting the system evolve for $\tau = 380\,\mathrm{ns}$ corresponding to a near perfect inversion of population at the resonant condition marked by an increase in P_S^{34}. The red dots mark the theoretical resonant condition, based on the Zeeman energies and individual exchange dependencies, which agrees well with the data. (b) Resonant $|S_{78}T_{34}^-\rangle \leftrightarrow |T_{78}^-S_{34}\rangle$ oscillations as a function of dwell time τ and $b_{34}^\dagger - b_{78}^\dagger$. The barriers are scanned along the dashed line in (a). The maximum oscillation amplitude corresponds to the resonant condition and the frequency is $hf = J_{48}$. (c) Resonant $|S_{78}T_{34}^-\rangle \leftrightarrow |T_{78}^-S_{34}\rangle$ oscillations as a function of dwell time τ and $b_{48}^\dagger$ at the resonant condition. (d) FFT of (c). The red dashed line is the exchange dependence $J_{48}(b_{48}^\dagger)$ extracted from the isolated Q_{48} oscillations which matches well with the observed FFT peak. The latter yields $J_{48}(b_{48}^\dagger)$ with the two neighbouring exchanges activated. The inset shows a sketch of the dots and interactions involved in the experiments (a)-(d). (e)-(h) Similar to (a)-(d) but for chain 2-1-5-6. In this case $b_{15}^\dagger$ was not virtualized due to the rather small crosstalk elements. (g) and (h) show data pertaining to the resonant $|S_{12}T_{34}^0\rangle \leftrightarrow |T_{12}^0S_{34}\rangle$ condition. The red dashed line in (h) is a fit and allows us to extract $J_{15}(b_{15}^\dagger)$ even without complete virtualization. (i)-(l) Similar to (a)-(d) but for chain 1-2-3-4. While we find good agreement with the predicted resonant condition in (i), the oscillation frequency in (j) and (k) is different from the expected value extracted from the isolated Q_{23} oscillations. We do find good agreement with the data if we correct the value $b_{0,23}^\dagger$ by $-6\,\mathrm{mV}$. This suggests that some residual, possibly non-linear crosstalk remains, which will require more sophisticated mitigation strategies to account for.

it requires less overall knowledge of the device. These considerations make this method also a good candidate for automated calibrations [5, 7] which can be easily integrated into existing routines [8].

With our findings, we have shed further light on the intricate crosstalk behavior in multi-layered spin qubit devices. We also demonstrated that, despite the density of electrodes, linear crosstalk can be managed and corrected for. Generally, the designing of large spin-qubit arrays leaves room for improvement, for which this work provides valuable guidance. Furthermore, our results open the possibility of observing multi-spin physics in longer chains and two-dimensional geometries, with detailed knowledge of the underlying Hamiltonian.

5.7. SUPPLEMENTARY MATERIAL

5.7.1. DEVICE FABRICATION AND EXPERIMENTAL SETUP

The device is fabricated on a $Ge/Si_{0.2}Ge_{0.8}$ heterostructure with a quantum well buried 55 nm below the surface. The growth is performed by chemical vapor deposition starting from a Si substrate. After growing a thick layer of Ge on the substrate, the Si concentration is linearly increased to reach the desired composition (Fig. 5.6e)[29]. The fabrication starts with markers and SiN pads patterned via optical lithography. Subsequently, the ohmic contacts are defined via electron-beam lithography (Fig. 5.6a). The contact material is Pt which, after deposition, is annealed during the oxide deposition (7 nm of ALD grown Al_2O_3). In the following, we alternate ebeam lithography, metal deposition and oxide growth to define the barrier gate layer (Fig. 5.6b), the screening gate layer (Fig. 5.6c), and the plunger gate layer (Fig. 5.6d). The gate material is Ti/Pd with a thickness of 3/17 nm for the first gate layer, 3/27 nm for the second, and 3/37 for the third gate layer. All measurements are performed in an Oxford Triton dilution refrigerator at a nominal base temperature of 13 mK. We apply magnetic fields in-plane of 10 mT. The device was mounted on a custom-made printed circuit board (PCB). DC voltages from home-built serial peripheral interface (SPI) DAC modules and pulses from a Keysight M3202A arbitrary waveform generator are combined using on-PCB bias tees. RF reflectometry for charge sensing was done using SPI in-phase and quadrature (IQ) demodulation modules and on-PCB LC tank circuits. The demodulated signals were recorded by a Keysight M3102A digitizer.

The voltages necessary to tune the device into a regime with a single hole in each of the 8 quantum dots (except dot 2 where 3 holes are confined) and form single-hole transistors (SHTs) in the top left, top right, and bottom left dot are plotted as a heatmap in Fig. 5.7. We found that the bottom right sensor was faulty, which is why all voltages in that area are set to 0 V.

5.7.2. CROSSTALK MATRIX FOR PLUNGER VIRTUALIZATION

Virtual plunger gates ease device control and are rather straightforward to obtain from charge stability diagrams. Plunger to plunger crosstalk can be directly extracted from the slopes of the reservoir addition lines. In order to compensated for crosstalk from barriers to plungers it is important to account for the fact that an increased coupling, induced

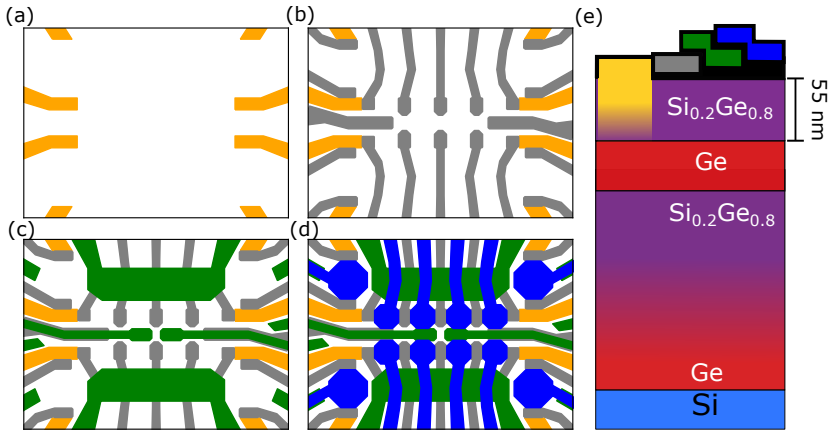

Figure 5.6: Device design and heterostructure. (a) In the first metal layer we deposit the Ohmic contacts. (b) After annealing while depositing the gate oxide, we proceed with the first barrier gate layer which also includes the sensor barriers to the leads. (c) In the third gate layer, we deposit screening gates and the two central barrier gates b_{26} and b_{37}. (d) Finally, we deposit the plunger gates including the sensors. (e) Sketch of the heterostructure and the gate stack on top. The thick black layers in between the gates symbolizes the gates oxides.

by the barrier, will also modify the plunger to plunger crosstalk element. We therefore must ensure we first start from a set of DC gate voltages close to the desired operating conditions. Once a suitable DC voltage configuration is found, we record charge stability diagrams and step the barriers. In this way, it is possible to track the center of the (1,1) charge stability region as a function of the barrier and compensate for this shift (in fact we use a manual version of the method described in [8]) (Fig. 5.8). The resulting virtual gate matrix is depicted in Fig. 5.9.

In a next step, we define detunings $\epsilon_{ij} = ap'_j - bp'_i$ and electro-chemical potentials $\mu_{ij} = cp'_j + dp'_i$ where a, b, c, d are coefficients that we experimentally determine. If the definitions of ϵ_{ij} as well as the barrier to plunger virtualization are correct, the ST^- avoided crossing position as a function of detuning and (virtual) barrier should be symmetric U-shaped (in the absence of modulations of the g factor) [32]. An example of an ill-defined virtualization leading to a skewed U-shape is depicted in Fig. 5.10a, while Fig. 5.10b shows the same measurement with corrected virtualizations. This step is crucial for the subsequent barrier to barrier compensation, since an unwanted detuning between the quantum dots would enhance the exchange of interest.

5.7.3. CROSSTALK EXTRACTION

Fig. 5.11 shows the process for extracting the crosstalk element. In Fig. 5.11a we show a linecut of the top leftmost panel of 5.3. The black dashed line is a gaussian fit from which we are able to extract the position of the avoided crossing. The white crosses in Fig. 5.11b mark the extracted avoided crossing positions to which we can fit the red dashed line. The crosstalk element $\alpha^1_{56}2$ is simply the slope multiplied by -1. Such a procedure is repeated for all the other barrier gates to fill out the crosstalk matrix.

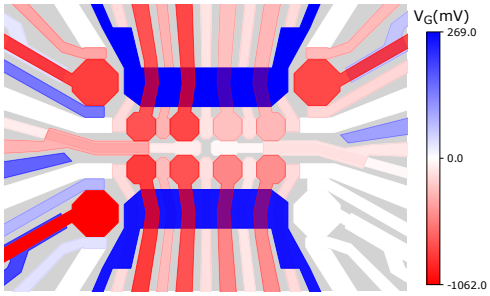

Figure 5.7: Typical DC voltage configuration in the experiments presented in this work. The color scale reflects the voltage V_G applied to the individual electrodes. Electrodes in white are either grounded or have 0 V applied. All voltages on the bottom right sensor are at 0 V as the sensor plunger was faulty. Starting from the DC configuration, pulses on the AWG channels allow us to quickly change the charge state or the exchange.

5.7.4. CROSSTALK FOR OTHER BARRIERS

Fig. 5.12, 5.13, 5.14, 5.15, 5.16 and Fig. 5.17 present data analogous to the data shown in Fig. 5.9 for Q_{56}. Specifically, they show the avoided crossing features or exchange oscillations of Q_{12}, Q_{23}, Q_{34}, Q_{15}, Q_{48} and Q_{78}, respectively. In all the figures, the plots associated with the respective barriers are organized to reflect the geometry of the device. We always chose the ranges in a way to not induce any exchange for nearest neighbor barriers. For Q_{23} we do not have access to direct PSB readout. Therefore, we opted to initialize the state $|\downarrow\uparrow\downarrow\downarrow\rangle$ in the top row and record exchange oscillations at a fixed duration τ and scan b'_{23} against b'_{mn}. We record the probability $P^{12}_{\downarrow\uparrow}$ which, with b'_{12} and b'_{34} not inducing any exchange, oscillates at a frequency determined by b'_{23}. While the resulting features are not as clear and isolated as the ones from the avoided crossing, they still allow us to extract a crosstalk element. Fig. 5.13b shows exchange oscillations between spins 2 and 3, again recorded as $P^{12}_{\downarrow\uparrow}$ which are not influenced by any of the $b^{\dagger}_{mn}$ demonstrating that crosstalk is compensated.
Lastly, we note that the crosstalk elements reported in Fig. 5.4b are the ones we used in the experiments in Fig. 5.5 and are not necessarily the same as the slopes in the measurements here would suggest.

5.7.5. INITIALIZATION AND READ-OUT SCHEMES

Fig. 5.18 schematically shows the different initialization and read-out schemes. A fast pulse (Fig. 5.18c) initializes and reads $|S\rangle$, a ramped pulse starting after the avoided crossing (Fig. 5.18e) initializes $|\downarrow\uparrow\rangle$ or $|\uparrow\downarrow\rangle$, while a ramped pulse starting before the avoided crossing initializes $|\downarrow\downarrow\rangle$. During the time evolution in (1,1) we pulse on a barrier to induce exchange. Combining the initialization with an appropriate pulse shape to the read-out point unveils ST^0 oscillations (Fig. 5.18d), exchange oscillations (Fig. 5.18f) or ST^- oscillations (Fig. 5.18h).

5.7.6. G-FACTORS

We extract the resonance frequencies f_i of our spins by means of electric dipole spin resonance (EDSR) and find our effective g-factors as $g_i = \frac{f_i}{\mu_B B} h$ at a field of $B = 10\,\mathrm{mT}$. h

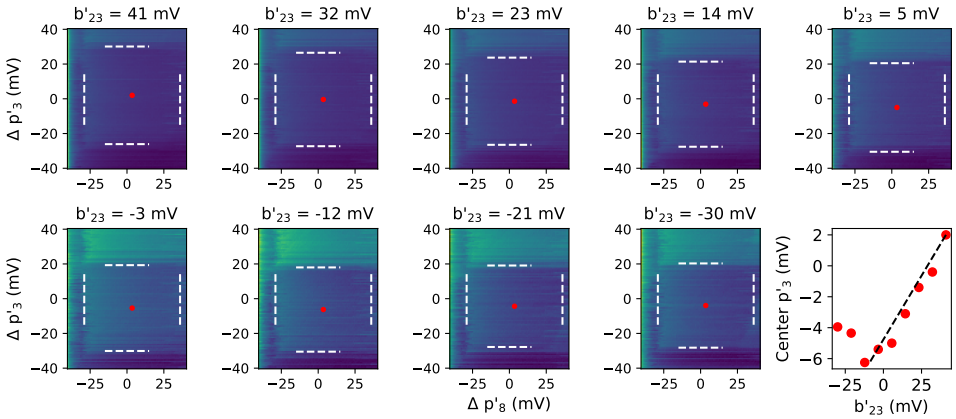

Figure 5.8: Plunger against barrier virtualization. The plots show charge stability diagrams of p'_8 vs p'_3 while stepping b'_{23}. The white dashed lines mark the charge transitions of dot 8 (vertical) and dot 3 (horizontal). The red dot is the center of the charge stability region which we can follow in all the plots as we lower the value of b'_{23}. The last panel in the bottom right shows the extracted center position of p'_3 for the different barrier voltages. The black dashed line allows us to extract the crosstalk correction between b'_{23} and p'_3. However, we notice that for very negative barrier voltages the center position deviates from this line indicating that the crosstalk has changed. Similar observations were made in reference [8] and will require more sophisticated non-linear correction schemes.

is Plank's constant. The results are summarized in Fig. 5.19.

5.7.7. EXCHANGE PROFILES FOR BARRIER GATES

We typically operate every singlet-triplet qubit at its symmetry point ($\epsilon_{ij} = 0$). Here the exchange is determined solely by the height of the tunnel barrier ($J = \frac{2t^2}{U}$). It is common practice to approximate the exchange dependence on the barrier by an exponential function $J(b_{ij}) = J_0 \exp\left(k(b_{ij} - b_{0ij})\right)$ where b_{0ij} is an offset determined by the DC voltage configuration and $J_0 = 1\,\text{MHz}$. k can be interpreted as a barrier lever arm, e.g. how strongly the barrier voltage affects the exchange. This is dependent on the gate layout and the DC voltage configuration. Fig. 5.20 shows the exchange profiles of the singlet triplet qubits we measured alongside their FFTs and fits the to the exchange formula. Table 5.1 summarizes the extracted values for all the singlet triplet qubits measured.

5.7.8. SINGLET-TRIPLET RESONANT CONDITIONS

In this subsection we want to further elucidate the reasoning behind the resonant 4-spin ST^- and ST^0 conditions which are plotted in Fig. 5.5 of the main text. In the presence of an external magnetic field B and isotropic but site dependent g-factors g_i, with $\hbar = 1$, the Heisenberg Hamiltonian assumes the form:

$$H = \sum_i g_i \mu_B B S_{z,i} + \sum_i \Delta_{SO,i} S_{x,i} + \sum_{<i,j>} J_{ij} \left(\boldsymbol{S_i S_j} - \frac{1}{4} \right) \tag{5.3}$$

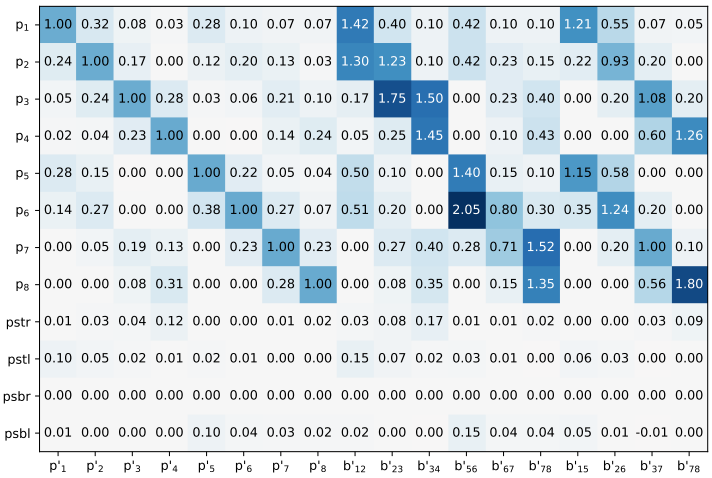

Figure 5.9: crosstalk matrix for a first layer of gate virtualization. The linear combination of p_i and b_{ij} to orthogonally control the dot potentials is obtained from the inverse of this matrix. "pstr", "pstl", "psbr" and "psbl" refer to the **p**lunger of **s**ensor **t**op ((b)ottom) **r**ight ((l)eft), respectively. As a consequence of depositing the barrier gates as a first gate layer, large correction pulses on the plungers are needed to compensate for barrier pulses as highlighted by the large crosstalk elements. For example, a pulse on b'_{56} would require a pulse of twice the amplitude on p_6 in order to maintain the electrochemical potential of dot 6 unchanged.

where $\mathbf{S} = (S_x, S_y, S_z)$ is the spin operator on site i. Here, Δ_{SO} consists of anisotropic g-tensor components and the intrinsic spin-orbit interaction in the spin-orbit frame [47]. The influence of additional S_y terms in the spin-orbit term can neglected if we only analyze the isolated ST^- (ST^0) subspace [32]. For four spins i, j, k, l it is instructive to write the basis states of the different spin subspaces in the familiar singlet-triplet basis of two-spin states. These are summarized in table 5.2. Without the spin-orbit interaction, a spin system initialized in one of these subspaces should evolve only within that subspace, e.g. the total spin number is conserved. We particularly want to draw the attention to the two lowest states in the T^0 and T^- subspace. These states contain one singlet and one triplet each.

$|ST^-\rangle, |T^-S\rangle$ SUBSPACE

If we reduce ourselves to the basis $\{|S_{ij}S_{kl}\rangle, |S_{ij}T^-_{kl}\rangle, |T^-_{ij}S_{kl}\rangle, |T^-_{ij}T^-_{kl}\rangle\}$ the Hamiltonian takes the form [32]:

$$H_{ST^-} = \begin{pmatrix} -J_{ij} - J_{kl} & \frac{\Delta_{SO,kl}}{2} & \frac{\Delta_{SO,ij}}{2} & 0 \\ \frac{\Delta_{SO,kl}}{2} & -J_{ij} - \overline{E}_{z,kl} & -\frac{J_{jk}}{4} & \frac{\Delta_{SO,ij}}{2} \\ \frac{\Delta_{SO,ij}}{2} & -\frac{J_{jk}}{4} & -\overline{E}_{z,ij} - J_{kl} & \frac{\Delta_{SO,kl}}{2} \\ 0 & \frac{\Delta_{SO,ij}}{2} & \frac{\Delta_{SO,kl}}{2} & -2\overline{E}_{z,ijkl} + \frac{J_{jk}}{4} \end{pmatrix}$$

Compared to eq. 5.5 of the main text we have included the spin-orbit part as well which gives rise to leakage terms outside of the $|S_{ij}T^-_{kl}\rangle, |T^-_{ij}S_{kl}\rangle$ subspace. However, these occur only at the respective avoided crossings ($J_{ij} = \overline{E_{Zij}}$) and it is easy to operate away

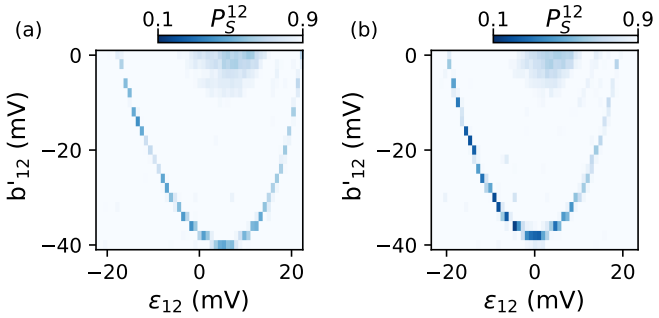

Figure 5.10: a) ST- avoided crossing of Q_{12} as a function of ϵ_{12} and b'_{12} with an improper first layer of virtualization leading to a skewed U-shape. b) same measurement as in a) but with corrected virtualization returning a symmetric U-shape.

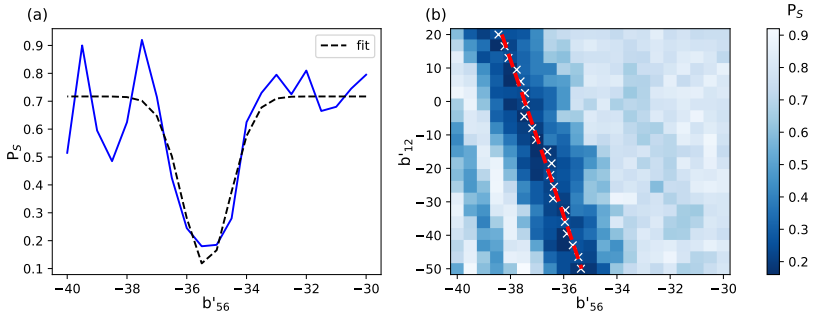

Figure 5.11: (a) Line cut of panel (b) corresponding to the top right panel in Fig. 5.3a). we fit a gaussian to the data to extract the position of the minimum in the singlet probability. We repeat this for every value of b'_{12}. b) crosstalk extraction $\alpha^1_{56}2$. The white crosses are the extracted minima in P_S. The red dashed line is a fit to the data. The slope returns -$\alpha^1_{56}2$.

gate	k(mV^{-1})	$b^\dagger_0$(mV)
$b^\dagger_{12}$	-79.29	11.7
$b^\dagger_{23}$	-94.72	44.1
$b^\dagger_{34}$	-96.69	21.0
$b^\dagger_{15}$	-90.05	20.2
b'_{26}	-90.02	-9.8
b'_{37}	n.m	n.m
$b^\dagger_{48}$	-86.38	22.6
$b^\dagger_{56}$	-90.00	13.2
b'_{67}	n.m	n.m
$b^\dagger_{78}$	-71.6	50.1

Table 5.1: Summary of the measured exchange dependences on the barrier gates. b'_{37} and b'_{67} have not been measured and that b'_{26} is not virtualized. The DC voltages ensure that $|b^\dagger_{0,ij}| < 50$ mV, enabling a large on-off ratio within a comfortable pulse amplitude for the AWG.

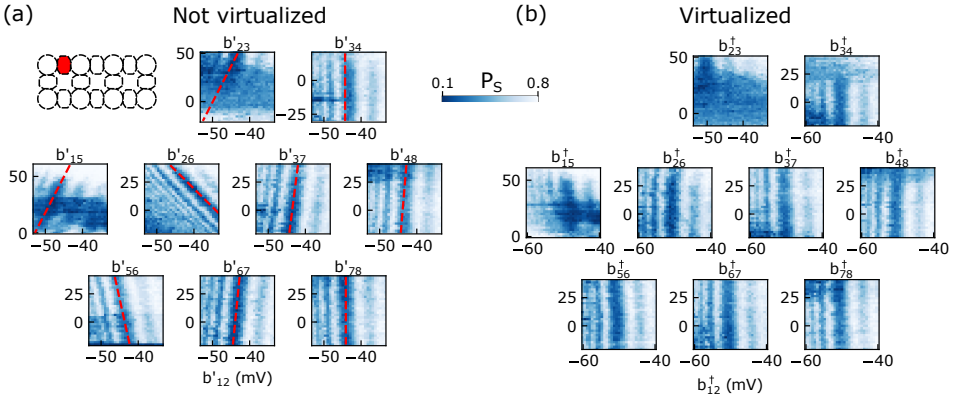

Figure 5.12: (a) ST^- avoided crossing of Q_{12} as a function of b'_{12} and all the other barriers b'_{ij}. The slopes return the crosstalk element α^{mn}_{12}. (b) ST^- avoided crossing of Q_{12} as a function of $b^{\dagger}_{12}$ and all the other virtual barriers $b^{\dagger}_{ij}$.

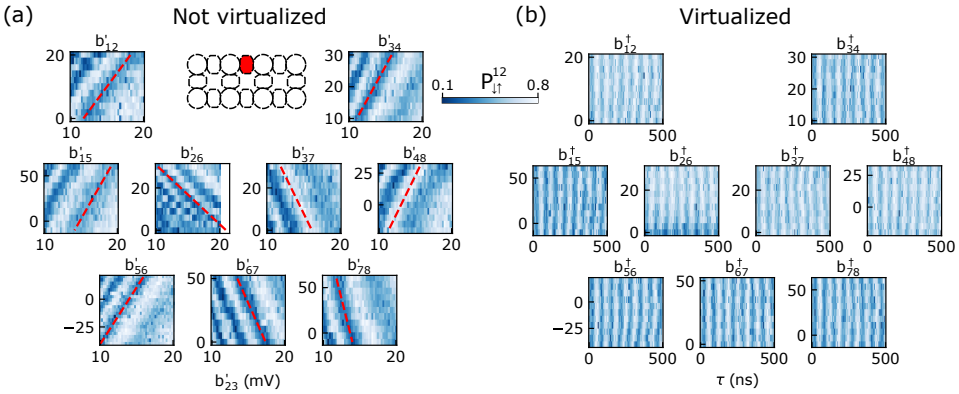

Figure 5.13: (a) Exchange oscillations of Q_{12} as a function of b'_{23} and all the other barriers b'_{ij}. Since we do not have direct access to the ST^- avoided crossing in Q_{23} we opted to initialize $|\downarrow\uparrow\downarrow\downarrow\rangle$ in the top row and record $P^{12}_{\downarrow\uparrow}$. By fixing the evolution time τ and scanning b'_{23} against the other barriers we are still able to follow features and extract the crosstalk element, although no feature stands out more than others. (b) Exchange oscillations of Q_{12} as a function of $b^{\dagger}_{mn}$ and duration τ. None of the virtual barriers $b^{\dagger}_{ij}$ affect the oscillation frequency which indicates that the crosstalk to $b^{\dagger}_{23}$ is correctly compensated.

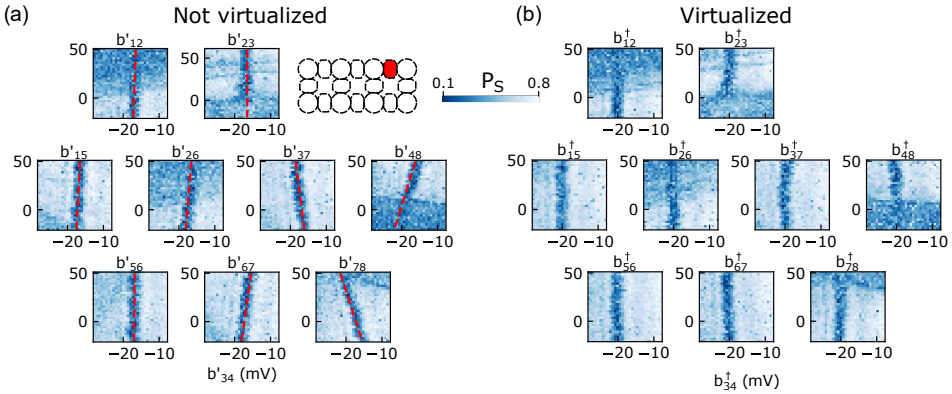

Figure 5.14: (a) ST^- avoided crossing of Q_{34} as a function of b'_{34} and all the other barriers b'_{ij}. The slopes return the crosstalk element α^{mn}_{34}. (b) ST^- avoided crossing of Q_{34} as a function of $b^{\dagger}_{34}$ and all the other virtual barriers $b^{\dagger}_{ij}$.

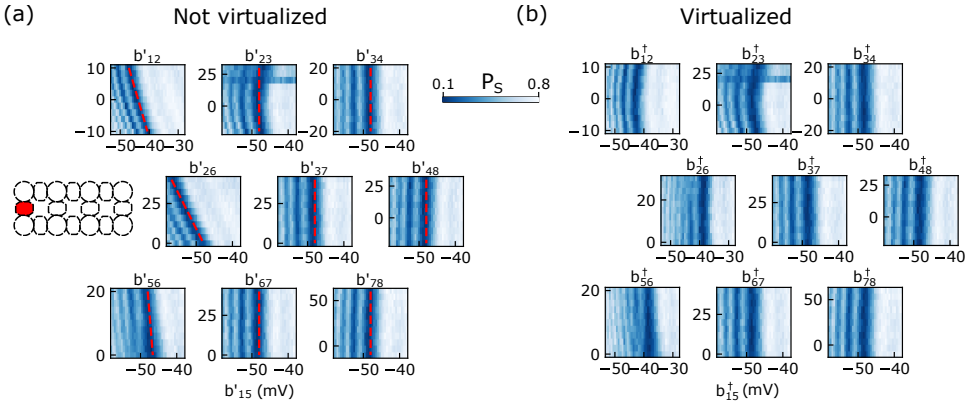

Figure 5.15: (a) ST^- avoided crossing of Q_{15} as a function of b'_{15} and all the other barriers b'_{ij}. The slopes return the crosstalk element α^{mn}_{15}. (b) ST^- avoided crossing of Q_{15} as a function of $b^{\dagger}_{15}$ and all the other virtual barriers $b^{\dagger}_{ij}$. Except for $b^{\dagger}_{23}$ all the virtualizations are correct. We note that when a gate crosstalk element is zero $b'_{mn} = b^{\dagger}_{mn}$ for this case and we simply reproduced the plots from (a) also in (b).

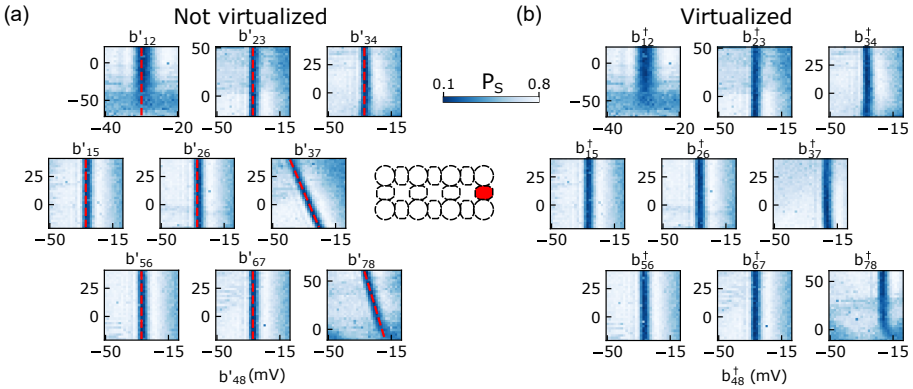

Figure 5.16: (a) ST^- avoided crossing of Q_{48} as a function of b'_{48} and all the other barriers b'_{ij}. The slopes return the crosstalk element α^{mn}_{48}. (b) ST^- avoided crossing of Q_{48} as a function of $b^{\dagger}_{48}$ and all the other virtual barriers $b^{\dagger}_{ij}$. We note that when a gate crosstalk element is zero $b'_{mn} = b^{\dagger}_{mn}$ for this case and we simply reproduced the plots from (a) also in (b).

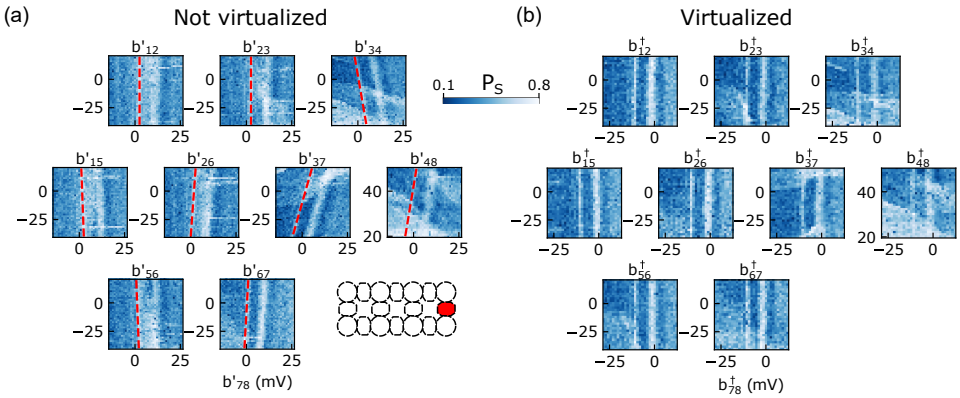

Figure 5.17: (a) ST^- avoided crossing of Q_{78} as a function of b'_{78} and all the other barriers b'_{ij}. The slopes return the crosstalk element α^{mn}_{78}. (b) ST^- avoided crossing of Q_{78} as a function of $b^{\dagger}_{78}$ and all the other virtual barriers $b^{\dagger}_{ij}$.

Subspace	(S, m_S)	two-qubit basis states
Q	$(2,\pm2)$	$\lvert T^{\pm}_{ij}T^{\pm}_{kl}\rangle$
	$(2,\pm1)$	$\frac{1}{\sqrt{2}}(\lvert T^{0}_{ij}T^{\pm}_{kl}\rangle+\lvert T^{\pm}_{ij}T^{0}_{kl}\rangle)$
	$(2,0)$	$\frac{1}{\sqrt{6}}(\lvert T^{+}_{ij}T^{-}_{kl}\rangle+\lvert T^{-}_{ij}T^{+}_{kl}\rangle+2\lvert T^{0}_{ij}T^{0}_{kl}\rangle)$
$T^{\pm}$	$(1,\pm1)$	$\frac{1}{\sqrt{2}}(\lvert T^{0}_{ij}T^{\pm}_{kl}\rangle-\lvert T^{\pm}_{ij}T^{0}_{kl}\rangle)$
		$\lvert T_{ij^{\pm}}S_{kl}\rangle$
		$\lvert S_{ij}T^{\pm}_{kl}\rangle$
T^0	$(1,0)$	$\frac{1}{\sqrt{2}}(\lvert T^{+}_{ij}T^{-}_{kl}\rangle-\lvert T^{-}_{ij}T^{+}_{kl}\rangle)$
		$\lvert T^{0}_{ij}S_{kl}\rangle$
		$\lvert S_{ij}T^{0}_{kl}\rangle$
S	$(0,0)$	$\frac{1}{\sqrt{3}}(\lvert T^{+}_{ij}T^{-}_{kl}\rangle+\lvert T^{-}_{ij}T^{+}_{kl}\rangle-\lvert T^{0}_{ij}T^{0}_{kl}\rangle)$
		$\lvert S_{ij}S_{kl}\rangle$

Table 5.2: Four-spin shared eigenstates of $\hat{S}^2$ and $\hat{S}^z$ expressed in a basis of two-spin singlets and triplets. As the Heisenberg Hamiltonian is spin conserving, it only couples states within the same subspace. Note that these states are, in general, not eigenstates of the Heisenberg Hamiltonian. The lowest two states of the T^0 and T^- subspace in the table are used to find resonant four spin conditions in Fig. 5.5.

from these locations. When $|J_{ij}-\overline{E}_{Z,ij}|=|J_{kl}-\overline{E}_{Z,kl}|$ the middle two diagonal terms are equal and the off diagonal terms $\frac{J_{jk}}{4}$ become dominant. Initializing $|S_{ij}T^{-}_{kl}\rangle$ and pulsing quickly to this condition will induce $|S_{ij}T^{-}_{kl}\rangle \leftrightarrow |T^{-}_{ij}S_{kl}\rangle$ oscillations with a frequency $f_{ST^-}=\frac{J_{jk}}{h}$ [26].

$|ST^0\rangle, |T^0S\rangle$ SUBSPACE

If we reduce ourselves to the basis $\{|S_{ij}S_{kl}\rangle, |S_{ij}T^0_{kl}\rangle, |T^0_{ij}S_{kl}\rangle, |T^0_{ij}T^0_{kl}\rangle\}$ the Hamiltonian takes the form:

$$H_{ST^0}=\begin{pmatrix} -J_{ij}-J_{kl} & \Delta E_{Z,kl} & \Delta E_{Z,ij} & -\frac{J_{jk}}{4} \\ \Delta E_{Z,kl} & -J_{ij} & -\frac{J_{jk}}{4} & \Delta E_{Z,ij} \\ \Delta E_{Z,ij} & -\frac{J_{jk}}{4} & -J_{kl} & \Delta E_{Z,kl} \\ -\frac{J_{jk}}{4} & \Delta E_{Z,ij} & \Delta E_{Z,kl} & 0 \end{pmatrix}$$

Similar to the Hamiltonian 5.7.8, we can identify a resonant condition: $\sqrt{J^2_{ij}+\Delta E^2_{Z,ij}}=\sqrt{J^2_{kl}+\Delta E^2_{Z,kl}}$. Again we will find that at these special conditions we can induce $|S_{ij}T^0_{kl}\rangle \leftrightarrow |T^0_{ij}S_{kl}\rangle$ oscillations at a frequency $f_{ST^0}=\frac{J_{jk}}{h}$. In this case, however, the leakage terms outside this subspace are given by $\Delta E_{Z,ij,kl}$ and are slightly more difficult to avoid. In fact, we need to ensure that $J_{ij}\gg\Delta E_{Z,ij}$ and $J_{kl}\gg\Delta E_{Z,kl}$ which, for the top right quadrants in Fig. 4a,e,i is not always given. These notions are summarized in Fig. 5.21. In Fig. 5.21a we plot the energy diagram of the 4-spin system 2-1-5-6 as a function of $b^\dagger_{56}-b^\dagger_{12}$ as scanned in Fig. 5.5b with a small exchange between spins 1 and 5 in the chain induced by $b^\dagger_{15}$. The overlap with the 4 important states in the legend is color and thickness coded. We can observe 2 avoided crossings, one between $|ST^-\rangle \leftrightarrow |T^-S\rangle$ and

another for $|ST^0\rangle \leftrightarrow |T^0S\rangle$. The fact that the avoided crossings occur at different gate voltages reflects the slightly different requirements for J_{12} and J_{56}. However, the size of both avoided crossings is equal and solely determined by J_{15}.

Finally, we point out that since the read-out in PSB is not capable of distinguishing $|T^0\rangle$ from $|T^-\rangle$ we will find more 'leakage' features that, while not directly coupling the different subspaces, will lead to deviations from the expected resonant condition positions. This can be appreciated in Fig. 5.21c where we record the $S_{12}T^0_{56}$ resonant condition. Apart from the expected diagonal feature, we also observe two horizontal features indicated by the arrows. One can be attributed to ST^0 oscillations in Q_{12}, the other to ST^- oscillations at the spin-orbit anticrossing of Q_{12}. Apart from the spin-orbit induced leakage terms, the Hamiltonian which we use to simulate the system contains all the necessary information to reproduce the experimental results.

5.7.9. ADDITIONAL DATA FOR 1256 RESONANT CONDITION

Fig. 5.22 shows additional measurements of the $S_{12}T^-_{56}$ resonant condition as we step $b^\dagger_{15}$. We notice the maximum of the oscillation amplitude always in the same point for $b^\dagger_{56} - b^\dagger_{12}$ which suggests that we have likely compensated the crosstalk to $b^\dagger_{15}$ correctly. The chevron pattern becomes more spread as a result of an increase in J_{15} which is reflected also by the minimum oscillation frequency in each plot.

5.7.10. SIMULATIONS OF THE HEISENBERG CHAIN

We perform the simulations of our experiments with the python package Qutip and assume that the system evolves under the Heisenberg Hamiltonian defined in eq. 5.5. We incorporate the experimentally determined g-factors and exchange profiles. For the 4-spin chains we operate far away from the spin-orbit avoided crossing and therefore omit them in the simulations for simplicity. Our model still captures the relevant parts of the system dynamics. Furthermore, in our analysis we have ignored g-factor modulations due to barrier gate voltages. In fact, for high enough exchange, a small deviation of the g-factors will not alter the dynamics of the system considerably. Fig. 5.23 simulates the results for Fig. 4a,b, and c, Fig. 5.24 pertains to the experiments in Fig. 4e,f, and g, while Fig. 5.25 simulates the results for the linear chain obtained in Fig. 4,i,j, and k of the main text. In these three figures the red dashed lines are the same as in the corresponding figure of the main text.

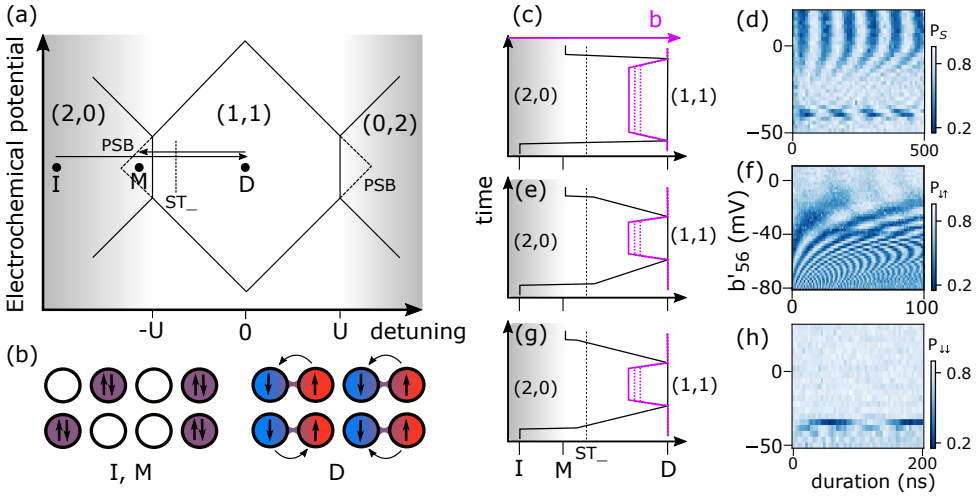

Figure 5.18: (a) Schematic of a charge stability diagram of a double quantum dot as a function of detuning and the electro-chemical potentials of the two dots, which are uniformly varied. When the detuning is equal to the charging energy U, charges get transferred between the dots through the vertical transition lines. The region inside the dashed triangle corresponds to the metastable region where Pauli-spin-blockade occurs assuming the triplet excited state falls outside the triangle (otherwise the triangle gets truncated). A typical experiment starts with two charges in one of the two dots ((2,0) or (0,2) charge region, as depicted in the left sketch in (b)). We then pulse the system into the (1,1) region at the dwell point D. Depending on the ramp type ((c), (e) or (g)) we initialize $|S\rangle$, $|\downarrow\uparrow\rangle$ or $|\downarrow\downarrow\rangle$. After letting the system evolve we pulse back to the measurement point M and perform single-shot readout of the final state. (b) Sketch of the typical charge and spin configuration at the initialization (I) and measurement (M) point (left) as well as at the dwell point (D) (right). (c) Pulse scheme to obtain ST^0 oscillations when initializing in S and reading S (by "reading a state", we mean distinguishing this state from the other three states in the two-qubit space). After pulsing the detuning quickly to D we diabatically pulse on the barrier voltage and next diabatically pulse the detuning back to M. A typical oscillation pattern as in (d) emerges. (d) Singlet-triplet oscillations of Q_{56} as a function of b'_{56}. For more positive barrier voltages we clearly see $S-T^0$ oscillations at a frequency $hf = \Delta g_{56}\mu_B B$. As the barrier voltage is lowered and exchange increases, the oscillation frequency increases and the visibility is lowered indicating the initial $|S\rangle$ is now an eigenstate of the system. Around $b'_{56} = -40$ mV another oscillation can be observed corresponding to $S-T^-$ oscillations at the ST^- avoided crossing. (e) Pulse scheme to obtain exchange oscillations for initialization and readout of $|\uparrow\downarrow\rangle$. By ramping adiabatically with respect to $\Delta g\mu_B B$ (after diabatically sweeping over the ST^- avoided crossing) we are able to initialize an antiparallel spin state at the dwell point. A diabatic pulse on the barrier will then induce SWAP oscillations between $|\uparrow\downarrow\rangle$ and $|\downarrow\uparrow\rangle$. Ramping the detuning back adiabatically until the avoided crossing and then diabatically until the measurement point takes the final $|\uparrow\downarrow\rangle$ state onto a singlet (2,0) during readout effectively returning $P_{\uparrow\downarrow}$. (f) Exchange oscillations as a function of b'_{56} utilizing the pulse scheme in (e). This time we see the amplitude of the oscillations increase as we lower the barrier voltage and exchange is enhanced, as expected for SWAP oscillations starting from $|\downarrow\uparrow\rangle$. (g) Pulse scheme to obtain oscillations when initializing and reading $|T^-\rangle$ by adiabatically ramping over the ST^- avoided crossing. The same adiabatic ramp before read-out takes $|T^-\rangle$ onto a singlet (2,0) during read-out effectively returning $P_{\downarrow\downarrow}$. Between initialization and readout, a diabatic barrier pulse is applied. (h) With the pulse scheme in (g) we now only see oscillations at the ST^- avoided crossing as expected when starting from $|T^-\rangle$.

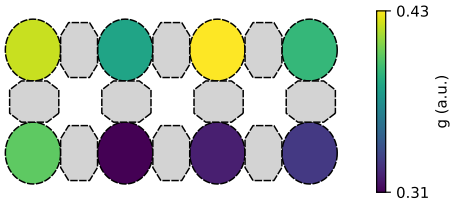

Figure 5.19: g-factors for the spins in the different dots. The g-factors were extracted from electric dipole spin resonance experiments (data not shown).

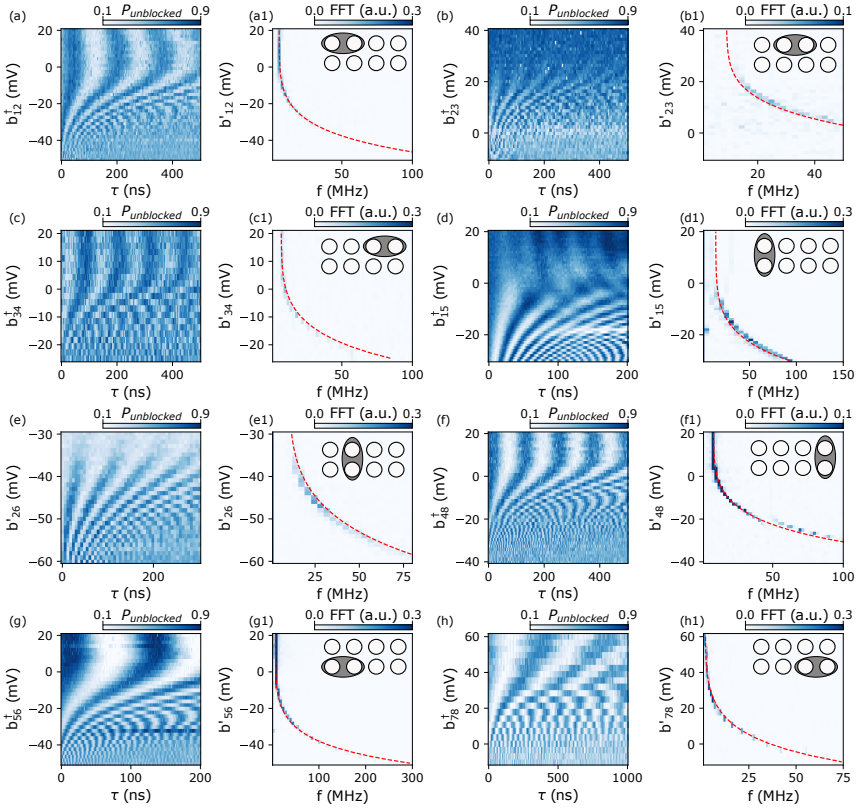

Figure 5.20: (a)-(h) Exchange oscillations as a function of the barriers. (a1)-(h1) FFTs of the oscillations and fit to the exchange formula. The insets schematically show which ST qubit is activated. All other exchanges are switched off.

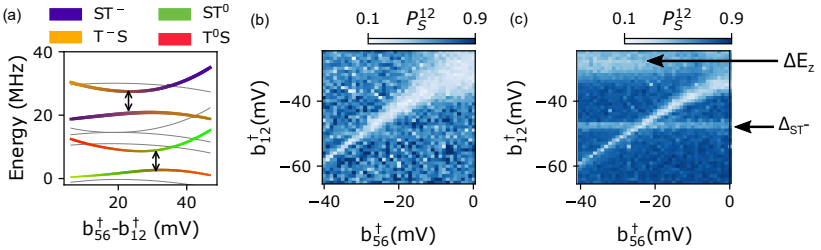

Figure 5.21: (a) Simulated energy diagram of the 4-spin system 2-1-5-6 as a function of $b_{56}^{\dagger} - b_{12}^{\dagger}$ as scanned in Fig. 5.5b. The overlap with the 4 important states in the legend is color and thickness coded. We can observe 2 avoided crossings, one between $|ST^{-}\rangle \leftrightarrow |T^{-}S\rangle$ and another for $|ST^{0}\rangle \leftrightarrow |T^{0}S\rangle$. The fact that the avoided crossings occur at different gate voltages reflects the slightly different requirements for J_{12} and J_{56}. However, the size of both avoided crossings is equal and solely determined by J_{15}. (b) same as Fig. 5.5a. (c) Resonant $|S_{12}T_{56}^{0}\rangle$ condition as a function of $b_{56}^{\dagger}$ and $b_{12}^{\dagger}$. We initialize $|S_{12}T_{56}^{0}\rangle$ and let the system evolve for 100 ns at each voltage point with a small exchange opened through $b_{15}^{\dagger}$. Like in (b) we can identify a sharp resonant condition which occurs at slightly different gate voltages than (b) as $|S_{12}T_{56}^{0}\rangle$ evolves to $|T_{12}^{0}S_{56}\rangle$. In the bottom left quadrant, however, the two resonant conditions approach each other. This is expected since J_{12} and J_{56} become the dominant energies in the system. We can also identify two leakage features indicated by the black arrows. One pertains to the singlet triplet avoided crossing of Q_{12} (Δ_{SO}), while the other, at more positive voltages of $b_{12}^{\dagger}$ can be attributed to ST^{0} oscillations in Q_{12} since $J_{12} \approx \Delta E_{Z,12}$.

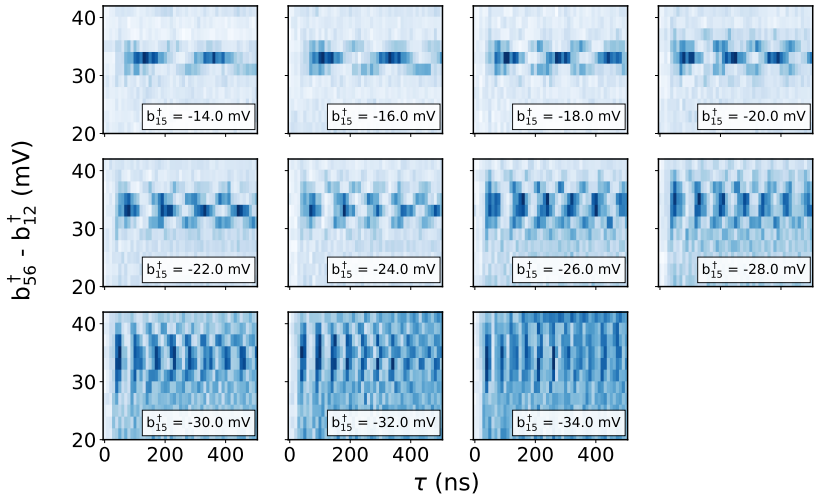

Figure 5.22: Resonant $|S_{12}T_{56}^{0}\rangle$ condition. The color scale reflects the return probability P_S^{12} like in Fig. 5.5b. We scan $b_{56}^{\dagger}$ from -7 to +3 mV while scanning $b_{12}^{\dagger}$ from -27 to -37 mV and stepping $b_{15}^{\dagger}$. The resonant condition is marked by a maximum in oscillation amplitude and a minimum in oscillation frequency. We observe a stable position of the resonant condition as we decrease the voltage on $b_{15}^{\dagger}$ showing that J_{12} and J_{56} remain unaltered (or more specifically, that $J_{56} - J_{12}$ remains unaltered). The chevron pattern we observe becomes broader as we decrease $b_{15}^{\dagger}$ which is expected as the off diagonal term in the reduced 4-spin Hamiltonian increases.

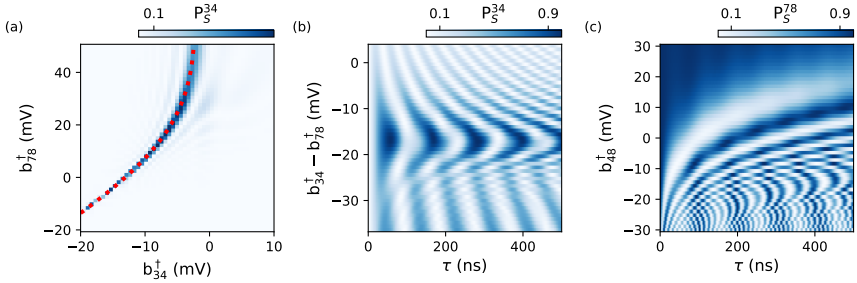

Figure 5.23: Simulations of the chain spanned by dots 3-4-8-7. (a) We plot the simulated singlet return probability P_S^{34} as a function of $b_{34}^\dagger$ and $b_{78}^\dagger$ with an exchange opened between spins 4 and 8. The red dotted line is the same as in Fig. 5.5a of the main text and marks the condition $|J_{34} - E_{Z34}| = |J_{78} - E_{Z78}|$. We find excellent agreement with the data. (b) Resonant $S_{34}T_{78}^-$ condition. We sweep $b_{34}^\dagger$ and $b_{78}^\dagger$ like in the experiment in Fig. 5.5b and report P_S^{34} finding again good agreement with the data. The leakage features for low values of $b_{34}^\dagger - b_{78}^\dagger$ are not prominent in the experiment which we attribute to a low sensor contrast. (c) Resonant $S_{34}T_{78}^-$ oscillations as a function of $b_{48}^\dagger$ at the resonant ST^- condition. This time we report P_S^{78} as in the experiment. The simulation matches the experiment in Fig. 5.5c very well.

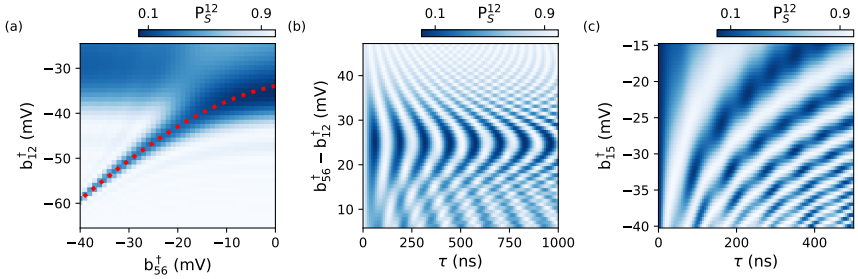

Figure 5.24: Simulations of the chain spanned by dots 2-1-5-6. (a) We plot the simulated singlet return probability P_S^{12} as a function of $b_{56}^\dagger$ and $b_{12}^\dagger$ with an exchange opened between spins 1 and 5. The red dotted line is the same as in Fig. 5.5e of the main text and marks the condition $|J_{12} - E_{Z12}| = |J_{56} - E_{Z56}|$. We find good agreement with the data. (b) Resonant $S_{12}T_{56}^-$ condition. We sweep $b_{56}^\dagger$ and $b_{12}^\dagger$ like in the experiment in Fig. 5.5f and again report P_S^{12} finding again good agreement with the data. For low values of $b_{56}^\dagger - b_{12}^\dagger$ we can also observe leakage features due to ST^0 oscillations in Q_{12}, just like in the experiment. (c) Resonant $S_{12}T_{56}^0$ oscillations as a function of $b_{15}^\dagger$ at the resonant ST^0 condition. The simulation matches the experiment in Fig. 5.5g very well.

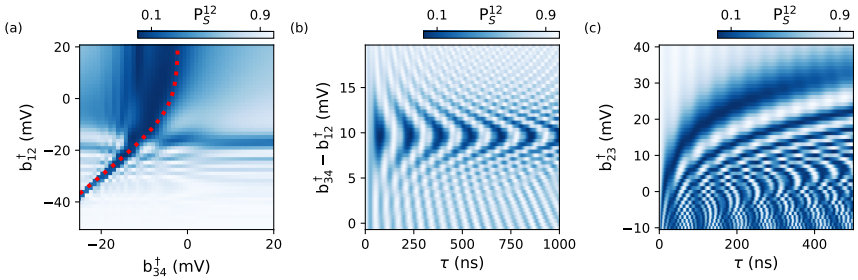

Figure 5.25: Simulations of the chain spanned by dots 1-2-3-4. (a) We plot the simulated singlet return probability P_S^{12} as a function of $b_{34}^\dagger$ and $b_{12}^\dagger$ with an exchange opened between spins 2 and 3. The red dotted line is the same as in Fig. 5.5i of the main text and marks the condition $|J_{34} - E_{Z34}| = |J_{12} - E_{Z12}|$. We find good agreement with the data. (b) Resonant $S_{12}\,T_{34}^-$ condition. We sweep $b_{34}^\dagger$ and $b_{12}^\dagger$ like in the experiment in Fig. 5.5j and report P_S^{12} finding again good agreement with the data except for the leakage features which are not present in the data, probably due to low visibility. (c) Resonant $S_{12}\,T_-^{34}$ oscillations as a function of $b_{23}^\dagger$ at the resonant ST^- condition. The simulation matches the experiment in Fig. 5.5k well.

BIBLIOGRAPHY

[1] P. Stano and D. Loss. “Review of performance metrics of spin qubits in gated semiconducting nanostructures”. *Nature Reviews Physics* 4.10 (2022), pp. 672–688.

[2] G. Burkard et al. “Semiconductor spin qubits”. *Reviews of Modern Physics* 95.2 (2023), p. 025003.

[3] P. Barthelemy and L. M. K. Vandersypen. “Quantum Dot Systems: a versatile platform for quantum simulations”. *Annalen der Physik* 525.10-11 (2013), pp. 808–826.

[4] C. Volk et al. “Loading a quantum-dot based “Qubyte” register”. *npj Quantum Information* 5.1 (2019), p. 29.

[5] C. J. van Diepen et al. “Automated tuning of inter-dot tunnel coupling in double quantum dots”. *Applied Physics Letters* 113.3 (2018), p. 033101.

[6] H. Qiao et al. “Coherent Multispin Exchange Coupling in a Quantum-Dot Spin Chain”. *Physical Review X* 10.3 (2020), p. 031006.

[7] A. R. Mills et al. “Computer-automated tuning procedures for semiconductor quantum dot arrays”. *Applied Physics Letters* 115.11 (2019), p. 113501.

[8] A. S. Rao et al. “Modular Autonomous Virtualization System for Two-Dimensional Semiconductor Quantum Dot Arrays”. *Physical Review X* 15.2 (2025), p. 021034.

[9] F. Fedele et al. “Simultaneous Operations in a Two-Dimensional Array of Singlet-Triplet Qubits”. *PRX Quantum* 2.4 (2021), p. 040306.

[10] M. T. Mądzik et al. *Operating two exchange-only qubits in parallel*. 2025.

[11] K. Takeda et al. “Quantum tomography of an entangled three-qubit state in silicon”. *Nature Nanotechnology* 16.9 (2021), pp. 965–969.

[12] S. G. J. Philips et al. “Universal control of a six-qubit quantum processor in silicon”. *Nature* 609.7929 (2022), pp. 919–924.

[13] L. M. K. Vandersypen et al. “Interfacing spin qubits in quantum dots and donors—hot, dense, and coherent”. *npj Quantum Information* 3.1 (2017), p. 34.

[14] J. M. Boter. “Spiderweb Array: A Sparse Spin-Qubit Array”. *Physical Review Applied* 18.2 (2022).

[15] C.-A. Wang et al. “Operating semiconductor quantum processors with hopping spins”. *Science* 385.6707 (2024), pp. 447–452.

[16] N. W. Hendrickx et al. “A four-qubit germanium quantum processor”. *Nature* 591.7851 (2021), pp. 580–585.

[17] M. T. Mądzik et al. “Precision tomography of a three-qubit donor quantum processor in silicon”. *Nature* 601.7893 (2022), pp. 348–353.

[18] C. A. Stafford and S. Das Sarma. “Collective Coulomb blockade in an array of quantum dots: A Mott-Hubbard approach”. *Physical Review Letters* 72.22 (1994), pp. 3590–3593.

[19] T. Hensgens et al. “Quantum simulation of a Fermi–Hubbard model using a semiconductor quantum dot array”. *Nature* 548.7665 (2017), pp. 70–73.

[20] E. Barnes, J. M. Nichol, and S. E. Economou. “Stabilization and manipulation of multispin states in quantum-dot time crystals with Heisenberg interactions”. *Physical Review B* 99.3 (2019), p. 035311.

[21] J. P. Dehollain et al. “Nagaoka ferromagnetism observed in a quantum dot plaquette”. *Nature* 579.7800 (2020), pp. 528–533.

[22] R. E. Throckmorton and S. Das Sarma. “Studying many-body localization in exchange-coupled electron spin qubits using spin-spin correlations”. *Physical Review B* 103.16 (2021), p. 165431.

[23] X. Wang et al. “Experimental realization of an extended Fermi-Hubbard model using a 2D lattice of dopant-based quantum dots”. *Nature Communications* 13.1 (2022), p. 6824.

[24] J. Knörzer et al. “Long-range electron-electron interactions in quantum dot systems and applications in quantum chemistry”. *Physical Review Research* 4.3 (2022), p. 033043.

[25] D. Buterakos and S. Das Sarma. “Magnetic phases of bilayer quantum-dot Hubbard model plaquettes”. *Physical Review B* 108.23 (2023), p. 235301.

[26] C.-A. Wang et al. “Probing resonating valence bonds on a programmable germanium quantum simulator”. *npj Quantum Information* 9.1 (2023), p. 58.

[27] A. Nico-Katz et al. *Identifying Many-Body Localization in Realistic Dot Arrays*. 2023.

[28] C. J. van Diepen et al. “Quantum Simulation of Antiferromagnetic Heisenberg Chain with Gate-Defined Quantum Dots”. *Physical Review X* 11.4 (2021), p. 041025.

[29] M. Lodari et al. “Low percolation density and charge noise with holes in germanium”. *Materials for Quantum Technology* 1.1 (2021), p. 011002.

[30] F. Vigneau et al. “Probing quantum devices with radio-frequency reflectometry”. *Applied Physics Reviews* 10.2 (2023), p. 021305.

[31] T.-K. Hsiao et al. “Exciton Transport in a Germanium Quantum Dot Ladder”. *Physical Review X* 14.1 (2024), p. 011048.

[32] X. Zhang et al. “Universal control of four singlet–triplet qubits”. *Nature Nanotechnology* 20.2 (2025), pp. 209–215.

[33] J. Levy. “Universal Quantum Computation with Spin-$1/2$ Pairs and Heisenberg Exchange”. *Physical Review Letters* 89.14 (2002), p. 147902.

[34] J. R. Petta et al. “Coherent Manipulation of Coupled Electron Spins in Semiconductor Quantum Dots”. *Science* 309.5744 (2005), pp. 2180–2184.

[35] D. Jirovec et al. “A singlet-triplet hole spin qubit in planar Ge”. *Nature Materials* 20.8 (2021), pp. 1106–1112.

[36] D. Loss and D. P. DiVincenzo. “Quantum computation with quantum dots”. *Physical Review A* 57.1 (1998), pp. 120–126.

[37] Z. Zhou et al. “The exchange interaction between neighboring quantum dots: physics and applications in quantum information processing”. *Journal of Semiconductors* 45.10 (2024), p. 101701.

[38] F. Martins et al. “Noise Suppression Using Symmetric Exchange Gates in Spin Qubits”. *Physical Review Letters* 116.11 (2016), p. 116801.

[39] D. Jirovec et al. “Dynamics of Hole Singlet-Triplet Qubits with Large g-Factor Differences”. *Physical Review Letters* 128.12 (2022), p. 126803.

[40] J. Saez-Mollejo et al. “Exchange anisotropies in microwave-driven singlet-triplet qubits”. *Nature Communications* 16.1 (2025), p. 3862.

[41] P. M. Mutter. “All-electrical control of hole singlet-triplet spin qubits at low-leakage points”. *Physical Review B* 104.19 (2021).

[42] D. J. Niegemann et al. *Parity and singlet-triplet high fidelity readout in a silicon double quantum dot at 0.5 K*. 2022.

[43] L. Mauro et al. “Geometry of the dephasing sweet spots of spin-orbit qubits”. *Physical Review B* 109.15 (2024), p. 155406.

[44] W. Ha et al. “A Flexible Design Platform for Si/SiGe Exchange-Only Qubits with Low Disorder”. *Nano Letters* 22.3 (2022), pp. 1443–1448.

[45] A. J. Weinstein et al. “Universal logic with encoded spin qubits in silicon”. *Nature* 615.7954 (2023), pp. 817–822.

[46] H. C. George et al. “12-Spin-Qubit Arrays Fabricated on a 300 mm Semiconductor Manufacturing Line”. *Nano Letters* 25.2 (2025), pp. 793–799.

[47] S. Geyer et al. “Anisotropic exchange interaction of two hole-spin qubits”. *Nature Physics* 20.7 (2024), pp. 1152–1157.

6

SITE-RESOLVED MAGNON AND TRIPLON DYNAMICS ON A PROGRAMMABLE QUANTUM DOT SPIN LADDER

Quasi-particle dynamics in interacting systems in the presence of disorder challenges the notion of internal thermalization, but proves difficult to investigate theoretically for large particle numbers. Engineered quantum systems may offer a viable alternative, as witnessed in experimental demonstrations in a variety of physical platforms, each with its own capabilities and limitations. Semiconductor gate-defined quantum dot arrays are of particular interest since they offer both a direct mapping of their Hamiltonian to Fermi-Hubbard and Heisenberg models and the in-situ tunability of (magnetic) interactions and onsite potentials. In this work, we use an array of germanium quantum dots to simulate the dynamics of both single-spin excitations (magnons) and two-spin excitations (triplons). We develop a methodology that combines digital spin qubit operations for state preparation and readout with analog evolution under the full system Hamiltonian. Using these techniques, we can reconstruct quantum walk plots for both magnons and triplons, and for various configurations of Heisenberg exchange couplings. We furthermore explore the effect of single-site disorder and its impact on the propagation of spin excitations. The obtained results can provide a basis for simulating disorder-based solid-state phenomena such as many-body localization.

This chapter has been published as: **Pablo Cova Fariña**, Daniel Jirovec, Xin Zhang, Elizaveta Morozova, Stefan D. Oosterhout, Stefano Reale, Tzu-Kan Hsiao, Giordano Scappucci, Menno Veldhorst & Lieven M. K. Vandersypen, "Site-resolved magnon and triplon dynamics on a programmable quantum dot spin ladder", arXiv:2506.08663 (2025).

6.1. INTRODUCTION

The observation of correlated many-body phenomena is one of the most promising applications of quantum simulators [1–3]. For example, studying the dynamics of spin excitations under a given many-body spin model can provide insight into the system's underlying Hamiltonian and its magnetic properties. A fascinating open question pertains to the properties of isolated quantum systems in the presence of disorder, which competes with interactions and can significantly alter the propagation of spin excitations or the thermalization properties of the system [4]. While different simulator platforms have implemented this Hamiltonian class [5–12], a rigorous study of such models ideally requires precise tunability of both spin-spin interactions and single-site disorder, as well as reliable initialization and readout of the spin states with single-site resolution. When comparing different quantum simulation platforms, atomic systems [13–16] can reach large sizes but are often limited in their local control capabilities, while solid-state-based systems [17–19] offer a high degree of tunability but need to tackle other challenges such as crosstalk, homogeneity and scalability.

In this context, gate-defined semiconductor quantum dots provide a versatile platform to perform quantum simulations of Fermi-Hubbard [19–23] and Heisenberg-type [24, 25] physics. Precise control of onsite energies and local couplings is routinely achieved through voltages applied on dedicated electrodes. Additionally, quantum dot arrays naturally emulate the Heisenberg model at half filling, making them a promising candidate for simulating spin physics. Among the available semiconductor platforms, Ge/SiGe quantum dots have been rapidly scaled up in recent years [26–31], enabling the fabrication of 2D quantum dot arrays and device sizes approaching the many-body regime. Moreover, significant variations of the g-tensors of hole spins in germanium quantum dots and their principal axes are commonly observed, which has enabled qubit addressability for spin-qubit experiments [31, 32]. In the context of this work, this g-tensor variability also provides a native realization of random single-site disorder. Finally, individual spin exchange couplings, arising due to wavefunction overlap between neighboring dots, can be quickly turned on or off by gate voltage pulses, in principle allowing to observe the evolution of the system after a Hamiltonian quench.

In this work, we explore the dynamics of two kinds of spin excitations, namely magnons and triplons, and their propagation for different exchange coupling configurations in a semiconductor 2×4 quantum dot ladder. For this purpose, we use an analog-digital experimental framework [33, 34]. For initialization and readout, we combine quantum gates and transitions with a controlled degree of adiabaticity, which allows us to prepare spin excitations on arbitrary sites and track their position over time. In between, we allow the system to evolve under its native Hamiltonian. We first investigate the dynamics of single-spin excitations, or magnons, under different coupling topologies and disorder-to-interaction ratios, for which we leverage on a recently developed crosstalk mitigation protocol for exchange couplings in dense quantum dot arrays [35]. We develop methods to prepare a magnon in any site of the ladder and probe the presence of a magnon in a site-resolved manner, allowing us to reconstruct quantum walks [36–38]. Next, we study the propagation of two-spin excitations, or triplons [39–41], along a chain of dimerized sites, building on previous work on singlet-triplet qubit control across a quantum dot ladder [42]. We demonstrate a method to initialize a triplon in any site,

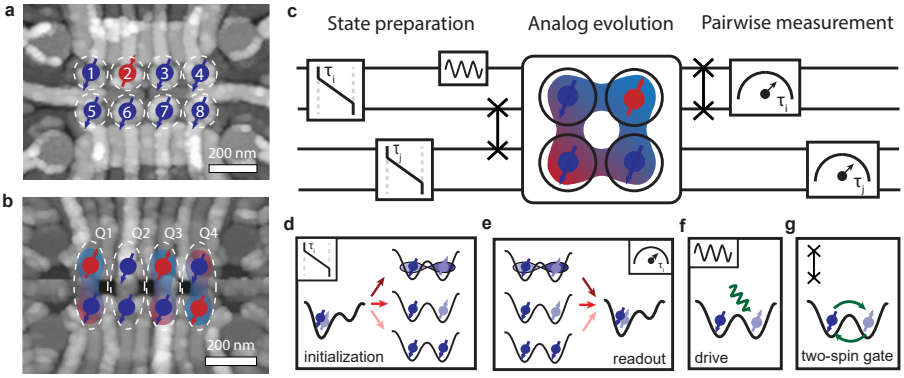

Figure 6.1: Atomic-force microscopy images of the two germanium 2×4 quantum dot devices used in this work. Spins are schematically depicted to highlight the two different types of encoding: (a) single-spin and (b) singlet-triplet. (c) Schematics of a digital-analog circuit: During the state preparation and readout phases, performed in the computational (Zeeman) basis, a combination of ramp times τ_i of the interdot detunings with single- and two-qubit gates allows the preparation of a variety of states as well as the extraction of single-site spin information. During the analog evolution part, spin-exchange couplings can be diabatically or adiabatically turned on, resulting in spin dynamics under the system's native Hamiltonian, as described in the main text. Schematic depiction of (d) initialization (see main text), (e) readout (see main text), (f) single-spin drive using microwaves and (g) two-spin gates based on Heisenberg exchange utilized in this work.

fully and independently tune interactions and on-site disorder, and detect the presence or absence of a triplon on three sites in a single-shot manner.

6.2. DEVICE AND MODE OF OPERATION

Fig. 6.1a and b show two atomic-force microscopy images of the two Ge/SiGe 2×4 quantum dot devices used in this work. While Fig. 6.1a corresponds to the device used for the magnon propagation experiments (Sections 6.4 and 6.5), we use the device in Fig. 6.1b to explore triplon propagation in the singlet-triplet basis (Section 6.6). On this same device, universal control of four singlet-triplet qubits was previously demonstrated [42].

The device of Fig. 6.1a incorporates a few small but relevant changes with respect to the previous version [42]. First, the barrier gates are patterned in the first metal layer to increase their lever arm and, consequently, the ability to tune the exchange interaction strengths. Additionally, the charge sensors, used for tuning and readout purposes, are not tunnel coupled to the device while maintaining a high capacitive coupling, which improved the sensing dot tunability (see Fig. 6.10 for details on the device layout).

We operate both devices in a mixed analog-digital fashion (Figs. 6.1 c-g). We rely on pairwise spin initialization and readout based on Pauli-spin blockade (PSB) by controlling the ramp speed between the (2,0) and (1,1) states (see Section 6.4), where (n_l, n_r) represent the number of charges in the left and right dot of a quantum dot pair. Although the key element of these experiments is the analog evolution part, we also employ single- and two-qubit gates as a means to quickly and reliably prepare any desired initial state relevant for this work, and to access additional readout bases. Note that for this particular work, microwave driving is only used for qubit spectroscopy, since we operate at a

low magnetic field of 10 mT, where microwave-driven gates are slow [43–46].

6.3. SPIN HAMILTONIANS

The Hamiltonian of an array of quantum dots with a single spin per site and an external magnetic field B is given by a Heisenberg model with exchange interactions J_{ij} and site-dependent g-factors g_i:

$$H_0 = \sum_{\langle i,j \rangle} J_{ij} \mathbf{S_i} \cdot \mathbf{S_j} + \mu_B B \sum_i g_i S_i^z, \tag{6.1}$$

where the first sum runs only over nearest neighbors i and j, $\mathbf{S_i}$ is the vector of spin operators $(S_i^x, S_i^y, S_i^z) = \frac{\hbar}{2}(\sigma_i^x, \sigma_i^y, \sigma_i^z)$, using the Pauli matrices for each spin i. For holes in germanium quantum dots, this Hamiltonian is only an approximation, neglecting the tensorial nature of J_{ij} and g_i [47]. These terms, and additional intrinsic spin-orbit spin flip components, are typically captured by an additional term of the form $\sum_i \Delta_{ST,i} S_{x,i}$, with Δ_{ST} the spin-orbit strength, a term we will exploit for initialization and readout but ignore during the analog evolution. Despite these simplifications, the Hamiltonian of Eq. 6.1 suffices to model the experimental data revealing magnon propagation, see also the discussion in Section 6.7. Important for studies of spin dynamics, the spin exchange interactions are individually tunable through the gate voltage that controls the interdot tunnel coupling. Also the individual g-tensors have been demonstrated to be electrically tunable by modulating the shape of the quantum dot wavefunction [27, 28, 46, 48]. However, this tunability is often hard to predict in practice since it is highly dependent on microscopic device details.

Next we consider an array of singlet-triplet qubits, where each rung i of the ladder encodes a single qubit in the singlet-triplet basis (see Fig. 6.1b). When projected onto the S-T$^-$ subspace, the coupling Hamiltonian of two singlet-triplet qubits can be mapped to [42]:

$$\begin{aligned} H_{ST} = &\frac{1}{4} \sum_{\langle i,j \rangle} J_{ij}^{\parallel} \left[\sigma_i^x \sigma_j^x + \sigma_i^y \sigma_j^y + \frac{1}{2} \left(\sigma_i^z - I \right) \left(\sigma_j^z - I \right) \right] \\ &+ \frac{1}{2} \sum_i (\bar{E}_{z,i} - J_i^{\perp}) \sigma_i^z, \end{aligned} \tag{6.2}$$

where $J_{ij}^{\parallel}$ and $J_i^{\perp}$ are the exchange couplings between different rungs i, j and within each rung i, respectively. In this case, single-site energy terms become programmable by means of $J_i^{\perp}$. Note that in Eq. 6.2 we also neglect the spin-orbit coupling (SOC) terms [42], which would result in deviations from the isotropic behavior. This is only valid far from the spin-orbit induced avoided crossings, which is the case during the analog evolution part. In contrast, for initialization and readout, we explicitly pulse to the spin-orbit induced S-T$^-$ avoided crossing to achieve single-qubit rotations (see Section 6.6).

Interestingly, the interaction terms of Eqs. 6.1 and 6.2 realize two different spin XXZ Hamiltonians of the form

$$H_{\text{int}} \propto \sum_{\langle i,j \rangle} \left[\sigma_i^x \sigma_j^x + \sigma_i^y \sigma_j^y + \Delta \sigma_i^z \sigma_j^z \right], \tag{6.3}$$

Encoding	Single-spin	Singlet-triplet
Number of sites for N dots	N	$N/2$
Interaction Hamiltonian (neglecting SOC)	XXX ($\Delta = 1$)	XXZ ($\Delta = 0.5$)
Interaction tunability	Yes	Yes
Disorder source	g-factor variability	$\tilde{E}_z - J^{\perp}$
Disorder tunability	Global (B-field) Limited local tunability (g-tensor modulation)	Yes
Site-resolved readout	PSB + SWAP	PSB

Table 6.1: Comparison between single-spin and singlet-triplet encodings.

with Δ the anisotropy parameter [36]. While Eq. 6.1 is a Heisenberg or XXX Hamiltonian with $\Delta = 1$, in the triplon case we find $\Delta = 0.5$ (Eq. 6.2). Table 6.1 summarizes both encodings.

6.4. STATE INITIALIZATION AND READOUT

Fig. 6.2a shows the typical energy diagram of a germanium double quantum dot [27, 49] as a function of detuning $\varepsilon_{ij} = \frac{1}{2}(\mu_j - \mu_i)$, with μ_i the electrochemical potentials of two neighboring dots i and j. This energy diagram is simulated using the lowest energy levels of a two-site Fermi-Hubbard model (see Eq. 6.4 of the Supplementary Material). The detuning axis is chosen such that the total charge occupation of the system is conserved. At the symmetry point $\varepsilon_{ij} = 0$, there is one charge per quantum dot (charge state (1,1)) and, at small tunnel coupling values t_{ij}, the spin eigenstates are the four product states $\{|\downarrow\downarrow\rangle, |\uparrow\downarrow\rangle, |\downarrow\uparrow\rangle, |\uparrow\uparrow\rangle\}$. Away from $\varepsilon = 0$ (leaving out the subscripts for simplicity), the wavefunction overlap between the two charges increases, resulting in an increased exchange coupling J. The spin-orbit induced anticrossing between the singlet and triplet branches occurs at $J = \tilde{E}_z$. Finally, at very positive or negative detuning, with absolute values larger than the quantum dot charging energies, both charges sit on the same quantum dot, and the ground state of the system is a singlet (S(2,0) or S(0,2), respectively).

The initialization procedure is derived from this energy diagram. Starting from S(2,0), we ramp to the symmetry point at $\varepsilon = 0$ with a ramp time τ. Crucially, the state we initialize depends on the ramp rate $v = \frac{dE}{d\tau}$ and two relevant energy scales: the S-T$^-$ anticrossing size Δ_{ST} and the Zeeman energy difference between the two dots ΔE_z [50, 51].

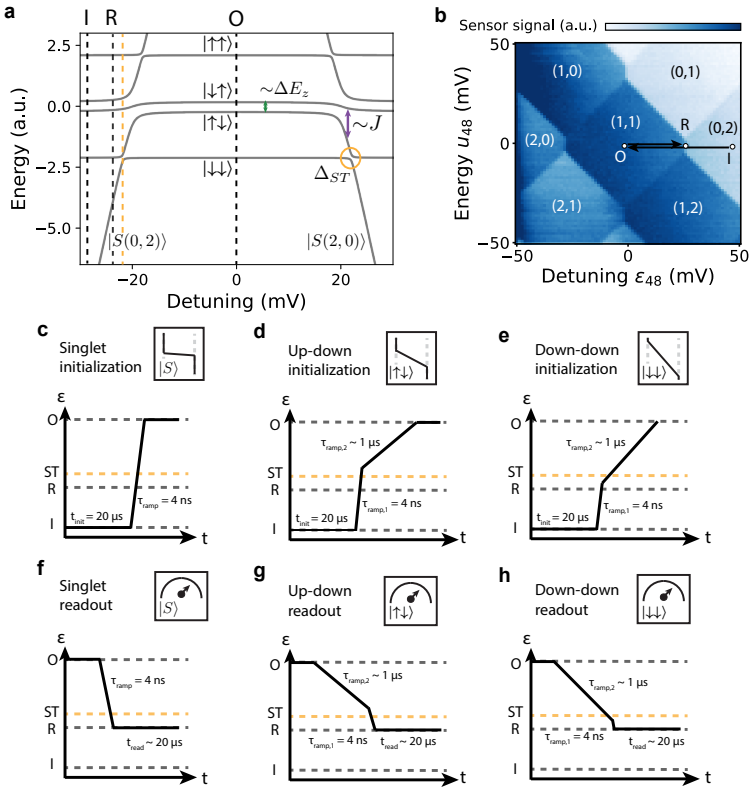

Figure 6.2: Pairwise initialization and readout of a pair of hole spins. (a) Energy diagram for a pair of spins. The black dashed lines represent the initialization (I), operation (O) and readout (R) points, respectively. The S-T$^-$ anticrossing is highlighted in yellow. (b) Charge stability diagram of quantum dot pair 4-8. Along the x-axis, we scan the detuning $\varepsilon_{48} = \frac{1}{2}(vp_8 - vp_4)$, and the global chemical potential $u_{48} = vp_8 + vp_4$ is scanned along the y-axis. For each combination of gate voltages, we record the sensor signal. The numbers (n_1, n_2) represent the double dot charge occupation. The three voltage points I (initialization), O (operation) and R (readout) lie along the detuning axis and are calibrated for each quantum dot pair. (c) Pulse scheme to initialize the state $|S(1,1)\rangle$. After waiting 20 µs at point I to initialize the state $|S(2,0)\rangle$, we pulse to the operation point with a ramp speed of 4 ns, which is diabatic and conserves the total spin state. (d) Pulse scheme to initialize the state $|\uparrow\downarrow\rangle$. After waiting 20 µs at point I, we first pulse fast (4 ns) just over the ST$^-$ anticrossing (shown as a yellow dashed line), conserving the spin singlet state. Subsequently, a slow (∼ 1 µs ramp) is used, which adiabatically maps the singlet into the $|\uparrow\downarrow\rangle$ state. (e) Pulse scheme to initialize the state $|\downarrow\downarrow\rangle$. After waiting 20 µs at point I, we first pulse fast (4 ns) just before the ST$^-$ anticrossing. Subsequently, a slow (∼ 1 µs ramp) is used, which adiabatically maps the singlet into the $|\downarrow\downarrow\rangle$ state. (f) Pulse scheme to readout a singlet state $|S(1,1)\rangle$. (g) Pulse scheme to readout the state $|\uparrow\downarrow\rangle$. (h) Pulse scheme to readout the state $|\downarrow\downarrow\rangle$.

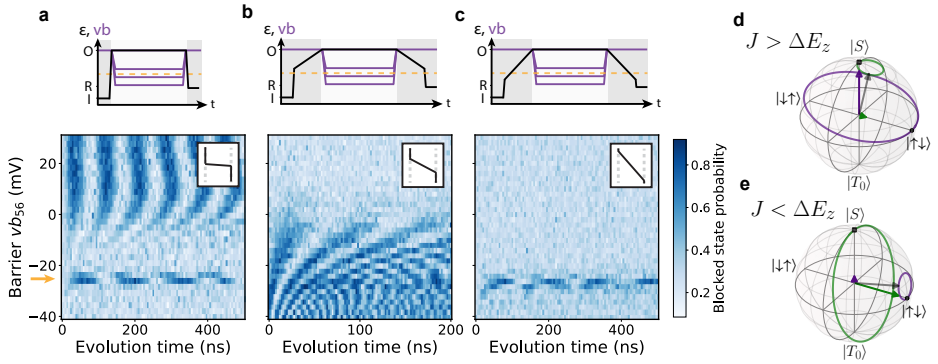

Figure 6.3: Experimentally observed dynamics of the spin state of quantum dot pair 5-b, as a function of initialization and readout ramp speed, and as a function of barrier voltage vb_{56}. (a) A singlet is initialized and read out using pulse schemes of Fig. 6.2c,f. S-T^0 oscillations are visible at low exchange (positive barrier voltage). Additional oscillations at high exchange (negative barrier voltage) are consistent with an evolution at the S-T^- anticrossing. (b) The state $|\uparrow\downarrow\rangle$ is initialized and read out using pulse schemes of Fig. 6.2d,g. Exchange oscillations are visible at high values of J. (c) The state $|\downarrow\downarrow\rangle$ is initialized and read out using pulse schemes of Fig. 6.2e,h. The only observed dynamics is at the S-T^- anticrossing. The diagrams above the data schematically show the corresponding pulse schemes for both detuning (black lines) and barrier voltage (purple lines). The gray shaded regions correspond to initialization and readout. (d) Bloch sphere depiction of the time evolution of a singlet and a $|\uparrow\downarrow\rangle$ state for an interaction-dominated Hamiltonian ($J > \Delta E_z$). (e) Bloch sphere depiction of the time evolution of a singlet and a $|\uparrow\downarrow\rangle$ state for a disorder-dominated Hamiltonian ($J < \Delta E_z$).

Using realistic experimental parameters, we simulate the initialized states as a function of ramp speed (Fig. 6.15) and recognize three distinct regimes. At diabatic ramp speeds $\hbar v \gg \Delta E_z^2$, $\hbar v \gg \Delta_{ST}^2$, the initial spin state is conserved, resulting in the state $S(1,1)$. In contrast, at adiabatic speeds, the ground state of the system $|\downarrow\downarrow\rangle$ is initialized. At intermediate speeds, when the ramp speed is adiabatic only with respect to the Zeeman energy difference, the state $|\uparrow\downarrow\rangle$ is initialized, with the spin-up corresponding to the dot with the lowest g-factor.

The same reasoning applies to readout, which is based on Pauli spin blockade [52–57]. The ramp rate from the symmetry point to the readout point determines which two-spin state is unblocked and therefore distinguished from the three other, orthogonal, spin states. While a diabatic ramp will result in an unblocked S(1,1) state, the state $|\downarrow\downarrow\rangle$ ($|\uparrow\downarrow\rangle$) is unblocked for adiabatic (intermediate) ramp speeds. To further improve the initialization and readout fidelities, we make use of composite ramps as depicted in Figs. 6.2c-e for initialization and Figs. 6.2f-h for readout. Note that more complex ramps could be implemented to further optimize initialization and readout [58].

We experimentally demonstrate the initialization, readout and exchange control capabilities in Fig. 6.3a-c. Each of the panels shows the evolution of a two-spin initial state for quantum dot pair 56 as a function of its corresponding virtual barrier [35] voltage vb_{56} for diabatic, intermediate and adiabatic initialization and readout ramps, respectively. The dynamics in Figs. 6.3a and b can be understood through a Bloch sphere representation in the S-T^0 basis [27] (Figs. 6.3d and e). At positive barrier voltages, the exchange interaction between dots is minimized ($J \ll \Delta E_z$, disorder-dominated regime) and the

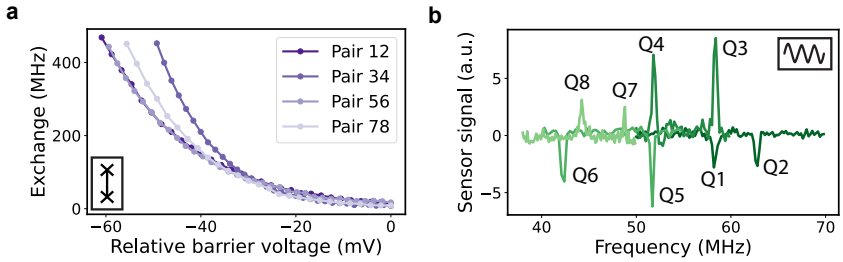

Figure 6.4: Characterization of exchange coupling and Zeeman energies for the full 4×2 array. (a) Exchange coupling tunability as a function of barrier gate voltage, extracted from Fig. 6.13. We obtain interaction strengths of up to 500 MHz and down to well below 1 MHz for each dot pair, highlighting the excellent individual tunability of the exchange couplings. In particular, we can comfortably reach the $J \gg \Delta E_z$ and $J \ll \Delta E_z$ regimes. (b) Zeeman energy extraction through EDSR. For each pair of spins, the resonances are assigned depending on the driving gate (we flipped half of the signals for clarity). This sets the single-particle disorder landscape. We find that neighboring spins differ in frequency by 5-15 MHz at a magnetic field of 10 mT.

eigenstates are well approximated by the eigenstates of the Zeeman Hamiltonian, i.e. the product states $\{|\downarrow\downarrow\rangle, |\uparrow\downarrow\rangle, |\downarrow\uparrow\rangle, |\uparrow\uparrow\rangle\}$. An initial $|S\rangle$ state, being an equal superposition of $|\uparrow\downarrow\rangle$ and $|\downarrow\uparrow\rangle$, should therefore oscillate with maximum visibility, while an initial $|\uparrow\downarrow\rangle$ state should not oscillate. The opposite behavior is expected at negative barrier voltages, i.e. high exchange couplings ($J \gg \Delta E_z$, interaction-dominated regime). In either of the two cases, the $|\downarrow\downarrow\rangle$ state should not evolve since it is an eigenstate of both the Zeeman and the Heisenberg Hamiltonians. Figs. 6.3a-c show the expected evolution patterns, highlighting not only the initialization and readout capability in different bases, but also the excellent control over the ratio between interactions and Zeeman energy differences. Note that at interaction strengths $J = \tilde{E}_z$, we observe an extra set of oscillations for all three initialized states, consistent with the position of the S-T$^-$ anticrossing, and validated through simulations (see Fig. 6.16).

We demonstrate this behavior for all four spin pairs individually (see Fig. 6.12 and 6.13) and extract exchange interaction values of up to 500 MHz and down to well below 1 MHz within a comfortable dynamical range in the barrier gate voltages of < 100 mV (Fig. 6.4a). Note that the onset of oscillations for the $|\uparrow\downarrow\rangle$ plots depends on the ΔE_z value of each pair, which differs due to the difference in g-factors. This well-known behavior for two spins forecasts a more generic behavior, where a spin excitation which can propagate along an array of spins under the influence of exchange interactions J becomes localized when disorder in the local Zeeman energies ΔE_z exceeds spin exchange.

We make use of microwave driving to extract the individual Zeeman energies via electric-dipole spin resonance (EDSR) (Fig. 6.4b). We obtain the resonance frequencies by initializing a product state for each pair and driving with different plunger gates to pinpoint which resonance line corresponds to which spin, or by measuring the exchange splitting of the resonance lines as a function of neighboring barrier voltages (see Fig. 6.26). For the applied in-plane field of 10 mT, the Zeeman energy differences are of the order of 5-15 MHz, while the Zeeman energies correspond to g-factors of $0.30 < g_i < 0.44$, slightly higher than the values reported in the literature [32]. This could

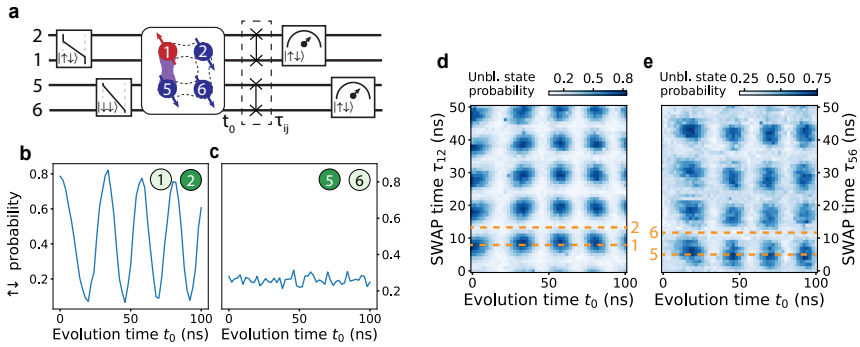

Figure 6.5: Calibration of SWAP times and reconstruction of single-site probabilities. (a) Circuit diagram for simultaneous calibration of SWAP times τ_{12} and τ_{56}. For this particular experiment, the only exchange that is switched on during the analog evolution is J_{15}. $|\uparrow\downarrow\rangle$-readout allows to obtain the spin-up probability of the quantum dot with the lowest g-factor for each pair. (b) $|\uparrow\downarrow\rangle$ probability for quantum dot pair 1-2 as a function of evolution time t_0, recorded after running the quantum circuit in panel (a) without the SWAP operations. (c) $|\uparrow\downarrow\rangle$ probability for quantum dot pair 5-6 as a function of evolution time t_0, recorded after running the quantum circuit in panel (a) without the SWAP operations. (d) and (e) Unblocked state probability for (d) pair 1-2 and (e) pair 5-6 after executing the quantum circuit of panel (a), as a function of t_0 and the SWAP times as indicated. From these 2D maps, we extract the SWAP times which correspond to spin-up readout for each of the four spins (indicated by the dashed orange lines).

be caused by misalignment of the external magnetic field, leading to a small out-of-plane field component.

6.5. SWAP GATES, SINGLE-SITE READOUT AND QUANTUM WALKS

Building on the tools for initialization and readout showcased in section 6.4, we can study the propagation of single-spin excitations or magnons in extended quantum dot arrays. The three different readout types outlined above allow us to discriminate a single unblocked two-spin state ($|S\rangle$, $|\uparrow\downarrow\rangle$ or $|\downarrow\downarrow\rangle$ respectively) from the states in its orthogonal subspace. This does not directly translate to single-spin probabilities. For instance, reading out at an intermediate ramp speed yields the probability of measuring $|\uparrow\downarrow\rangle$, but the readout signal would not distinguish between the states $|\downarrow\uparrow\rangle$, $|\downarrow\downarrow\rangle$, and $|\uparrow\uparrow\rangle$ which are all blocked. However, apart from the $|\uparrow\downarrow\rangle$ and $|\downarrow\downarrow\rangle$ readouts demonstrated in section 6.4, we can also read out the orthogonal state $|\downarrow\uparrow\rangle$ by implementing a SWAP gate before ramping to the readout point (Fig. 6.5a). Since the exchange control permits to reach $J \gg \Delta E_z$ for all dot pairs, the SWAP gate is a native two-qubit gate of the system, achievable by pulsing the barrier gates for a time $\tau_{\mathrm{SWAP}} = \pi/J$. In this way, readout of three orthogonal two-spin states is possible from which the fourth can be inferred through normalization, allowing us to reconstruct all single-spin probabilities. Importantly, if only a single excitation is present in the array, only two of the three readouts are necessary since $P(|\uparrow\uparrow\rangle) = 0$. In this case, $P(|\uparrow_i\rangle) = P(|\uparrow_i\downarrow_j\rangle)$ and $P(|\uparrow_j\rangle) = P(|\downarrow_i\uparrow_j\rangle)$. This is the case for all quantum walk data shown in Fig. 6.5 and 6.6.

In Fig. 6.5a-e, we show a method for simultaneously calibrating two SWAP gates in a four-spin system and to obtain site-resolved quantum walk plots. For this example,

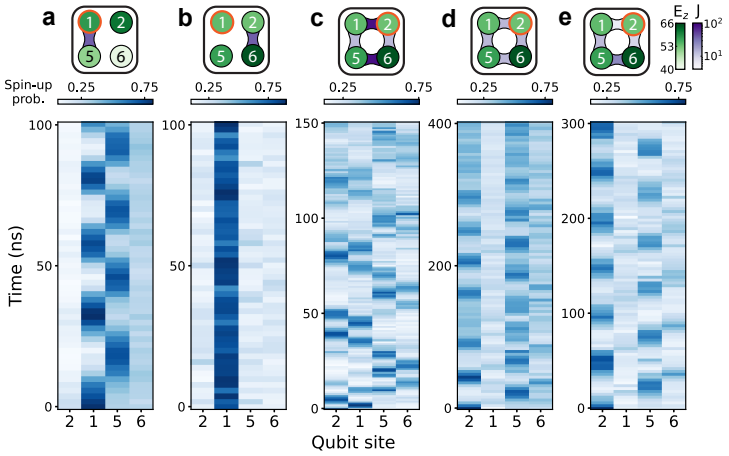

Figure 6.6: Magnon propagation for the left half of the 2×4 array with various coupling configurations. (a) Four-spin quantum walk corresponding to the circuit in Fig. 6.5a and extracted from the 2D plots pf Fig. 6.5d and e, showing evolution of the spin-up probability for the sites 2, 1, 5 and 6 as a function of t_0. For this and the following quantum walk plots, the border of the quantum dot with the initial spin-up is highlighted in orange, the magnitude of the Zeeman energies is color-coded in green, and the exchange interaction strengths in purple. (b) Four-spin quantum walk in a 2×2 array with $J_{26} \approx 40$ MHz and the other exchanges switched off. (c) Four-spin quantum walk in a configuration with $J_{12} \approx J_{56} \approx 100$ MHz and $J_{15} \approx J_{26} \approx 25$ MHz. (d) Four-spin quantum walk in a 2×2 ring with homogeneous exchange couplings ($J_{ij} \approx 21$ MHz). The excitation mainly oscillates between dots 2 and 5, a beating pattern is additionally observed. (e) Four-spin quantum walk in a 2×2 ring with disorder in the J_{ij} values, with barrier voltages slightly tuned away from the homogeneous exchange point. A rather regular oscillation pattern mainly between dots 2 and 5 is observed.

we initialize the spin state $|1\rangle = |\uparrow_1\downarrow_2\downarrow_5\downarrow_6\rangle$. During the analog evolution, the exchange coupling J_{15} is activated for a period of time t_0, which should yield a simple oscillatory pattern between spins 1 and 5. After the evolution, we either perform $|\uparrow\downarrow\rangle$-readout directly on pairs 1-2 and 5-6, or we activate the exchanges J_{12} and J_{56} for a variable time τ_{12} and τ_{56} before readout. This is depicted as a quantum circuit in Fig. 6.5a. For this four-spin experiment, the g-factor landscape corresponds to Fig. 6.4b. This means that the dots with the lowest g-factors are dot 1 for the top pair and dot 6 for the bottom pair.

When no SWAP gate is applied before readout (Figs. 6.5b and c), we observe an oscillating pattern for the top pair and a constant low probability for the bottom pair, consistent with the readout of spins 1 and 6. Figs. 6.5d and e show the measured spin probabilities as a function of time t_0 and the SWAP time before readout. At SWAP times $\tau_{ij} = 2\pi/J_{\mathrm{SWAP},ij}$, the line cuts correspond to Figs. 6.5b and c. In contrast, when $\tau_{ij} = \pi/J_{\mathrm{SWAP},ij}$, we obtain the readout of dots 2 and 5, respectively, resulting in oscillations of the bottom pair and a low constant signal for the top pair. From this 2D map, we extract the correct SWAP times and reconstruct the four-spin quantum walk in Fig. 6.6a, showing spin oscillations between sites 1 and 5, as expected. Notably, the 2D maps in Figs. 6.5d and e also contain readout probabilities of other two-spin operators for intermediate SWAP times, which might prove useful to directly obtain other observables of interest [59].

Looking closely at Figs. 6.5d,e, we observe that the oscillations as a function of SWAP time are slightly offset in phase compared to what one would ideally expect. Additionally, the oscillation frequency is below its steady value for short times t_0 in Figs. 6.5b,d,e. We attribute the former mainly to the use of 15 ns ramp times on the barrier pulses, and the latter to gate voltage pulse distortions.

This methodology allows us to experimentally observe quantum walks with different coupling topologies, where the interplay between disorder, interactions and evolution time becomes crucial. As a first example and in contrast to the free spin propagation of Fig. 6.6a, Fig. 6.6b shows an initial magnon remaining localized in quantum dot 1, in a regime where the exchange values to its nearest neighbors are much smaller than the Zeeman energy differences ($J_{12}, J_{15} \ll \Delta E_{15}, \Delta E_{12}$), favoring localization. In Fig. 6.6c, we tune the exchange couplings such that $J_{12} \approx J_{56} \approx 100$ MHz, more than an order of magnitude larger than the average Zeeman energy differences, and $J_{15} \approx J_{26} \approx 25$ MHz. We recognize two distinct oscillation frequencies: fast oscillations within each double dot pair, and a slow transfer of the spin excitation from the top to the bottom channel. This topology corresponds to two weakly coupled pairs of spins, where for the evolution time of 150 ns, the Zeeman energy disorder does not play a role (see simulations of Fig. 6.19). We observe a decay of the signal after 100 ns, consistent with a reduced coherence time at high exchange interaction values.

We furthermore explore the interesting regime in between the two aforementioned cases, where the exchange interactions and the Zeeman energy differences are similar (Figs. 6.6d and e). For Fig. 6.6d, using a previously reported method to equalize exchange interactions in a four-spin array [24, 25], we tune all $J_{ij} \sim 21$ MHz, which is about 3.5 times larger than the average disorder in Zeeman energies. We observe an oscillation pattern between quantum dots 2 and 5, as expected for a ring with homogeneous exchanges, where the initial excitation only constructively interferes on the opposite site of the array. However, we observe an additional beating pattern, which we can attribute to the underlying Zeeman energy disorder (see simulations in Figs. 6.21 and 6.22). Therefore, the observed dynamics is a consequence of the competition of both energy scales. Additionally, we leverage on our largely independent barrier control [35] to explore the effect of locally introducing disorder in the exchange interactions. We find an exchange voltage configuration which seems to compensate for the underlying Zeeman energy disorder, yielding a regular oscillation pattern between dots 2 and 5 (Fig. 6.6e). We again validate this with simulations (Figs. 6.20 and 6.22), from which we extract J_{12} =11.5 MHz, J_{56} =27.0 MHz, J_{15} =20.0 MHz and J_{26} =15.5 MHz. We further show our independent tunability of exchange interactions explicitly in Fig. 6.23 by looking at the dependence of the oscillations on barrier gate voltages, which is in good agreement with simulations.

Additionally, instead of changing the initialization ramp times to select which spin(s) to initialize in the excited state, one can also utilize the SWAP gates to move the initial excitation across the array before the analog evolution. We show this in Fig. 6.7b (with Fig. 6.7a showing the corresponding quantum circuit). For this experiment, we first prepare the full 2×4 array in the state $|2\rangle = |\downarrow_1\uparrow_2\downarrow_3 ... \downarrow_8\rangle$ in all cases, and subsequently perform selected SWAP operations to take the excitation from dot 2 to any of the seven other dots. Finally, we read out pairs 3-4 and 5-6 followed by readout of pairs 1-2 and 7-8. Without (with) the readout SWAPs, the readout returns the probability of finding the

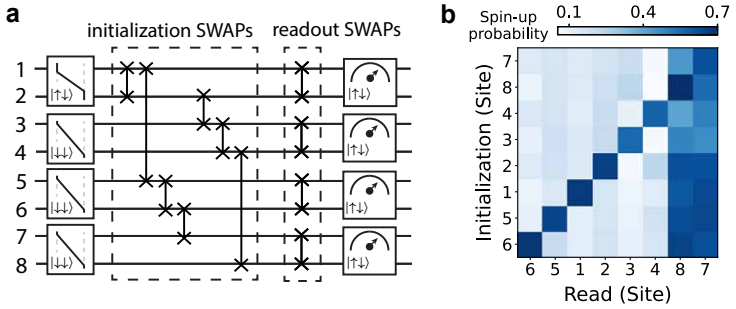

Figure 6.7: Initialization of magnon product states using SWAP gates. (a) Circuit diagram depicting the preparation of any initial state $|i\rangle$, with a single spin-up initialized in site i. After preparing the state $|2\rangle$ adjusting the speed of the initialization ramps, the single excitation is swapped around the array. Finally, the resulting state is read out. Initialization and readout happen sequentially and not simultaneously (see depiction of Fig. 6.5a, but are drawn here on top of each other for compactness. (b) Spin-up probability for the full 8-site array as a function of readout site and target initial state.

excitation in dots 1, 4, 6 and 8 (2, 3, 5 and 7). As seen in the figure, we can successfully prepare any single-magnon product state with this method, with typical SWAP times below 10 ns, and detect in which dot the magnon was initialized in two repetitions of the protocol. We note that, in this case, the contrast for the readout of dots 7 and 8 is quite low, which we attribute to a low readout visibility at the time of this measurement.

Note that these methods are not only limited to initializing single excitations but also allow to prepare up to four spin-up excitations, corresponding to a Néel state (or permutations thereof). This is demonstrated in Fig. 6.24. Furthermore, we could append an intermediate-speed ramp back to (1,1) after PSB readout, such that the post-measurement state coincides with the pre-measurement state. Applying a SWAP operation and performing another PSB readout would allow us to record both ↑↓ and ↓↑ in a single execution. Ramping back semi-adiabatically once more and reading out again but now adiabatically, would give access to all four probabilities for each pair, and thus all eight single-spin probabilities, in every run, similar in spirit to a recent demonstration on two spins [57].

6.6. QUANTUM WALK WITH SINGLET-TRIPLET ENCODING

We next turn to methods for exploring the propagation of two-spin excitations, also known as triplons [39–41], in the 2×4 quantum dot ladder. The two-spin excitation is here given by the lowest-energy spin triplet state, T^-, with two-spin singlets along the rungs of the ladder forming the ground state. Singlet-triplet physics of a pair of quantum dots and qubit encodings in the singlet-triplet basis have been widely explored in the literature [27, 42, 49]. Encoding a qubit in the S-T^- subspace has the advantage that even at low magnetic fields, fast, high-fidelity and baseband single-qubit operations are available through rotations at the S-T^- anticrossing [42], which at the 10 mT in-plane field used for this experiment are as fast as 10 MHz. Coupling two singlet-triplet qubits together results in an effective spin-spin Hamiltonian (see Eq. 6.2) where, in the lan-

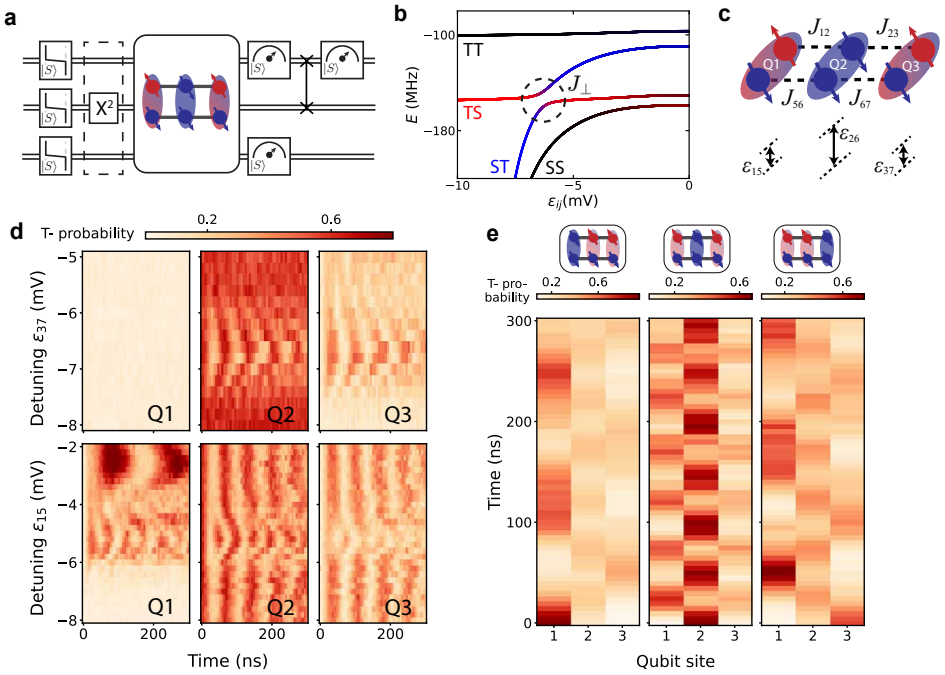

Figure 6.8: Triplon propagation in a dimerized quantum dot array. (a) Quantum circuit showing the state preparation and readout as well the analog evolution of a single triplon state. (b) Energy diagram for two coupled S-T$^-$ qubits, showing the four lowest energy branches as a function of detuning within one of the dot pairs. At a finite detuning value, an avoided crossing between the ST^- and T^-S branches occurs, the size of which is given by the average exchange coupling between both qubits. (c) Schematics of the detuning configuration at the start of the calibration procedure. (d) Two-step calibration of the homogeneous exchange point for three coupled singlet-triplet pairs. The measured T^- probability is shown for each of the three qubits (as indicated) as a function of the detuning ε_{37} (top three panels) and ε_{15} (bottom three panels), and as a function of the analog evolution time. A triplon, initially confined in Q2, can propagate to Q3 (top) and through the full three-site system (bottom) at the respective homogeneous conditions (see main text). (e) Three-site quantum walk of a single triplon, initialized on Q1, Q2 or Q3, respectively, at the homogeneous condition. The T^- probability is plotted for each of the three sites as a function of the analog evolution time.

guage of propagating spin excitations, both the interaction and the disorder terms are gate-voltage tunable. Furthermore, this encoding allows for direct site-resolved readout via PSB. All this comes at the expense of halving the number of available sites, and we will operate the device in an effective 1D configuration.

Fig. 6.8a shows a circuit diagram depicting initialization, propagation and readout of three interacting singlet-triplet qubits. The initialized state $|S_1 T_2 S_3\rangle$ corresponds to a single triplon in the center of the array. After the analog evolution, successive PSB readouts (including a SWAP operation for spin transfer) enable the retrieval of all three singlet-triplet probabilities in every single run, in principle allowing us not only to extract the individual single-qubit probabilities, but also all spin-spin correlation terms $C_{ij} = P^T_{i,j} - P^T_i P^T_j$ [36], where P^T_i is the probability of finding a triplon in site i, and $P^T_{i,j}$ is the joint probability of finding triplons in sites i and j.

To observe magnon propagation without disorder, the terms $\propto S_{z,i}$ in Eq. 6.2 should be made equal for all pairs. This effectively requires satisfying the condition of Eq. 6.8 for all qubit pairs (i, j), which we call the homogeneous condition. For two qubits, this reduces to $\tilde{E}_{z,i} - J^{\perp}_i = \tilde{E}_{z,j} - J^{\perp}_j$, corresponding to the avoided crossing of Fig. 6.8b, where we depict the energy levels of the S-T$^-$ subspace of two qubits as a function of the inter-dot detuning within each pair, which we use to control the respective exchanges. At this avoided crossing, coherent $|ST^-\rangle \leftrightarrow |T^-S\rangle$ oscillations can be induced, with a frequency given by the average $J^{\parallel}_{ij}$ between the pairs [42].

To tune to the homogeneous condition and enable magnon propagation through the array, we resort to an iterative method, illustrated in Fig. 6.8c and d. First, we start with a detuning configuration away from the symmetry point $\varepsilon_{26} > \varepsilon_{15}, \varepsilon_{37}$, where the perpendicular exchange coupling corresponding to Q2 is the largest (Fig. 6.8c). Next, we scan the detuning ε_{37}, effectively increasing $J^{\perp}_3$. We observe coherent oscillations between Q2 and Q3 (top right panels of Fig. 6.8d), which display a minimum frequency and a maximum visibility at the homogeneous condition. These are only visible in the Q2 and Q3 readout signals, as expected. Next, we fix the detuning values for Q2 and Q3 at this voltage point and scan ε_{15}. Away from the homogeneous condition, the speed of the Q2-Q3 oscillations remain unchanged, as expected. At the homogeneous condition point for all three qubits, a second set of oscillations is visible, which can now also be seen in the Q1 readout signal. This is a signature that the excitation that was first confined to pairs 2 and 3 can propagate all the way to pair 1. Again, at the minimum oscillation speed, all disorder (single-particle) terms are equal and the propagation speed is only given by the exact values of $J^{\parallel}_{ij}$. Note that the second set of oscillations visible in the bottom left panel of Fig. 6.8d corresponds to single-qubit rotations of Q1 (i.e. when $\tilde{E}_{z,1} = J^{\perp}_1$), which occur well outside the homogeneous point, not affecting the magnon propagation. The data shown in Fig. 6.8d correspond to tuning three singlet-triplet pairs, but this iterative method can be extended to larger arrays (see Fig. 6.30 for data on four pairs).

Fig. 6.8e shows quantum walk plots for three coupled pairs at the homogeneous condition. In each plot, a single triplon is initialized in different positions in the array. In this case, the readout fidelity of Q3 is significantly lower than that of Q1 and Q2, which explains the difference in oscillation amplitude between the columns. Simulating the quantum walk data with Eq. 6.2 yields an excellent agreement (see Fig. 6.27) and we extract $J^{\parallel}_{12} \approx J^{\parallel}_{23} = 14$ MHz. Additionally, we can extract all correlations C_{ij} as shown in

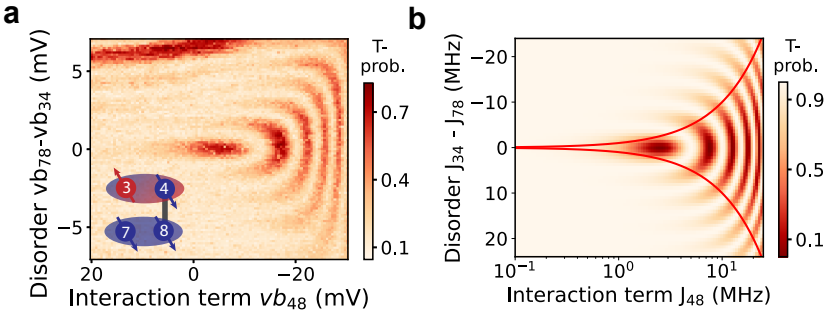

Figure 6.9: Demonstration of independent interaction and disorder tunability for two coupled S-T$^-$ qubits. (a) Two-site "phase diagram" as a function of interactions (vb_{48}, tuning $J_\parallel$ in Eq. 6.2) and disorder (vb_{78} and vb_{34}, controlling $\tilde{E}_z - J_\perp$). After initializing a state $|ST^-\rangle$ and allowing it to evolve for a fixed duration of 200 ns, we retrieve the top site T^- probability for different values of vb_{48} and vb_{78}-vb_{34}. (b) Simulated evolution of an initial state $|ST^-\rangle$ under the Hamiltonian of Eq. 6.2. The x-axis corresponds to the coupling term $J_\parallel = J_{48}$, while on the y-axis, the difference in single-site disorder is scanned using the exchange couplings $J_{\perp,1} = J_{34}$ and $J_{\perp,2} = J_{78}$. The simulated pattern is in good agreement with the experimental results. In addition, the red line corresponds to the "phase boundary" where the single-site disorder is equal to the exchange coupling strength.

Fig. 6.28. As an example, the correlation value C_{13} in Fig. 6.28b is negative at the point where the triplon is delocalized between sites 1 and 3: if it is measured to be in site 1, it will not appear in site 3, and vice versa. This is consistent with the expected generation of entanglement between Q1 and Q3, though measurements in additional bases would be needed to confirm the presence of entanglement [42].

Finally, we explicitly demonstrate the tunability of interactions and disorder in Fig. 6.9a. For a two-site system (as depicted on the figure inset), we initialize $|ST^-\rangle$ and evolve for a fixed duration of 200 ns, before retrieving the triplet probability of the top channel. We do so as a function of virtual barrier voltage vb_{48}, which controls the coupling J_{48} between the two sites, and barriers vb_{34} and vb_{78} which control J_{34} and J_{78}, respectively, and therefore the single-site disorder for the top and bottom sites. At the relative value $vb_{78}-vb_{34} = 0$, the system is at the homogeneous condition with no disorder between the two sites, and oscillations are observed for a wide range of values of vb_{48}. As vb_{78} and vb_{34} are asymmetrically scanned away from zero, the single-site disorder between the two sites increases, leading to localization of the triplon for small J_{48} (positive vb_{48}). Only when J_{48} is large enough to overcome disorder (negative vb_{48}), the triplon propagates. Note that there is an extra line of high triplet probability on the top right corner of the plot, consistent with the S-T$^-$ anticrossing of quantum dot pair 3-4. Overall, this plot can be viewed as a two-site phase diagram, and highlights the independent tunability of the interaction and single-site disorder terms. This measurement is in good agreement with the simulated results (Fig. 6.9b), where the solid red line represents the points in the phase diagram where interaction and disorder terms are equal, serving as a "phase boundary" between the interaction-dominated and the disorder-dominated regimes (see Fig. 6.29 for more information on the simulation).

6.7. DISCUSSION AND OUTLOOK

In this work, we have observed the dynamics of spin excitations as they propagate through an array of exchange-coupled quantum dots. We expand upon the methodologies for initialization, manipulation and readout of germanium quantum dot spin qubits, while also building on analog simulation techniques for semiconductor quantum dot arrays. This analog-digital framework has allowed us to initialize, control and track the propagation of excitations in an extended quantum dot array, while maintaining a high degree of control over individual Hamiltonian parameters. This highlights the power offered by the combination of analog and digital techniques for quantum simulations with quantum dots. By exploring two different types of spin excitations, magnons and triplons, we present the advantages, operation techniques and challenges of both approaches.

We note that in the present work we neglected the tensorial components of the exchange interaction terms, as similarly done in a related work [25]. Since we are able to model the quantum walk plots with an isotropic model, we speculate that this anisotropy is either small for our particular device, or that we successfully avoid unwanted rotations on any spin-orbit induced anticrossing in the full energy spectrum during the analog evolution. Although outside the scope of this work, and since these effects might become more relevant for larger arrays or more complex geometries, we encourage further research to quantitatively and systematically model and measure the J-tensor of coupled germanium quantum dots, as done in the literature for hole spins in silicon dots [60]. In this regard, it would be worthwhile to investigate spin dynamics at different magnetic field strengths and orientations, as the spin Hamiltonian parameters, including spin-orbit terms, have an explicit dependence on the magnetic field orientation [44, 49, 60, 61].

Interestingly, by coupling all eight spins and observing the evolution of single-spin probabilities of highly excited states such as the Néel state, one could already explore the thermalization properties of the system under the respective spin Hamiltonians as a function of disorder, spin-spin interaction strengths and topologies. While such measurements could yield a first indication of the many-body localized or ergodic phases, one could additionally resort to further witnesses such as excited state spectroscopy and energy level distribution [9, 62–64] among others, to further probe the nature of the underlying Hamiltonians.

Such studies will cross the many-body threshold as the quantum dot arrays are scaled up to larger sizes while maintaining a high level of control, high initialization and readout fidelities and state coherence. We envision that these techniques can be readily applied to extended (quasi one-dimensional) quantum dot ladders, and, with more effort, to two-dimensional and even three-dimensional [65] arrays. Still, there are several challenges to tackle moving in this direction. Even in the present work, the precise and simultaneous tuning of all interactions within the array was slowed down by the fact that any single gate voltage affects the on-site energy and tunnel coupling of neighboring sites. We have nonetheless been able to dial in the Hamiltonian parameters largely independently through the use of virtualization techniques [24, 25, 66] and have expanded on these in a recent, related work [35], enabling the present experiments. Although the present results still remain in the few-body regime and can be efficiently benchmarked with classical simulations based on exact diagonalization, we achieve significant mile-

stones that can potentially be scaled up to larger systems, likely with the aid of automated tuning routines [67, 68]. All in all, this work lays the groundwork for the exploration of the rich phase diagram and excitation dynamics in extended single-spin and dimer lattices.

6.8. SUPPLEMENTARY MATERIAL

6.8.1. DEVICE FABRICATION AND EXPERIMENT SETUP

The devices used in this work were fabricated on a $Ge/Si_{0.2}Ge_{0.8}$ heterostructure grown on a silicon wafer, with the quantum well buried 55 nm below the surface. Details about the heterostructure and the growth process can be found in Ref. [69].

Fig. 6.10 shows two atomic-force microscopy images of the two devices used in this work. Device 1 (Fig. 6.10a) was used for the magnon propagation experiment, with device 2 (Fig. 6.10b) being used to measure triplon propagation. As a first fabrication step, Pt (device 1) or Al (device 2) Ohmics are defined using electron beam lithography and subsequently annealed so that the metal diffuses into the heterostructure to directly contact the quantum well. Subsequently, three layers of Ti/Pd gate electrodes are patterned to electrostatically define the potential landscape, with thicknesses of 3/17 nm, 3/27 nm and 3/37 nm, respectively. The three layers correspond to plunger gates, which control the electrochemical potential of the quantum dots; barrier gates, to control the tunnel coupling and exchange interaction between nearest neighbors; and screening gates to screen unwanted accumulation of charges near the device's active area. The fabrication order of the gate electrodes is barriers-screening-plungers for device 1 (Fig. 6.10c) and screening-plungers-barriers for device 2 (Fig. 6.10d). All gate layers are separated from each other with Al_2O_3 grown by atomic layer deposition (ALD), each of them 5 nm thick.

The experiments are carried out in Oxford Triton (device 1) and Bluefors XLD (device 2) dilution refrigerators with base temperatures of around 10 mK. Each gate electrode is connected with DC lines to the ports of home-built serial peripheral interface (SPI) DAC modules to individually set DC voltages. In addition, all plunger and barrier gates are connected to a Keysight M3202A arbitrary waveform generator (AWG) for baseband pulse control. Both DC and AC signals are combined on the printed circuit board (on which the sample is glued and bonded) using bias tees with resistor-capacitor time constants of 100 ms, orders of magnitude higher than the duration of each single experimental shot. Between shots, a compensation pulse is applied to all AC gates whose area is equal and opposite to the accumulated DC offset during the measurement to mitigate bias-tee charging. AC lines are attenuated and thermally anchored to each dilution refrigerator plate using cryogenic attenuators. Additionally, these lines are filtered using common-mode ferrite chokes at room temperature to filter out low-frequency noise. The high-frequency noise on the DC lines is filtered using resistor-capacitor filters and copper-powder filters at the mixing chamber plate.

Charge sensors are used to read out the charge state of the devices as a result of their capacitive coupling to neighboring dots. The state of the sensors themselves is read out using radiofrequency (RF) reflectometry via one of the two Ohmic contacts, which is bonded to an off-chip NbTiN inductor forming a inductor-capacitor (LC) tank circuit. Every inductor is fabricated to have a different inductance, which results in a different

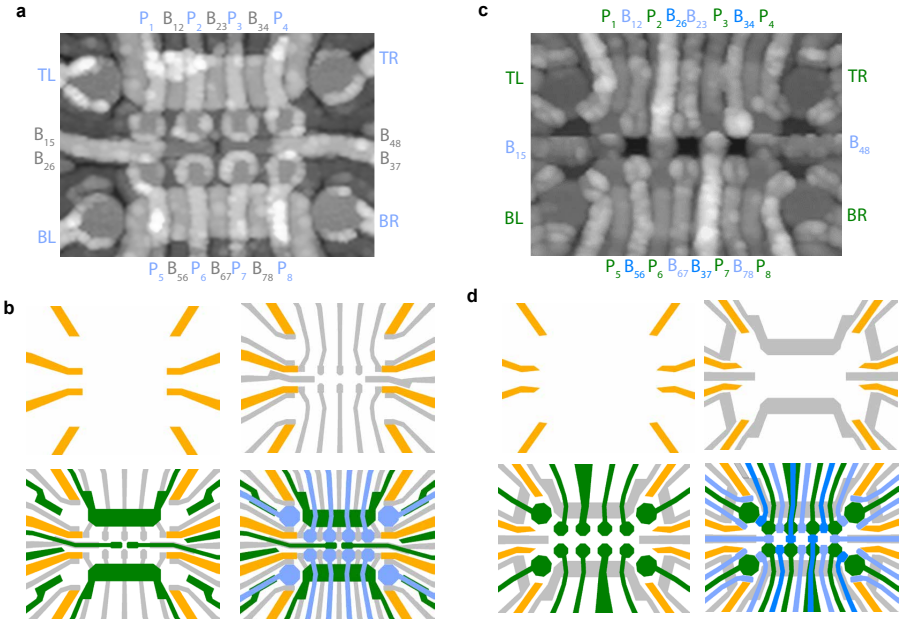

Figure 6.10: (a) AFM of 2×4 device used for the magnon propagation experiments. (b) Corresponding multi-layer gate layout. The four panels display the four different fabrication layers: Ohmic contacts, barrier gates, screening gates and plunger gates. Between each fabrication step, an Al_2O_3 ALD layer is deposited, preventing contact between different fabrication layers. (c) AFM of 2×4 device used for the triplon propagation experiments. (d) Corresponding multi-layer gate layout. The four panels display the four different fabrication layers: Ohmic contacts, screening gates, plunger gates and barrier gates. Note the difference in ordering with respect to panel (b). Between each fabrication step, an Al_2O_3 ALD layer is deposited, preventing contact between different fabrication layers. The barrier layer was deposited in two steps to avoid unwanted shorting of the gates.

resonance frequency for each tank circuit. This allows for simultaneous readout of all sensors by multiplexing all Ohmics to a single RF line, and modulation and demodulation measurements using custom-built SPI RF generators and in-phase and quadrature (IQ) demodulators.

Note that, while the loading of charges into the quantum dot array happens via the sensing dot for device 2, which requires the sensor to be tunnel-coupled to its neighboring quantum dot, loading happens directly from the Ohmics in device 1. In this case, half of the Ohmics are shared between sensing dot and quantum dot (see device schematics in Figs. 6.10c and d). This comes at the expense of increasing the sensor-to-dot distance by about 30 %, which does not significantly affect the sensing capabilities, but which makes the independent tunability of sensing dot and quantum dots easier.

6.8.2. CHARGE STABILITY DIAGRAM, INITIALIZATION AND READOUT RAMPS

In Fig. 6.11, we schematically represent the pulse scheme used for pairwise initialization throughout this work. To navigate the charge state of the system and correctly calibrate the detuning axes, we first record the charge stability diagrams (Fig. 6.11a) for each quantum dot pair. Most detuning pulses used in this work rely on three different voltage points: “I", the initialization point deep in the (0,2) charge state, where a singlet is initialized after a typical waiting time of 20 µs; “O", the operation point in the center of the (1,1) charge configuration; and “R", the readout point where Pauli spin blockade is performed. As outlined in the main text, we use three different ramp configurations between “I" and “O" to initialized three different states: S(1,1) (6.11b), $|\uparrow\downarrow\rangle$ (6.11c) and $|\downarrow\downarrow\rangle$ (6.11d). By choosing either fast or slow ramps, we ensure to be either adiabatic or diabatic with respect to the ST^- anticrossing (which is represented as a yellow dashed line at the corresponding detuning value) and the Zeeman energy difference ΔE_z. More information is outlined in the main text.

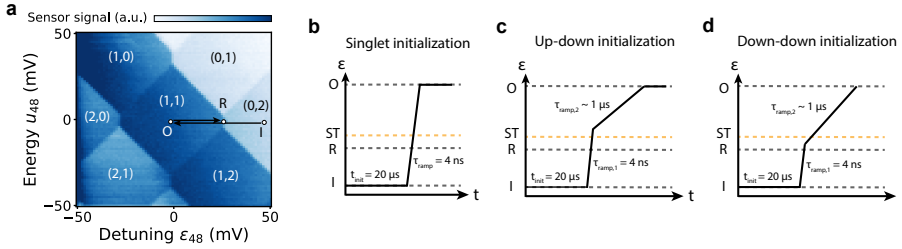

Figure 6.11: Schematics of pulsed initialization. (a) Charge stability diagram of quantum dot pair 4-8. Along the x-axis, we scan the detuning $\varepsilon_{48} = \frac{1}{2}(vp_8 - vp_4)$, and the global chemical potential $u_{48} = vp_8 + vp_4$ is scanned along the y-axis. For each combination of gate voltages, we record the sensor signal. The numbers (n_1, n_2) represent the double dot charge occupation. The three voltage points I (initialization), O (operation) and R (readout) lie along the detuning axis and are calibrated for each quantum dot pair. (b) Pulse scheme to initialize the state $|S(1,1)\rangle$. After waiting 20 µs at point I to initialize the state $|S(2,0)\rangle$, we pulse to the operation point with a ramp speed of 4 ns, which is diabatic and conserves the total spin state. (b) Pulse scheme to initialize the state $|\uparrow\downarrow\rangle$. After waiting 20 µs at point I, we first pulse fast (4 ns) just over the ST^- anticrossing (shown as a yellow dashed line), conserving the spin singlet state. Subsequently, a slow (~ 1 µs ramp) is used, which adiabatically maps the singlet into the $|\uparrow\downarrow\rangle$ state. (c) Pulse scheme to initialize the state $|\downarrow\downarrow\rangle$. After waiting 20 µs at point I, we first pulse fast (4 ns) just before the ST^- anticrossing. Subsequently, a slow (~ 1 µs ramp) is used, which adiabatically maps the singlet into the $|\downarrow\downarrow\rangle$ state.

6.8.3. TWO-SPIN DYNAMICS FOR ALL FOUR PAIRS

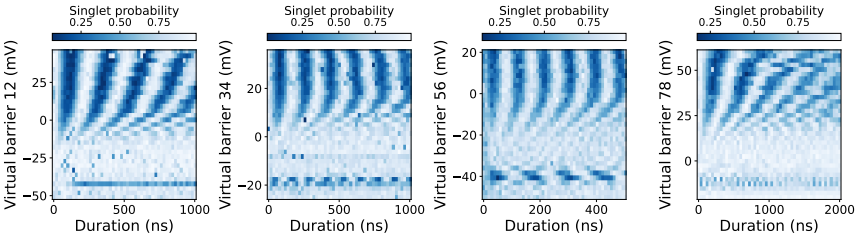

Figure 6.12: Dynamics of an initial state $|S\rangle$ as a function of interaction strength for each pair of quantum dots in the array. At positive barrier voltages, we observe ST^0 oscillations, corresponding to the regime of low exchange. At more negative barrier voltages (high exchange interaction), the singlet is an eigenstate and does not oscillate. Each of the four pairs shows oscillations at the ST^- anticrossing at $J = \tilde{E}_z$.

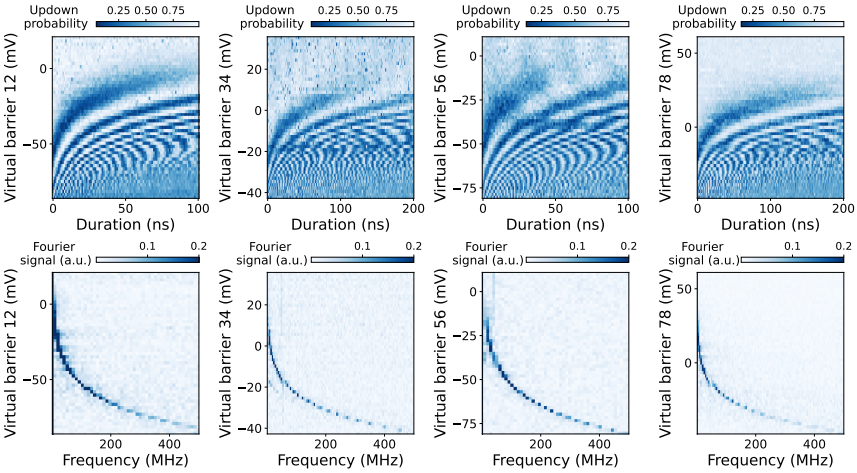

Figure 6.13: Top: Dynamics of an initial state $|\uparrow\downarrow\rangle$ as a function of interaction strength for each pair of quantum dots in the array. At positive barrier voltages, $|\uparrow\downarrow\rangle$ is an eigenstate and does not oscillate. At more negative barrier voltages (high exchange interaction), we observe SWAP oscillations. Each of the four pairs shows oscillations at the ST^- anticrossing at $J = \tilde{E}_z$. Bottom: corresponding Fourier transforms of the signal, showing oscillation speeds reaching 500 MHz for all pairs. These Fourier spectra are fitted to extract the exchange values reported in Fig. 6.4a.

6.8.4. COHERENT SWAPS AT HIGH EXCHANGE FOR PAIR 34

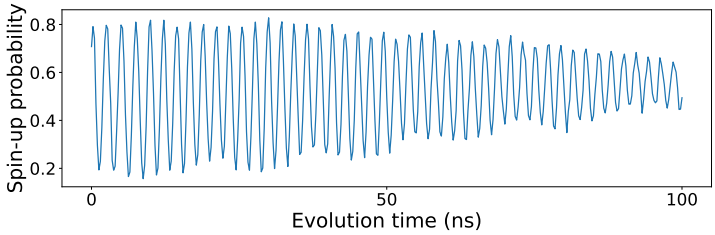

Figure 6.14: Fast exchange oscillations of an initial state $|\uparrow\downarrow\rangle$ on quantum dot pair 34. The obtained exchange speed is $J = 460\,\text{MHz}$. Even at this high exchange, for this particular quantum dot pair, we retain a high quality factor, highlighting the potential operation of quantum dot devices at high exchange coupling values, as well as ultra-fast two-qubit gates in the regime where $J \gg \Delta E_z$.

6.8.5. SIMULATION OF ENERGY DIAGRAM AND INITIALIZATION FIDELITY

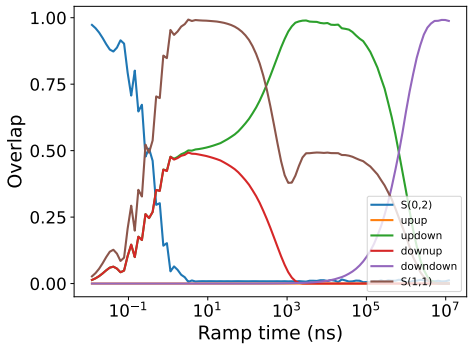

Figure 6.15: Simulation of initialization fidelity as a function of ramp time from the (2,0) to the (1,1) state. The simulation shows four distinct regimes. (a) S(0,2) initialization: the ramp time is diabatic with respect to tunnel coupling. (b) S(1,1) initialization: ramping is adiabatic with respect to tunnel coupling, but diabatic with respect to all spin energy scales. (c) $|\downarrow\uparrow\rangle$ initialization: ramping is diabatic with respect to Δ_{ST} and adiabatic otherwise. (d) $|\downarrow\downarrow\rangle$ initialization: ramping is adiabatic with respect to all energy scales. For this simulation, we include not only a ramp in detuning but also on tunnel coupling, consistent with experimental values. Simulation input parameters: $U = U_1 = U_2 = 300\,\text{GHz}$, $E_{z,1} = 40\,\text{MHz}$, $E_{z,2} = 55\,\text{MHz}$, $t_{\text{SO,x}} = t_{\text{SO,y}} = t_{\text{SO,z}} = 20\,\text{MHz}$, $\varepsilon_0 = -2U$, $\varepsilon_f = 0$, $t_0 = 20\,\text{GHz}$, $t_f = 0.2\,\text{GHz}$. For this simulation, the ramp is chosen to be linear, while in experiments, we resort to composite ramps to increase initialization speed and fidelity.

The Hamiltonian to describe the lowest energy levels of a double quantum dot is given by [49]:

$$H = \begin{pmatrix} U+\varepsilon & -t_{\text{so}}^x + i\,t_{\text{so}}^y & t_0 - i\,t_{\text{so}}^z & -t_0 - i\,t_{\text{so}}^z & -t_{\text{so}}^y - i\,t_{\text{so}}^x \\ -t_{\text{so}}^y - i\,t_{\text{so}}^x & \bar{E}_z & 0 & 0 & 0 \\ t_0 + i\,t_{\text{so}}^z & 0 & \Delta E_z & 0 & 0 \\ -t_0 + i\,t_{\text{so}}^z & 0 & 0 & -\Delta E_z & 0 \\ -t_{\text{so}}^y + i\,t_{\text{so}}^x & 0 & 0 & 0 & -\bar{E}_z \end{pmatrix}, \tag{6.4}$$

written in the basis $\{S(0,2), |\downarrow\downarrow\rangle, |\downarrow\uparrow\rangle, |\uparrow\downarrow\rangle, |\uparrow\uparrow\rangle\}$.

To simulate state initialization as a function of ramp time, we solve the time-dependent Schrödinger equation

$$i\frac{\partial}{\partial t}|\psi(t)\rangle = H(t)|\psi(t)\rangle \tag{6.5}$$

using QuTip. We introduce the time dependency in the detuning as $\varepsilon(t) = \varepsilon_0 + vt$ and $t_c(t) = t_0 - vt$, where v is the ramp rate in GHz/ns. The final state can be simulated by finding the evolution operators

$$U(t, t+\Delta t) = e^{-iH(t)\Delta t} \tag{6.6}$$

for small Δt values and sequentially calculating the state vectors at every time step. The results can be seen in Fig. 6.15. We observe four distinct regimes emerge, depending on the degree of (a-)diabaticity with respect to three energy scales: tunnel coupling t_c, Zeeman energy difference ΔE_z and spin-orbit anticrossing Δ_{ST}. In the simulation, while using realistic experimental parameters, we make sure that these timescales are separable. In the experiment, if the spin-orbit anticrossing is too large or the difference in Zeeman energy too small, we resort to composite ramps as highlighted in the main text, which allow us to cross each anticrossing individually with the desired speed and ensure proper initialization of all relevant states.

6

6.8.6. SIMULATION OF OSCILLATION PATTERNS OF FIG. 6.3

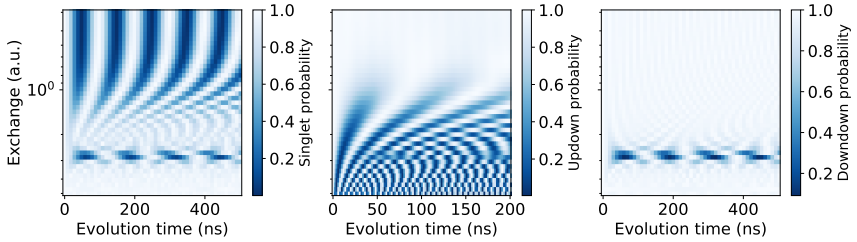

Figure 6.16: Simulation of oscillation patterns in Fig.6.3a-c. The simulated results match with $E_{z,1} = 50$ MHz and $E_{z,2} = 55$ MHz, slightly higher than the Zeeman energy values we find in Fig. 6.4b. A possible explanation is g-factor modulation through the barrier pulses, which also explains the strong bending of the S-T^0-oscillations for higher barrier voltages. For these simulations, we use the initial states that result from the ramped initialization simulations of Fig. 6.15 for the ramp speeds with the highest overlap with the desired state.

6.8.7. EDSR SPECTRA

In Fig. 6.17, we report the EDSR lines corresponding to quantum dots 1, 2, 5 and 6 for the magnon experiment. This corresponds to the quantum dots of the left half of the array, at a time where only those four quantum dots were populated. In Table 6.2, we list and compare the extracted resonance frequencies with those reported in Fig. 6.4b, when the full array was tuned during a second cooldown. Interestingly, the disorder landscape differs significantly, which can result from different tuning voltages between two different cooldowns, but predominantly from the fact that even within the same cooldown, tuning half of the array or the full array also requires significantly different voltages. As remarked in the main text and observed experimentally (see Fig. 6.26 below), the g-tensor of germanium quantum dots can be electrically modulated.

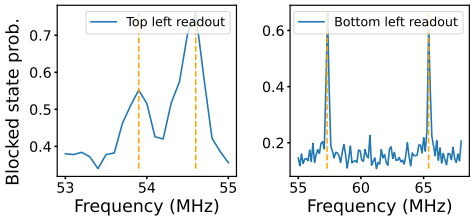

Figure 6.17: EDSR spectra corresponding to the resonance frequencies of spins 1 and 2 (left panel) and 5 and 6 (right panel) for the magnon experiment, measured during the first cooldown. At this point, only the left half of the 2×4 array was tuned, resulting in different resonance frequencies as compared to those reported in Fig. 6.4b.

Qubit number	Resonance frequency (first cooldown)	Resonance frequency (second cooldown)
Q1	54.6	58.2
Q2	53.9	62.8
Q3	–	58.4
Q4	–	51.8
Q5	57.3	51.7
Q6	65.4	42.4
Q7	–	48.8
Q8	–	44.2

Table 6.2: Summary of EDSR frequencies for Fig. 6.17 (left table) and Fig. 6.4b, corresponding to the two different cooldowns and tuning regimes used for the data in this paper. The disorder landscape of the left table corresponds to the quantum walk plots of Fig. 6.6c-e, while the right table corresponding to all other plots of Figs. 6.3, 6.5, 6.6 and 6.7.

One important consequence of this change in resonance frequencies is that it crucially changes which spin is initialized as spin-up during the pairwise initialization stage, when the ramps are chosen such that the state $|\uparrow\downarrow\rangle$ is initialized. As outlined in the main text, the spin with the lowest g-factor per pair will be initialized in the up-state, while the other will be down. During the first cooldown (left data in Table 6.2), dots 2 and 5 had the lowest g-factors, while during the second cooldown (right data), it was dots 1 and 6.

6.8.8. 2D PLOTS AND QUANTUM WALKS FOR STATIC AND PAIR PLOTS

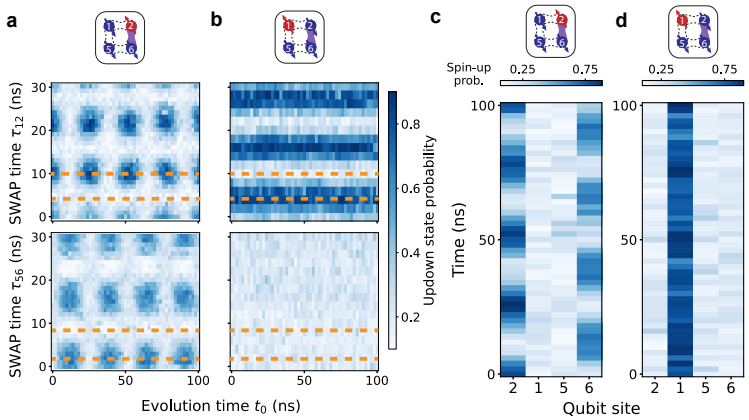

Figure 6.18: (a) $|\uparrow\downarrow\rangle$ state probability as a function of evolution time and readout SWAP times τ_{12} and τ_{56} (see main text), after executing the quantum circuit of panel 6.5a, but with only J_{26} turned on during the analog evolution phase. The top and the bottom panels correspond to the top (pair 12) and bottom (pair 56) readouts, respectively. (b) Same circuit as for panel (a), but initializing the spin excitation in dot 1. From these 2D maps, we extract the SWAP times which correspond to spin-up readout for each of the four spins (indicated by the dashed orange lines), used to extract the quantum walk data shown in panels (c) and (d). (c) Spin quantum walk corresponding to exchange configuration (a). We observe the magnon oscillate between sites 2 and 6, as expected. (d) Spin quantum walk corresponding to exchange configuration (d), where the magnon remains localized in dot 1. This figure corresponds to Fig. 6.6b.

6.8.9. SIMULATION OF QUANTUM WALK DATA

The quantum walk data simulations reported in the subsections below are performed using QuTip. We use the Zeeman energy values reported in Table 6.2 as well as estimated values of all exchange couplings as input parameters to generate the Hamiltonian matrices of Eq. 6.1 (for the magnon simulations) and Eq. 6.2 (for the triplon simulations). Since our spin Hamiltonians are time-independent, we can compute the time evolution by calculating the Hamiltonian's matrix exponential for each time step. Finally, we can compute the single-site magnetization value for each time step and plot the results in the same way as the measured quantum walks. We iterate over various interaction values $\{J_i\}$ around the expected exchange configuration and compare to the measured data.

6.8.10. 2D PLOTS, QUANTUM WALKS AND SIMULATION OF WEAKLY COUPLED PAIRS

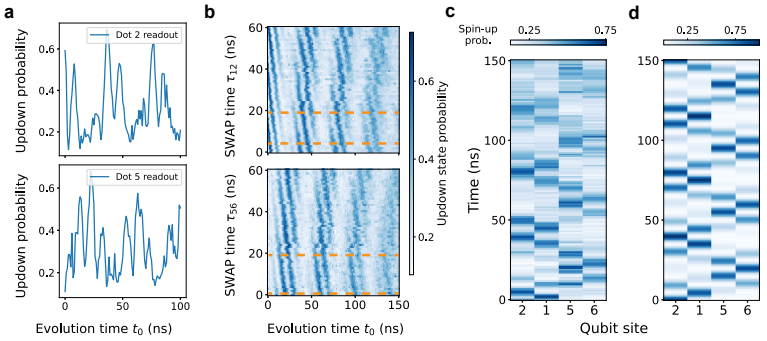

Figure 6.19: Measurements and simulation of the dynamics of a single excitation $|2\rangle = |\downarrow_1\uparrow_2\downarrow_3\downarrow_4\rangle$ in a 2×2 array of weakly coupled pairs, corresponding to Fig. 6.6c. (a) Unblocked state probability for pair 12 (top panel) and pair 56 (bottom panel) after a variable evolution time t_0. The readout was performed ramping with an intermediate speed to the PSB point, where the unblocked state is expected to be $|\uparrow\downarrow\rangle$ (see main text). For a single excitation in the array and the g-factor landscape at this time of tuning, this corresponds to the spin-up probabilities of dots 2 and 5, respectively. (b) Readout as a function of SWAP time τ_{12} (top panel) and τ_{56} (top panel). The dashed horizontal lines correspond to rotations by π and 2π (top panel) or 0 and π (bottom panel), which can be inferred by comparison to the measurements without the SWAP gate (panel (a)). The dashed lines then correspond to all four single-spin probabilities. (c) Site-resolved quantum walk, where the spin-up probabilities for each site are plotted as a function of evolution time. (d) Simulated quantum walk for this exchange coupling configuration, and using the Zeeman energy values of table 6.2 (left column), showing good agreement with the measured data. From the simulation, we extract $J_{12} = J_{56} = 100$ MHz and $J_{15} = J_{26} = 25$ MHz.

6.8.11. 2D PLOTS, QUANTUM WALKS AND SIMULATION OF 2×2 RING WITH INHOMOGENEOUS EXCHANGE COUPLINGS

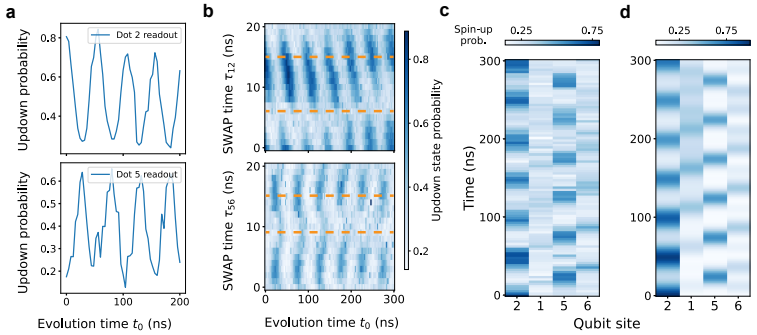

Figure 6.20: Measurements and simulation of the dynamics of a single excitation $|2\rangle = |\downarrow_1\uparrow_2\downarrow_3\downarrow_4\rangle$ in a 2×2 array with all exchange couplings on, corresponding to Fig. 6.6e. (a) Unblocked state probability for pair 12 (top panel) and pair 56 (bottom panel) after a variable evolution time t_0. The readout was performed ramping with an intermediate speed to the PSB point, where the unblocked state is expected to be $|\uparrow\downarrow\rangle$ (see main text). For a single excitation in the array and the g-factor landscape at this time of tuning, this corresponds to the spin-up probabilities of dots 2 and 5, respectively. (b) Readout as a function of SWAP time τ_{12} (top panel) and τ_{56} (top panel). The dashed horizontal lines correspond to rotations by π and 2π (top panel) or 2π and 3π (bottom panel), which can be inferred by comparison to the measurements without the SWAP gate (panel (a)). The dashed lines then correspond to all four single-spin probabilities. (c) Site-resolved quantum walk, where the spin-up probabilities for each site are plotted as a function of evolution time. (d) Simulated quantum walk for an exchange coupling configuration $J_{12} = 11.5$ MHz, $J_{56} = 27.0$ MHz, $J_{15} = 20.0$ MHz and $J_{26} = 15.5$ MHz, and using the Zeeman energy values of table 6.2 (left column), showing good agreement with the measured data.

6.8.12. 2D PLOTS, QUANTUM WALKS AND SIMULATION OF 2×2 RING WITH HOMOGENEOUS EXCHANGE COUPLINGS

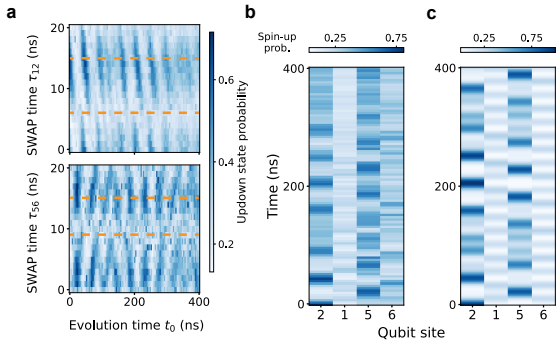

Figure 6.21: Measurements and simulation of the dynamics of a single excitation $|2\rangle = |\downarrow_1\uparrow_2\downarrow_3\downarrow_4\rangle$ in a 2×2 array with all exchange couplings on and tuned homogeneously, corresponding to Fig. 6.6d. (a) Unblocked state probability for pair 12 (top panel) and pair 56 (bottom panel) after a variable evolution time t_0 and as a function of SWAP time τ_{12} (top panel) and τ_{56} (top panel). The readout was performed ramping with an intermediate speed to the PSB point, where the unblocked state is expected to be $|\uparrow\downarrow\rangle$ (see main text). The dashed horizontal lines correspond to rotations by π and 2π (top panel) or 2π and 3π (bottom panel), these SWAP times are the same as in Fig. 6.20. These lines correspond to all four single-spin probabilities. (c) Site-resolved quantum walk, where the spin-up probabilities for each site are plotted as a function of evolution time. (d) Simulated quantum walk for an exchange coupling configuration $J_{12} = J_{56} = J_{15} = J_{26} = 21$ MHz and using the Zeeman energy values of table 6.2 (left column), showing good agreement with the measured data. The slight deviation can be explained by a small g-tensor modulation that could be caused by the barrier voltage pulses.

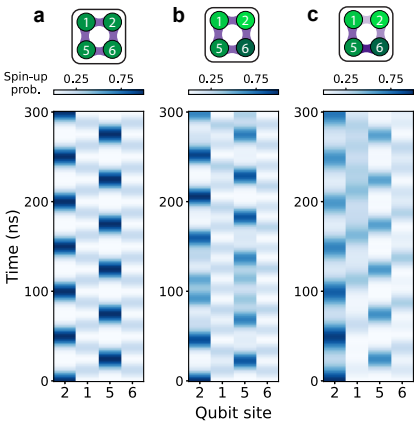

Figure 6.22: Simulated quantum walk for three different parameter regimes, with a single initial spin excitation in dot 2. (a) All g-factors are equal (no single-site disorder) and all exchange couplings are equal J =20 MHz (no exchange disorder). The excitation fully refocuses on the other side of the array (dot 5). (b) The Zeeman energies correspond to those measured experimentally, and all exchange couplings are equal J =21 MHz (single-site disorder, but no exchange disorder). The obtained pattern is less regular and captures the main features of Fig. 6.6d, where we aimed to experimentally tune the exchange couplings homogeneously. (c) The Zeeman energies correspond to those measured experimentally, and the input exchange interactions are J_{12} =11.5 MHz, J_{56} =27.0 MHz, J_{15} =20.0 MHz and J_{26} =15.5 MHz (single-site disorder and exchange disorder). The obtained pattern captures the main features of Fig. 6.6e.

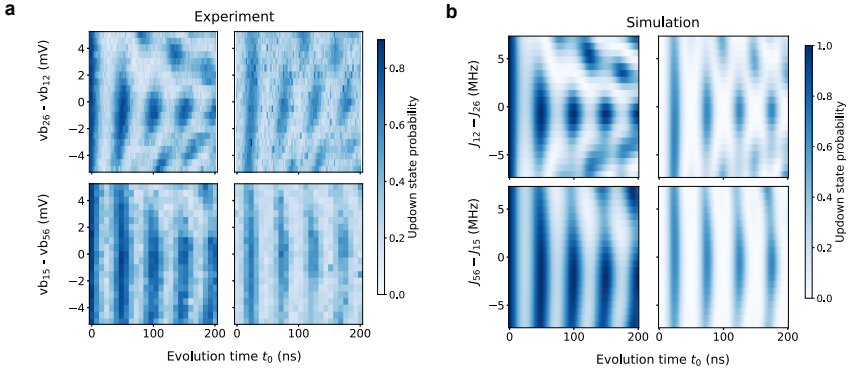

Figure 6.23: Dynamics of a single excitation $|2\rangle = |\downarrow_1\uparrow_2\downarrow_3\downarrow_4\rangle$ in a 2×2 array with all exchange couplings on, corresponding to the quantum walk of Fig. 6.6e, as a function of barrier voltage combinations vb_{26} - vb_{12} (top two panels) and vb_{15} - vb_{56} (bottom two panels). For each row, the first plot corresponds to the readout of pair 12, the second plot to the readout of pair 56. The relative voltage value of 0 corresponds to the voltage configuration for which Fig. 6.6e was taken. Away from that center point, the oscillations (corresponding to the spin-up probabilities of dots 2 and 5, respectively) become less regular and show a more complex pattern. (b) Simulation of the data in (a), starting at the exchange configuration of Fig. 6.22c, showing good agreement with the experimentally observed oscillation patters. This supports the correctness of the previously simulated exchange interaction values.

6.8.13. 8-SPIN QUANTUM WALK OF FOUR UNCOUPLED PAIRS

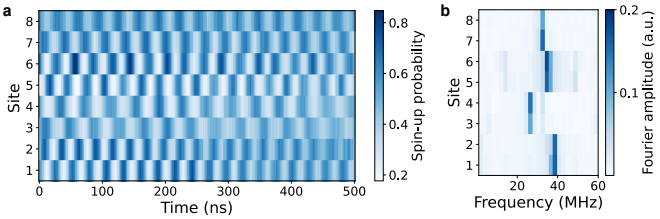

Figure 6.24: (a) 8-site quantum walk with staggered couplings, resulting in four uncoupled pairs. The initial state is a Néel state (up to a single initial SWAP for pair 34). The evolution pattern is consistent with four uncoupled pairs, where each spin excitation does not leave the pair it was initialized in. This plot demonstrates the ability to simultaneously initialize all spins in the array. State readout was performed in two separate experimental rounds. In the first round, all spin pairs were read out sequentially, resulting in four bits of information, corresponding to the spin-up probability of the spin in each pair with the lowest g-factors (see main text). In the second round, a SWAP gate is applied on each pair before readout, allowing us to obtain the spin-up probability of the other dot. Note that, for some pairs, a small phase mismatch is observed for longer evolution times, which we attribute to imprecise SWAP gate calibration. (b) Fourier transform of (a). For each quantum dot pair, the oscillation frequency is the same for the two spins, consistent with the spins only oscillating between the dots of the same pair.

6.8.14. MEASURED INITIALIZATION DATA CORRESPONDING TO FIG. 6.7B

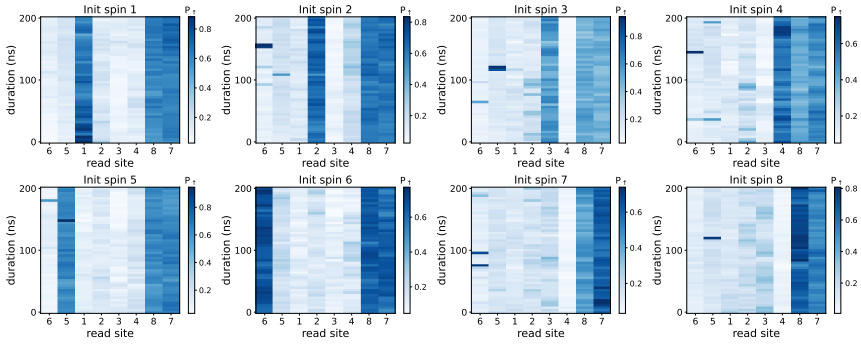

Figure 6.25: Static quantum walk plots for single magnons initialized in different locations in the array, corresponding to the data shown in Fig. 6.7b after averaging over the y-axis. For each plot, the state $|2\rangle = |\downarrow_1\uparrow_2\downarrow_3\downarrow_4\downarrow_5\downarrow_6\downarrow_7\downarrow_8\rangle$ was initialized, with a single magnon in dot 2. Subsequently, a sequence of SWAP gates was applied to move the excitation around, as depicted on the quantum circuit of Fig. 6.7a. For dots 1-6, the measurement results in the expected initialized spin-up. For dot pair 7-8, the readout visibility was very low at the time of measurement, resulting in a seemingly always high signal.

6.8.15. EDSR, EXCHANGE SPLITTING AND g-FACTOR MODULATION

In this work, we have used EDSR as a method to spectroscopically determine the resonance frequency of each spin. Since we obtain two different resonances for each quantum dot pair, we need to identify which resonance corresponds to which spin within each pair. Fig. 6.26a and b show the resonance frequencies of Q1 and Q2 at a magnetic field of 20 mT, and as a function of barrier voltages vb_{15} and vb_{26}, respectively. Spins 5 and 6 are not initialized for this experiment and thus remain in a mixed state. We observe the expected branching of the resonance frequencies as a function of exchange interaction. Given that the rightmost resonance branches with increased J_{15} (Fig. 6.26a), we infer that this frequency corresponds to dot 1. Similarly, J_{26} causes the branching of the leftmost resonance (Fig. 6.26b), which we then attribute to dot 2. Thus, this straightforward technique allows us to identify which resonance corresponds to which spin for each quantum dot pair, which is relevant especially for the initialization of the state $|\uparrow\downarrow\rangle$, where the spin-up is initialized (and read out) on the spin with the lowest Zeeman energy. This data corresponds to the first cooldown, where only the left half of the array was tuned (see Fig. 6.17).

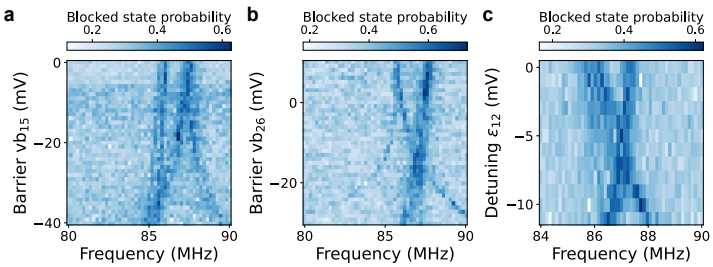

Figure 6.26: Microwave spectroscopy of Zeeman energies, exchange control and g-factor modulation. (a) Resonances as a function of barrier vb_{15}. Exchange splitting is only observed for the rightmost resonance, which corresponds to dot 1. The splitting is a direct measure of J_{15}. (b) Resonances as a function of barrier vb_{26}. Exchange splitting is only observed for the leftmost resonance, which corresponds to dot 2. The splitting is a direct measure of J_{26}. An additional splitting is observed for dot 1, which we attribute to bad virtualization of J_{15} with respect to barrier voltage vb_{26}. (c) EDSR resonance of spins 1 and 2 as a function of detuning ε_{12}. A g-factor crossing is observed at $\varepsilon_{12} \approx 6$ mV.

Additionally, we can demonstrate g-factor tunability for this quantum dot pair exemplarily, where we scan the detuning ε_{12} as we record the position of both resonance frequencies (Fig 6.26c). Strikingly, for this quantum dot pair, the Zeeman energies are modulated such that they cross at negative detunings. This is not observed for each pair: the tunability of the g-factors relies on microscopic details such as local disorder in the heterostructure and the shape of the quantum dot wavefunction.

6.8.16. THEORY OF EXCHANGE-COUPLED SINGLET-TRIPLET QUBITS

We consider the Hamiltonian of Eq. 6.1 describing an array of exchange-coupled spins. As outlined in the main text, for this discussion it suffices to consider this isotropic Hamiltonian and neglect spin-orbit terms (a full derivation of the two-qubit Hamiltonian of two singlet-triplet qubits can be found in [42]). Projecting this Hamiltonian onto the S-T$^-$ basis of two qubits, spanned by $\{|SS\rangle, |ST^-\rangle, |T^-S\rangle, |T^-T^-\rangle\}$, we obtain the Hamiltonian of Eq. 6.2 [42] for two qubits. Rewritten so that we treat interaction and disorder terms separately, this Hamiltonian reads:

$$\begin{aligned} H_{ST,2Q} = &\frac{1}{2}\left(\tilde{E}_{z,1} - J_1^{\perp} - \frac{J_{12}^{\parallel}}{4}\right)\sigma_1^z \\ &+ \frac{1}{2}\left(\tilde{E}_{z,2} - J_2^{\perp} - \frac{J_{12}^{\parallel}}{4}\right)\sigma_2^z \\ &+ \frac{J_{12}^{\parallel}}{4}\left(\sigma_i^x\sigma_j^x + \sigma_i^y\sigma_j^y + \frac{1}{2}\sigma_i^z\sigma_j^z\right), \end{aligned} \tag{6.7}$$

where the first two terms represent the single-site disorder, and the last term is the qubit-qubit interaction. For a two-site system, tuning to the homogeneous condition is equivalent to finding $J_1^{\perp}$ and $J_2^{\perp}$ such that $\tilde{E}_{z,1} - J_1^{\perp} = \tilde{E}_{z,2} - J_2^{\perp}$. However, when considering a one-dimensional chain of N sites, also the individual, parallel exchange interactions need to be considered. Even if all parallel interactions are tuned equally, i.e. $J_{12}^{\parallel} = J_{23}^{\parallel} = ... = J_{N-1,N}^{\parallel} = J^{\parallel}$, the first and last site would have a different disorder contribution due to the absence of periodic boundary conditions. For $N = 3$ qubits, the corresponding homogeneous condition reads:

$$\tilde{E}_{z,1} - J_1^{\perp} - \frac{J_{12}^{\parallel}}{4} = \tilde{E}_{z,2} - J_2^{\perp} - \frac{J_{12}^{\parallel}}{4} - \frac{J_{23}^{\parallel}}{4} = \tilde{E}_{z,3} - J_3^{\perp} - \frac{J_{23}^{\parallel}}{4} \tag{6.8}$$

The calibration procedure outlined in the main text allows for the independent and sequential calibration of all $J_i^{\perp}$ terms, allowing us to achieve the condition above for any values of $J_{12}^{\parallel}$ and $J_{23}^{\parallel}$. For the regime where both parallel exchanges are equal, which we tuned up for the measurements of Fig. 6.8d-e, the final interaction Hamiltonian is an XXZ Hamiltonian with an anisotropy parameter $\Delta = 0.5$, which simply reads:

$$H_{3Q,int} = \frac{J^{\parallel}}{4}\sum_{i=1}^{2}\left(\sigma_i^x\sigma_{i+1}^x + \sigma_i^y\sigma_{i+1}^y + \frac{1}{2}\sigma_i^z\sigma_{i+1}^z\right). \tag{6.9}$$

Given the iterative nature of the calibration procedure, this method can be scaled in principle to obtain the Hamiltonian above for any N-site chain of singlet-triplet qubits.

We use Eq. 6.9 to simulate the triplon propagation of Fig. 6.8e, which is plotted in Fig. 6.27, and find excellent agreement with the measured propagation pattern. The simulation yields an exchange interaction $J^{\parallel} = 14$ MHz. The difference in visibility of the experimental data and the simulations can be explained by the difference in readout fidelity for Q1, Q2 and Q3. Also, small differences can be attributed to slightly different values of $J_{12}^{\parallel}$ and $J_{23}^{\parallel}$.

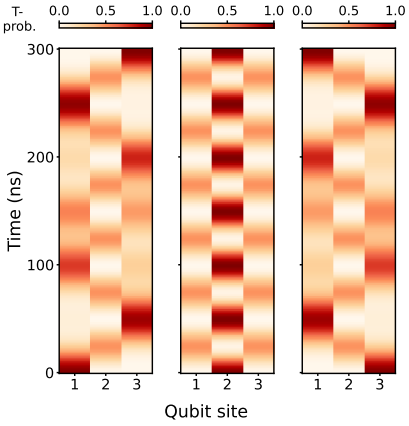

Figure 6.27: Simulated three-site quantum walk plot of a triplon excitation initialized in Q1, Q2 and Q3, respectively. For this simulation, we let each initial state evolve under the Hamiltonian of Eq. 6.9 and we assume equal parallel exchange couplings $J^{\parallel} = 14\,\text{MHz}$. This simulation is in excellent agreement to the measured triplon quantum walks of Fig. 6.8e.

6.8.17. CORRELATION PLOTS FOR TRIPLON QUANTUM WALKS

Fig. 6.28 shows all site-site correlations C_{ij} corresponding to the quantum walk data of Fig. 6.8e. When $i \neq j$, we observe the correlation plots become negative for all combinations of i and j and irrespective of the site in which the triplon is initialized. This is consistent with the propagation of the triplon across the array and the generation of entanglement. Note that the magnitudes of the correlation values remain still relatively small, mainly due to the reduced readout fidelity.

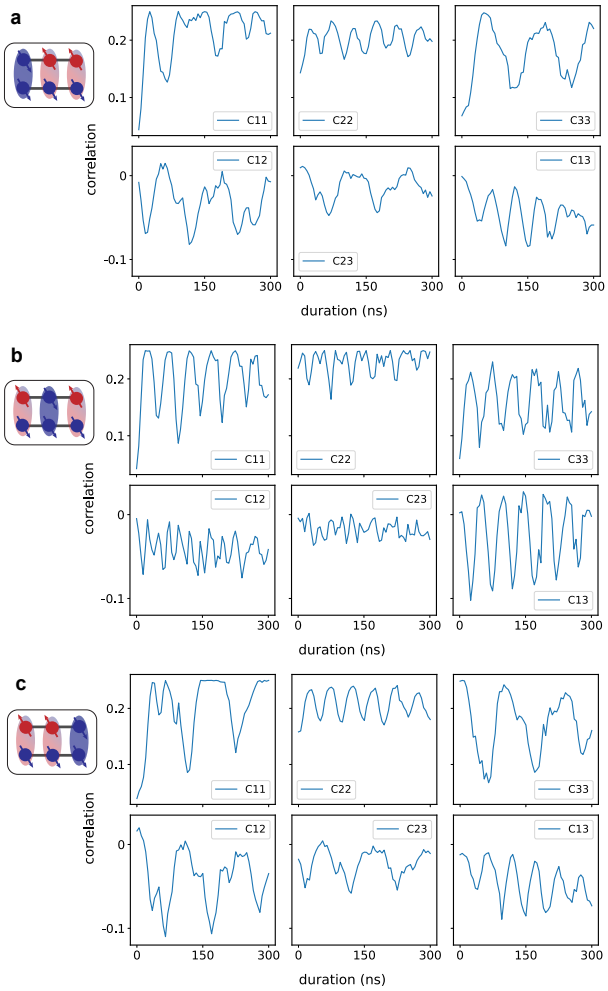

Figure 6.28: Site-site correlations C_{ij} for every pair of sites (i, j), corresponding to the quantum walks of 6.8e, where a triplon excitation was initialized in site 1, 2 or 3, respectively.

6.8.18. SIMULATION OF ST$^-$ TWO-SITE PHASE DIAGRAM

In Fig. 6.29, we simulate the evolution of an initial state $|ST^-\rangle$ of a two-site system subject to the Hamiltonian of Eq. 6.2, where $J_{\perp,1} = J_{34}$, $J_{\perp,2} = J_{78}$ and $J_{\parallel} = J_{48}$, corresponding to the labels used in section 6.6 and Fig. 6.9b. As in the experiment, the initial state is allowed to evolve for 200 ns, and we vary both the interaction as well as the disorder terms independently. In the simulation, for each combination of exchange terms, we retrieve the magnetization for the first site, where the exchange interactions are scanned in an exponential way which corresponds to a linear scan in barrier gate voltage. The resulting pattern agrees very well with Fig. 6.9a and is consistent with a variation of coupling strength of more than two orders of magnitude. The red line corresponds to the points where the coupling and the disorder terms are equal, serving as a “phase boundary" between the regions of high interaction-to-disorder ratio, where the excitation can freely evolve, and that of low interaction-to-disorder ratio, where the excitation remains localized. Note that, for simplicity, we set the average Zeeman energy of both singlet-triplet qubits to 50 MHz, which is approximately the real experimental values.

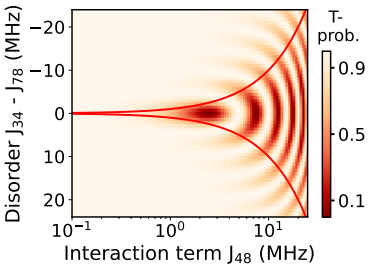

Figure 6.29: Simulated evolution of an initial state $|ST^-\rangle$ under the Hamiltonian of Eq. 6.2, and corresponding to the measurement of Fig. 6.9a. The x-axis corresponds to the coupling term $J_{\parallel} = J_{48}$, while on the y-axis, the difference in single-site disorder is scanned using the exchange couplings $J_{\perp,1} = J_{34}$ and $J_{\perp,2} = J_{78}$. The simulated pattern is in good agreement with the experimental results. In addition, the red line corresponds to the points where the single-site disorder is equal to the coupling strength.

6.8.19. TRIPLON QUANTUM WALK FOR FOUR SITES

Fig. 6.30 shows the measured triplon quantum walk data for a chain of four coupled singlet-triplet qubits, i.e. using all eight spins of the 2×4 ladder, with the circuit diagram corresponding to the measurements depicted in Fig. 6.30a. The data shown corresponds to the initialization of either a single triplon (6.30b) or two triplons (6.30c). In this case, the visibility of the oscillations seems to vary strongly between the different panels, suggesting either inhomogeneities in the exchange coupling configuration or, most likely, strong differences in readout visibility for each site.

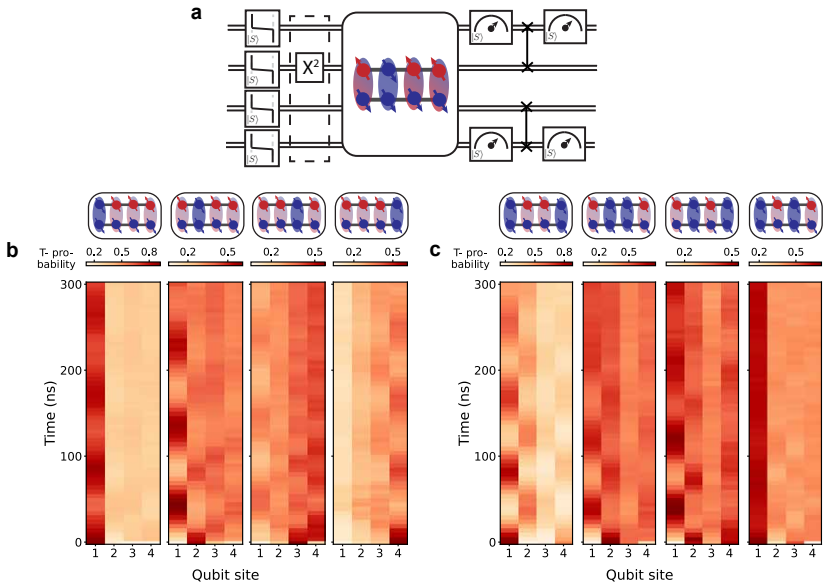

Figure 6.30: Triplon quantum walk for four coupled singlet-triplet qubits. (a) Circuit diagram showing the state preparation, evolution and readout steps for the 4-site triplon quantum walk. Readout is performed in two steps, with a SWAP gate in between to transfer the population of Q2 (Q3) to Q1 (Q4). (b) Quantum walk results for a single excitation initialized in sites 1, 2, 3 or 4, respectively. Note that at the point of the experiment, the readout fidelity of the right side of the device was much lower than for the left side, resulting in a lower visibility for the readout of Q3 and Q4. We do not correct for the difference in readout visibility. (c) Quantum walk results for two excitations in the array and for different initial states.

BIBLIOGRAPHY

[1] R. P. Feynman. “Simulating physics with computers”. *International Journal of Theoretical Physics* 21.6 (1982), pp. 467–488.

[2] S. Lloyd. “Universal Quantum Simulators”. *Science* 273.5278 (1996), pp. 1073–1078.

[3] I. M. Georgescu, S. Ashhab, and F. Nori. “Quantum simulation”. *Reviews of Modern Physics* 86.1 (2014), pp. 153–185.

[4] D. A. Abanin et al. “Colloquium: Many-body localization, thermalization, and entanglement”. *Reviews of Modern Physics* 91.2 (2019), p. 021001.

[5] M. Schreiber et al. “Observation of many-body localization of interacting fermions in a quasirandom optical lattice”. *Science* 349.6250 (2015), pp. 842–845.

[6] S. S. Kondov et al. “Disorder-Induced Localization in a Strongly Correlated Atomic Hubbard Gas”. *Physical Review Letters* 114.8 (2015), p. 083002.

[7] J. Smith et al. “Many-body localization in a quantum simulator with programmable random disorder”. *Nature Physics* 12.10 (2016), pp. 907–911.

[8] J.-y. Choi et al. “Exploring the many-body localization transition in two dimensions”. *Science* 352.6293 (2016), pp. 1547–1552.

[9] P. Roushan et al. “Spectroscopic signatures of localization with interacting photons in superconducting qubits”. *Science* 358.6367 (2017), pp. 1175–1179.

[10] K. Xu et al. “Emulating Many-Body Localization with a Superconducting Quantum Processor”. *Physical Review Letters* 120.5 (2018), p. 050507.

[11] W. Morong et al. “Observation of Stark many-body localization without disorder”. *Nature* 599.7885 (2021), pp. 393–398.

[12] N. Mehta et al. “Down-conversion of a single photon as a probe of many-body localization”. *Nature* 613.7945 (2023), pp. 650–655.

[13] I. Bloch, J. Dalibard, and S. Nascimbène. “Quantum simulations with ultracold quantum gases”. *Nature Physics* 8.4 (2012), pp. 267–276.

[14] R. Blatt and C. F. Roos. “Quantum simulations with trapped ions”. *Nature Physics* 8.4 (2012), pp. 277–284.

[15] A. M. Kaufman and K.-K. Ni. “Quantum science with optical tweezer arrays of ultracold atoms and molecules”. *Nature Physics* 17.12 (2021), pp. 1324–1333.

[16] S. L. Cornish, M. R. Tarbutt, and K. R. A. Hazzard. “Quantum computation and quantum simulation with ultracold molecules”. *Nature Physics* 20.5 (2024), pp. 730–740.

[17] M. Kjaergaard et al. “Superconducting Qubits: Current State of Play”. *Annual Review of Condensed Matter Physics* 11.Volume 11, 2020 (2020), pp. 369–395.

[18] D.-J. Choi et al. “Colloquium: Atomic spin chains on surfaces”. *Reviews of Modern Physics* 91.4 (2019), p. 041001.

[19] T. Hensgens et al. “Quantum simulation of a Fermi–Hubbard model using a semiconductor quantum dot array”. *Nature* 548.7665 (2017), pp. 70–73.

[20] P. Barthelemy and L. M. K. Vandersypen. “Quantum Dot Systems: a versatile platform for quantum simulations”. *Annalen der Physik* 525.10-11 (2013), pp. 808–826.

[21] J. P. Dehollain et al. “Nagaoka ferromagnetism observed in a quantum dot plaquette”. *Nature* 579.7800 (2020), pp. 528–533.

[22] M. Kiczynski et al. “Engineering topological states in atom-based semiconductor quantum dots”. *Nature* 606.7915 (2022), pp. 694–699.

[23] T.-K. Hsiao et al. “Exciton Transport in a Germanium Quantum Dot Ladder”. *Physical Review X* 14.1 (2024), p. 011048.

[24] C. J. van Diepen et al. “Quantum Simulation of Antiferromagnetic Heisenberg Chain with Gate-Defined Quantum Dots”. *Physical Review X* 11.4 (2021), p. 041025.

[25] C.-A. Wang et al. “Probing resonating valence bonds on a programmable germanium quantum simulator”. *npj Quantum Information* 9.1 (2023), p. 58.

[26] F. van Riggelen et al. “A two-dimensional array of single-hole quantum dots”. *Applied Physics Letters* 118.4 (2021), p. 044002.

[27] D. Jirovec et al. “A singlet-triplet hole spin qubit in planar Ge”. *Nature Materials* 20.8 (2021), pp. 1106–1112.

[28] G. Scappucci et al. “The germanium quantum information route”. *Nature Reviews Materials* 6.10 (2021), pp. 926–943.

[29] F. Borsoi et al. “Shared control of a 16 semiconductor quantum dot crossbar array”. *Nature Nanotechnology* 19.1 (2024), pp. 21–27.

[30] C.-A. Wang et al. “Operating semiconductor quantum processors with hopping spins”. *Science* 385.6707 (2024), pp. 447–452.

[31] V. John et al. *A two-dimensional 10-qubit array in germanium with robust and localised qubit control*. 2024.

[32] N. W. Hendrickx et al. “A four-qubit germanium quantum processor”. *Nature* 591.7851 (2021), pp. 580–585.

[33] A. Parra-Rodriguez et al. “Digital-analog quantum computation”. *Physical Review A* 101.2 (2020), p. 022305.

[34] T. I. Andersen et al. “Thermalization and criticality on an analogue–digital quantum simulator”. *Nature* 638.8049 (2025), pp. 79–85.

[35] D. Jirovec et al. *Exchange cross-talk mitigation in dense quantum dot arrays*. 2025.

[36] T. Fukuhara et al. “Microscopic observation of magnon bound states and their dynamics”. *Nature* 502.7469 (2013), pp. 76–79.

[37] P. Jurcevic et al. “Quasiparticle engineering and entanglement propagation in a quantum many-body system”. *Nature* 511.7508 (2014), pp. 202–205.

[38] Z. Yan et al. “Strongly correlated quantum walks with a 12-qubit superconducting processor”. *Science* 364.6442 (2019), pp. 753–756.

[39] E. Dagotto, J. Riera, and D. Scalapino. “Superconductivity in ladders and coupled planes”. *Physical Review B* 45.10 (1992), pp. 5744–5747.

[40] T. Giamarchi. “Quantum Phase Transitions in Quasi-One-Dimensional Systems”. *Understanding Quantum Phase Transitions*. CRC Press, 2010. ISBN: 978-0-429-07562-9.

[41] K. Nawa et al. “Triplon band splitting and topologically protected edge states in the dimerized antiferromagnet”. *Nature Communications* 10.1 (2019), p. 2096.

[42] X. Zhang et al. “Universal control of four singlet–triplet qubits”. *Nature Nanotechnology* (2024), pp. 1–7.

[43] D. V. Bulaev and D. Loss. “Electric Dipole Spin Resonance for Heavy Holes in Quantum Dots”. *Physical Review Letters* 98.9 (2007), p. 097202.

[44] N. W. Hendrickx et al. “Sweet-spot operation of a germanium hole spin qubit with highly anisotropic noise sensitivity”. *Nature Materials* 23.7 (2024), pp. 920–927.

[45] F. N. M. Froning et al. “Ultrafast hole spin qubit with gate-tunable spin–orbit switch functionality”. *Nature Nanotechnology* 16.3 (2021), pp. 308–312.

[46] L. Mauro et al. “Geometry of the dephasing sweet spots of spin-orbit qubits”. *Physical Review B* 109.15 (2024), p. 155406.

[47] B. Hetényi. “Exchange interaction of hole-spin qubits in double quantum dots in highly anisotropic semiconductors”. *Physical Review Research* 2.3 (2020).

[48] C.-A. Wang et al. “Modeling of planar germanium hole qubits in electric and magnetic fields”. *npj Quantum Information* 10.1 (2024), pp. 1–9.

[49] D. Jirovec et al. “Dynamics of Hole Singlet-Triplet Qubits with Large g-Factor Differences”. *Physical Review Letters* 128.12 (2022), p. 126803.

[50] P. Harvey-Collard et al. “Spin-orbit Interactions for Singlet-Triplet Qubits in Silicon”. *Physical Review Letters* 122.21 (2019), p. 217702.

[51] E. G. Kelly et al. *Identifying and mitigating errors in hole spin qubit readout*. 2025.

[52] K. Ono et al. “Current Rectification by Pauli Exclusion in a Weakly Coupled Double Quantum Dot System”. *Science* 297.5585 (2002), pp. 1313–1317.

[53] H.-A. Engel et al. “Measurement Efficiency and n-Shot Readout of Spin Qubits”. *Physical Review Letters* 93.10 (2004), p. 106804.

[54] J. R. Petta et al. “Coherent Manipulation of Coupled Electron Spins in Semiconductor Quantum Dots”. *Science* 309.5744 (2005), pp. 2180–2184.

[55] A. E. Seedhouse et al. “Pauli Blockade in Silicon Quantum Dots with Spin-Orbit Control”. *PRX Quantum* 2.1 (2021), p. 010303.

[56] T. Lundberg et al. “Non-symmetric Pauli spin blockade in a silicon double quantum dot”. *npj Quantum Information* 10.1 (2024), pp. 1–12.

[57] M. Nurizzo et al. “Complete Readout of Two-Electron Spin States in a Double Quantum Dot”. *PRX Quantum* 4.1 (2023), p. 010329.

[58] C. V. Meinersen, S. Bosco, and M. Rimbach-Russ. *Quantum geometric protocols for fast high-fidelity adiabatic state transfer*. 2024.

[59] A. Impertro et al. "Local Readout and Control of Current and Kinetic Energy Operators in Optical Lattices". *Physical Review Letters* 133.6 (2024), p. 063401.

[60] S. Geyer et al. "Anisotropic exchange interaction of two hole-spin qubits". *Nature Physics* 20.7 (2024), pp. 1152–1157.

[61] J. Saez-Mollejo et al. "Exchange anisotropies in microwave-driven singlet-triplet qubits". *Nature Communications* 16.1 (2025), p. 3862.

[62] P. Jurcevic et al. "Spectroscopy of Interacting Quasiparticles in Trapped Ions". *Physical Review Letters* 115.10 (2015), p. 100501.

[63] M. Serbyn and J. E. Moore. "Spectral statistics across the many-body localization transition". *Physical Review B* 93.4 (2016), p. 041424.

[64] V. Oganesyan and D. A. Huse. "Localization of interacting fermions at high temperature". *Physical Review B* 75.15 (2007), p. 155111.

[65] A. S. Ivlev et al. "Coupled vertical double quantum dots at single-hole occupancy". *Applied Physics Letters* 125.2 (2024), p. 023501.

[66] H. Qiao et al. "Coherent Multispin Exchange Coupling in a Quantum-Dot Spin Chain". *Physical Review X* 10.3 (2020), p. 031006.

[67] A. S. Rao et al. "Modular Autonomous Virtualization System for Two-Dimensional Semiconductor Quantum Dot Arrays". *Physical Review X* 15.2 (2025), p. 021034.

[68] T.-K. Hsiao et al. "Efficient Orthogonal Control of Tunnel Couplings in a Quantum Dot Array". *Physical Review Applied* 13.5 (2020), p. 054018.

[69] M. Lodari et al. "Low percolation density and charge noise with holes in germanium". *Materials for Quantum Technology* 1.1 (2021), p. 011002.

7

CONCLUSION AND OUTLOOK

As long as there is a mystery for humankind, there will be poetry!

Gustavo Adolfo Bécquer

7.1. CONCLUSION

This thesis investigates two distinct parameter regimes of the Fermi-Hubbard model on a 2 × 4 Ge/SiGe quantum dot ladder. We explore the emergence and propagation of correlated spin and charge phenomena in the form of two types of quasiparticles: excitons and magnons. In chapter 4, the long-range Coulomb interaction and a difference in global detuning between both ladder legs reveal a region of electrochemical potentials where excitons are formed and can be transported using voltage pulses. In this parameter regime, around quarter filling, it is the Coulomb repulsion terms V (or, to be precise, the individual $V_{i,i+4}$ between dots in both ladder legs) which constitute the dominant energy scales. In contrast, at half filling (one spin per site), the Heisenberg exchange interaction terms $J_{i,j}$ dominate, leading to the observation of magnon and triplon propagation. These results, discussed in chapter 6, have been enabled by both applying, extending and developing methods for charge and spin tuning, initialization, local control and readout. One concrete example is the development of a barrier-barrier virtualization technique based on the spin-orbit anticrossing (Δ_{SO}), as showcased in chapter 5, which enabled the individual control of exchange interaction values over a wide range of voltages.

While the results achieved in this thesis have been extensively discussed, it is also informative to look at the broader goals that we set ourselves at the start of these experiments. For the exciton work, it was our intention to go beyond the slow charge sensing measurements reported in Fig. 4.5 to measurements of current, with the idea of observing correlations between the charge flow in the top and the bottom legs of the ladder. While we started exploring fast charge shuttling [1] and observing current flow upon biasing of the channels, we seemed to be limited by the presence of background currents in the device, which were likely emerging outside of the device's active area and were hard to calibrate out. For the magnon work, we aimed at observing a first signature of many-body localization by looking at the evolution of a Néel state for different values of exchange-over-disorder ratio [2]. While the preparation and readout of such a state was possible (see Fig. 6.24), we ran into sensor signal issues when trying to diabatically turn on many exchange interactions simultaneously during the analog evolution phase.

These two examples highlight what I personally consider one of the greatest challenges looking forward: an increasing device complexity also results in a growing number of failure modes and immensely complicates the tuning procedure. Many months of experimental work were spent navigating the multi-dimensional voltage space of the ladder device, carefully defining all voltage points and ramps required to operate an ever-increasing number of experimental steps. Ultimately, the experiments were limited by a combination of this complexity and other unknowns, which become increasingly more difficult to debug compared to small-scale devices. As opposed to other analog simulation platforms like ultracold atoms, where the starting point is a remarkably homogeneous potential landscape, this variability of local parameters is natural to the solid state. In this regard, the possibility of local control is not only an attractive feature of a quantum dot quantum simulator, but also a necessary requirement to even out local variability and enable any experiment in the first place.

It might be tempting to declare that, as device size and experimental complexity scale even further, the amount of time required to tune up and perform experiments

could soon surpass the timeline of a PhD contract[1]. But similar to the developments in the past decade concerning video-mode tuning, the standardization of routines and the development and establishment of new experimental techniques could speed up spin experiments with large quantum dot arrays in the future. Concretely, I believe that automatic or semi-automatic tuning routines with the aid of machine learning will not only be a subject of active research, but will soon become part of the standard operation and calibration of large quantum dot arrays. This, combined with the progress in material purity and the creation of regular gate stacks in industrial cleanrooms, leaves room for hope for the future quantum dot scientists, which should spend less time dealing with device jumps and long calibration routines, and devote more of their efforts to the acquisition of data and exploration of interesting physical phenomena.

I want to further highlight that, for digital quantum computing, one exciting experimental direction that is recently gaining traction is the development of high-fidelity shuttling protocols [4–6], which are surely moving the focus of the field from the realization of dense quantum dot arrays to sparse device architectures. These would not only enable non-local device connectivity, but also significantly reduce crosstalk between gates, ideally easing calibration and tuning routines. For analog simulators, the simultaneous activation of couplings still requires a dense operation. However, spin initialization and readout could be still performed away from the "interaction" area, similar in spirit to experimental realizations and proposals with reconfigurable arrays of atoms in optical tweezers [7].

All in all, the challenges ahead are substantial. But it does appear that large challenges are often matched in size by exciting scientific and technical developments. The work in this thesis hopes to not only highlight the existence of the former, but to have played a role in the development of the latter. I hope that in future years, more experimental and theoretical groups are convinced to join the efforts to build analog quantum simulators based on semiconductor quantum dots. This could be expected, as more complex quantum dot devices are becoming increasingly available to the broad scientific community, until very recently limited to few-qubit experiments.

7.2. OUTLOOK AND FUTURE DIRECTIONS

In this section, I will further outline possible experimental directions for future quantum simulation experiments, which either seem feasible in the short term, or worth exploring in the long run.

7.2.1. GEOMETRIC FRUSTRATION

Antiferromagnetic ordering, with antiparallel spin-spin correlations between neighboring spins, is prevented for certain lattice geometries. In the simple case of a triangular lattice, there is no straight-forward way to arrange spins such that all nearest neighbors

[1] There was a time where even the charge state tuning of large quantum dot arrays was questioned in the group due to its complexity. The time spent tuning the gate voltages as a function of the number of quantum dots anecdotally appeared to scale exponentially, an observation that became known informally as "Tim's law". [3]. Luckily, the establishment of RF reflectomentry and video-mode tuning, as well as the standardization of the tuning procedures, significantly aided charge tuning, which now can be done by hand in a matter of hours.

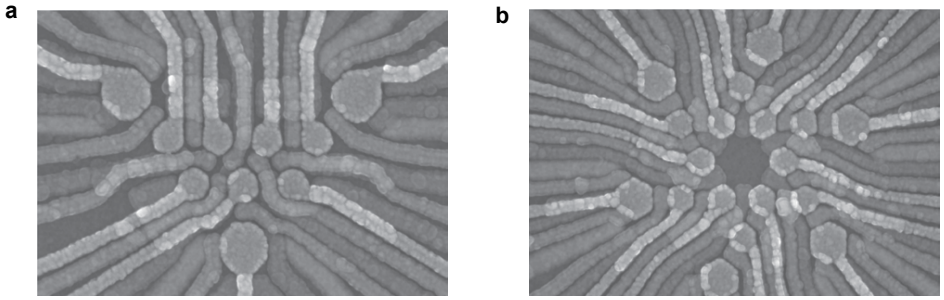

Figure 7.1: Scanning electron microscope images of two quantum dot lattices which could exhibit geometric frustration: (a) a triangular ladder, and (b) a Kagome unit cell.

are antiparallel with respect to each other. This so-called geometric frustration [8] can prevent spin ordering at low temperatures for real materials. Especially for lattices with a high degree of frustration like the Kagome lattice, it is debated whether the ground state can form a **quantum spin liquid**: a seemingly unordered but highly entangled macroscopic spin state. Probing quantum spin liquids still remains a challenging endeavour, with progress done with real materials and quantum simulators [9, 10].

With progress in scaling up beyond one dimensional quantum dot arrays, some of which demonstrated by the work in this thesis, larger and more complex quantum dot structures can be envisioned for future experiments. Fig. 7.1 showcases two SEMs of two quantum dot test structures fabricated in-house by Davide Degli Esposti, with quantum dots arranged in geometries which could allow for first experiments on magnetic frustration. Fig. 7.1a shows a triangular ladder, with seven quantum dots and three charge sensors and nearest-neighbor tunneling control for all quantum dot pairs. Fig. 7.1b showcases 12 quantum dots and 6 charge sensors arranged in a Kagome geometry, also with local tunnel coupling control. In both cases, the fabrication contains the same number of layers as for the square ladders of Fig. 3.1, and is experimentally compatible with the PCBs currently used in our experiments.

Probing magnetic frustration could require the measurement of spin-spin correlations, which were introduced in section 6.6 for the triplon quantum walk. For a simple three-dot system hosted within the ladder of Fig. 7.1a, correlations between single spins could be easily measured by projecting each of the three spins onto other neighboring spins, which would be used as ancillas. To tune to the homogeneous condition for three spins, initial simulations show that for $J_{12} = J_{23} = J_{13}$, an initial state $|S\rangle|\downarrow\rangle$ or $|S\rangle|\uparrow\rangle$ should not oscillate for a system with isotropic interactions [11], given the high symmetry of the system and degeneracy of spin eigenstates. Corrections due to differences in g-factors or exchange anisotropies should be explored and taken into account. Note that, precisely for a triangular quantum dot system, a novel three-qubit gate has been proposed which exploits the existence of strong spin-orbit coupling [12].

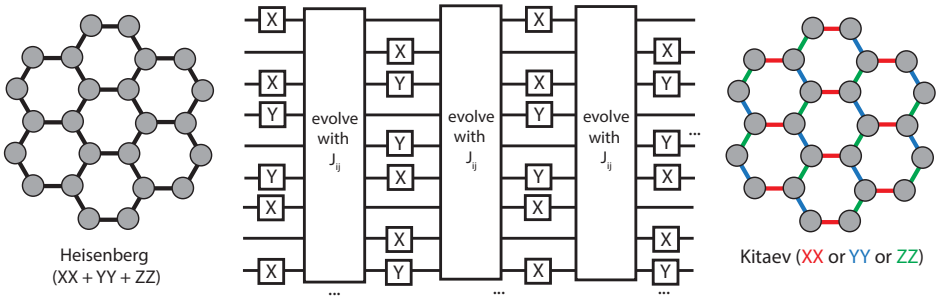

Figure 7.2: Proposal for simulating the Kitaev honeycomb model on a honeycomb lattice of quantum dots. At half filling, the combination of a native, Heisenberg Hamiltonian (left sketch) and interleaved single-qubit rotations (middle circuit) results in an average Hamiltonian of staggered XX, YY and ZZ couplings, depicted on the right side. This Hamiltonian is predicted to host a quantum spin liquid with non-abelian properties.

7.2.2. ANALOG-DIGITAL SIMULATIONS WITH SINGLE-QUBIT GATES

One fundamental limitation of purely analog quantum simulators is their non-universal character: we restrict ourselves to simulations of either the physical Hamiltonian that natively describes the platform, or of those which can directly be mapped to the Hamiltonian of the system. As we have demonstrated throughout this thesis, the Fermi-Hubbard nature of holes in quantum dot arrays already provides a plethora of regimes worth exploring. This is no surprise given the richness of the (extended) Fermi-Hubbard model itself, where many distinct phases of matter emerge (or are predicted to emerge) as a function of doping, geometries and interaction strengths. In chapter 6, we additionally demonstrate that we can combine analog and digital methods in a single framework, leveraging the capabilities of single- and two-qubit control for fast initialization of many different states as well as readout in different bases.

We can in principle extend this analog-digital approach to include single-qubit gates during the evolution phase, either with a local or global drive. This methodology, already theorized and explored for other physical platforms [13, 14], can enable the simulation of other, non-native Hamiltonians, and relies on the framework of **average Hamiltonian** theory [15]. This framework has been particularly useful to develop dynamical decoupling sequences which are either resilient to certain types of errors, or decouple complex spin-spin interactions in NMR systems [16].

In the case of analog simulations with quantum dots, an interesting use-case would be the simulation of the Kitaev honeycomb model [17, 18]. This analytically solvable model relies on the introduction of alternating XX, YY and ZZ couplings on the honeycomb lattice (see Fig. 7.2), and can be shown to host a quantum spin liquid with non-abelian properties. For an array of quantum dots arranged in a honeycomb lattice, and where the spin-spin interactions are described by the Heisenberg Hamiltonian at half filling, it is possible to envision a combination of single-qubit X and Y-rotations which, interleaved, result in the Hamiltonian of the Kitaev model (see circuit in Fig. 7.2). The introduced single-qubit sequences, of the CPMG or XY-4 type, should also introduce an additional decoupling of quasi-static noise, alleviating decoherence. Recently, the Kitaev

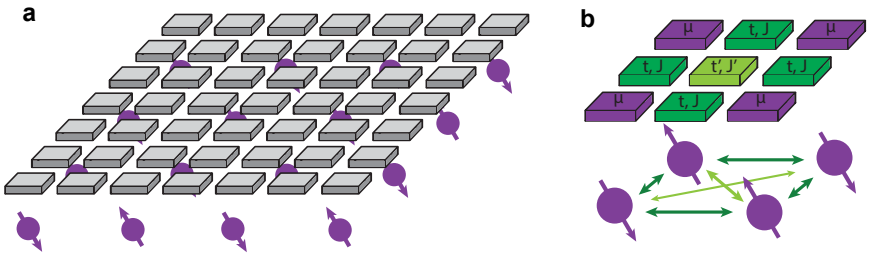

Figure 7.3: (a) A unit cell of a Fermi-Hubbard quantum simulator with control over t'/t. A central barrier gate could enable controllable diagonal coupling. (b) A two-dimensional Fermi-Hubbard (or Heisenberg) lattice of quantum dots. In addition to t' control, such a regular lattice of gates could enable the realization of multiple two-dimensional geometries within a single device.

model has been simulated using Rydberg atoms in optical tweezers [19].

A thorough theoretical analysis is beyond the scope of this thesis. Especially, the introduction of gates can itself add a further source of errors which propagate through the system in a similar way as for digital quantum computers. I mainly introduce this example to spark curiosity about the prospects of combining digital and analog tools beyond what is experimentally demonstrated in this thesis, and consistent with the current capabilities of spin qubit control in extended quantum dot arrays.

7.2.3. BACK TO THE FERMI-HUBBARD MODEL

One of the long-standing questions of solid-state research over the past half a century is the origin of high-temperature superconductivity [20]. Unlike conventional superconductivity, where the electron pairing is well-understood by electron-phonon coupling within the BCS framework [21], the physical origin of high temperature superconductors is still very much debated. In the paradigmatic example of cuprates [22], the phase diagram exhibits an antiferromagnetic Mott insulating ordering at zero doping, hinting at electron-electron interactions within the Fermi-Hubbard model as a possible origin of unconventional superconductivity. Understanding this phenomenon can be considered the holy grail of Fermi-Hubbard quantum simulators.

The arguments in favor of using semiconductor quantum dot arrays as Fermi-Hubbard simulators often include the achievable energy scales of $t/T > 10$ and $U/T > 100$ [23], with T the electron temperature, which could allow the simulation of the Hamiltonian ground state, as well as the local and in-situ control of Hamiltonian parameters. Apart from past quantum simulation experiments which explicitly explore the Fermi-Hubbard nature of quantum dots [23, 24], the following proposals explore other possible experimental directions.

CONTROL OF NEXT-NEAREST NEIGHBOR HOPPING

A recent theoretical study claims to demonstrate the absence of superconductivity in the "simple" Fermi-Hubbard model [25]. Concretely, other phases of matter such as stripe ordering [26] compete with the superconducting phase, making it challenging to compute which phase will have a lower energy. It has been speculated that the addition of

other elements to the Fermi-Hubbard model, such as beyond-nearest neighbor tunneling t', could stabilize the superconducting phase [25, 27]. Diagonal tunneling can also enable other novel phases of matter such as alter-magnetism [28]. These additional elements could be difficult to engineer in atomic systems, though there exist proposals for their realization [28].

Diagonal coupling control has been already reported in the literature for semiconductor quantum dots [29]. A relatively straight-forward way of adding a controllable, diagonal t' element to quantum dot arrays is by an additional control gate b_{ij} in the center of each plaquette (see Fig. 7.3a) [24, 29]. This geometry could allow for a wide range of tunability of t/t'. Note that a single barrier gate would be responsible for two diagonal couplings, rendering the homogenization of couplings challenging. While enabling this sort of two-dimensional geometry is currently challenging in academic cleanrooms using a lift-off process, progress in this direction has recently demonstrated in industrially fabricated samples using vias. In general, a dense two-dimensional array of quantum dots as depicted in Fig. 7.3b, could additionally benefit from reconfigurability [7], where quantum dots could be electrostatically defined with a combination of several gates and at different locations, potentially enabling the realization of different geometries within a single device.

RESILIENCE TO LONG-RANGE COULOMB REPULSION

One additional question is the interplay between long-range Coulomb repulsion and superconductivity in the Fermi-Hubbard model. Recent theoretical work has shown that in mixed-dimensional ladders, where an energy detuning between ladder legs boosts the strength of hole pairing, superconductivity is surprisingly robust to long-range Coulomb repulsion [30]. Interestingly, in this work, a dome-like feature at finite doping, similar to that of the cuprate phase diagram, seems to result from the addition of long-range Coulomb repulsion to the Hubbard model. While our platform offers a natural realization of long-range Coulomb repulsion, V tends to be much larger than tunneling. We encourage the theoretical exploration of the phase diagram of the two-dimensional Hubbard model for quantum dot arrays with realistic parameters, in order to assess the feasibility of our platform as a possible quantum simulator of the superconducting phase of the Fermi-Hubbard model.

EXPLORATION OF CHARGE DYNAMICS

Besides exploring the properties of ground states, observing the dynamics of charges and spins in analog simulators can shed light on the properties of the underlying Hamiltonian. For quantum dot arrays, it is generally believed that charge qubits (see sec. 2.3.1) are a sub-optimal qubit realization due to their short coherence times. While charges naturally couple strongly to charge noise, also the evolution timescales can be made very short (sub-ns) given the achievable tunnel couplings in the GHz range. Especially for Ge/SiGe, while the material properties have been consistently improved over the years, no charge qubit experiments have been attempted thus far.

In the field of analog simulations, an interesting use-case beyond the measurement of a single charge qubit could be the exploration of the collective dynamics of charges in a quantum dot ladder at quarter filling (see Fig. 7.4) [31]. As depicted in Fig. 7.4a, we consider a 2×4 ladder at quarter filling with suppressed tunnel couplings along the legs,

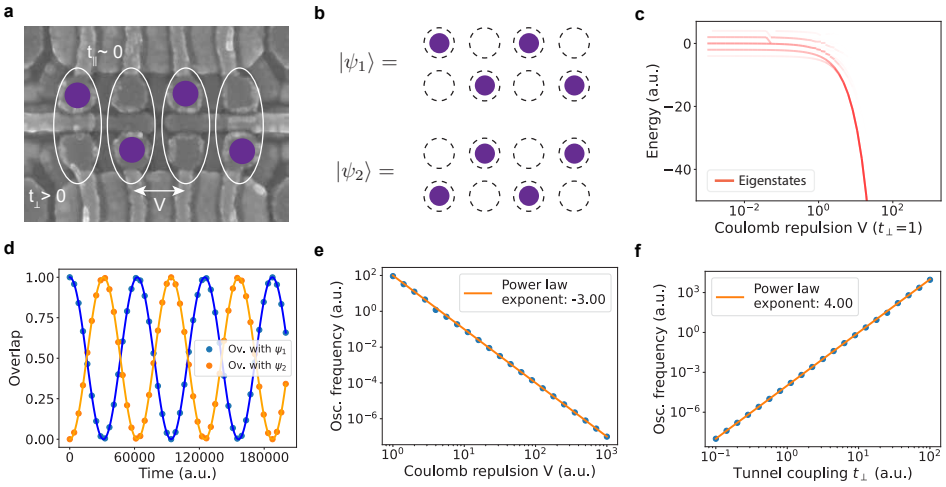

Figure 7.4: Proposal to study coherent and collective charge dynamics in a quantum dot ladder in the presence of long-range Coulomb repulsion. (a) SEM of 2 × 4 device at quarter filling, with one charge per rung (double quantum dot). Opposite to the exciton transport work, tunneling along the legs of the ladder is suppressed. Still, Coulomb repulsion is present between adjacent sites, and tunneling $t_\perp$ is allowed within the rungs. (b) In the presence of strong Coulomb repulsion and homogeneous parameters, the low-energy states $|\psi_1\rangle$ and $|\psi_2\rangle$ should be degenerate in energy. For the following simulations, we assume homogeneous V and $t_\perp$ throughout the array. (c) Simulation of the overlap of $|\psi_1\rangle$ with all charge eigenstates with total charge state of 4 for different $V/t_\perp$ ratios. At $V \gg t_\perp$, the state overlaps with two eigenstates of the system with a small energy splitting $t_\perp^4 \cdot V^{-3}$. (d) Simulation of the dynamics of an initial state $|\psi_1\rangle$ at $V/t_\perp = 100$. The overlap with the states $|\psi_1\rangle$ and $|\psi_2\rangle$ is plotted and fitted with a sine function, from which the oscillation frequency can be extracted. (e) Scaling of oscillation frequency as a function of V for fixed $t_\perp = 1$. A power law fit recovers the expected scaling exponent of -3. (f) Scaling of the collective charge oscillation frequency as a function of $t_\perp$ for fixed $V = 100$. A power law fit recovers the expected scaling exponent of 4.

but in the presence of intra-dimer coupling $t_\perp$ and nearest-neighbor Coulomb repulsion V. Through the long-range Coulomb interaction, the system's ground state is expected to be a superposition of the two "zig-zag" states $|\psi_1\rangle = |101010...\rangle$ and $|\psi_2\rangle = |010101...\rangle$ (Fig. 7.4b). This occurs at sufficiently large Coulomb interaction $V \gg t_\perp$, as simulated in Fig. 7.4c. Starting from an initial state $|\psi_1\rangle$, charges are expected to collectively oscillate between $|\psi_1\rangle$ and $|\psi_2\rangle$ with a frequency of $t^N \cdot V^{N-1}$, with N the number of ladder rungs. We simulate this oscillation behavior in Fig. 7.4d for $V/t_\perp = 100$, and observe the expected power law dependency of the oscillation frequency in Figs. 7.4e and f as a function of V and $t_\perp$, respectively.

While the resilience with respect to charge noise and parameter variability should be explored, an experiment like this could be an exciting first demonstration of correlated charge dynamics in quantum dot arrays.

BIBLIOGRAPHY

[1] A. R. Mills et al. “Shuttling a single charge across a one-dimensional array of silicon quantum dots”. *Nature Communications* 10.1 (2019), p. 1063.

[2] D. A. Abanin et al. “Colloquium: Many-body localization, thermalization, and entanglement”. *Reviews of Modern Physics* 91.2 (2019), p. 021001.

[3] Baart. “CCD operation and long-range coupling of spins in quantum dot arrays” (2016).

[4] I. Seidler et al. “Conveyor-mode single-electron shuttling in Si/SiGe for a scalable quantum computing architecture”. *npj Quantum Information* 8.1 (2022), p. 100.

[5] F. van Riggelen-Doelman et al. “Coherent spin qubit shuttling through germanium quantum dots”. *Nature Communications* 15.1 (2024), p. 5716.

[6] M. De Smet et al. “High-fidelity single-spin shuttling in silicon”. *Nature Nanotechnology* 20.7 (2025), pp. 866–872.

[7] D. Bluvstein et al. “Logical quantum processor based on reconfigurable atom arrays”. *Nature* 626.7997 (2024), pp. 58–65.

[8] C. Lacroix, P. Mendels, and F. Mila, eds. *Introduction to Frustrated Magnetism: Materials, Experiments, Theory*. Vol. 164. Springer Series in Solid-State Sciences. Berlin, Heidelberg: Springer, 2011. ISBN: 978-3-642-10588-3 978-3-642-10589-0.

[9] M. R. Norman. “*Colloquium*: Herbertsmithite and the search for the quantum spin liquid”. *Reviews of Modern Physics* 88.4 (2016).

[10] G. Semeghini et al. “Probing topological spin liquids on a programmable quantum simulator”. *Science* 374.6572 (2021), pp. 1242–1247.

[11] C. Esteve Boncompte. “Homogenization of exchange couplings in quantum dot arrays”. *Master thesis* (2023).

[12] M. T. P. Nguyen et al. “Single-step high-fidelity three-qubit gates by anisotropic chiral interactions”. *PRX Quantum* 6.3 (2025), p. 030326.

[13] J. Choi. “Robust Dynamic Hamiltonian Engineering of Many-Body Spin Systems”. *Physical Review X* 10.3 (2020).

[14] A. Kyprianidis, A. J. Rasmusson, and P. Richerme. “Interaction graph engineering in trapped-ion quantum simulators with global drives”. *New Journal of Physics* 26.2 (2024), p. 023033.

[15] A. Brinkmann. “Introduction to average Hamiltonian theory. I. Basics”. *Concepts in Magnetic Resonance Part A* 45A.6 (2016), e21414.

[16] L. M. K. Vandersypen. “NMR techniques for quantum control and computation”. *Reviews of Modern Physics* 76.4 (2005), pp. 1037–1069.

[17] A. Kitaev. “Anyons in an exactly solved model and beyond”. *Annals of Physics*. January Special Issue 321.1 (2006), pp. 2–111.

[18] M. T. P. Nguyen, M. Rimbach-Russ, and S. Bosco. *Color it, Code it, Cancel it: k-local dynamical decoupling from classical additive codes*. 2025.

[19] S. J. Evered et al. “Probing the Kitaev honeycomb model on a neutral-atom quantum computer”. *Nature* 645.8080 (2025), pp. 341–347.

[20] X. Zhou et al. “High-temperature superconductivity”. *Nature Reviews Physics* 3.7 (2021), pp. 462–465.

[21] J. Bardeen. “Theory of Superconductivity”. *Physical Review* 108.5 (1957), pp. 1175–1204.

[22] C. Proust and L. Taillefer. “The Remarkable Underlying Ground States of Cuprate Superconductors”. *Annual Review of Condensed Matter Physics* 10.Volume 10, 2019 (2019), pp. 409–429.

[23] T. Hensgens et al. “Quantum simulation of a Fermi–Hubbard model using a semiconductor quantum dot array”. *Nature* 548.7665 (2017), pp. 70–73.

[24] J. P. Dehollain et al. “Nagaoka ferromagnetism observed in a quantum dot plaquette”. *Nature* 579.7800 (2020), pp. 528–533.

[25] M. Qin et al. “Absence of Superconductivity in the Pure Two-Dimensional Hubbard Model”. *Physical Review X* 10.3 (2020), p. 031016.

[26] D. Bourgund et al. “Formation of individual stripes in a mixed-dimensional cold-atom Fermi–Hubbard system”. *Nature* 637.8044 (2025), pp. 57–62.

[27] E. Pavarini. “Band-Structure Trend in Hole-Doped Cuprates and Correlation with Tcmax”. *Physical Review Letters* 87.4 (2001).

[28] P. Das. “Realizing Altermagnetism in Fermi-Hubbard Models with Ultracold Atoms”. *Physical Review Letters* 132.26 (2024).

[29] N. Wang et al. “Highly Tunable 2D Silicon Quantum Dot Array with Coupling beyond Nearest Neighbors”. *Nano Letters* 24.42 (2024), pp. 13126–13133.

[30] H. Lange. “Pairing dome from an emergent Feshbach resonance in a strongly repulsive bilayer model”. *Physical Review B* 110.8 (2024).

[31] E. Demler and L. M. K. Vandersypen. *Private communication.*

ACKNOWLEDGEMENTS

This thesis, like the overwhelming majority of scientific work, is not and could not be carried out by a single person. Over these last five years, I have been extremely lucky to be surrounded by extraordinary people that have supported me scientifically and personally. I want to extend my deepest gratitude to all of them for their support throughout these wonderful and intense years.

Lieven, from the first time I heard one of your talks in 2019, it was your ability to transmit your passion for your research that caught my eye. Since then, you have not only supported me scientifically throughout all these years, by sharing your knowledge and expertise and by giving me the freedom to develop and pursue my own goals. You have also given me the space to share the more emotional aspects of my PhD, with kindness and understanding. I think this combination is unique and makes you a remarkable leader. Since the start of your spin qubit endeavours, you have not only accomplished a long list of achievements. You have done so by assembling a team of smart and kind people that make it a pleasure to be part of your group. I will always be grateful that you have given me the opportunity to work together.

Giordano, thank you for being my ~~co~~promotor. Your work and that of your amazing team lays the foundation of any of the experiments that we are able to do in the spin qubit groups, which should make you proud and for which I am immensely grateful. I have personally enjoyed all our conversations, whether to discuss the intricacies of germanium quantum dots, or about the best places to surf in Tenerife. Looking forward to your next birthday party!

Thank you also to **Immanuel**, **Gloria**, **Sander** and **Anasua** for agreeing to be part of my defense committee, I am honored and excited for the upcoming discussions.

Hanifa, starting and finishing our PhDs the same week hasn't just been a beautiful coincidence, and a fun fact about our friendship. It has meant that we have been able to grow as scientists and experience many of the good and ugly parts of this journey together. We have traveled, sung, sailed, partied, laughed and been angry at the world, and I cannot imagine a better person and friend to have lived through all of our adventures with. As the world keeps on spinning, and we keep on exploring it, I hope that our paths never stop crossing. Don't forget that we're still peaking!

Daniel, it is scary to meet someone whose brain works so similarly in so many ways. Working together has been a pleasure, squaredly exciting, and sometimes a bite intense. Even as Vienna was waiting for you, you stuck around for enough time to make the most amazing piece of work, a real tour de France effort! Now seriously, I have learned so many things from you throughout these years, and not just about singlet-triplet qubits. You didn't just become a very close friend, but someone to look up to, as a scientist and as a person.

Working on quantum simulations can be a challenging endeavor, and I have been extremely lucky to have the amazing quantum simulation team to do this with.

Tzu-Kan, throughout the first two years of my PhD, you guided me through my first steps and taught me everything there was to know about fridges, device designing, testing, tuning, and so much more. We fought together to tune a device which turned out to be not the easiest to work with, but in the end we managed to make a paper we can both be proud of. I always admired your patience and dedication, and I will forever be grateful to have started this quest alongside you.

Sjaak, when I started my PhD, I was soon aware that yours were big shoes to fill. It was a beautiful coincidence that our paths crossed again so many years later, thank you for all these (very!) productive writing sessions and coffee drinking, as well as our discussions about what our next life steps will be. I'm happy we've both made a decision, and that it entails to stay in the same city for some more time.

Liza, it has been a pleasure to be the group's quantum simulation PhDs together. And how intense has this time been! I'm grateful that we have been able to share our struggles and also our happy moments throughout this time. You should be proud of the experiments and results that you have achieved, even if sometimes they don't feel like everything you wanted (believe me, I know the feeling). We have a wonderful year full of terraforming and brunches ahead of us.

Xin, your patience and perseverance are admirable. You pushed through with very complex experiments on a complex device, and did so with determination and ambition. I am very happy that we have been able to share these years together. I wish that your future experiments with germanium bring you more joy and perhaps a bit less complexity. And the same goes for the beautiful adventure of becoming a father.

Luckily, the future of quantum simulations with quantum dot arrays is in good hands (no pressure)! **Stefano**, it was great to share some months of exciting measurements in the lab at the start of your postdoc, I hope you're not already missing STM qubits or Korean food too much. **Noah**, I was very happy to see you bringing in a lot of discipline and knowledge to the team from the start, and I'm very curious to see where your PhD takes you. **Jaime**, after many years of seeing each other at conferences, I'm really happy that you decided to join Delft and bring in your germanium knowledge and your kindness to the team. **Elia**, good luck with the measurements, I'm sure your dedication and curiosity will pay off and you'll soon measure the longest of chains.

But there is more to life than quantum simulations. The spin qubit groups are filled with smart, hard-working people that I've had the pleasure to meet, work and become friends with.

Davide, your kindness and willingness to help others with their problems in the lab really bring the groups forward, especially when there is "so much nonsense" around. But of course, the thing I'm most grateful about is our friendship! Now that we both have decided to stay around Delft for some more time, I'm looking forward to many more bike rides to the beach, lots of pasta a la norma and singing non-heterobasic songs together.

Uri, spending time with you brightens my days. Whether it is drinking cappuccinos in cute cafés, traveling the world together, getting all competitive when playing board games, or just making weird noises: I'm very grateful that we got to spend all these years together. I hope that we get to share the same city again soon, and be the loudest and most beautiful potaxies the world has ever seen (gawk!). Estic molt agraït per la nostra amistat.

Brennan, your brilliant mind and your kind heart have made you accomplish an excellent PhD (you're almost there!). Thank you for always being there for a healing hug. I will miss our intense life catch-ups playing Twilight Struggle, and nerding out over crosswords and trivia questions with you. As scary and uncertain new life chapters can be, I look forward to hearing all your exciting new adventures, and being part of them when I get to crash on your couch again.

Irene, I am grateful that I have been able to meet a person like you through this journey, who shares the same passion for fundamental science and who I could spend hours discussing many-body physics with. Thank you for the long hours bonding over our very Spanish upbringings and having deep, philosophical and spiritual conversations trying to make sense of what's going on. I hope the next life chapter brings you the peace, the sun and the thrill that you deserve. I shall keep on sleeping in your guest room, wherever you are.

Maia, I met you when you were a Bachelor student learning what the hell was going on in the lab (turns out, so was I!). Since then, you've become a dear friend, we have shared a stage together and so many fun memories, with many more to come. Keep on singing your heart out, aunque sea sinmigo. Basel is lucky to have you.

Karina, ever since Hanifa and I lured you to come to Delft, you have blessed QuTech with equal parts of solid-state knowledge and exquisite style. I have always enjoyed our hours-long catch-ups over a beer or a fancy dinner. I am sure many of those will keep on happening this year.

Alberto, you're not just a smart and capable scientist, and a passionate and driven founder, but you also have the ability to brighten the day of the people who are around you. Thank you for all these wonderful years, all the sailing and dancing together, I hope we get to share many more nights of pasta eating, guitar playing, saunas and salsa parties.

Eline, being semi-office mates allowed us to share a laugh or a little rant every now and then, and I have missed you around since. Thank you for the good times we had touring the US and for the wholesome evenings with **Jasper**, **Cas** and **Lena**. Luckily, Mechelen is not far away from Delft.

Bea, you definitely brought the right energy to the labs, getting us all out of the COVID mindset and into the "let's do things" one. Now fate has decided that we should become doctors the same day, but I hope there will be many more occasions to celebrate our friendship together.

Offices are places where people spend a big portion of their work life, and I have been lucky to share these hours with great people. **Kenji**, sharing an office with you has not just been fun, but has also made me finally realize that you're not a Master student anymore. I hope we can share many more intense game nights and future train rides to Belgium with you and **Eliana** (and perhaps her brother). **Yuta**, you are a true inspiration to be around with, always coming up with new and exciting research ideas, which are sometimes hard to understand but somehow always work. Keep on being who you are and rocking the lab and the basketball field. **Corny**, beyond the short period of office-sharing, thanks for all the fun times bonding over choir harmonies or the beautiful Polish language. Thank you for being the best bober a friend could hope for. **Amir** and **Luka**, although for a short time, I really enjoyed being work roomies!

Maxim, you are the true example that hard work and perseverance pay off in the end, you should be proud of all the great results you have achieved. I hope we get to share many more Belgian beers, brunches and garden barbecues.

Carles, thank you for being a very disciplined and hard-working Master student, you made supervising you the easiest job in the world. I always enjoyed our scientific discussions and our Catalan with Carles sessions. TNO is lucky to have you!

Nicola, I enjoy spending time with you and I deeply appreciate you acknowledging my puns. I wish you a big aaarmy of people to help you accomplish your PhD goals. **Sander**, you've heard this many times before, but: your work truly enables so many of the things we do in the lab, and I'm extremely grateful for it. It's also beautiful to see that you're having fun while doing it. I hope we can share the stage again very soon. **Tobias**, it has been great to see you come back to the group and share a few years in the lab. The third PhD year is tough, but I'm sure you will make the best out of it. Also for you, **Parsa**, I hope those resonators start resonating soon and get you to produce amazing results. **Minh**, I'm excited to see how many more different and colorful science you get up to during the next years. **Sam**, keep on making people's tuning lives easier, I hope to bump into you in many more weddings. **Marcin**, good luck shuttling spins around!

Big shout-out to our fab-ulous fab team! **Stefan**, your work in the cleanroom is quite literally the reason any of the papers in this thesis exist, for which I am immensely grateful. You work with dedication and thoroughness, systematically iterating through many fab rounds and learning from them. Like this, you managed to fabricate the silver device, and then the golden one. We have been truly lucky to have you. **Lara**, you have not only been a hard-working and dedicated fab engineer, but also a lovely person to spend time and discuss with, whether at a sunny conference in San Sebastián or with a nice breakfast before work. I hope we keep on sharing croissants at Michel for much longer.

Working in the Vandersypen lab also means that we stand on the shoulders of giants. **Stephan**, I wasn't just lucky to learn from your wisdom, knowledge and help at the beginning of my PhD, but to continue hanging out even after you moved on to your next life chapter. Here's to many more ramen dates to come. **Anne-Marije**, I have always felt like I could count on you: Whether to learn from your experience as a PhD student, to discuss the best interpretation of quantum mechanics, to go through the QuTech band set-list or just to talk about how we are feeling. I hope to see you Grooving for many more years. **Will**, I really enjoyed sharing my first year PhD experiences with you over many (!) beers, the times we got to jam together, and being able to catch up about life and research every time someone defends their PhD. Hopefully the next catch-up is happening soon. **Florian**, you're one of the first people I met in Delft, thank you introducing me to the Delft life and for enabling the Groyo. I hear that Australia is treating you well, perhaps I should pass by for a climbing session or some croissant-making together. **Rick**, you were not just a great Master student, but also an excellent beer drinking companion. Thank you for introducing me to the Dutch student life, it's great to see you being a big ol' Rick at TNO now. **Jurgen**, we have been working close to each other for so many years, and I was very happy to see all those great results you got after lots of hard work and perseverance. I'm excited to see you defend soon too. **Xiao**, you are a true legend of spin qubits! I expect some great results coming from your lab very soon. Also, I hope I didn't annoy you too much with my broken Mandarin all those years ago (it didn't really get better over

time). **Job**, thank you for all those nice coffee breaks and bike tips at the beginning of my PhD. **Alexandra**, I'm very happy to see you having fun with STM spins and catching up with you at TPKV or reggaeton parties. **Tobias**, **Patrick**, **Sergey**, **Mateusz**, **Nodar** and **Guoji**, it was a pleasure to share the first part of my PhD with you.

Not only the Vandersypen lab, but also all the spin qubit groups are filled with amazing people that I have had the honor to work with.

Asser, you have mastered the art of tuning up germanium spins, I always enjoyed our chats and discussions and all the fun times outside the lab. I hope there will be many more snakey terraforming evenings soon. **Desa**, you're the perfect combination of a dedicated scientist, an amazing singer and a fun person to party with. To more Macumba parties together! **Barnaby**, you're brilliant both with spins and with bikes, we should finally go for a ride together this spring. **Floor**, thank you for all the music we've made together and for all the nice discussions about science and beyond. **Valentin**, it was great to be able to share our struggles and problems when working on large germanium devices, I'm excited to see where your Munich adventure takes you. **Chien-An**, you are a source of knowledge and inspiration, I hope superconducting systems are treating you as well as germanium spins did. **Francesco**, thank you for all the insightful discussions about germanium and for all the help and tips. I hope Copenhaguen is treating you well. **Lucas**, thank you for all those nice chats around the coffee table, and congratulations on your well-deserved PhD. **Sasha**, your cleverness and dedication are admirable, I hope you can squeeze out lots of sweet results from your sugarcane device. **Damien**, the same goes for you, it is amazing to see you come back to the (dark) academic side. **Corentin**, seeing you become everyone's postdoc in your group says a lot about your dedication and ability to make things work better. **Cecile**, I hope you keep on being an avid board game player and that Majoranas are treating you well. **Marion**, we had a short overlap in the lab, but I would love to catch up around QuTech soon. **Vlad**, congratulations on finally earning your well-deserved PhD. **Daan**, thank you for being a coding genius and making our lives easier in the lab. **Luca**, thanks for opening the office door for me countless times. **Elisa**, I'm sure you will accomplish great things in the cleanroom. **Menno**, thank you for all the insightful discussions about germanium and all the things I have been able to learn from you and your group, it's always a pleasure to witness your creative mind at work. **Max**, learning from your infinite theory wisdom has been a pleasure over these years. **Stefano**, I was very happy to see you join QuTech and for our discussions about many-body physics and germanium anisotropies.

Also a big shout-out to the new generation, a.k.a. the high-schoolers! **Zarije**, we became friends so many years ago in Munich, and it is so exciting to see you now thriving as a PhD student and an amazing singer in the QuTech band. To more music and coffee breaks together. **Chris**, the fact that we share our German school upbringing, slept in the same dorm in Munich and our partners work in Belgium makes me wonder whether I should have become a theorist too. **Michèle**, your dry humor always makes me happy, keep on being awesome. **Federico**, I wish that you have as much fun tuning spins as you have dancing to techno. **Dario**, with or without bilayers, I'm sure you will get to do great things during your PhD. **Edmondo**, I'm glad that you got convinced you to join QuTech after showing you how nice interview dinners can be. **Alice**, I was very happy to see you join the groups after your Masters, I hope we get to spend some more time together soon.

But not only the spin qubit groups are filled with amazing people!

Nick, thank you for all the chill evenings and heartwarming conversations about life. Let's have as many spontaneous pizza dates and coffee breaks as we can this year. And as hard as it is to get two southern Europeans to plan stuff, I hope our island exchange trip happens very soon.

Matteo, thank you all of the amazing music together, whether with the band, Fridays after work or with the great Mariachis. You have truly made me love playing music more than I did before. For more years of fun and jams to come, getting hit by flacas one more time. Barcelona 2027?

Julia, ever since we started planning an Uitje together, I knew that this was the start of a wonderful friendship. I'm grateful for becoming wine moms together, and all those nice double dates filled with food of variable lekker-ness and exciting jewel hunting. Good luck to you and **Bart** on your new adventure across the pond.

Nina, thank you for all those lovely and therapeutic coffee dates, it is always so easy with you to speak my heart out and to share our thoughts and feelings. Now that **Stefan**, you and I have made it back to Delft, I hope that many of these will happen again soon.

Gustavo, over these years, we haven't just shared a stage, exciting innuendos and countless tiramisus. You have become a close friend who I could hang around with for hours, listening to your cousin-related adventures or learning about the best workout routines. Keep on being a caring and loving father to **Cecilia** and **Francisco**, a hard-working TNOer and simply an awesome person.

Vicky, hanging out with you was always this beautiful combination of laughing and crying about all of the crazy ups and downs of PhD life and the world. I hope you pass your oposiciones with flying colors and that you get to work on something that brings you joy. I also hope you come visit to Delft soon to share another fancy breakfast at Kek.

Christina, I always enjoyed our chill coffees and brunches, and bonding over being the odd quantum simulation people in a gate-based world. I am sure the end of your PhD will give you lots of peace and that you will be proud of all the things you have achieved. Shall we try to tackle those music sheets again soon?

Luc, whether it is planning Uitjes, rocking it on stage, running the longest of trails or making a useful quantum business: nothing can stop you! I'm glad that we got to share many of these moments together, whether on stage or around a brunch table. I'm sure that many more will happen soon.

Tobi, your positive energy is contagious, it's always really fun to hang out with you. I heard that your go-no go went amazingly well, and I'm sure the next years of PhD will be the same.

Stephan, I love that me stopping you in the halls of QuTech to discuss interpretations of quantum mechanics led to beautiful evenings of philosophical discussions and you crushing me at chess. I'm glad to see you've join the academic side once again.

QuTech is so much more than the PIs, PhD students and postdocs. A really big thank you to the QuTech technicians, who make our lives as PhD students infinitely easier. **Olaf** and **Jason**, thanks for all of the help in getting the fridges and the bonder up and running, and with putting up with the most basic questions you could possibly imagine to answer. Thank you also to **Raymond**, **Raymond**, **Tom**, **Jelle**, **Vinod**, **Roy**, **Erik** and **Siebe** for your amazing work. **Marja**, thank you for putting up with our chaos and for making our work

so much smoother behind the scenes. I hope the retirement life is getting more and more exciting over time. **Aldo**, thank you for actively promoting and supporting science communication and for all those wonderful QuTech Speaker events. **Erik**, thank you for always counting on me for many lab tours. And very importantly, a big thank you to the food truck people who make our stomachs full and give us the energy to keep on working. **Romy** and **Simone**, I owe you both a party at Ferry.

My time at QuTech wouldn't have been the same without the Wednesday rehearsals, the dinners at Il Peperoncino and the fun gigs with the QuTech band. **Gustavo**, **Matteo**, **Maia**, **Floor**, **Anne-Marije**, **Will**, **Luc**, **Desa**, **Zarije**, **Hanifa**, **Sander**, **Laurens**, **Bart**, **Chris**, **Hans**, **Guido**, **Julia**, and **Nick**: thank you for the music!

I am honored to be able to stick around QuTech for some more time by pursuing a postdoc in the Kouwenhoven lab. **Leo**, thank you so much for this exciting opportunity, I'm looking forward to many insightful discussions. **Francesco**, **Bart**, **Nick**, **Vincent**, **Florian**, **Antonio**, **Sabpreet**, and the rest of the QuRe team: I'm looking forward to getting to know you over the next months, and to all the exciting results that will follow! **Sebastian**, I hope that we can stay in touch and we can share some nice discussions even as you move to Switzerland.

I am very grateful for the friends outside of QuTech who have made life in the Netherlands so much more fun. **Laura**, I cannot imagine a better person to share a hotpot, a chill board game evening or our love for Hannah Montana with. Thank you for being the best free real estate agent, and a loyal member of the exclusive yaughties club with the amazing **Kees** and **Nayan**. I am sure that Basel will bring you lots of fun and exciting moments, and I hope that I can share many of those with you soon.

Margot and **Fija**, sharing a house with you was the best way to start my life in the Netherlands. Thank you for showing me the depths of the Dutch language and culinary experience, for dealing together with frat boys and a bite creepy neighbors, and for your understanding when the kaasschaaf went "missing". Margot, I'm looking forward to a beautiful 2026 of extra roomie time, and perhaps one or two more lasertag games.

Noa, thanks for being a kind and thoughtful friend, for being open to exploring your nerdy phase together with the amazing **Podge**, and for motivating each other to work and feeling the royal-est at the KB. And of course, thank you for the beautiful cover design.

Garazi, eskerrik asko for sharing with me the beautiful landscapes of your hometown, and for all those deep conversations over a coffee or a tasty lunch.

Ayla, thank you for having the best music taste and your strong and courageous political engagement, I hope 2026 brings more latino music festivals and ceviches together.

A big thank you to the Munich people for all those amazing study years. **Andi**, dank dir habe ich die wunderbare Welt der Quantenphysik entdeckt. Ich bin dankbar für unsere Freundschaft, und ich bleibe sehr gespannt darüber, wohin deine Start-up-Reise führt. **Oskar**, **Mabroor**, **Benni**, **Maxi**, **Stefan** und **Baki**, danke für die tolle und intensive Zeit, wo wir die faszinierende und frustrierende Welt der Physik gemeinsam erkundet haben (auch wenn sie uns oft nur einen Zeh zeigt). **Daniela** und **Sarah**, danke für die wunderschönen Jahre voller Reisen, Lieder und Pancakes.

Diana, **Brigitte**, **Gotthard**, **Timo** und **Christian**, die Zeit mit euch in Meilschnitz ist immer eine wunderschöne und heilende Auszeit vom stressigen Alltag, danke für all die schönen Momente und für eure Zärtlichkeit und Gelassenheit. Ich bin echt dankbar,

euch als meine deutsche Familie zu haben.

A todos mis amigos de Tenerife: gracias por todo el amor y el apoyo durante tantos años. En especial, **Victoria**, además de conocernos desde hace casi 25 años, en este último tiempo me has sabido apoyar con todo tu cariño y me has ayudado a mantenerme sano en los momentos más complicados. Espero que sigamos formando parte de nuestras vidas muchos años más. **Ruti**, también a ti te agradezco muchísimo todo tu cariño y amistad, crecer junto a ti ha sido de lo mejor que me ha podido pasar. A las dos: gracias por compartir este día tan especial conmigo.

Juanga, a pesar de la distancia, siempre has sido como un tío para mí. Significa mucho que estes aquí compartiendo un día tan importante conmigo.

Papá, **mamá**, **hermanita** y **Marisa**: no podría imaginarme celebrar un momento tan importante para mí sin ustedes a mi lado. Gracias por estar siempre ahí para mí, apoyándome en los momentos difíciles, celebrando las alegrías y ayudándome a seguir soñando. Por muchos más viajes y momentos felices juntos. ¡Les quiero muchísimo!

Ralf, it was a long time ago when you came back from Delft full of excitement, and you were able to convince me that maybe this could be our next life step. It turned out that Delft also seemed to have a quantum physics institute. So it is safe to say that this thesis is quite literally a product of your charming (and thinking) skills. Danke für diese wundervollen Jahre, die stetige Unterstützung, deine Offenheit, Zärtlichkeit und Liebe. Du strahlst und machst die Welt schöner für alle Menschen um dich herum. Por muchísimos años más compartiendo la vida juntos. Te quiero.

CURRICULUM VITÆ

Pablo COVA FARIÑA

05-09-1996 Born in Santa Cruz de Tenerife, Spain

EDUCATION

2014–2017 Bachelor of Science in Physics
Technische Universität München, Munich

2017–2020 Master of Science in Condensed Matter Physics
Technische Universität München, Munich
Thesis: Dynamical decoupling of erbium spin ensembles with strong anisotropic interactions
Supervisor: Prof. Dr. Andreas Reiserer

2017 Exchange student
Nanyang Technological University, Singapore

2020–2025 PhD. Physics
Delft University of Technology, Delft
Thesis: Analog quantum simulation of spin and charge quasiparticles on a quantum dot ladder
Promotor: Prof. dr. ir. L.M.K. Vandersypen
Co-Promotor: dr. G. Scappucci

LIST OF PUBLICATIONS

7. D. Jirovec*, S. Reale*, **P. Cova Fariña**, C. Ventura-Meinersen, M. T. P. Nguyen, X. Zhang, S. D. Oosterhout, G. Scappucci, M. Veldhorst, M. Rimbach-Russ, S. Bosco, L. M. K. Vandersypen, *Many-body interferometry with semiconductor spins*, arXiv preprint arXiv:2511.04310 (2025).

6. **P. Cova Fariña***, D. Jirovec*, X. Zhang*, E. Morozova*, S. D. Oosterhout, S. Reale, T.-K. Hsiao, G. Scappucci, M. Veldhorst, L. M. K. Vandersypen, *Site-resolved magnon and triplon dynamics on a programmable quantum dot spin ladder*, arXiv preprint arXiv:2506.08663 (2025).

5. D. Jirovec*, **P. Cova Fariña***, S. Reale, S. D. Oosterhout, X. Zhang, E. Morozova, S. de Snoo, A. Sammak, G. Scappucci, M. Veldhorst, L. M. K. Vandersypen, *Mitigation of exchange crosstalk in dense quantum dot arrays*, Phys. Rev. Applied **24**, 034051 (2025).

4. X. Zhang*, E. Morozova*, M. Rimbach-Russ, D. Jirovec, T.-K. Hsiao, **P. Cova Fariña**, C.-A. Wang, S. D. Oosterhout, A. Sammak, G. Scappucci, M. Veldhorst, L. M. K. Vandersypen, *Universal control of four singlet–triplet qubits*, Nature Nanotechnology **20**, 209–215 (2025).

3. T.-K. Hsiao*, **P. Cova Fariña***, S. D. Oosterhout, D. Jirovec, X. Zhang, C. J. van Diepen, W. I. L. Lawrie, C.-A. Wang, A. Sammak, G. Scappucci, M. Veldhorst, E. Demler, L. M. K. Vandersypen, *Exciton transport in a germanium quantum dot ladder*, Phys. Rev. X **14**, 011048 (2024).

2. B. Merkel*, **P. Cova Fariña***, N. Herrera Valencia, A. Reiserer, *Dynamical Decoupling of Spin Ensembles with Strong Anisotropic Interactions* , Phys. Rev. Lett. **127**, 030501 (2021).

1. **P. Cova Fariña***, B. Merkel*, N. Herrera Valencia, P. Yu, A. Ulanowski, A. Reiserer, *Coherent Control in the Ground and Optically Excited States of an Ensemble of Erbium Dopants*, Phys. Rev. Applied **15**, 064028 (2021).

**These authors contributed equally*

ISBN: 978-94-6518-257-5